# On Controllable Elastohydrodynamic Fluid Film Bearings

**Haugaard, Martin Asger; Klit, Peder**

*Publication date:*
2011

*Document Version*
Publisher's PDF, also known as Version of record

# On Controllable Elastohydrodynamic Fluid Film Bearings

PhD Thesis

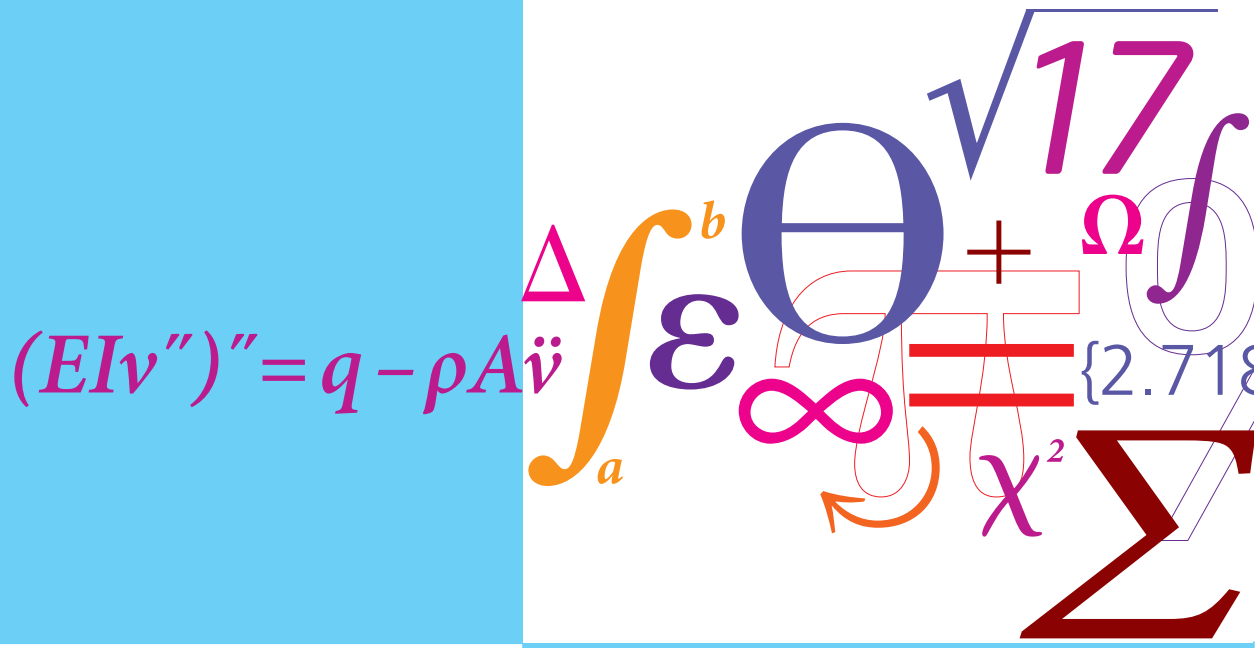


Asger Martin Haugaard
DCAMM Special Repport No. S125
May 2010

DTU Mechanical Engineering
Department of Mechanical Engineering

On Controllable Elastohydrodynamic Fluid Film Bearings

Asger Martin Haugaard
Section for Solid Mechanics
Department of Mechanical Engineering
Technical University of Denmark
2800 Lyngby, Denmark

Published in Denmark by
Technical University of Denmark



Section for Solid Mechanics
Department of Mechanical Engineering
Technical University of Denmark
Nils Koppels Alle, Building 404, DK-2800 Kgs. Lyngby, Denmark
www.mek.dtu.dk

Publication Reference Data:
Haugaard, A.M.
On Controllable Elastohydrodynamic Fluid Film Bearings
PhD Thesis
Technical University of Denmark, Section for Solid Mechanics
March 2011
ISBN No.: 978-87-90416-47-8
DCAMM Special Report No.: S125
Key words: Tribology, control, vibrations, fluid structure interaction, dimensional analysis

"We have shown that scientific knowledge consists of a sequence of abstract models, preferably formal, occasionally material in nature. We shall now proceed to examine the results of carrying model-making to the limit. Consider first material models. They start by being rough approximations, surrogates for the real facts studied. Let the model approach asymptotically the complexity of the original situation. It will tend to become identical with that original system. As a limit it will become that system itself. That is, in a specific example, the best material model for a cat is another, or preferably the same cat." (Rosenblueth and Wiener 1945 [1]).

# Preface

This thesis is submitted as partial fulfilment of the requirements for awarding the Danish Ph.D. degree. It documents research, which was undertaken by the author from March 2007 to May 2010 under the supervision of Associate Professor Dr.-Ing. Ilmar Ferreira Santos at the Department of Mechanical Engineering (MEK), Technical University of Denmark (DTU). In august 2010 Associate Professor Santos decided that he could not continue in his role as supervisor. At that point Professor (and former student of the late Jørgen W. Lund) Peder Klit agreed to take over. For this, I am indebted to Peder.

Part of the project was carried out at the Centre for Intelligent Machines (CIM) at McGill University, Montreal, Québec, Canada under the supervision of Professor Jorge Angeles. I would like to thank him and everybody at CIM for making this possible.

Also, I would like to thank Associate Professor, dr.techn. Jon Juel Thomsen for playing a pivotal, if informal, role in my professional development. Some readers will recognise Jon's indirect influence on this thesis.

In addition, several people deserve recognition for moral support beyond expectation, proofreading and in some cases for qualified academic inspiration. Ze Pedro Albergaria Amaral Blasques, Ramin Moslemian, Mads Wissenberg, Martin Nymann Svendsen, Edgar Estupiñan, Alejandro Cerda and Bo Bjerregaard Nielsen have all contributed in each their own way. This thesis is as much as anything a product of their help and inspiration.

Finally, I wish to thank my sister Anna and my father Kjeld for their support and patience.

# Abstract in English

This thesis gives a theoretical description of the active tilting-pad journal bearing (ATPJB). It provides the qualified reader with the tools to model an ATPJB, while staying clear of pitfalls. The model is based on well known techniques and allows for local stability analyses, harmonic stationary analyses as well as nonlinear time domain analyses of ATPJBs. Examples of all of these analysis types are presented. As opposed to some of the more convoluted modelling methods in the literature, the presented one permits dimensional analysis in a straight forward and intuitive manner. Dimensional analyses are performed for a tilting-pad journal bearing (TPJB) and an ATPJB under static conditions, followed by a generalisation to dynamic conditions (transient as well as stationary harmonic). These analyses will be of interest to experimentalists, since they permit experiments performed on scaled down test rigs to be extrapolated to the full size product in a confident manner. Finally, a selection of simulation results is presented. These prove that ATPJBs show promise in attenuating some of the limitations of TPJBs. But also, they show that ATPJBs should be modelled, tuned and implemented with great care, since the addition of a control system may just as well harm rotor-bearing performance as improve it.

# Resumé på dansk

Denne afhandling beskriver teorien bag regulerede vippeskolejer. Den giver den indviede læser værktøjerne til at udvikle en matematisk model af et reguleret vippeskoleje, og samtidig holde sig fri af faldgruberne. Modellen baserer sig på velkendte metoder, og kan benyttes til lokal stabilitetsanalyse, stationær harmonisk frekvens respons analyse samt beregning af ikke lineære tidsserier. I modsætning til nogle af de mere omstændelige modelleringsmetoder fra faglitteraturen, er den præsenterede fremgangsmåde velegnet til dimensionsanalyse. Dimensionsanalyse er nyttig i eksperimentplanlægning, da den forklarer lovmæssighederne bag ekstrapolering af eksperimentelle resultater fra nedskalerede laboratorieopstillinger til produkter i fuld skala. Dimensionsanalyser udføres for et passivt vippeskoleje og for et reguleret vippeskoleje under statiske forhold. Efterfølgende generaliseres analyserne til dynamiske tilstande. Til slut præsenteres udvalgte simuleringsresultater. De viser at regulering er et lovende værktøj til håndteringen af vippeskolejers ellers iboende begrænsninger. Men samtidig må det konkluderes at matematisk modellering, justering og implementering af reguleringssystemer i vippeskolejer bør foretages med stor omhu, da reguleringssystemet lige så vel kan ødelægge lejets egenskaber som forbedre dem.

# List of publications

The work in this thesis is complemented by papers in journals and conference proceedings. The journal papers are included in appendix C.

## Journal papers

A. M. Haugaard, I. F. Santos, Elastohydrodynamics Applied to Active Tiliting-Pad Journal Bearings, ASME Journal of Tribology 132 (2) (2009) 1–10

A. M. Haugaard, I. F. Santos, Multi Orifice Active Tilting-Pad Journal Bearings - Harnessing of Synergetic Coupling Effects, Tribology International 43 (8) (2010) 1374–1391

A. M. Haugaard, I. F. Santos, Stability of Multi Orifice Active Tilting-Pad Journal Bearings, Tribology International 43 (9) (2010) 1742–1750

## Conference papers

A. M. Haugaard, I. F. Santos, Flexibility Effects in Tilting-Pad Journal Bearings with Radial Oil Injection, in: EURODYN 2008, 7. European Conference on Structural Dynamics, Southampton, UK, 2008, pp. 1–12, paper ID: E187

A. M. Haugaard, I. F. Santos, Flexibility Effects in Tilting-Pad Journal Bearings with Controllable Radial Oil Injection, in: NORDTRIB 2008, 13. Nordic Symposium in Tribology (ISBN: 978-952-15-1959-8), Tampere, Finland, 2008, pp. 1–17, paper ID: NT2008-43-4

A. M. Haugaard, I. F. Santos, Modeling of Flexible Tilting Pad Journal Bearings with Radial Oil Injection, in: 2008 Proceedings of the STLE/ASME International Joint Tribology Conference (ISBN: 978-0-7918-3837-2), Miami, Florida, USA, 2008, pp. 335–337

A. M. Haugaard, I. F. Santos, Fast Solution of Fluid Structure Interaction Problems in the Frequency Domain - with an Application (in print), in: 11th Pan-American Congress of Applied Mechanics - PACAM XI, Foz do Iguaçu, Paraná - BRAZIL, 2010, pp. 1–6

# Nomenclature

Table 1: Nomenclature - upper-case Latin letters.

| | | |
|---|---|---|
| $\mathbf{A}$ | Pressure system matrix | $[\frac{\mathrm{m}^5}{\mathrm{Ns}}]$ |
| $C_{\underline{\mathrm{a}}}$ | Assembled clearance | [m] |
| $C_{\underline{\mathrm{m}}}$ | Machined clearance | [m] |
| $\mathbf{D}$ | Generalized damping matrix | - |
| $\mathbf{D}_{\underline{\mathrm{q\text{-}q}}}$ | Flow damping matrix | $[\frac{\mathrm{Vs}^2}{\mathrm{m}^3}]$ |
| $D_{\underline{\mathrm{r}}}$ | Rotor diameter | [m] |
| $E$ | Young's modulus | $[\frac{\mathrm{N}}{\mathrm{m}^2}]$ |
| $F$ | Characteristic force | [N] |
| $\mathbb{F}$ | Set of fluid nodes | - |
| $\mathbb{F}^3$ | Set of fluid displacement degrees of freedom | - |
| $\mathbf{G}_{\underline{\mathrm{P}}}$ | Proportional gain matrix | $[\frac{\mathrm{V}}{\mathrm{m}}]$ |
| $\mathbf{G}_{\underline{\mathrm{D}}}$ | Derivative gain matrix | $[\frac{\mathrm{Vs}}{\mathrm{m}}]$ |
| $\mathbf{K}$ | Generalized stiffness matrix | - |
| $K_{\underline{\mathrm{pq}}}$ | Flow-pressure constant | $[\frac{\mathrm{m}^3}{\mathrm{Vs}}]$ |
| $\mathbf{K}_{\underline{\mathrm{pq}}}$ | Valve flow-pressure relation matrix | $[\frac{\mathrm{m}^5}{\mathrm{Ns}}]$ |
| $\mathbf{K}_{\underline{\mathrm{q\text{-}q}}}$ | Flow stiffness matrix | $[\frac{\mathrm{Vs}}{\mathrm{m}^3}]$ |
| $\mathbf{K}_{\underline{\mathrm{s}}}$ | Solid stiffness matrix | $[\frac{\mathrm{N}}{\mathrm{m}}]$ |
| $\mathbf{K}_{\underline{\mathrm{r}}}$ | Rotor stiffness matrix | $[\frac{\mathrm{N}}{\mathrm{m}}]$ |
| $K_{\underline{\mathrm{v}}}$ | Valve static amplification | $[\frac{\mathrm{m}^3}{\mathrm{Vs}}]$ |
| $\mathrm{L}_{ijkl}$ | Solid constitutive tensor | $[\frac{\mathrm{N}}{\mathrm{m}^2}]$ |
| $L$ | Characteristic length | [m] |
| $L_{\underline{\mathrm{b}}}$ | Bearing length | [m] |
| $\mathbf{M}$ | Generalized mass matrix | - |
| $\mathbf{M}_{\underline{\mathrm{q\text{-}q}}}$ | Flow mass matrix | $[\frac{\mathrm{Vs}^3}{\mathrm{m}^3}]$ |
| $\mathbf{M}_{\underline{\mathrm{r}}}$ | Rotor mass matrix | [kg] |
| $\mathbf{M}_{\underline{\mathrm{s}}}$ | Solid mass matrix | [kg] |
| $N_{\underline{\mathrm{o}}}$ | Number of orifice arrays | - |
| $\mathbf{Q}$ | Orifice flow-pressure relation matrix | $[\frac{\mathrm{m}^5}{\mathrm{Ns}}]$ |
| $R_{\underline{\mathrm{r}}}$ | Rotor radius | [m] |
| $R_{\underline{\mathrm{p}}}$ | Pad inner surface radius | [m] |
| $\mathbb{S}$ | Set of solid nodes | - |
| $\mathbb{S}^3$ | Set of solid displacement degrees of freedom | - |
| $U$ | Tangential rotor speed | $[\frac{\mathrm{m}}{\mathrm{s}}]$ |
| $U_{\underline{\mathrm{p}}}$ Tangential pad speed | | $[\frac{\mathrm{m}}{\mathrm{s}}]$ |
| $\mathbf{V}_{\underline{\mathrm{s}}}$ | Matrix of solid modes of vibration | - |
| $V_{\underline{\mathrm{inj}}}$ | Fluid injection velocity profile | $[\frac{\mathrm{m}}{\mathrm{s}}]$ |
| $\mathbf{V}$ | Reduction matrix | - |
| $W$ | Pressure system cross coupling matrix | $[\frac{\mathrm{m}^5}{\mathrm{Ns}}]$ |

Table 2: Nomenclature - lower-case Latin letters.

| | | |
|---|---|---|
| $\mathbf{b}$ | Modal coordinate vector | [m] |
| $(\mathbf{b}_1, \mathbf{b}_2, \mathbf{b}_3)$ | Curvilinear coordinate basis vectors | [m] |
| $\mathbf{d}_{\underline{\mathrm{g}}}$ | Generalised displacement vector | - |
| $d_{\underline{\mathrm{r}}}$ | Rotor damping or characteristic damping | $[\frac{\mathrm{Ns}}{\mathrm{m}}]$ |
| $\mathbf{f}$ | Nodal force vector | [N] |
| $\mathbf{f}_{\underline{\mathrm{g}}}$ | Generalised force vector | - |
| $f_{\underline{\mathrm{r}}}$ | Rotor force | [N] |
| $\mathbf{f}_{\underline{\mathrm{r}}}$ | Rotor force vector | [N] |
| $g_i$ | Orifice flow shape function | $[\mathrm{m}^2]$ |
| $h$ | Fluid film thickness | [m] |
| $k_{\underline{\mathrm{r}}}$ | Rotor stiffness or characteristic stiffness | $[\frac{\mathrm{N}}{\mathrm{m}}]$ |
| $l_{\underline{0}}$ | Orifice inlet length | [m] |
| $m_{\underline{\mathrm{r}}}$ | Rotor mass or characteristic mass | [kg] |
| $p$ | Fluid pressure | [Pa] |
| $\mathbf{p}$ | Generalised vector of nodal pressure values | [Pa] |
| $p_{\underline{\mathrm{inj}}i}$ | Injection pressure | [Pa] |
| $q_{\underline{\mathrm{L}}}$ | Leak flow | $[\frac{\mathrm{m}^3}{\mathrm{s}}]$ |
| $q_{\underline{\mathrm{v}}}$ | Valve flow | $[\frac{\mathrm{m}^3}{\mathrm{s}}]$ |
| $\mathbf{r}$ | Pressure right hand side | $[\frac{\mathrm{m}^3}{\mathrm{s}}]$ |
| $r_{\underline{0}i}$ | Orifice radius | [m] |
| $\overline{\underline{\mathrm{res}}}\mathbf{r}$ | Residual vector | - |
| $t$ | Time | [s] |
| $u_i$ | Displacement | [m] |
| $\mathbf{u}_{\underline{\mathrm{v}}}$ | Valve input signal vector | [V] |
| $\mathbf{u}_{\underline{\mathrm{vr}}}$ | Valve reference signal vector | [V] |
| $u_{\underline{\mathrm{ch}}}$ | Valve characteristic signal voltage | [V] |
| $v_i$ | Fluid velocity vector or test function | $[\frac{\mathrm{m}}{\mathrm{s}}]$ or - |
| $x_i$ | Inertial coordinates | [m] |

Table 3: Nomenclature - upper-case Greek letters.

| | | |
|---|---|---|
| $\Delta_i$ | Perpendicular distance to orifice $i$ | [m] |
| $\Gamma$ | Fluid boundary | - |
| $\Lambda$ | Solid boundary | - |
| $\Lambda_{\underline{\mathrm{s}}}$ | Diagonal matrix of squared eigenvalues | $[\mathrm{s}^{-2}]$ |
| $\Pi$ | Solid domain | - |
| $\Phi$ | Fluid domain | - |
| $\Omega$ | Fundamental frequency or rotational speed | $[\mathrm{s}^{-1}]$ |

Table 4: Nomenclature - lower-case Greek letters.

| | | |
|---|---|---|
| $\delta_{ij}$ | Kronecker's delta | - |
| $\varepsilon_{ij}$ | Strain tensor | - |
| $\zeta$ | Isoparametric coordinate | - |
| $\eta$ | Isoparametric coordinate | - |
| $\mu$ | Fluid viscosity | $[\frac{\mathrm{Ns}}{\mathrm{m}^2}]$ |
| $\nu$ | Poisson's ratio | - |
| $\xi$ | Isoparametric coordinate | - |
| $\xi_{\underline{\mathrm{v}}}$ | Valve damping ratio | - |
| $\rho$ | Solid density or fluid density | $[\frac{\mathrm{kg}}{\mathrm{m}^3}]$ |
| $\phi_i$ | Shape function | - |
| $\chi_i$ | Curvilinear coordinates | [m] |
| $\omega_{\underline{\mathrm{v}}}$ | Valve eigenfrequency | $[\mathrm{s}^{-1}]$ |

# Contents

# Chapter 1

# Introduction

The present thesis is of a theoretical nature. No experimental data will be presented. However, the thesis is written under the premise, that the work is justified if and only if it contributes directly or indirectly to the design and construction of improved machine elements. As such, the work falls into the category of applied science.

Eventual industrial application of the results of the this thesis will contribute to reliable and confident implementation and operation of ATPJBs. As shall be reported in later sections, the addition of a control system to a TPJB is by no means fool proof, and can result in undesired effects. In the worst case scenario, improper tuning of an ATPJB can destabilise the rotor-bearing system. At this point, we may define rotor-bearing stability as the stability of the equilibrium corresponding to nominal bearing operation. E.g., a fluttering pad corresponds to a stable limit cycle, but not a stable bearing, as per our definition of rotor-bearing stability.

TPJBs operate in a wide range of applications. Though, what these applications have in common is, firstly, that radial rotor motion is critical and, secondly, that the application is such, that it merits a relatively expensive machine element with low tolerance requirements. In cheap, mass produced machines where predictability, long service life and low noise are not selling points, TPJBs are not ideal. TPJBs find their niche in machines operating under heavy load, where emergency maintenance is cheaper than unit replacement, where planned maintenance is much cheaper than emergency maintenance and where no maintenance at all is much cheaper than planned maintenance. TPJBs are predictable, have potentially infinite service life under the right conditions, and have the ability to handle large rotational speeds and severe radial loads. Figure 1.1[9] shows an application of TPJBs to a very large shaft, connecting a hydropower turbine to a generator.

Despite the merits of TPJBs, as with any machine element, there are limits to their performance. For instance, while increasing the rotational speed increases the bearings radial stiffness, its ability to dissipate vibration energy remains largely constant. That is, given that the stiffness increases, the damping ratio drops. Ultimately, the bearing itself may become unstable [10, 11]. Also, crossing rotor-bearing resonance frequencies, e.g. during a start-up, may produce large amplitudes of vibration, resulting in wear - also in the TPJB. Furthermore, often, other shaft components or the shaft itself will produce speed dependent loads, which impose stability limits on machine operational range regardless of the bearing type [12]. But proper bearing design (and tuning) can potentially push these limits. Hence, there is reason to investigate possible improvements in the design of TPJBs. The ATPJB is one such proposal out of several. As all designs, it has its advantages and drawbacks. It is described in detail in the following sections.

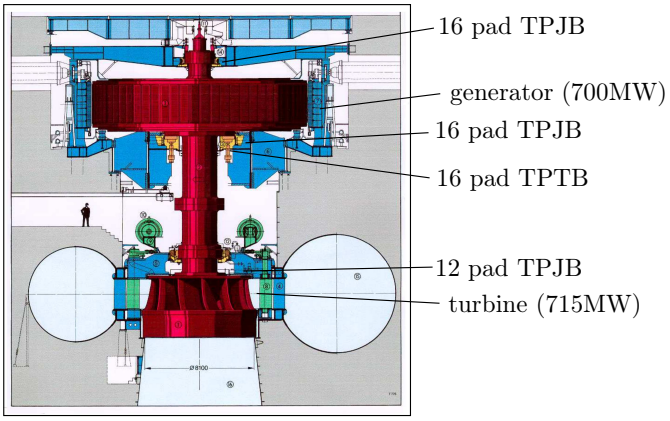


Figure 1.1: Schematic representation of a hydrogenerator at the ITAIPU hydropowerplant in Brazil. Two TPJBs and a tilting-pad thrust bearing (TPTB) are shown. The image is adapted from the presentation of [9], courtesy of Dr. Geraldo Brito, senior engineer at ITAIPU.

## 1.1 Plain journal bearings

Stodola [13] is generally credited as the first person to perform linear frequency domain analysis of a fluid film bearing, due to his 1925 paper. He did not coin the terms "bearing stiffness" or "bearing damping" rather, he referred to oil film flexibility. Nevertheless, the concepts of bearing stiffness and damping originate with his work. Together with Jeffcott's 1919 publication on rotor dynamics [14], this meant that the dynamic behaviour of shafts supported by fluid films could be assessed. In 1967 Orcutt and Arwas [15] extended fluid film bearing analysis to account for lubricant turbulence through an extension of the Reynolds equation [16]. The extension introduced two new parameters which were function of the Reynolds number. However, in general, viscous forces dominate in oil lubricated bearings. Indeed the differences between purely laminar and generalised results in [15] were noticeable, but not dramatic. The authors investigated cases with Reynolds numbers reaching 13000. In the present study, the Reynolds numbers are kept much lower.

## 1.2 Tilting-pad journal bearings

While Boyd and Raimondi performed static analyses of pivoted pad bearings as early as from 1953 [17, 18], the first thorough theoretical study of the dynamics of TPJBs was that of Jørgen Lund in 1964 [19]. The computational work of bearing analysis was, and still is substantial. Given that the year was 1964, Lund had to mitigate this problem somehow. He did this so elegantly that his work is still relevant today, and will be in the future. Lund limited his analysis to linear stationary (harmonic) vibrations. This enabled him to prescribe a rotor motion of a given amplitude and frequency. Given the prescribed rotor motion, the system of equations was decoupled into several scalar equations - one for each pad. Thus he could compute the force response from each pad individually. After computing each force response, a vectorial sum provided the total force response, i.e., that felt by the journal. This method reduced the computational work load enough, that the equations could be solved even on a 1964 computer. The price

that Lund knowingly paid, was that his analysis was restricted to frequency response computation. It could not be used for stability analysis.

In 1980 Ettles [20] performed comprehensive analyses of tilting pad journal bearings. To reduce simulation time, Ettles employed a semi-analytical method to solve for the pressures and responses. At the time, both the finite element and finite difference methods were available, but considered too time consuming. Ettles' model considered thermal effects and deformation.

In 1981 Allaire, Parsell and Barrett [21] published a paper which addressed the limitations of Lund's method. They succeeded in setting up linearised equations of motion for the tilting-pad journal bearing with no prescribed rotor motion. This yielded a system of equations which, while small by today's standards, was substantially larger than that of Lund's method. The advantage was that this system of equations could be used for both local stability analysis as well as frequency response computations. As opposed to the work of Ettles [20], which was essentially a phenomenological extension of a onedimensional model, Allaire, Parsell and Barrett's work encompassed full twodimensional solutions to the Reynolds equation. However, in retrospect, the two main contributions of [21] were, firstly, to provide a detailed manual, as to how to set up the linearised equations of motion for a tilting pad journal bearing and, secondly, to explain in unmistakable terms to the tribology community, that frequency dependent dynamic coefficients cannot be used for stability analysis of tilting pad journal bearings. In 1993 Brockett and Barrett [22] correctly stated that *"Results from a stability analysis, therefore, might be quite misleading if synchronously-reduced bearing coefficients are used instead of complete tilting-pad bearing models"*. They proposed an "Exact" dynamic reduction, which yielded a condensed 2×2 system of equations for the journal. The terms depended on the complex frequency, which was treated as an unknown, thus the reduction made no assumption on journal motion in time. However, it introduced a truncation error with respect to the frequency. Since the year was 1993, and substantial computing power was available, one must ask if it was worth while to condense a 7×7 system (5 pads) of equations to a 2×2 at the cost of a noticeable error.

As mentioned in [21]. The years that passed after Lund's paper [19] and [21] saw some leading authors using Lund's dynamic coefficients in stability analysis, for instance Nicholas, Gunter and Barrett [23]. As mentioned, such use is erroneous. Lund was aware of his method's limitations as Nicholas states in his comprehensive review paper from 2003 [24] *"Lund pointed out that it is mathematically incorrect to use a synchronous frequency for a stability calculation.* He went on to say that *"...the damped natural frequency should be used instead."* [24]. However, Lund's method was also used by Nicholas, Gunter and Allaire to conduct an elegant and useful parameter study of bearing stationary harmonic performance [25]. Here the effect of pad preload and offset pivoting was investigated for a bearing with five pads.

If frequency dependent dynamic coefficients are used in a stability analysis of TPJBs, the computation is strictly valid if and only if one of the below conditions is satisfied

#1 The real parts of all of the eigenvalues are zero and the imaginary parts of all of the eigenvalues are equal to the perturbation frequency.

#2 The, now nonlinear, eigenvalue problem is solved as such. I.e., iteratively. [26].

Condition #1 entails that the stability threshold of all modes of vibration be the same. That is, they must all become unstable at exactly the same set of parameters and operating conditions. In practice, this never happens. Furthermore, #1 requires that all modes of vibration have the same eigenfrequency as the perturbation frequency. Again, in practice this hardly ever happens [27]. The concept of stability it thoroughly explained in, e.g., Thomsen's book on vibrations [28]. Of course, the analyst may assume the real part of the critical eigenvalue to be zero [29], as per the definition of a critical eigenvalue. But the

frequency of vibration must be kept as an unknown (as in [29]). In a dynamic condensation, synchronous or non-synchronous, it is not kept as an unknown. At least two publications have compared true stability analysis, and stability analysis with frequency dependent dynamic coefficients [30, 31]. In both studies, the use of dynamic coefficients overpredicted the rotor-bearing stability. That is, in the investigated cases, use of frequency dependent dynamic coefficients for stability analysis could result in bearing failure. It is worth noting, that as long as a dynamic perturbation procedure involves perturbations of all relevant degrees of freedom, it will capture the stationary harmonic, as well as the transient (stability) behaviour of the rotor-bearing system. Thus, for instance, a passive plain journal bearing can be represented generally as a $2\times2$ system of equations, even if the matrices result from a dynamic perturbation with the assumption of stationary harmonic vibrations. Here the dynamic perturbation can be viewed as a parameter identification procedure. The assumption of harmonic motion is useful in an experimental determination of bearing dynamic coefficients. However, in a model, the assumption of harmonic motion is redundant and the matrices will be independent of the frequency. The question is then: Why assume stationary harmonic vibrations, if it does not simplify the problem? Perturbations of displacement and velocity will yield the exact same system, and are simpler to perform.

In 1989 Someya based a model on the preceding years of research, and used it to perform the most comprehensive parameter study of journal bearings to date, the results were published in the "Journal Bearing Databook" [32]. The book contains values of stiffness and damping for a variety of fluid film bearing configurations at a variety of operating conditions. Since then, the book has been cited widely.

In 1992 Chan and White [33] performed steady state analyses of a five pad journal bearing. The bearing was excited at sub synchronous frequency. The analysis revealed that bearing damping is small at low frequencies, when comparing to the damping at synchronous frequency, especially at low pad preload. Thus the potential exists for large vibration amplitude spikes if the rotor-bearing system is excited at lower excitation frequencies.

As computing power increased through the nineties, scientists began to refine tilting-pad journal bearing models. Pivot flexibility as well as a simplified pad compliance model was developed by Lund and Thomsen in 1987 [34]. As a precursor to their previously mentioned work [30], Earles, Palazzolo and Armentrout provided a more general methodology in [35]. Their method solved the Reynolds equation on a two dimensional mesh, and captured finite bearing length effects. Their pad compliance calculation was that of infinitely long pads through a plane strain assumption. It made use of a twodimensional finite element grid. However, deformation results were condensed to their influence on effective pad radius. Thus, their analysis considered the pads perfectly circular, even in the deformed state. Their study also neglected thermal deformations. This was in 1990, so their model was advanced for its time, and it is evident that the simplifications were very prudent. In 1994 the field took a leap forward with the work of Desbordes, Fillon, Chan Hew Wai and Frêne [36]. Their model resembled that of [35] but allowed arbitrary twodimensional pad deformations. Since some of the analyses in [36] were for heavily loaded bearings, it was decided not to linearise the model. Thus the analysis was limited to the study of time series. So as to not introduce high frequencies, and thus a low limit on the maximum time step, pad inertia was limited to that of the tilting motion. The simulations revealed pad deformations to be of significance to the journal orbit radius, maximum pressure, and minimum film thickness, at least for the heavily loaded bearings. In [37] a similar study was conducted by Desbordes, Fillon and Frêne. This time including full three dimensional pad deformation, but still neglecting the inertia of higher pad modes. In parallel, a similar model including thermal effects was presented in [38]. In the work [39] by Monmousseau and Fillon, thermal effects were included along with a Hertz contact model for the pivots. comparison with experimental results was conducted. Among other things, the work confirmed thermal effects to be slower than mechanical effects. That is, in the words of the authors, the *"...thermal transient period.."* was much

longer than the *"...mechanical transient period..."*. This, in itself, does however not permit neglecting all thermal effects. But it allows the analyst to treat thermal effects as a static phenomenon.

Brancati, Rocca and Russo [40] performed stability analysis of nonlinear journal orbits, i.e., phase planes. They calculated the nonlinear orbits by introduction of a series expansion and separation of the equations into terms of equal power. I.e., a finite perturbation method was employed. However, the stability analysis was of the nonlinear orbits themselves, not of the bearing in a given equilibrium position. I.e. given that the bearing was stable in a certain equilibrium, Brancati and colleagues gave the answer to which orbit around this stable equilibrium it would then follow. Thus, prior to employing the method in [40], a local stability analysis should be performed. Recently, Qiao, Wang and Zheng [41] published a consistent and well written paper on local stability calculations of TPJBs.

Pivot flexibility has been shown to affect bearing performance [42, 43]. In [43], it was shown experimentally as well as theoretically, that pivot flexibility can affect the performance of tilting-pad journal bearings. Among other things, the study concluded that pivot flexibility tends to decrease bearing harmonic stationary damping at higher frequencies.

## 1.3 Active fluid film journal bearings

Active fluid film journal bearings have not yet found as widespread use as their passive counterparts. This also holds for the particular case of active tilting-pad journal bearings. So far, the ATPJBs of the type investigated in this thesis do not appear in industrial applications, and with good reason. In particular, until now, there are no trustworthy stability calculations for the designer to rely on. The stability analyses performed so far on the ATPJBs, of the type investigated in this thesis, e.g. in [44], rely on frequency dependent system matrices. As shall be explained in the following, they cannot be trusted.

As early as 1981 Stanway and Burrows [45] investigated the controllability and observability of a fluid film bearing. They introduced the idea of actively controlling the position of the bearing housing. Their investigation, which was theoretical, revealed the concept to be promising, and paved the way for further development.

In 1989 Ulbrich and Althaus [46] performed experimental investigations of an active TPJB with movable pads. Their test rig controlled the pads through electromagnetic linear actuators. This was probably the first active TPJB to be built. In the same study, the authors proposed the use of piezoelectric actuators and hydraulic chambers for the active pad motion. The latter concept was investigated by Fürst, Althaus and Ulbrich in [47] and by Althaus and Ulbrich in [48]. This idea was extended to TPJBs in 1993 by Santos [49]. Piezoactuators as a rotor control element was the subject of investigation in [50]. In the 2004 paper by Deckler, Veillette, Braun and Choy [51] the bearing was controlled by active pivots as in [46]. That is, the pivots were moved in the radial direction with linear actuators. Each pad could be controlled individually, and parameters were identified, so as to allow independent control of stiffness and damping. The results in [51] were theoretical, but followed by an experimental investigation by Wu, Cai and Queiroz in 2007 [52].

Another possibility of bearing control is to introduce a flexible sleeve, or arc, controlled by a variable pressure chamber, as described by Sun and Krodkiewski in 2000 [53]. Other methods include, but are not exclusive to, the use of magneto-rheological lubricant, local heating of the lubricant or deformation of the lubricated surface. An exhaustive overview shall not be given here. The recent work by Glavatskih and Höglund [54] gives a good overview of the presently available control methods, and proposes the generic term "tribotronics".

The first journal paper to deal with the concept of radial oil injection into the gap between journal

and bearing was the 1998 publication by Santos and Scalabrin [55]. The idea had been introduced four years earlier in 1994 at the IUTAM conference that year [56]. They introduced a method of computing the pressure profile resulting from coupled hydrodynamic and hydrostatic lubrication, so called "hybrid lubrication". The work was a forerunner for the subsequent years of research into the control of shaft vibrations through active hybrid lubrication. Also, the authors coined the term *"modified Reynolds equation"*. The method retains the concept of the oil film thickness, even in the orifice region. Here, as in the rest of the wetted surface, the no slip condition is applied. The assumption would be valid if the orifice diameter was much smaller than the oil film gap. This is rarely the case, as the diameter of the injection orifice is typically more than an order of magnitude larger than the oil film gap. However, except for extreme parameter choices the pressure profile in the orifice region is all but constant [55]. Most often, the mesh will need refinement in and around the orifice, so as to describe the circular profile. Thus the size of the discretised pressure problem is increased. This is particularly true when using the finite difference method, which is restricted to rectangular elements. For this reason, the finite element method is far more convenient. In 1986 Klit and Lund [57] used six node triangular elements in a finite element solution of the Reynolds equation. The method developed in [55] was the first of its kind and is adopted in the present study as well as in others. If, in a future study, more accurate flows in the orifice region are desired, a more advanced method should be employed. Similar remarks were made in 2008 by Heinrichson and Santos [58] in their study of TPTPs with recesses. In 1997 and 1994 Braun and co workers [59, 60] solved the Navier-Stokes equations for a hydrostatic journal bearing pocket with radial lubricant injection. Here the flow fields were seen to approach that of [55] in the "jet dominated" case or when far from the fluid film gap inside the injection orifice.

In two papers from 1998 and 2001 Santos and Nicoletti [61, 62] performed simultaneous solution of the Reynolds and energy equations to gain insight into the thermal implications of radial oil injections. As of yet, these are the only internationally published documents to consider the thermal aspect of the hybrid lubrication method which was introduced in [55]. Injecting oil into the bearing gap at a given pressure is an open loop control technique, since no feedback is considered. In 2003 Santos and Nicoletti [63] included a controllable servo-valve into the system, thus producing a closed loop controllable bearing. The servo-valve model was simple, but captured the most important phenomenon; namely the limited servo-valve bandwidth. It was reported, that above the servo-valve eigenfrequency, the servo-valve based control system looses its effect.

In [64], the servo-valve motion was considered stationary harmonic. A stability analysis was performed a posteriori. Similarly, in [44], a frequency dependent system of equations was derived so as to represent an ATPJB. Synchronous motion was assumed. Subsequently the system was used for calculation of complex eigenvalues and stability considerations. Such use [64, 44] of dynamic coefficients is not recommended. This is for the same reason, which was explained above, that frequency dependent bearing coefficients for TPJBs cannot be used in stability analysis. Firstly, it is not mathematically stringent, secondly, results may be misleading. When including servo-valve dynamics, each servo-valve adds one degree of freedom to the system. This means that even a plain journal bearing, if it is active, is not represented fully as a $2\times2$ system of equations and it means that an ATPJB with, e.g., four rigid pads is not represented fully as a $6\times6$ system of equations.

## 1.4 Main contributions of this thesis

The present investigation adopts the active lubrication method of [55, 64, 65], though with "general" perturbations. That is, no assumption is made with regard to the motion of the perturbation in time.

Thus the model can be used for local stability analysis as well as harmonic response analysis with equal validity. As mentioned, previous attempts at assessing the stability of the bearing type under investigation have not been successful. It has now been 16 years after the bearing type was first introduced in 1994.

The model presented in this thesis is benchmarked against several authors with good agreement. Both time domain analysis and frequency domain analysis show the model to agree with those of previous investigators.

The stability analysis of [4] is extended to further combinations of parameters. Also, a dimensional analysis is performed and tested for validity, through computation of dimensionless rotor orbits.

The "hydroelastic number" is derived, and a limiting value of this number is computed. This allows future researchers to neglect pad compliance for certain system parameters.

Frequency response functions for rotor-bearing systems are computed for different values of rotor mass, revealing that the frequency, at which the control system no longer yields a reduction in amplitude of vibration, depends on rotor mass.

Three simple adaptive control strategies are implemented, and studied through their impact on system eigenvalues and rotor motion time series. Finally, a guide to mathematically and physically stringent stability prediction of ATPJBs is presented.

## 1.5 The candidates publications

In addition to this thesis, several publications have been made, that document the progress of the past three years of research [5, 6, 7, 2, 8, 3, 4].

In [5] the fluid film thickness and bearing dynamic coefficients were calculated for a range of pad elastic moduli and injection pressures. That is, the investigation was concentrated on hybrid lubrication of compliant bearings.

In [6] a simple closed loop control model was implemented and added to the model of [5]. Valve dynamics were neglected. That is, servo-valve bandwidth was assumed infinite. Still, at least one important conclusion could be made with confidence. Namely that if a closed loop control system is tuned based on model predictions, then negligence of pad compliance could lead to significant error, and unexpected behaviour by the active bearing. It was demonstrated that a control system tuned for a bearing with the elastic modulus of steel, would not perform as expected in a bearing with the elastic modulus of aluminium, and vice versa. The model was expanded to include harmonic valve dynamics in [7], which focussed entirely on the modelling procedure, and did not present any results. In the abstract of [7] the word "stability" appears, although the model was not suited for stability (complex eigenvalue) calculations.

In [2] valve dynamics were included and general perturbations were made, so as to yield the linearised system of equations for the bearing with compliant pads and controllable servo-valves. The pads were discretised with finite elements. On the middle of each pad, an injection orifice was placed. The simulations in [2] proved to be very time consuming, with parameter studies lasting weeks. In [8] this was addressed with the proposal of a fast solution method. Though, this method was later abandoned in favour of more conventional and proven techniques.

The rotor-bearing model was extended and modified in [3]. As in [2] the pads were discretised with finite elements, but the pad finite element model was used solely for computation of the pad mode shapes. These mode shapes were then used for pseudo modal reduction of the pads, truncating their movement to the first four mode shapes. This method proved to be fast, while still capturing essential pad behaviour. Several orifice configurations were tested, and stationary harmonic performance was evaluated. The control system was seen to have the biggest influence, when orifices were placed far from the pivot line.

In [4] the stability of active compliant bearings was evaluated. Eigenvalues were computed for a range of parameters. It appeared that poor choice of control gains could destabilise the bearing. Furthermore it was demonstrated that those gains leading to a stable bearing appear as connected sets.

## 1.6 Thesis structure

The thesis is divided into the following chapters.

Chapter 2 provides the reader with a detailed derivation of the mathematical model. A reader with previous knowledge of mechanics, partial differential equations and the finite element method will be able to reproduce the mathematical model after reading this chapter.

Chapter 3 derives the non-dimensional form of the system of equations. Key dimensionless parameter groups are identified for later use.

Chapter 4 validates the model through benchmarking against other authors and a convergence study.

Chapter 5 shows selected simulation results generated with the mathematical model. Curves for the frequency response function, stability plots, time series and rotor orbits are presented. Emphasis is placed on the influence of the control system on rotor-bearing behaviour. The dimensional analysis is used to illustrate the usefulness of similitude and determine a limiting value for the hydroelastic number, beyond which pad compliance can be neglected.

Chapter 6 summarises the most important conclusions with respect to bearing design considerations and model validity. A general recommendation for the direction of future research within the field is given.

# Chapter 2

# Mathematical modelling

Fluid film lubrication, may be modelled in a variety of fashions. The fluid film pressure distribution may be modelled using short bearing or long bearing theory or the twodimensional Reynolds equation. If the Reynolds number is large, fluid inertia may be included. In the case of gas bearings, compressibility may be included. Leading edge lubricant build up may be modelled through full threedimensional computational fluid dynamics if deemed necessary.

In the case of tilting pad journal bearings, the motion of the pads needs to be accounted for. This can be captured by a rigid body model, or deformation can be included through a beam model, plate theory or a threedimensional finite element mesh. Typically one will assume linear elasticity with small strains and rotations. If thermal effects are estimated to play a role, they may be included into the model through thermal energy considerations.

If a parameter study is to be undertaken, the model must be simple enough that many simulations can be run in a reasonable time.

In this study, the oil film is taken to be described by the twodimensional Reynolds equation. The pads are modelled as linearly elastic with small strains and rotations. They are discretised with a threedimensional finite element mesh. The nodes on the lubricated surface of the pad coincide with the nodes on the oil film. In this way, computation of pressure forces from the oil film onto the pads becomes intuitive and straight forward through Gauss quadrature. If desired, the pads may be subsequently reduced by a modal reduction. The mode-shapes of the pads alone (without oil film forces) are used for the pseudo modal reduction. This, along with a condensation, will yield a system of equations of manageable size.

Index notation will appear in certain places. To avoid confusion, while retaining a consistent nomenclature, summation of repeated indices is not employed, thus all summations are stated explicitly. Underlined indices are part of variable names and indices without underline are used for numbering, e.g. $q_{\underline{\mathrm{v}}i}$ is the valve flow of servo-valve number $i$. A Nomenclature is provided in Tabs. 1, 2, 3 and 4.

Figure 2.1 shows the domains relevant to the continuous parts of the problem, i.e., the pads and the fluid film. The valves are not shown. The solid domain and its boundary are denoted $\Pi$ and $\Lambda$, respectively. The fluid domain and its boundary are denoted $\Phi$ and $\Gamma$, respectively. Note that $\Phi$ is a subset of $\Lambda$. The figure also indicates provision for radial oil injection, through two generic domains where the injection terms are non zero. Furthermore, the cartesian coordinate system $(x_1, x_2, x_3)$ and the curvilinear coordinate system $(\chi_1, \chi_2, \chi_3)$ are defined.

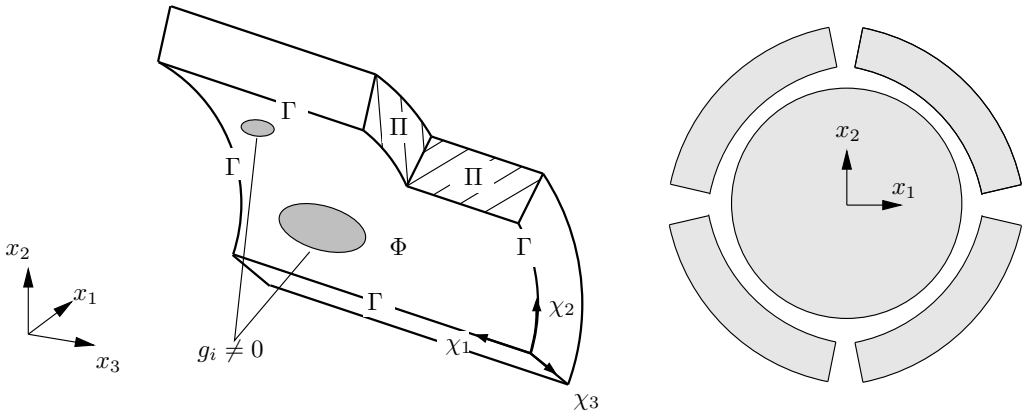


Figure 2.1: Generic pad with a cutaway. The solid domain is $\Pi$ and the fluid domain is $\Phi$. Their boundaries are denoted $\Lambda$ (not shown) and $\Gamma$, respectively. Note that $\Phi \subset \Lambda$. The regions where $g_i \neq 0$ are the orifices of lubricant injection into the gap. Note that each pad may have more than one injection orifice.

## 2.1 From the Navier-Stokes equations to the Reynolds equation

The general motion of a fluid is well described by the Navier-Stokes equations, which capture many effects. These equations, while encompassing, are time consuming to solve. For the present application, at very little loss of accuracy, the fluid can be taken to follow the far simpler Reynolds equation. Here we shall derive the Reynolds equation from the Navier-Stokes equations, explaining the assumptions step by step. The derivation follows that of [49]. The main assumptions are as follows

- Newtonian fluid (stress independent viscosity).
- Laminar flow.
- Negligible inertia.
- A fluid film gap much smaller than all other dimensions, thus permitting the negligence of curvature.
- Averaged fluid properties across the gap.

The reasoning behind these approximations is explained in detail in [66].

We recall, that the velocity field is a function of position as well as time, thus

$$v_i = v_i(\chi_1, \chi_2, \chi_3, t), \quad i = 1, 2, 3 \tag{2.1}$$

where $v_i$ is the velocity of a fluid particle in the $\chi_i$ direction. The acceleration is the total derivative of the velocity, i.e., it must account for fictitious forces due to the moving reference frame. Defining

$$\frac{d\chi_i}{dt} = v_i, \quad i = 1, 2, 3 \tag{2.2}$$

and plugging into Eq. (2.1), we arrive at

$$\dot{v}_i = \frac{dv_i}{dt} = v_1 \frac{\partial v_i}{\partial \chi_1} + v_2 \frac{\partial v_i}{\partial \chi_2} + v_3 \frac{\partial v_i}{\partial \chi_3} + \frac{\partial v_i}{\partial t}, \quad i = 1, 2, 3 \tag{2.3}$$

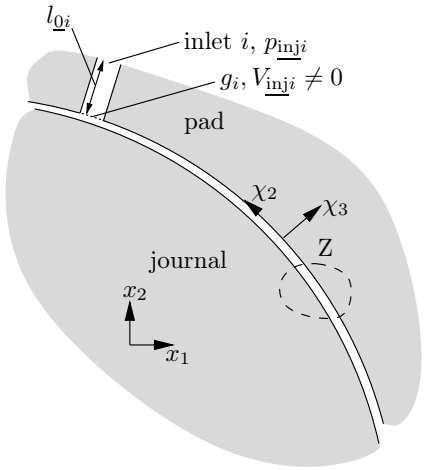


Figure 2.2: Generic picture of a journal, a pad and the gap in between. An injection orifice is also shown.

The Navier-Stokes equations can be found in many textbooks, e.g. [67]. For a Newtonian fluid, they take the form of Eq. 2.4.

$$\begin{aligned}
\rho\dot{v}_1 &= -\frac{\partial p}{\partial \chi_1} + \frac{\partial}{\partial \chi_1}\left(\mu\left(2\frac{\partial v_1}{\partial \chi_1} - \frac{2}{3}\left(\frac{\partial v_1}{\partial \chi_1} + \frac{\partial v_2}{\partial \chi_2} + \frac{\partial v_3}{\partial \chi_3}\right)\right)\right) + \\
&\frac{\partial}{\partial \chi_2}\left(\mu\left(\frac{\partial v_1}{\partial \chi_2} + \frac{\partial v_2}{\partial \chi_1}\right)\right) + \frac{\partial}{\partial \chi_3}\left(\mu\left(\frac{\partial v_3}{\partial \chi_1} + \frac{\partial v_1}{\partial \chi_3}\right)\right) \\
\rho\dot{v}_2 &= -\frac{\partial p}{\partial \chi_2} + \frac{\partial}{\partial \chi_2}\left(\mu\left(2\frac{\partial v_2}{\partial \chi_2} - \frac{2}{3}\left(\frac{\partial v_1}{\partial \chi_1} + \frac{\partial v_2}{\partial \chi_2} + \frac{\partial v_3}{\partial \chi_3}\right)\right)\right) + \\
&\frac{\partial}{\partial \chi_3}\left(\mu\left(\frac{\partial v_2}{\partial \chi_3} + \frac{\partial v_3}{\partial \chi_2}\right)\right) + \frac{\partial}{\partial \chi_1}\left(\mu\left(\frac{\partial v_1}{\partial \chi_2} + \frac{\partial v_2}{\partial \chi_1}\right)\right) \\
\rho\dot{v}_3 &= -\frac{\partial p}{\partial \chi_3} + \frac{\partial}{\partial \chi_3}\left(\mu\left(2\frac{\partial v_3}{\partial \chi_3} - \frac{2}{3}\left(\frac{\partial v_1}{\partial \chi_1} + \frac{\partial v_2}{\partial \chi_2} + \frac{\partial v_3}{\partial \chi_3}\right)\right)\right) + \\
&\frac{\partial}{\partial \chi_1}\left(\mu\left(\frac{\partial v_3}{\partial \chi_1} + \frac{\partial v_1}{\partial \chi_3}\right)\right) + \frac{\partial}{\partial \chi_2}\left(\mu\left(\frac{\partial v_2}{\partial \chi_3} + \frac{\partial v_3}{\partial \chi_2}\right)\right)
\end{aligned} \tag{2.4}$$

where $\rho$ is the density of the fluid, $p$ is the pressure and $\mu$ is the dynamic viscosity.

We assume incompressible flow, thus the volume dilation is set to zero, i.e.

$$\frac{\partial v_1}{\partial \chi_1} + \frac{\partial v_2}{\partial \chi_2} + \frac{\partial v_3}{\partial \chi_3} = 0 \tag{2.5}$$

also, since the Reynolds number is low for the applications we shall consider, we can neglect inertia

$$\rho \dot{v}_i = 0, \quad i = 1, 2, 3 \tag{2.6}$$

Thus the Navier-Stokes equations for incompressible flow at low Reynolds number, are

$$0 = -\frac{\partial p}{\partial \chi_1} + \frac{\partial}{\partial \chi_1}\left(2\mu \frac{\partial v_1}{\partial \chi_1}\right) + \frac{\partial}{\partial \chi_2}\left(\mu\left(\frac{\partial v_1}{\partial \chi_2} + \frac{\partial v_2}{\partial \chi_1}\right)\right) + \frac{\partial}{\partial \chi_3}\left(\mu\left(\frac{\partial v_3}{\partial \chi_1} + \frac{\partial v_1}{\partial \chi_3}\right)\right) \tag{2.7}$$

$$0 = -\frac{\partial p}{\partial \chi_2} + \frac{\partial}{\partial \chi_2}\left(2\mu \frac{\partial v_2}{\partial \chi_2}\right) + \frac{\partial}{\partial \chi_3}\left(\mu\left(\frac{\partial v_2}{\partial \chi_3} + \frac{\partial v_3}{\partial \chi_2}\right)\right) + \frac{\partial}{\partial \chi_1}\left(\mu\left(\frac{\partial v_1}{\partial \chi_2} + \frac{\partial v_2}{\partial \chi_1}\right)\right) \tag{2.8}$$

$$0 = -\frac{\partial p}{\partial \chi_3} + \frac{\partial}{\partial \chi_3}\left(2\mu \frac{\partial v_3}{\partial \chi_3}\right) + \frac{\partial}{\partial \chi_1}\left(\mu\left(\frac{\partial v_3}{\partial \chi_1} + \frac{\partial v_1}{\partial \chi_3}\right)\right) + \frac{\partial}{\partial \chi_2}\left(\mu\left(\frac{\partial v_2}{\partial \chi_3} + \frac{\partial v_3}{\partial \chi_2}\right)\right) \tag{2.9}$$

we assume the fluid to be homogeneous, i.e., that the viscosity is independent of the position. So

$$\frac{\partial \mu}{\partial \chi_1} = 0, \quad \frac{\partial \mu}{\partial \chi_2} = 0, \quad \frac{\partial \mu}{\partial \chi_3} = 0 \tag{2.10}$$

This limits the analyses to isothermal cases. The resulting error is discussed in section 5.7.

With this, we arrive at

$$\begin{aligned}
0 &= -\frac{\partial p}{\partial \chi_1} + 2\mu \frac{\partial}{\partial \chi_1}\left(\frac{\partial v_1}{\partial \chi_1}\right) + \mu \frac{\partial}{\partial \chi_2}\left(\frac{\partial v_1}{\partial \chi_2} + \frac{\partial v_2}{\partial \chi_1}\right) + \mu \frac{\partial}{\partial \chi_3}\left(\frac{\partial v_3}{\partial \chi_1} + \frac{\partial v_1}{\partial \chi_3}\right) \\
0 &= -\frac{\partial p}{\partial \chi_2} + 2\mu \frac{\partial}{\partial \chi_2}\left(\frac{\partial v_2}{\partial \chi_2}\right) + \mu \frac{\partial}{\partial \chi_3}\left(\frac{\partial v_2}{\partial \chi_3} + \frac{\partial v_3}{\partial \chi_2}\right) + \mu \frac{\partial}{\partial \chi_1}\left(\frac{\partial v_1}{\partial \chi_2} + \frac{\partial v_2}{\partial \chi_1}\right) \\
0 &= -\frac{\partial p}{\partial \chi_3} + 2\mu \frac{\partial}{\partial \chi_3}\left(\frac{\partial v_3}{\partial \chi_3}\right) + \mu \frac{\partial}{\partial \chi_1}\left(\frac{\partial v_3}{\partial \chi_1} + \frac{\partial v_1}{\partial \chi_3}\right) + \mu \frac{\partial}{\partial \chi_2}\left(\frac{\partial v_2}{\partial \chi_3} + \frac{\partial v_3}{\partial \chi_2}\right)
\end{aligned} \tag{2.11}$$

Furthermore, we assume that any change in the $\chi_3$ direction dominates any change in the other directions

$$\frac{\partial}{\partial \chi_1} << \frac{\partial}{\partial \chi_3} >> \frac{\partial}{\partial \chi_2} \tag{2.12}$$

With these approximations, we arrive at

$$\begin{aligned}
\frac{\partial p}{\partial \chi_1} &= \mu \frac{\partial^2 v_1}{\partial \chi_3^2} \\
\frac{\partial p}{\partial \chi_2} &= \mu \frac{\partial^2 v_2}{\partial \chi_3^2} \\
\frac{\partial p}{\partial \chi_3} &= 2\mu \frac{\partial^2 v_3}{\partial \chi_3^2}
\end{aligned} \tag{2.13}$$

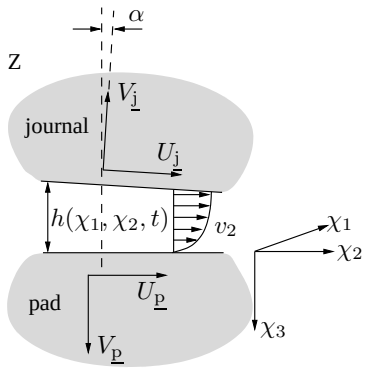


Figure 2.3: Zoom of a part of figure Fig. 2.2

Assuming the pressure constant across the gap ($\frac{\partial p}{\partial \chi_3} = 0$) and integrating Eq. (2.13) twice in the $\chi_3$ direction and rearranging we arrive at

$$\begin{aligned} v_1 &= \frac{1}{\mu}\frac{\partial p}{\partial \chi_1}(k_1\chi_3^2 + k_2\chi_3 + k_3) \\ v_2 &= \frac{1}{\mu}\frac{\partial p}{\partial \chi_2}(k_4\chi_3^2 + k_5\chi_3 + k_6) \\ v_3 &= \frac{1}{\mu}(k_7\chi_3 + k_8) \end{aligned} \tag{2.14}$$

Where, $k_1$ through $k_8$ are integration constants and determined by the boundary conditions. We, apply the following boundary conditions to (2.14)

$$\begin{aligned} \text{Pad surface:} \quad & (\chi_3 = 0) \\ & v_1 = 0 \\ & v_2 = U_{\underline{p}} \\ & v_3 = V_{\underline{p}} + V_{\underline{\text{inj}}} \\ \text{Journal surface:} \quad & (\chi_3 = -h) \\ & v_1 = 0 \\ & v_2 = U_{\underline{j}}\cos(\alpha) - V_{\underline{j}}\sin(\alpha) \\ & v_3 = -V_{\underline{j}}\cos(\alpha) + U_{\underline{j}}\sin(\alpha) \end{aligned} \tag{2.15}$$

Since the angle between journal and pad $\alpha$ (see Fig. 2.3) is small, then

$$\begin{aligned} \cos(\alpha) &\approx 1 \\ \sin(\alpha) &\approx 0 \end{aligned} \tag{2.16}$$

Thus, from (2.14), (2.15) and (2.16) we arrive at

$$\begin{aligned} v_1 &= \frac{1}{2\mu}\frac{\partial p}{\partial \chi_1}(\chi_3^2 + \chi_3 h) \\ v_2 &= \frac{1}{2\mu}\frac{\partial p}{\partial \chi_2}(\chi_3^2 + \chi_3 h) + \frac{U_{\underline{\mathrm{p}}}(\chi_3 + h) - U_{\underline{\mathrm{j}}}\chi_3}{h} \\ v_3 &= \frac{(V_{\underline{\mathrm{p}}} - V_{\underline{\underline{\mathrm{inj}}}})(\chi_3 + h) + V_{\underline{\mathrm{j}}}\chi_3}{h} \end{aligned} \tag{2.17}$$

The radial flow profile $V_{\underline{\underline{\mathrm{inj}}}}$ is most often zero. When inside an orifice it is non-zero. Figure 2.3 shows a zoom of the oil film with indication of the boundary conditions. Figure 2.2 shows an area where $V_{\underline{\underline{\mathrm{inj}}}}$ is non-zero. Note that the no slip condition is taken to apply - even inside the orifice area.

The further derivation follows that of [66], chapter 7. We write Eq. (2.5) in integral form as

$$\int_0^{-h} \left( \frac{\partial v_1}{\partial \chi_1} + \frac{\partial v_2}{\partial \chi_2} + \frac{\partial v_3}{\partial \chi_3} \right) d\chi_3 = 0 \tag{2.18}$$

By use of Eqs. (2.17), the first two terms of (2.18) become

$$\begin{aligned} \int_0^{-h} \left( \frac{\partial v_1}{\partial \chi_1} \right) d\chi_3 &= \frac{\partial}{\partial \chi_1} \int_0^{-h} v_1 d\chi_3 + v_1|_{\chi_3 = -h} \frac{\partial h}{\partial \chi_1} = \frac{1}{12}\frac{\partial}{\partial \chi_1}\left( \frac{h^3}{\mu}\frac{\partial p}{\partial \chi_1} \right) \\ \int_0^{-h} \left( \frac{\partial v_2}{\partial \chi_2} \right) d\chi_3 &= \frac{\partial}{\partial \chi_2} \int_0^{-h} v_2 d\chi_3 + v_2|_{\chi_3 = -h} \frac{\partial h}{\partial \chi_2} = \frac{1}{12}\frac{\partial}{\partial \chi_2}\left( \frac{h^3}{\mu}\frac{\partial p}{\partial \chi_2} \right) - \frac{U_{\underline{\mathrm{j}}} + U_{\underline{\mathrm{p}}}}{2}\frac{\partial h}{\partial \chi_2} \end{aligned} \tag{2.19}$$

Henceforth, we assume that the tangential velocity of the pad is zero and drop the index on $U_{\underline{\mathrm{j}}}$, thus

$$U = U_{\underline{\mathrm{j}}} + U_{\underline{\mathrm{p}}} \tag{2.20}$$

The treatment of the third term of (2.18) differs slightly from that of [66] due to the extra injection terms. We have

$$\int_0^{-h} \left( \frac{\partial v_3}{\partial \chi_3} \right) d\chi_3 = [v_3]_0^{-h} = -V_{\underline{\mathrm{j}}} - V_{\underline{\mathrm{p}}} + V_{\underline{\underline{\mathrm{inj}}}} \tag{2.21}$$

For convenience, let us define the film thickness rate as

$$\dot{h} = V_{\underline{\mathrm{j}}} \cos(\alpha) + V_{\underline{\mathrm{p}}} \approx V_{\underline{\mathrm{j}}} + V_{\underline{\mathrm{p}}} \tag{2.22}$$

where

$$\dot{h} = \frac{\partial h}{\partial t} \tag{2.23}$$

Now, applying Eq. (2.18) with Eq. (2.19), Eq.(2.20) and Eq. (2.22), we are left with

$$\frac{1}{12}\sum_{i=1}^{2} \frac{\partial}{\partial \chi_i}\left( \frac{h^3}{\mu}\frac{\partial p}{\partial \chi_i} \right) = \frac{U}{2}\frac{\partial h}{\partial \chi_2} + \dot{h} - V_{\underline{\underline{\mathrm{inj}}}} \tag{2.24}$$

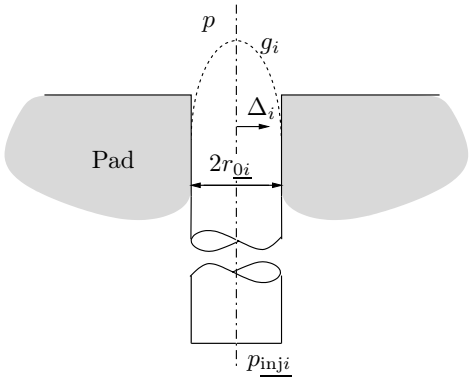


Figure 2.4: The perpendicular orifice distance, radius and velocity profile.

The injection velocity profice can be written as the sum of the contributions from each orifice, thus

$$V_{\underline{\text{inj}}} = \sum_{i=0}^{N_{\underline{\text{o}}}} V_{\underline{\text{inj}}i} \tag{2.25}$$

As in [55], the injection velocity profile is taken to be that of a pressure driven, fully developed, laminar flow in a circular pipe (Poiseuille pipe flow). Thus

$$V_{\underline{\text{inj}}i} = \frac{p_{\underline{\text{inj}}i} - p}{4\mu l_{\underline{0}i}} g_i, \quad i = 1, 2, ..., N_{\underline{\text{o}}} \tag{2.26}$$

where

$$g_i(\chi_1, \chi_2) = \begin{cases} r_{\underline{0}i}^2 - \Delta_i(\chi_1, \chi_2)^2, & \Delta_i < r_{\underline{0}i} \\ 0, & \Delta_i \geq r_{\underline{0}i} \end{cases}, \quad i = 1, 2, ..., N_{\underline{\text{o}}} \tag{2.27}$$

and $N_{\underline{\text{o}}}$ is the number of orifices, $l_{\underline{0}i}$ is the length of inlet $i$, $p_{\underline{\text{inj}}i}$ is the injection pressure and $\Delta_i$ is the perpendicular distance to orifice $i$. See Fig. 2.4 for an explanation.

Thus $(p_{\underline{\text{inj}}i} - p)$ is the pressure drop over the length of the pipe (inlet) number $i$. See [67] for a detailed description of flow in pipes.

Inserting Eq. (2.26) and Eq. (2.27) into Eq. (2.24), we arrive at the modified Reynolds equation, which is subject to all the assumptions made in this section.

$$\frac{1}{12} \sum_{i=1}^{2} \frac{\partial}{\partial \chi_i} \left( \frac{h^3}{\mu} \frac{\partial p}{\partial \chi_i} \right) = \frac{U}{2} \frac{\partial h}{\partial \chi_2} + \dot{h} + \sum_{j=1}^{N_{\underline{\text{o}}}} \frac{g_j (p - p_{\underline{\text{inj}}j})}{4\mu l_{\underline{0}j}} \tag{2.28}$$

As mentioned, the specific choice of flow profile has little influence on the solution for the pressure, since the injection terms typically dominate in Eq. (2.28). Letting $1/(\mu l_{\underline{0}j})$ approach infinity simply yields the solution $p = p_{\underline{\text{inj}}j}$ in the orifice domain, where $g_j$ is non-zero. This does however not mean that the pressure is assumed constant in the orifice domain - simply that the solution happens to be close to constant.

## 2.2 Discretisation

Before we derive the discrete equations for the fluid and the solid, we introduce the discretisation method.

The discretisation is performed with second order serendipity finite elements. Serendipity elements are second order elements, with midnodes on their edges. Since we are dealing with somewhat complex geometries, the finite element is far more convenient than, e.g. the finite difference method. For example, the finite element method is ideally suited to describe the circular orifices. Figure 2.5 shows a twenty node threedimensional serendipity element. The local node numbers are shown.

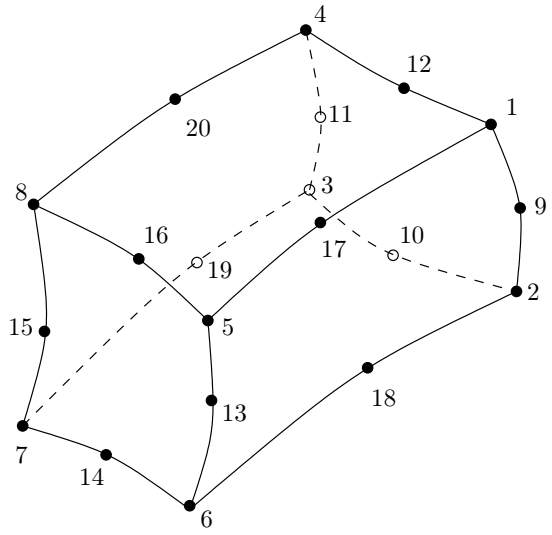


Figure 2.5: Twenty node serendipity element.

The element is defined locally in the isoparametric coordinates $(\xi, \eta, \zeta)$. In Fig. 2.6 the coordinates are seen mapped onto the element. These coordinates facilitate numerical integration using Gauss quadrature as well as operations on relevant element fields.

If the element has a wetted surface, i.e., is in contact with the fluid, then the nodes of the relevant face are numbered locally, and define an eight node twodimensional serendipity element. One such situation is depicted in Fig. 2.7, where the surface defined by $\xi = 1$ is in contact with the fluid.

With the given numbering defined in Fig. 2.5, the isoparametric shape functions have the following expressions.

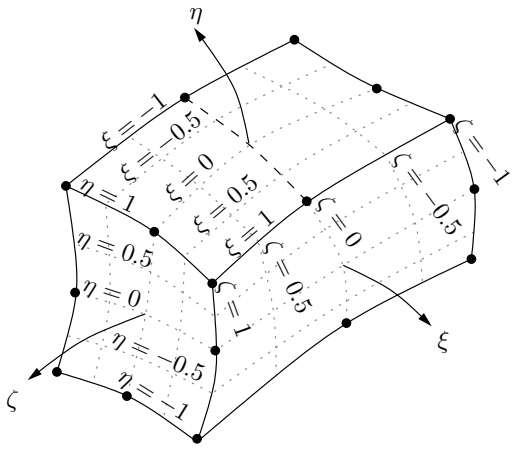


Figure 2.6: Isoparametric coordinates.

$$\begin{aligned}
\phi_i(\xi,\eta,\zeta) &= \frac{1}{8}(1+\xi\xi_i)(1+\eta\eta_i)(1+\zeta\zeta_i)(\xi\xi_i+\eta\eta_i+\zeta\zeta_i-2), \quad i=1,2...8 \\
\phi_i(\xi,\eta,\zeta) &= \frac{1}{4}(1-\xi^2)(1+\eta\eta_i)(1+\zeta\zeta_i), \quad i=9,11,13,15 \\
\phi_i(\xi,\eta,\zeta) &= \frac{1}{4}(1-\eta^2)(1+\zeta\zeta_i)(1+\xi\xi_i), \quad i=10,12,14,16 \\
\phi_i(\xi,\eta,\zeta) &= \frac{1}{4}(1-\zeta^2)(1+\xi\xi_i)(1+\eta\eta_i), \quad i=17,18,19,20
\end{aligned} \tag{2.29}$$

where $\xi_i$ is the $\xi$ value of node $i$ and so forth.

Isoparametric coordinates are convenient, since they do not change from element to element, i.e. they are independent of the specific elements shape, size, orientation and position. The $(x_1, x_2, x_3)$ coordinates are given directly as function of the nodal positions and the isoparametric coordinates $(\xi, \eta, \zeta)$

$$x_i = \sum_{j=1}^{20} \phi_j(\xi,\eta,\zeta) x_{ij}, \quad i=1,2,3 \tag{2.30}$$

where $x_{ij}$ is the nodal position in $x_i = (x_1, x_2, x_3)$ coordinates of node $j$.

As we shall see, to solve the equations governing the solid and the fluid, we need to be able to define partial derivatives with respect to the inertial coordinates $(x_1, x_2, x_3)$ as well as the curvilinear coordinates $(\chi_1, \chi_2, \chi_3)$. The partial derivatives with respect to isoparametric coordinates can be written in therms of partial derivatives with respect to inertial coordinates as

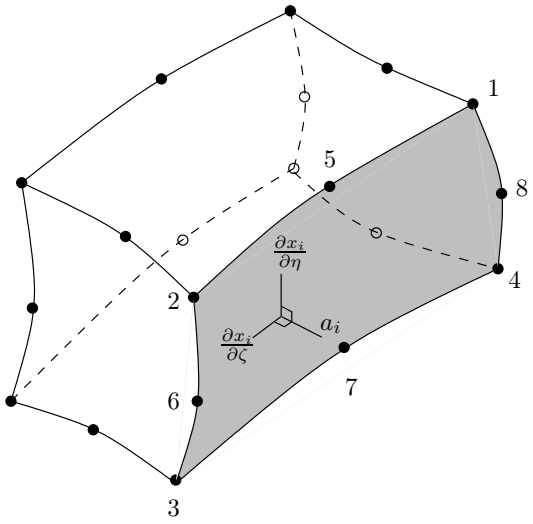


Figure 2.7: Element with wetted surface.

$$\begin{Bmatrix} \frac{\partial}{\partial \xi} \\ \frac{\partial}{\partial \eta} \\ \frac{\partial}{\partial \zeta} \end{Bmatrix} = \begin{bmatrix} \frac{\partial x_1}{\partial \xi} & \frac{\partial x_2}{\partial \xi} & \frac{\partial x_3}{\partial \xi} \\ \frac{\partial x_1}{\partial \eta} & \frac{\partial x_2}{\partial \eta} & \frac{\partial x_3}{\partial \eta} \\ \frac{\partial x_1}{\partial \zeta} & \frac{\partial x_2}{\partial \zeta} & \frac{\partial x_3}{\partial \zeta} \end{bmatrix} \begin{Bmatrix} \frac{\partial}{\partial x_1} \\ \frac{\partial}{\partial x_2} \\ \frac{\partial}{\partial x_3} \end{Bmatrix} \tag{2.31}$$

So to get the partial derivatives with respect to inertial coordinates, we simply invert the matrix. Thus

$$\begin{Bmatrix} \frac{\partial}{\partial x_1} \\ \frac{\partial}{\partial x_2} \\ \frac{\partial}{\partial x_3} \end{Bmatrix} = \begin{bmatrix} \frac{\partial x_1}{\partial \xi} & \frac{\partial x_2}{\partial \xi} & \frac{\partial x_3}{\partial \xi} \\ \frac{\partial x_1}{\partial \eta} & \frac{\partial x_2}{\partial \eta} & \frac{\partial x_3}{\partial \eta} \\ \frac{\partial x_1}{\partial \zeta} & \frac{\partial x_2}{\partial \zeta} & \frac{\partial x_3}{\partial \zeta} \end{bmatrix}^{-1} \begin{Bmatrix} \frac{\partial}{\partial \xi} \\ \frac{\partial}{\partial \eta} \\ \frac{\partial}{\partial \zeta} \end{Bmatrix} \tag{2.32}$$

To get partial derivatives with respect to curvilinear coordinates is slightly more complicated. First we define the inward normal of an element $\mathbf{a}$ as

$$\mathbf{a}_{\underline{3}} = a_{\underline{3}k} = \sum_{i,j=1}^{3} e_{jik} \left.\frac{\partial x_j}{\partial \zeta}\right|_{\xi=1} \left.\frac{\partial x_i}{\partial \eta}\right|_{\xi=1}, \quad k = 1, 2, 3 \tag{2.33}$$

where $e_{jik}$ is the permutation symbol. In vector notation, thus

$$\mathbf{a}_{\underline{3}} = \left.\frac{\partial \mathbf{x}}{\partial \zeta}\right|_{\xi=1} \times \left.\frac{\partial \mathbf{x}}{\partial \eta}\right|_{\xi=1} \tag{2.34}$$

Now, let us define the axial direction of the rotor as $\mathbf{v}_{\underline{\mathrm{r}}}$ where the left hand rule applies, i.e., the rotor is rotating clockwise with $\mathbf{v}_{\underline{\mathrm{r}}}$ pointing out of the paper. Then the projection of this axis onto the surface of an element is

$$\mathbf{a}_{\underline{1}} = \mathbf{v}_{\underline{\mathrm{r}}} - (\mathbf{v}_{\underline{\mathrm{r}}} \cdot \mathbf{a}_{\underline{3}})\mathbf{a}_{\underline{3}} \tag{2.35}$$

finally, let us define

$$\mathbf{a}_{\underline{2}} = \mathbf{a}_{\underline{3}} \times \mathbf{a}_{\underline{1}} \tag{2.36}$$

We then normalize, to yield

$$\mathbf{b}_{\underline{1}} = \frac{\mathbf{a}_{\underline{1}}}{|\mathbf{a}_{\underline{1}}|}, \quad \mathbf{b}_{\underline{2}} = \frac{\mathbf{a}_{\underline{2}}}{|\mathbf{a}_{\underline{2}}|}, \quad \mathbf{b}_{\underline{3}} = \frac{\mathbf{a}_{\underline{3}}}{|\mathbf{a}_{\underline{3}}|} \tag{2.37}$$

Note that in the present thesis, all analyses will assume the rotor to align with the $x_3$ direction. However, the above theory allows for axial rotor tilt inside the bearing.

The three vectors $(\mathbf{b}_{\underline{1}}, \mathbf{b}_{\underline{2}}, \mathbf{b}_{\underline{3}})$ form the local basis of the curvilinear coordinate system $(\chi_1, \chi_2, \chi_3)$. Thus we may write

$$\begin{Bmatrix} \frac{\partial}{\partial \chi_1} \\ \frac{\partial}{\partial \chi_2} \\ \frac{\partial}{\partial \chi_3} \end{Bmatrix} = \begin{bmatrix} b_{\underline{1}1} & b_{\underline{1}2} & b_{\underline{1}3} \\ b_{\underline{2}1} & b_{\underline{2}2} & b_{\underline{2}3} \\ b_{\underline{3}1} & b_{\underline{3}2} & b_{\underline{3}3} \end{bmatrix} \begin{Bmatrix} \frac{\partial}{\partial x_1} \\ \frac{\partial}{\partial x_2} \\ \frac{\partial}{\partial x_3} \end{Bmatrix} \tag{2.38}$$

Now, plugging in Eq. (2.32) we arrive at

$$\begin{Bmatrix} \frac{\partial}{\partial \chi_1} \\ \frac{\partial}{\partial \chi_2} \\ \frac{\partial}{\partial \chi_3} \end{Bmatrix} = \begin{bmatrix} b_{\underline{1}1} & b_{\underline{1}2} & b_{\underline{1}3} \\ b_{\underline{2}1} & b_{\underline{2}2} & b_{\underline{2}3} \\ b_{\underline{3}1} & b_{\underline{3}2} & b_{\underline{3}3} \end{bmatrix} \begin{bmatrix} \frac{\partial x_1}{\partial \xi} & \frac{\partial x_2}{\partial \xi} & \frac{\partial x_3}{\partial \xi} \\ \frac{\partial x_1}{\partial \eta} & \frac{\partial x_2}{\partial \eta} & \frac{\partial x_3}{\partial \eta} \\ \frac{\partial x_1}{\partial \zeta} & \frac{\partial x_2}{\partial \zeta} & \frac{\partial x_3}{\partial \zeta} \end{bmatrix}^{-1} \begin{Bmatrix} \frac{\partial}{\partial \xi} \\ \frac{\partial}{\partial \eta} \\ \frac{\partial}{\partial \zeta} \end{Bmatrix} \tag{2.39}$$

Now, with information of nodal positions in the inertial coordinates and rotor orientation, we can compute partial derivatives in both inertial and curvilinear coordinates.

For more detail on isoparametric coordinates, see [68].

## 2.3 The fluid film

In section 2.1 the Reynolds equation was derived from the Navier-Stokes equations. The Reynolds equation can be solved in a variety of ways. Here we choose the finite element method. This is for two reasons. Firstly, the solid will be discretised with the finite element method, so using it also for the fluid makes communication between the two systems straight forward. Secondly, because of the orifices in the lubricated surface, the geometry to be discretised is not simple. In previous studies [55, 61] the finite difference method has been used. While it is easy to implement, the finite difference method is restricted to rectangular grids, and thus requires many grid points to describe the circular orifice profiles.

Let us restate Eq. (2.28)

$$\frac{1}{12}\sum_{i=1}^{2} \frac{\partial}{\partial \chi_i}\left(\frac{h^3}{\mu}\frac{\partial p}{\partial \chi_i}\right) = \frac{U}{2}\frac{\partial h}{\partial \chi_2} + \dot{h} + \sum_{i}^{N_{\underline{\underline{o}}}} \frac{g_i(p - p_{\underline{\underline{\mathrm{inj}}}i})}{4\mu l_{\underline{0}i}}$$

With the assumption of a piecewise smooth pressure profile, the Reynolds equation can be written in weak form as

$$\int_\Phi \frac{1}{12}\sum_{i=1}^{2}\frac{\partial}{\partial\chi_i}\left(\frac{h^3}{\mu}\frac{\partial p}{\partial\chi_i}\right)vd\Phi = \int_\Phi \frac{U}{2}\frac{\partial h}{\partial\chi_2}vd\Phi + \int_\Phi \dot{h}vd\Phi + \int_\Phi \sum_{i}^{N_{\underline{o}}}\frac{g_i(p-p_{\underline{\text{inj}}i})}{4\mu l_{\underline{0}i}}vd\Phi \tag{2.40}$$

Where $v$ is a test function, i.e., it is a function that satisfies the same boundary conditions as $p$. Applying the divergence theorem to the left hand side we get

$$\int_\Phi \frac{1}{12}\sum_{i=1}^{2}\frac{\partial}{\partial\chi_i}\left(\frac{h^3}{\mu}\frac{\partial p}{\partial\chi_i}\right)vd\Phi = \int_\Gamma \frac{1}{12}\sum_{i=1}^{2}\frac{h^3}{\mu}\frac{\partial p}{\partial\chi_i}n_i vd\Gamma - \int_\Phi \frac{1}{12}\sum_{i=1}^{2}\frac{\partial v}{\partial\chi_i}\frac{h^3}{\mu}\frac{\partial p}{\partial\chi_i}d\Phi \tag{2.41}$$

where $n_i = [n_1, n_2]^T$ is the outward normal of the boundary of $\Phi$. Field quantities are now expanded in terms of shape functions as

$$h = \sum_{n\in\mathbb{F}} h_n\phi_n, \quad p = \sum_{n\in\mathbb{F}} p_n\phi_n, \quad v = \sum_{n\in\mathbb{F}} v_n\phi_n, \quad g_i = \sum_{n\in\mathbb{F}} g_{in}\phi_n \tag{2.42}$$

where $\mathbb{F}$ is the set of nodes in the fluid. Plugging this into Eqs. (2.40) and (2.41) produces

$$\begin{aligned}
&\int_\Gamma \frac{1}{12}\sum_{i=1}^{2}\frac{\left(\sum_{n\in\mathbb{F}} h_n\phi_n\right)^3}{\mu}\left(\sum_{n\in\mathbb{F}} p_n\frac{\partial\phi_n}{\partial\chi_i}\right)n_i\sum_{m\in\mathbb{F}}(\phi_m v_m)d\Gamma - \\
&\int_\Phi \frac{1}{12}\sum_{i=1}^{2}\left(\sum_{n\in\mathbb{F}} v_n\frac{\partial\phi_n}{\partial\chi_i}\right)\frac{\left(\sum_{n\in\mathbb{F}} h_n\phi_n\right)^3}{\mu}\left(\sum_{n\in\mathbb{F}} p_n\frac{\partial\phi_n}{\partial\chi_i}\right)d\Phi = \\
&\int_\Phi \frac{U}{2}\left(\sum_{n\in\mathbb{F}} h_n\frac{\partial\phi_n}{\partial\chi_2}\right)\left(\sum_{n\in\mathbb{F}} v_n\phi_n\right)d\Phi + \int_\Phi\left(\sum_{n\in\mathbb{F}}\dot{h}_n\phi_n\right)\left(\sum_{n\in\mathbb{F}} v_n\phi_n\right)d\Phi + \\
&\int_\Phi \sum_{i=1}^{N_{\underline{o}}}\left(\frac{\left(\sum_{n\in\mathbb{F}} g_{in}\phi_n\right)}{4\mu l_{\underline{0}i}}\left(\left(\sum_{n\in\mathbb{F}} p_n\phi_n\right) - p_{\underline{\text{inj}}i}\right)\right)\left(\sum_{n\in\mathbb{F}} v_n\phi_n\right)d\Phi
\end{aligned} \tag{2.43}$$

Since the shape functions $\phi_n, \quad n = 1, 2, 3...$, are also test functions, Eq. (2.43) must hold for any choice of $v_n, \quad n = 1, 2, 3....$ Thus we can eliminate $v_n$ and the summation over it. We arrive at the equations

$$\begin{aligned}
&\int_\Gamma \frac{1}{12}\sum_{i=1}^{2}\frac{\left(\sum_{n\in\mathbb{F}} h_n\phi_n\right)^3}{\mu}\left(\sum_{n\in\mathbb{F}} p_n\frac{\partial\phi_n}{\partial\chi_i}\right)n_i\phi_m d\Gamma - \\
&\int_\Phi \frac{1}{12}\sum_{i=1}^{2}\frac{\partial\phi_m}{\partial\chi_i}\frac{\left(\sum_{n\in\mathbb{F}} h_n\phi_n\right)^3}{\mu}\left(\sum_{n\in\mathbb{F}} p_n\frac{\partial\phi_n}{\partial\chi_i}\right)d\Phi = \\
&\int_\Phi \frac{U}{2}\left(\sum_{n\in\mathbb{F}} h_n\frac{\partial\phi_n}{\partial\chi_2}\right)\phi_m d\Phi + \int_\Phi\left(\sum_{n\in\mathbb{F}}\dot{h}_n\phi_n\right)\phi_m d\Phi + \\
&\int_\Phi \sum_{i=1}^{N_{\underline{o}}}\left(\frac{\left(\sum_{n\in\mathbb{F}} g_{in}\phi_n\right)}{4\mu l_{\underline{0}i}}\left(\left(\sum_{n\in\mathbb{F}} p_n\phi_n\right) - p_{\underline{\text{inj}}i}\right)\right)\phi_m d\Phi
\end{aligned} \tag{2.44}$$

We can state the discretised Reynolds equation more simply as

$$\sum_{n\in\mathbb{F}} A_{mn}p_n + \sum_{i=1}^{N_{\underline{o}}} W_{mi}p_{\underline{\text{inj}}i} = r_m, \quad m \in \mathbb{F} \tag{2.45}$$

where

$$A_{mn} = \int_\Phi \frac{1}{12}\sum_{i=1}^{2}\frac{\partial\phi_m}{\partial\chi_i}\frac{\left(\sum_{n\in\mathbb{F}} h_n\phi_n\right)^3}{\mu}\frac{\partial\phi_n}{\partial\chi_i}d\Phi + \int_\Phi \sum_{i=1}^{N_{\underline{o}}}\frac{\sum_{k\in\mathbb{F}} g_{ik}\phi_k}{4\mu l_{\underline{0}i}}\phi_n\phi_m d\Phi \tag{2.46}$$

,

$$W_{mi} = -\int_\Phi \frac{\sum_{n\in\mathbb{F}} g_{in}\phi_n}{4\mu l_{\underline{0}i}}\phi_m d\Phi, \quad i = 1, 2, ..., N_{\underline{o}} \tag{2.47}$$

and

$$\begin{aligned} r_m = &\int_\Gamma \frac{1}{12}\sum_{i=1}^{2}\frac{\left(\sum_{n\in\mathbb{F}} h_n\phi_n\right)^3}{\mu}\left(\sum_{n\in\mathbb{F}} p_n\frac{\partial\phi_n}{\partial\chi_i}\right)n_i\phi_m d\Gamma - \\ &\int_\Phi \frac{U}{2}\left(\sum_{n\in\mathbb{F}} h_n\frac{\partial\phi_n}{\partial\chi_2}\right)\phi_m d\Phi - \int_\Phi\left(\sum_{n\in\mathbb{F}}\dot{h}_n\phi_n\right)\phi_m d\Phi \end{aligned} \tag{2.48}$$

This accounts for the pressure distribution in the oil film. Let $\dim(\mathbb{F})$ denote the cardinality of the set $\mathbb{F}$. As we have $\dim(\mathbb{F})+N_{\underline{o}}$ variables and only $\dim(\mathbb{F})$ equations, the system as such has no unique solution. The following section considers the flow through the valve, and will provide the equations needed for a unique solution to exist.

### 2.3.1 The valve

The model of the valve is distinctly simple in order to keep model complexity reasonable. Real life valves are rather complex and display nonlinear behaviour. If the valve is overlapped, there exist positions of the valve piston, where supply to both orifices is shut off. If the valve is underlapped, there is always a flow to both orifices, albeit this flow may vary. It can be argued that an underlapped valve can be captured better by a linear model, than an overlapped valve, since a flow shut off is a strongly nonlinear phenomenon. The present valve model is that of an underlapped valve. This is however not only to make the modelling easier; a constant lubricant supply is desirable. The main assumptions with regard to the valve are as follows

- The leak flow can be prescribed, i.e., is independent of the orifice pressure.
- The internal orifice to orifice flow-pressure impedance $1/K_{\underline{\text{pq}}}$ is constant.

A refinement of the valve model would most prudently introduce a dependency between the leak flow and the orifice pressure. The resulting functional would depend on the reservoir pressure. Also, one would make the flow-pressure impedance depend on the flow. Such refinements would introduce further nonlinearities into the model. We shall refrain from this in the present study.

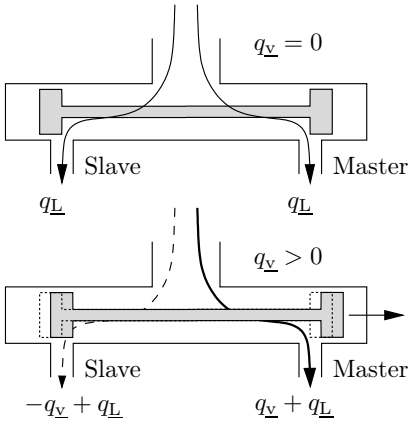


Figure 2.8: Schematic of generic underlapped servo-valve. The valve is shown in two situations. Top: No driven flow. Bottom: A positive piston flow, showing the positive orientation of the valve.

Figure 2.8 shows a servo-valve with two orifices and illustrates the concept of "master" and "slave" orifices. The master orifice is defined as the orifice through which the flow increases when $q_{\underline{v}}$ is increased. Henceforth, let us denote $q_{\underline{v}}$ the "piston flow".

Figure 2.9 shows the pressure driven flow in the servo-valve. Which will pass from the high pressure orifice to the low pressure orifice. The total flow through an orifice is the linear superposition of leak flow, piston flow and the pressure driven flow. Consider the special case of one valve connecting two orifices $i$ and $j$, i.e., $N_{\underline{o}} = 2$. If orifice $i$ (master) and $j$ (slave) are connected as a pair, the flows through them $q_i$ and $q_j$ would be computed as.

$$\begin{Bmatrix} q_i \\ q_j \end{Bmatrix} = \begin{bmatrix} -K_{\underline{pq}} & K_{\underline{pq}} \\ K_{\underline{pq}} & -K_{\underline{pq}} \end{bmatrix} \begin{Bmatrix} p_{\underline{inj}i} \\ p_{\underline{inj}j} \end{Bmatrix} + \begin{Bmatrix} q_{\underline{v}} \\ -q_{\underline{v}} \end{Bmatrix} + \begin{Bmatrix} q_{\underline{L}} \\ q_{\underline{L}} \end{Bmatrix} \tag{2.49}$$

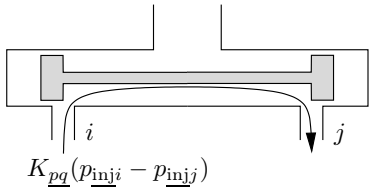


Figure 2.9: Schematic of generic underlapped servo-valve. The pressure driven flow is illustrated.

The piston flow is described by the second order ordinary differential equation [47]

$$\ddot{q}_{\underline{v}} + 2\xi_{\underline{v}}\omega_{\underline{v}}\dot{q}_{\underline{v}} + \omega_{\underline{v}}^2 q_{\underline{v}} = \omega_{\underline{v}}^2 K_{\underline{v}} u_{\underline{v}} \tag{2.50}$$

or

$$\frac{1}{\omega_{\underline{v}}^2 K_{\underline{v}}}\ddot{q}_{\underline{v}} + \frac{2\xi_{\underline{v}}}{\omega_{\underline{v}} K_{\underline{v}}}\dot{q}_{\underline{v}} + \frac{1}{K_{\underline{v}}} q_{\underline{v}} = u_{\underline{v}} \tag{2.51}$$

If more servo-valves are included, an uncoupled system of equations results, thus.

$$\mathbf{M}_{\underline{\text{q-q}}}\ddot{\mathbf{q}}_{\underline{\text{v}}} + \mathbf{D}_{\underline{\text{q-q}}}\dot{\mathbf{q}}_{\underline{\text{v}}} + \mathbf{K}_{\underline{\text{q-q}}}\mathbf{q}_{\underline{\text{v}}} = \mathbf{u}_{\underline{\text{v}}} \tag{2.52}$$

From the derivation of the modified Reynolds equation (2.28) we know that the flow through a given orifice into the gap can be written in terms of the pressure difference field over the orifice as

$$q_i = \int_\Phi g_i \frac{1}{4\mu l_{\underline{0}i}} \left( p_{\underline{\text{inj}}i} - p \right) d\Phi \tag{2.53}$$

where $g_i$ are shape functions, that describe the velocity profile in the orifice. Plugging Eq. (2.53) into Eq. (2.49) we arrive at

$$\left\{ \begin{array}{c} \int_\Phi g_i \frac{1}{4\mu l_{\underline{0}i}} \left( p_{\underline{\text{inj}}i} - p \right) d\Phi \\ \int_\Phi g_j \frac{1}{4\mu l_{\underline{0}j}} \left( p_{\underline{\text{inj}}j} - p \right) d\Phi \end{array} \right\} = \left[ \begin{array}{cc} -K_{\underline{\text{pq}}} & K_{\underline{\text{pq}}} \\ K_{\underline{\text{pq}}} & -K_{\underline{\text{pq}}} \end{array} \right] \left\{ \begin{array}{c} p_{\underline{\text{inj}}i} \\ p_{\underline{\text{inj}}j} \end{array} \right\} + \left\{ \begin{array}{c} q_{\underline{\text{v}}} \\ -q_{\underline{\text{v}}} \end{array} \right\} + \left\{ \begin{array}{c} q_{\underline{\text{L}}} \\ q_{\underline{\text{L}}} \end{array} \right\} \tag{2.54}$$

again, expanding in terms of shape functions

$$\begin{array}{c} \left\{ \begin{array}{c} \int_\Phi \left( \sum_{n\in\mathbb{F}} g_{in}\phi_n \right) \frac{1}{4\mu l_{\underline{0}i}} \left( \left( p_{\underline{\text{inj}}i} - \sum_{n\in\mathbb{F}} p_n\phi_n \right) \right) d\Phi \\ \int_\Phi \left( \sum_{n\in\mathbb{F}} g_{jn}\phi_n \right) \frac{1}{4\mu l_{\underline{0}j}} \left( \left( p_{\underline{\text{inj}}j} - \sum_{n\in\mathbb{F}} p_n\phi_n \right) \right) d\Phi \end{array} \right\} = \\ \left[ \begin{array}{cc} -K_{\underline{\text{pq}}} & K_{\underline{\text{pq}}} \\ K_{\underline{\text{pq}}} & -K_{\underline{\text{pq}}} \end{array} \right] \left\{ \begin{array}{c} p_{\underline{\text{inj}}i} \\ p_{\underline{\text{inj}}j} \end{array} \right\} + \left\{ \begin{array}{c} q_{\underline{\text{v}}} \\ -q_{\underline{\text{v}}} \end{array} \right\} + \left\{ \begin{array}{c} q_{\underline{\text{L}}} \\ q_{\underline{\text{L}}} \end{array} \right\} \end{array} \tag{2.55}$$

or

$$\sum_{m\in\mathbb{F}} W_{mi}p_m + \sum_{m=1}^{N_{\underline{\text{o}}}} Q_{im}p_{\underline{\text{inj}}m} + \sum_{m=1}^{N_{\underline{\text{o}}}} K_{\underline{\text{pq}}im}p_{\underline{\text{inj}}m} = r_{\underline{\text{inj}}i}, \quad i = 1, 2, ..., N_{\underline{\text{o}}} \tag{2.56}$$

where, in this case, $N_{\underline{\text{o}}} = 2$. The system matrices are defined as

$$Q_{in} = \left[ \begin{array}{cc} Q_{11} & Q_{12} \\ Q_{21} & Q_{22} \end{array} \right] = \left[ \begin{array}{cc} \int_\Phi \frac{\sum_{n\in\mathbb{F}} g_{1n}\phi_n}{4\mu l_{\underline{0}1}} d\Phi & \\ & \int_\Phi \frac{\sum_{n\in\mathbb{F}} g_{2n}\phi_n}{4\mu l_{\underline{0}2}} d\Phi \end{array} \right], \tag{2.57}$$

$$K_{\underline{\text{pq}}in} = \left[ \begin{array}{cc} K_{\underline{\text{pq}}11} & K_{\underline{\text{pq}}12} \\ K_{\underline{\text{pq}}21} & K_{\underline{\text{pq}}22} \end{array} \right] = \left[ \begin{array}{cc} K_{\underline{\text{pq}}} & -K_{\underline{\text{pq}}} \\ -K_{\underline{\text{pq}}} & K_{\underline{\text{pq}}} \end{array} \right] \tag{2.58}$$

and

$$r_{\underline{\text{inj}}i} = \{r\}_{\underline{\text{inj}}} = \left\{ \begin{array}{c} q_{\underline{\text{v}}} + q_{\underline{\text{L}}} \\ -q_{\underline{\text{v}}} + q_{\underline{\text{L}}} \end{array} \right\} \tag{2.59}$$

Restating Eq. (2.45) for the present special case of one servo-valve connecting two orifices ($N_{\underline{\text{o}}}$=2) yields

$$\sum_{n\in\mathbb{F}} A_{mn}p_n + \sum_{i}^{2} W_{mi}p_{\underline{\text{inj}}i} = r_m, \quad m \in \mathbb{F} \tag{2.60}$$

Thus, Eq. (2.60) and Eq. (2.56) make up the equations that describe the oil film pressure distribution, as well as the injection pressures. Extending to a system of two servo-valves, 1 and 2, connecting orifices 1 to 2 and 3 to 4, respectively, we get

$$\sum_{n\in\mathbb{F}} A_{mn}p_n + \sum_{i}^{4} W_{mi}p_{\underline{\text{inj}}i} = r_m, \quad m \in \mathbb{F}$$
$$\sum_{m\in\mathbb{F}} W_{mi}p_m + \sum_{m}^{4} Q_{im}p_{\underline{\text{inj}}m} + \sum_{m}^{4} K_{\underline{\text{pq}}m}p_{\underline{\text{inj}}m} = r_{\underline{\text{inj}}i}, \quad i = 1,2,3,4 \tag{2.61}$$

With this, the last four equations extend to

$$\begin{bmatrix} \mathbf{W}_1^T \\ \mathbf{W}_2^T \\ \mathbf{W}_3^T \\ \mathbf{W}_4^T \end{bmatrix} \{p\} +$$
$$\begin{bmatrix} \int_\Phi \frac{\sum_{n\in\mathbb{F}} g_{1n}\phi_n}{4\mu l_{\underline{0}1}} d\Phi & 0 & 0 & 0 \\ 0 & \int_\Phi \frac{\sum_{n\in\mathbb{F}} g_{2n}\phi_n}{4\mu l_{\underline{0}2}} d\Phi & 0 & 0 \\ 0 & 0 & \int_\Phi \frac{\sum_{n\in\mathbb{F}} g_{3n}\phi_n}{4\mu l_{\underline{0}3}} d\Phi & 0 \\ 0 & 0 & 0 & \int_\Phi \frac{\sum_{n\in\mathbb{F}} g_{4n}\phi_n}{4\mu l_{\underline{0}4}} d\Phi \end{bmatrix} \begin{Bmatrix} p_{\underline{\text{inj}}1} \\ p_{\underline{\text{inj}}2} \\ p_{\underline{\text{inj}}3} \\ p_{\underline{\text{inj}}4} \end{Bmatrix} +$$
$$\begin{bmatrix} K_{\underline{\text{pq}}} & -K_{\underline{\text{pq}}} & 0 & 0 \\ -K_{\underline{\text{pq}}} & K_{\underline{\text{pq}}} & 0 & 0 \\ 0 & 0 & K_{\underline{\text{pq}}} & -K_{\underline{\text{pq}}} \\ 0 & 0 & -K_{\underline{\text{pq}}} & K_{\underline{\text{pq}}} \end{bmatrix} \begin{Bmatrix} p_{\underline{\text{inj}}1} \\ p_{\underline{\text{inj}}2} \\ p_{\underline{\text{inj}}3} \\ p_{\underline{\text{inj}}4} \end{Bmatrix} = \begin{Bmatrix} q_{\underline{\text{v}}1} \\ -q_{\underline{\text{v}}1} \\ q_{\underline{\text{v}}2} \\ -q_{\underline{\text{v}}2} \end{Bmatrix} + \begin{Bmatrix} q_{\underline{\text{L}}1} \\ q_{\underline{\text{L}}1} \\ q_{\underline{\text{L}}2} \\ q_{\underline{\text{L}}2} \end{Bmatrix} \tag{2.62}$$

where $\mathbf{W}_1 = W_{m1}$, $\mathbf{W}_2 = W_{m2}$, $\mathbf{W}_3 = W_{m3}$ and $\mathbf{W}_4 = W_{m4}$ for $m \in \mathbb{F}$. Note that any orifice only couples to the orifices that connect to the same valve. Therefore, the matrix is block diagonal.

The extension to more servo-valves is trivial. In general, we write

$$\begin{bmatrix} \mathbf{A} & \mathbf{W} \\ \mathbf{W}^T & \mathbf{Q} + \mathbf{K}_{\underline{\text{pq}}} \end{bmatrix} \begin{Bmatrix} \mathbf{p} \\ \mathbf{p}_{\underline{\text{inj}}} \end{Bmatrix} = \begin{Bmatrix} \mathbf{r} \\ \mathbf{r}_{\underline{\text{inj}}} \end{Bmatrix} \tag{2.63}$$

Since $\mathbf{A}$, $\mathbf{Q}$ and $\mathbf{K}_{\underline{\text{pq}}}$ are symmetric, the system of equations is symmetric. This is only achieved if the Reynolds equation is stated in the form of Eq. (2.28). In the shown examples we have talked of one orifice per pad, i.e., one valve to couple two orifices. However, the equations are equally valid for cases with "orifice arrays", i.e. situations where lubricant is injected by the same servo-valve to many orifices on the same pad. The way to accomplish this, is to alter the laminar flow profile shape function $g_i$, so that it is defined in all the orifices of pad $i$. I.e. it will be non zero on many domains inside each pad. In figure 2.1 the flow profile shape function is non-zero in two domains inside one pad, thus this pad has an orifice array consisting of two orifices.

### 2.3.2 Fluid boundary conditions

The fluid is subject to two different boundary conditions.

- # 1: The pressure on the boundary ($\Gamma$) is set to zero. In reality the pressure is equal to the ambient pressure, however, as long as the fluid is incompressible, we may simply add the ambient pressure to all pressure results obtained, if we wish. Since the ambient pressure is hydrostatic, and acts on all pad faces, it does not affect the resulting force on the pads.
- # 2: The pressure gradient on the boundary is set to zero. This is sometimes called the Reynolds condition.
- # 3: Any computed negative pressure is set to zero. This is the Gumbell cavitation condition.

The first of these boundary conditions is a Dirichlet boundary condition while the second is a Neumann boundary condition. As it turns out, in this case, if condition #1 is satisfied, then condition #2 is automatically also satisfied. This can be realised by considering Eq. (2.48). The boundary condition is invoked by the method of zeros and ones, see, e.g., [68].

Condition #3 is the simplest possible cavitation model. Since TPJBs generally do not cavitate, the condition is seldom needed. This holds true in particular for the linearised analyses (stability and harmonic frequency response) since they assume infinitesimal perturbations about the static equilibrium state, which does most often not involve cavitation.

## 2.4 The pads

The solid is taken to be linearly elastic and isotropic. Small strains and rotations suffice for the description of the deformed state. The governing equation is traditionally given directly in integral form as the principle of virtual work

$$\sum_{i,j,k,l=1}^{3} \int_{\Pi} L_{ijkl}\varepsilon_{kl}\delta\varepsilon_{ij}d\Pi = -\sum_{i=1}^{3}\int_{\Pi}\rho\ddot{u}_i\delta u_i d\Pi + \sum_{i=1}^{3}\int_{\Lambda} T_i\delta u_i d\Lambda \tag{2.64}$$

where $\varepsilon_{kl}$ is the strain tensor, $\rho$ is the density of the solid, $T_i$ denotes the surface traction, $u_i$ is the displacement vector $\delta$ denotes an increment and $L_{ijkl}$ is the constitutive tensor for the material, and is given by

$$L_{ijkl} = \frac{E}{2(1+\nu)}\left(\delta_{ik}\delta_{jl} + \delta_{il}\delta_{jk} + \frac{2\nu}{1-2\nu}\delta_{ij}\delta_{kl}\right) \tag{2.65}$$

where $\delta_{jl}$ is Kronecker's delta. Since we consider the strains and rotations to be small, the relation between displacement and strain becomes

$$\varepsilon_{ij} = \frac{1}{2}\left(\frac{\partial u_i}{\partial x_j} + \frac{\partial u_j}{\partial x_i}\right), \quad i,j = 1,2,3 \tag{2.66}$$

where $E$ is Young's modulus and $\nu$ is Poisson's ratio. From equations Eq. (2.64) and Eq. (2.65) the stiffness and mass matrices of the solid can be derived. We expand the displacement vector field and traction field in terms of shape functions as

$$u_i = \sum_{n\in\mathbb{S}} u_{in}\phi_n, \quad T_i = \sum_{n\in\mathbb{S}} T_{in}\phi_n, \tag{2.67}$$

Where $u_{in}$ is the displacement of node $n$ in direction $x_i$, $T_{in}$ is the traction of node $n$ in direction $x_i$ and $\mathbb{S}$ is the set of nodes that belong to the solid. It is convenient to introduce

$$d_j = u_{in}, \quad j = 3(n-1)+i, \quad i = 1,2,3, \quad n \in \mathbb{S} \tag{2.68}$$

and

$$\psi_{ij} = \delta_{ik}\phi_n, \quad j = 3(n-1)+k, \quad i,k = 1,2,3, \quad n \in \mathbb{S} \tag{2.69}$$

that is

$$d_j = [u_{11}\ u_{12}\ u_{13}\ u_{21}\ ...]^T \tag{2.70}$$

and

$$\psi_{ij} = \begin{bmatrix} \phi_1 & & & \phi_2 & & & \\ & \phi_1 & & & \phi_2 & & ... \\ & & \phi_1 & & & \phi_2 & \end{bmatrix} \tag{2.71}$$

Thus, we can write the displacement field as

$$u_i = \sum_{n\in\mathbb{S}^3} \psi_{in} d_n \tag{2.72}$$

where $\mathbb{S}^3$ is the set of degrees of freedom in the (discrete) solid. thus, plugging into Eq. (2.66), we get

$$\varepsilon_{ij} = \frac{1}{2}\sum_{n\in\mathbb{S}} u_{in}\frac{\partial\phi_n}{\partial x_j} + u_{jn}\frac{\partial\phi_n}{\partial x_i} = \frac{1}{2}\sum_{n\in\mathbb{S}^3}\left(\frac{\partial\psi_{in}}{\partial x_j} + \frac{\partial\psi_{jn}}{\partial x_i}\right) d_n \tag{2.73}$$

and Eq. (2.64) becomes

$$\begin{aligned} &\sum_{i,j,k,l=1}^{3}\int_\Pi L_{ijkl}\frac{1}{4}\sum_{m\in\mathbb{S}^3}\left(\frac{\partial\psi_{km}}{\partial x_l}+\frac{\partial\psi_{lm}}{\partial x_k}\right)d_m \sum_{m\in\mathbb{S}^3}\left(\frac{\partial\psi_{in}}{\partial x_j}+\frac{\partial\psi_{jn}}{\partial x_i}\right)\delta d_n d\Pi = \\ &-\sum_{i=1}^{3}\int_\Pi \rho\sum_{m\in\mathbb{S}^3}\psi_{im}\ddot{d}_m\sum_{n\in\mathbb{S}^3}\psi_{in}\delta d_n d\Pi + \sum_{i=1}^{3}\int_\Lambda\sum_{m\in\mathbb{S}^3}T_{im}\phi_m\sum_{n\in\mathbb{S}^3}\psi_{in}\delta d_n d\Lambda \end{aligned} \tag{2.74}$$

Since the equations must hold for any $\delta d_n$, we can eliminate $\delta d_n$ to produce

$$\begin{aligned} &\sum_{i,j,k,l=1}^{3}\int_\Pi L_{ijkl}\frac{1}{4}\sum_{m\in\mathbb{S}^3}\left(\frac{\partial\psi_{km}}{\partial x_l}+\frac{\partial\psi_{lm}}{\partial x_k}\right)d_m\left(\frac{\partial\psi_{in}}{\partial x_j}+\frac{\partial\psi_{jn}}{\partial x_i}\right)d\Pi = \\ &-\sum_{i=1}^{3}\int_\Pi\rho\sum_{m\in\mathbb{S}^3}\psi_{im}\ddot{d}_m\psi_{in}d\Pi + \sum_{i=1}^{3}\int_\Lambda\sum_{m\in\mathbb{S}^3}T_{im}\phi_m\psi_{in}d\Lambda, \quad n\in\mathbb{S}^3 \end{aligned} \tag{2.75}$$

or

$$\begin{aligned} &\sum_{m\in\mathbb{S}^3}\left[\sum_{i,j,k,l=1}^{3}\int_\Pi L_{ijkl}\frac{1}{4}\left(\frac{\partial\psi_{km}}{\partial x_l}+\frac{\partial\psi_{lm}}{\partial x_k}\right)\left(\frac{\partial\psi_{in}}{\partial x_j}+\frac{\partial\psi_{jn}}{\partial x_i}\right)\right]d\Pi d_m = \\ &-\sum_{m\in\mathbb{S}^3}\left[\sum_{i=1}^{3}\int_\Pi\rho\psi_{im}\psi_{in}d\Pi\right]\ddot{d}_m + \sum_{i=1}^{3}\int_\Lambda\sum_{m\in\mathbb{S}^3}T_{im}\phi_m\psi_{in}d\Lambda, \quad n\in\mathbb{S}^3 \end{aligned} \tag{2.76}$$

thus arriving at the algebraic equations

$$\sum_{m\in\mathbb{S}^3} K_{\underline{s}nm} d_m + \sum_{m\in\mathbb{S}^3} M_{\underline{s}nm} \ddot{d}_m = f_n, \quad n \in \mathbb{S}^3 \tag{2.77}$$

or simply

$$\mathbf{K}_{\underline{s}}\mathbf{d} + \mathbf{M}_{\underline{s}}\ddot{\mathbf{d}} = \mathbf{f} \tag{2.78}$$

where

$$\begin{aligned}
K_{\underline{s}nm} &= \sum_{i,j,k,l=1}^{3} \int_{\Pi} L_{ijkl} \frac{1}{4} \left( \frac{\partial \psi_{km}}{\partial x_l} + \frac{\partial \psi_{lm}}{\partial x_k} \right) \left( \frac{\partial \psi_{in}}{\partial x_j} + \frac{\partial \psi_{jn}}{\partial x_i} \right) d\Pi, \quad m,n \in \mathbb{S}^3 \\
M_{\underline{s}nm} &= \sum_{i=1}^{3} \int_{\Pi} \rho \psi_{im} \psi_{in} d\Pi, \quad m,n \in \mathbb{S}^3 \\
f_n &= \sum_{i=1}^{3} \int_{\Lambda} \sum_{m\in\mathbb{S}^3} T_{im} \phi_m \psi_{in} d\Lambda, \quad n \in \mathbb{S}^3
\end{aligned} \tag{2.79}$$

These equations are derived in many textbooks, for instanve in [68].

### 2.4.1 Pad boundary conditions

The pads are free to rotate, that is, the only resistance to rotation is that coming from the fluid. But they are not free to translate. That is, we need to invoke a pivoting boundary condition. The simplest way to do this is to constrain a line of nodes. This is unphysical, since it corresponds to a pad, which balances on an infinitely sharp knifes edge, which is not the real life case. In a rigid body model that will not matter, since the pad does not deform. In a compliant pad model it introduces a mesh dependency and a stress singularity; as the mesh is refined, the pad will become increasingly "soft" and the stresses around the pivot will go to infinity. The solution will never converge. Other authors [37] have tackled this problem simply by supporting the pads along two lines of nodes. However, then the pad rotation must be introduced ad hoc.

A realistic pivot boundary condition can be invoked with relative ease. The idea is illustrated in Fig. 2.10. The solid stiffness matrix is transformed to a rotated coordinate system, where one coordinate axis is aligned with the direction from the relevant node to the pivot point. In this coordinate system, there is one, and only one coordinate direction corresponding to axial movement, i.e., movement toward the pivot. The degrees of freedom pointing in that coordinate direction are constrained with the method of zeros and ones [68]. After the degrees of freedom have been constrained, the solid stiffness matrix is transformed back to the ($x_1$,$x_2$,$x_3$) coordinate system. This means that invoking the pivot boundary condition, requires one coordinate transformation for each node to be constrained. Keep in mind though, that only the parts of the solid stiffness matrix, that couple to the relevant node, need be transformed.

It may seem tempting to simply add very stiff springs between the pivot point and the nodes. This will, however, introduce high frequencies into the system, and produce numerical difficulties.

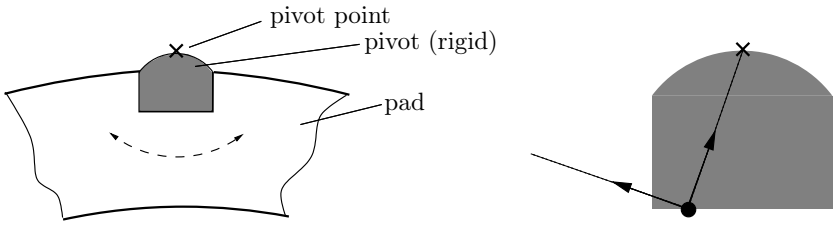


Figure 2.10: The pivot boundary condition. The pivot point is marked with an $\times$. A zoom is shown, where a node on the boundary is being constrained. The rotated pivot coordinate system is shown.

## 2.5 The rotor

The rotor is described as a two by two particle system, with provision for stiffness, damping and inertia. It is given directly as

$$\begin{bmatrix} k_{\underline{r}11} & k_{\underline{r}12} \\ k_{\underline{r}21} & k_{\underline{r}22} \end{bmatrix} \begin{Bmatrix} d_{\underline{r}1} \\ d_{\underline{r}2} \end{Bmatrix} + \begin{bmatrix} c_{\underline{r}11} & c_{\underline{r}12} \\ c_{\underline{r}21} & c_{\underline{r}22} \end{bmatrix} \begin{Bmatrix} \dot{d}_{\underline{r}1} \\ \dot{d}_{\underline{r}2} \end{Bmatrix} + \begin{bmatrix} m_{\underline{r}} & 0 \\ 0 & m_{\underline{r}} \end{bmatrix} \begin{Bmatrix} \ddot{d}_{\underline{r}1} \\ \ddot{d}_{\underline{r}2} \end{Bmatrix} = \begin{Bmatrix} f_{\underline{r}1} \\ f_{\underline{r}2} \end{Bmatrix} \tag{2.80}$$

As mentioned, henceforth the rotor shall be assumed to align with the $x_3$ coordinate direction, and move only laterally. The stiffness and damping matrices include off diagonal terms, to account for either structural damping in the rotor or aerodynamic cross coupling in a component on the rotor.

## 2.6 Coupling of the fluid, solid, valve and rotor

With all the subsystems and coupling equations defined, the global system of equations may be compiled. Figure 2.11 shows an example of a bearing with four pads connected in pairs by two servo-valves. The valves are responding to a rotor displacement.

Let us restate the equations for the fluid, the solid, the valve and the rotor.

Fluid:

$$\begin{bmatrix} \mathbf{A} & \mathbf{W} \\ \mathbf{W}^T & \mathbf{Q} + \mathbf{K}_{\underline{\mathrm{pq}}} \end{bmatrix} \begin{Bmatrix} \mathbf{p} \\ \mathbf{p}_{\underline{\mathrm{inj}}} \end{Bmatrix} = \begin{Bmatrix} \mathbf{r} \\ \mathbf{r}_{\underline{\mathrm{inj}}} \end{Bmatrix},$$

Solid:

$$\mathbf{K}\mathbf{d} + \mathbf{M}\ddot{\mathbf{d}} = \mathbf{f}$$

Valve:

$$\mathbf{M}_{\underline{\mathrm{q\text{-}q}}}\ddot{\mathbf{q}}_{\underline{\mathrm{v}}} + \mathbf{D}_{\underline{\mathrm{q\text{-}q}}}\dot{\mathbf{q}}_{\underline{\mathrm{v}}} + \mathbf{K}_{\underline{\mathrm{q\text{-}q}}}\mathbf{q}_{\underline{\mathrm{v}}} = \mathbf{u}_{\underline{\mathrm{v}}}$$

Rotor:

$$\begin{bmatrix} k_{\underline{r}11} & k_{\underline{r}12} \\ k_{\underline{r}21} & k_{\underline{r}22} \end{bmatrix} \begin{Bmatrix} d_{\underline{r}1} \\ d_{\underline{r}2} \end{Bmatrix} + \begin{bmatrix} c_{\underline{r}11} & c_{\underline{r}12} \\ c_{\underline{r}21} & c_{\underline{r}22} \end{bmatrix} \begin{Bmatrix} \dot{d}_{\underline{r}1} \\ \dot{d}_{\underline{r}2} \end{Bmatrix} + \begin{bmatrix} m_{\underline{r}} & 0 \\ 0 & m_{\underline{r}} \end{bmatrix} \begin{Bmatrix} \ddot{d}_{\underline{r}1} \\ \ddot{d}_{\underline{r}2} \end{Bmatrix} = \begin{Bmatrix} f_{\underline{r}1} \\ f_{\underline{r}2} \end{Bmatrix}$$

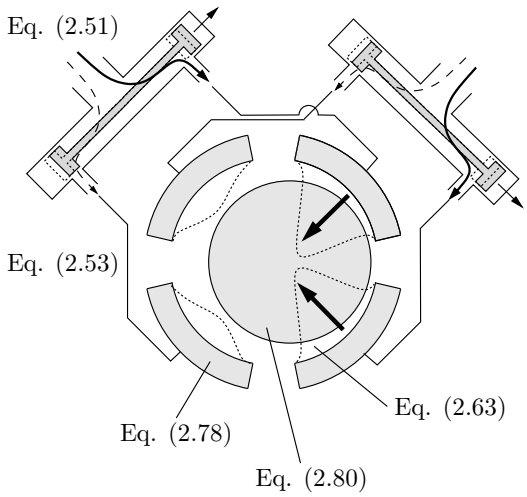


Figure 2.11: Generic rendering of the global system consisting of oil film (fluid), pads (solid), valve and rotor. Some of the relevant equations are indicated.

With slight abuse of notation, we can write the dependencies as

$$\begin{aligned}
\mathbf{r} &= \mathbf{r}(\mathbf{d}, \dot{\mathbf{d}}, \mathbf{d}_{\underline{\mathrm{r}}}, \dot{\mathbf{d}}_{\underline{\mathrm{r}}}) \\
\mathbf{A} &= \mathbf{A}(\mathbf{d}, \mathbf{d}_{\underline{\mathrm{r}}}) \\
\mathbf{f} &= \mathbf{f}(\mathbf{p}) \\
\mathbf{f}_{\underline{\mathrm{r}}} &= \mathbf{f}_{\underline{\mathrm{r}}}(\mathbf{p}) \\
\mathbf{u}_{\underline{\mathrm{v}}} &= \mathbf{u}_{\underline{\mathrm{v}}}(\mathbf{d}_{\underline{\mathrm{r}}}, \dot{\mathbf{d}}_{\underline{\mathrm{r}}}, ...)
\end{aligned} \tag{2.81}$$

Here we have indicated how the equations depend on each other. Immediately we see that the equations are nonlinear, since the parameters of one set of equations depend on the solution to the other set of equations.

With this, we may write the equations unified as

| | | | | | | | |
|---|---|---|---|---|---|---|---|
| Nodal solid equations: | $\mathbf{M}_{\underline{\mathrm{s}}}\ddot{\mathbf{d}}$ | + | | | $\mathbf{K}_{\underline{\mathrm{s}}}\mathbf{d}$ | = | $\mathbf{f}(\mathbf{p})$ |
| Rotor equations: | $\mathbf{M}_{\underline{\mathrm{r}}}\ddot{\mathbf{d}}_{\underline{\mathrm{r}}}$ | + | $\mathbf{D}_{\underline{\mathrm{r}}}\dot{\mathbf{d}}_{\underline{\mathrm{r}}}$ | + | $\mathbf{K}_{\underline{\mathrm{r}}}\mathbf{d}_{\underline{\mathrm{r}}}$ | = | $\mathbf{f}_{\underline{\mathrm{r}}}(\mathbf{p})$ |
| Nodal pressure equations: | $\mathbf{A}(\mathbf{d}, \mathbf{d}_{\underline{\mathrm{r}}})\mathbf{p}$ | + | | | $\mathbf{W}\mathbf{p}_{\underline{\mathrm{inj}}}$ | = | $\mathbf{r}(\mathbf{d}, \dot{\mathbf{d}}, \mathbf{d}_{\underline{\mathrm{r}}}, \dot{\mathbf{d}}_{\underline{\mathrm{r}}})$ |
| Injection pressure equations: | $\mathbf{W}^T\mathbf{p}$ | + | | | $(\mathbf{Q} + \mathbf{K}_{\underline{\mathrm{pq}}})\mathbf{p}_{\underline{\mathrm{inj}}}$ | = | $\mathbf{r}_{\underline{\mathrm{inj}}}(\mathbf{q}_{\underline{\mathrm{v}}})$ |
| Valve flow equations: | $\mathbf{M}_{\underline{\mathrm{q\text{-}q}}}\ddot{\mathbf{q}}_{\underline{\mathrm{v}}}$ | + | $\mathbf{D}_{\underline{\mathrm{q\text{-}q}}}\dot{\mathbf{q}}_{\underline{\mathrm{v}}}$ | + | $\mathbf{K}_{\underline{\mathrm{q\text{-}q}}}\mathbf{q}_{\underline{\mathrm{v}}}$ | = | $\mathbf{u}_{\underline{\mathrm{v}}}(\mathbf{d}_{\underline{\mathrm{r}}}, \dot{\mathbf{d}}_{\underline{\mathrm{r}}}, ...)$ |

We define the control system signal as the sum of proportional and derivative (P-D) contributions, as well as a reference signal. The P-D contributions respond to rotor movement. Thus

$$\mathbf{u}_{\underline{\mathrm{v}}} = -\mathbf{G}_{\underline{\mathrm{P}}}\mathbf{d}_{\underline{\mathrm{r}}} - \mathbf{G}_{\underline{\mathrm{D}}}\dot{\mathbf{d}}_{\underline{\mathrm{r}}} + \mathbf{u}_{\underline{\mathrm{vr}}} \tag{2.82}$$

Moving the control system gains to the left hand side, the servo-valve equations are written as

$$\mathbf{M}_{\underline{\text{q-q}}}\ddot{\mathbf{q}}_{\underline{\text{v}}} \;+\; \mathbf{D}_{\underline{\text{q-q}}}\dot{\mathbf{q}}_{\underline{\text{v}}} \;+\; \mathbf{K}_{\underline{\text{q-q}}}\mathbf{q}_{\underline{\text{v}}} + \mathbf{G}_{\underline{\text{P}}}\mathbf{d}_{\underline{\text{r}}} + \mathbf{G}_{\underline{\text{D}}}\dot{\mathbf{d}}_{\underline{\text{r}}} \;=\; \mathbf{u}_{\underline{\text{vr}}} \tag{2.83}$$

The matrices $\mathbf{G}_{\underline{\text{P}}}$ and $\mathbf{G}_{\underline{\text{D}}}$ are the matrices of control system proportional and derivative gains. The vector $\mathbf{u}_{\underline{\text{vr}}}$ represents the vector of reference signals. In all analyses in this study, the reference signal is set to zero.

In matrix form, we can write

$$\begin{bmatrix} \mathbf{M}_{\underline{\text{s}}} & & & & \\ & \mathbf{M}_{\underline{\text{r}}} & & & \\ & & & & \\ & & & & \\ & & & & \mathbf{M}_{\underline{\text{q-q}}} \end{bmatrix} \begin{Bmatrix} \ddot{\mathbf{d}} \\ \ddot{\mathbf{d}}_{\underline{\text{r}}} \\ \ddot{\mathbf{p}} \\ \ddot{\mathbf{p}}_{\underline{\text{inj}}} \\ \ddot{\mathbf{q}}_{\underline{\text{v}}} \end{Bmatrix} + \begin{bmatrix} & & & & \\ & \mathbf{D}_{\underline{\text{r}}} & & & \\ & & & & \\ & & & & \\ & & & \mathbf{G}_{\underline{\text{D}}} & \mathbf{D}_{\underline{\text{q-q}}} \end{bmatrix} \begin{Bmatrix} \dot{\mathbf{d}} \\ \dot{\mathbf{d}}_{\underline{\text{r}}} \\ \dot{\mathbf{p}} \\ \dot{\mathbf{p}}_{\underline{\text{inj}}} \\ \dot{\mathbf{q}}_{\underline{\text{v}}} \end{Bmatrix} +$$
$$\begin{bmatrix} \mathbf{K}_{\underline{\text{s}}} & & & & & \\ & \mathbf{K}_{\underline{\text{r}}} & & & & \\ & & \mathbf{A} & \mathbf{W} & & \\ & & \mathbf{W}^T & \mathbf{Q}+\mathbf{K}_{\underline{\text{pq}}} & & \\ & \mathbf{G}_{\underline{\text{P}}} & & & \mathbf{K}_{\underline{\text{q-q}}} & \end{bmatrix} \begin{Bmatrix} \mathbf{d} \\ \mathbf{d}_{\underline{\text{r}}} \\ \mathbf{p} \\ \mathbf{p}_{\underline{\text{inj}}} \\ \mathbf{q}_{\underline{\text{v}}} \end{Bmatrix} = \begin{Bmatrix} \mathbf{f} \\ \mathbf{f}_{\underline{\text{r}}} \\ \mathbf{r} \\ \mathbf{r}_{\underline{\text{inj}}} \\ \mathbf{u}_{\underline{\text{vr}}} \end{Bmatrix} \tag{2.84}$$

These equations are the starting point for any of the analyses presented in this thesis, be it in the time domain or frequency domain, linear or nonlinear.

## 2.7 Linearisation

From Eq. (2.84) let us define the residual equations.

$$\begin{Bmatrix} \underline{\text{res}}\mathbf{f} \\ \underline{\text{res}}\mathbf{f}_{\underline{\text{r}}} \\ \underline{\text{res}}\mathbf{r} \\ \underline{\text{res}}\mathbf{r}_{\underline{\text{inj}}} \\ \underline{\text{res}}\mathbf{u}_{\underline{\text{vr}}} \end{Bmatrix} = \begin{bmatrix} \mathbf{M}_{\underline{\text{s}}} & & & & \\ & \mathbf{M}_{\underline{\text{r}}} & & & \\ & & & & \\ & & & & \\ & & & & \mathbf{M}_{\underline{\text{q-q}}} \end{bmatrix} \begin{Bmatrix} \ddot{\mathbf{d}} \\ \ddot{\mathbf{d}}_{\underline{\text{r}}} \\ \ddot{\mathbf{p}} \\ \ddot{\mathbf{p}}_{\underline{\text{inj}}} \\ \ddot{\mathbf{q}}_{\underline{\text{v}}} \end{Bmatrix} + \begin{bmatrix} & & & & \\ & \mathbf{D}_{\underline{\text{r}}} & & & \\ & & & & \\ & & & & \\ & & & \mathbf{G}_{\underline{\text{D}}} & \mathbf{D}_{\underline{\text{q-q}}} \end{bmatrix} \begin{Bmatrix} \dot{\mathbf{d}} \\ \dot{\mathbf{d}}_{\underline{\text{r}}} \\ \dot{\mathbf{p}} \\ \dot{\mathbf{p}}_{\underline{\text{inj}}} \\ \dot{\mathbf{q}}_{\underline{\text{v}}} \end{Bmatrix} +$$
$$\begin{bmatrix} \mathbf{K}_{\underline{\text{s}}} & & & & \\ & \mathbf{K}_{\underline{\text{r}}} & & & \\ & & \mathbf{A} & \mathbf{W} & \\ & & \mathbf{W}^T & \mathbf{Q} & \\ & \mathbf{G}_{\underline{\text{P}}} & & & \mathbf{K}_{\underline{\text{q-q}}} \end{bmatrix} \begin{Bmatrix} \mathbf{d} \\ \mathbf{d}_{\underline{\text{r}}} \\ \mathbf{p} \\ \mathbf{p}_{\underline{\text{inj}}} \\ \mathbf{q}_{\underline{\text{v}}} \end{Bmatrix} - \begin{Bmatrix} \mathbf{f} \\ \mathbf{f}_{\underline{\text{r}}} \\ \mathbf{r} \\ \mathbf{r}_{\underline{\text{inj}}} \\ \mathbf{u}_{\underline{\text{vr}}} \end{Bmatrix} \tag{2.85}$$

The left hand side of Eq. (2.85) must be identically zero, for Eq. (2.84) to be satisfied. Let us seek the linear part of Eq. (2.85). Since the left hand side is identically zero (thus constant, regardless of solution), its derivative vanishes. We may therefore write the first order taylor expansion of Eq. (2.85) as

$$
\begin{bmatrix}
\frac{\partial^{\text{res}}\mathbf{f}}{\partial \ddot{\mathbf{d}}^T} & \frac{\partial^{\text{res}}\mathbf{f}}{\partial \ddot{\mathbf{d}}_{\underline{\text{r}}}^T} & \frac{\partial^{\text{res}}\mathbf{f}}{\partial \ddot{\mathbf{p}}^T} & \frac{\partial^{\text{res}}\mathbf{f}}{\partial \ddot{\mathbf{p}}_{\underline{\text{inj}}}^T} & \frac{\partial^{\text{res}}\mathbf{f}}{\partial \ddot{\mathbf{q}}_{\underline{\text{v}}}^T} \\
\frac{\partial^{\text{res}}\mathbf{f}_{\underline{\text{r}}}}{\partial \ddot{\mathbf{d}}^T} & \frac{\partial^{\text{res}}\mathbf{f}_{\underline{\text{r}}}}{\partial \ddot{\mathbf{d}}_{\underline{\text{r}}}^T} & \frac{\partial^{\text{res}}\mathbf{f}_{\underline{\text{r}}}}{\partial \ddot{\mathbf{p}}^T} & \frac{\partial^{\text{res}}\mathbf{f}_{\underline{\text{r}}}}{\partial \ddot{\mathbf{p}}_{\underline{\text{inj}}}^T} & \frac{\partial^{\text{res}}\mathbf{f}_{\underline{\text{r}}}}{\partial \ddot{\mathbf{q}}_{\underline{\text{v}}}^T} \\
\frac{\partial^{\text{res}}\mathbf{r}}{\partial \ddot{\mathbf{d}}^T} & \frac{\partial^{\text{res}}\mathbf{r}}{\partial \ddot{\mathbf{d}}_{\underline{\text{r}}}^T} & \frac{\partial^{\text{res}}\mathbf{r}}{\partial \ddot{\mathbf{p}}^T} & \frac{\partial^{\text{res}}\mathbf{r}}{\partial \ddot{\mathbf{p}}_{\underline{\text{inj}}}^T} & \frac{\partial^{\text{res}}\mathbf{r}}{\partial \ddot{\mathbf{q}}_{\underline{\text{v}}}^T} \\
\frac{\partial^{\text{res}}\mathbf{r}_{\underline{\text{inj}}}}{\partial \ddot{\mathbf{d}}^T} & \frac{\partial^{\text{res}}\mathbf{r}_{\underline{\text{inj}}}}{\partial \ddot{\mathbf{d}}_{\underline{\text{r}}}^T} & \frac{\partial^{\text{res}}\mathbf{r}_{\underline{\text{inj}}}}{\partial \ddot{\mathbf{p}}^T} & \frac{\partial^{\text{res}}\mathbf{r}_{\underline{\text{inj}}}}{\partial \ddot{\mathbf{p}}_{\underline{\text{inj}}}^T} & \frac{\partial^{\text{res}}\mathbf{r}_{\underline{\text{inj}}}}{\partial \ddot{\mathbf{q}}_{\underline{\text{v}}}^T} \\
\frac{\partial^{\text{res}}\mathbf{u}_{\underline{\text{vr}}}^T}{\partial \ddot{\mathbf{d}}^T} & \frac{\partial^{\text{res}}\mathbf{u}_{\underline{\text{vr}}}^T}{\partial \ddot{\mathbf{d}}_{\underline{\text{r}}}^T} & \frac{\partial^{\text{res}}\mathbf{u}_{\underline{\text{vr}}}^T}{\partial \ddot{\mathbf{p}}^T} & \frac{\partial^{\text{res}}\mathbf{u}_{\underline{\text{vr}}}^T}{\partial \ddot{\mathbf{p}}_{\underline{\text{inj}}}^T} & \frac{\partial^{\text{res}}\mathbf{u}_{\underline{\text{vr}}}^T}{\partial \ddot{\mathbf{q}}_{\underline{\text{v}}}^T}
\end{bmatrix}
\begin{Bmatrix}
\delta\ddot{\mathbf{d}} \\ \delta\ddot{\mathbf{d}}_{\underline{\text{r}}} \\ \delta\ddot{\mathbf{p}} \\ \delta\ddot{\mathbf{p}}_{\underline{\text{inj}}} \\ \delta\ddot{\mathbf{q}}_{\underline{\text{v}}}
\end{Bmatrix} +
$$

$$
\begin{bmatrix}
\frac{\partial^{\text{res}}\mathbf{f}}{\partial \dot{\mathbf{d}}^T} & \frac{\partial^{\text{res}}\mathbf{f}}{\partial \dot{\mathbf{d}}_{\underline{\text{r}}}^T} & \frac{\partial^{\text{res}}\mathbf{f}}{\partial \dot{\mathbf{p}}^T} & \frac{\partial^{\text{res}}\mathbf{f}}{\partial \dot{\mathbf{p}}_{\underline{\text{inj}}}^T} & \frac{\partial^{\text{res}}\mathbf{f}}{\partial \dot{\mathbf{q}}_{\underline{\text{v}}}^T} \\
\frac{\partial^{\text{res}}\mathbf{f}_{\underline{\text{r}}}}{\partial \dot{\mathbf{d}}^T} & \frac{\partial^{\text{res}}\mathbf{f}_{\underline{\text{r}}}}{\partial \dot{\mathbf{d}}_{\underline{\text{r}}}^T} & \frac{\partial^{\text{res}}\mathbf{f}_{\underline{\text{r}}}}{\partial \dot{\mathbf{p}}^T} & \frac{\partial^{\text{res}}\mathbf{f}_{\underline{\text{r}}}}{\partial \dot{\mathbf{p}}_{\underline{\text{inj}}}^T} & \frac{\partial^{\text{res}}\mathbf{f}_{\underline{\text{r}}}}{\partial \dot{\mathbf{q}}_{\underline{\text{v}}}^T} \\
\frac{\partial^{\text{res}}\mathbf{r}}{\partial \dot{\mathbf{d}}^T} & \frac{\partial^{\text{res}}\mathbf{r}}{\partial \dot{\mathbf{d}}_{\underline{\text{r}}}^T} & \frac{\partial^{\text{res}}\mathbf{r}}{\partial \dot{\mathbf{p}}^T} & \frac{\partial^{\text{res}}\mathbf{r}}{\partial \dot{\mathbf{p}}_{\underline{\text{inj}}}^T} & \frac{\partial^{\text{res}}\mathbf{r}}{\partial \dot{\mathbf{q}}_{\underline{\text{v}}}^T} \\
\frac{\partial^{\text{res}}\mathbf{r}_{\underline{\text{inj}}}}{\partial \dot{\mathbf{d}}^T} & \frac{\partial^{\text{res}}\mathbf{r}_{\underline{\text{inj}}}}{\partial \dot{\mathbf{d}}_{\underline{\text{r}}}^T} & \frac{\partial^{\text{res}}\mathbf{r}_{\underline{\text{inj}}}}{\partial \dot{\mathbf{p}}^T} & \frac{\partial^{\text{res}}\mathbf{r}_{\underline{\text{inj}}}}{\partial \dot{\mathbf{p}}_{\underline{\text{inj}}}^T} & \frac{\partial^{\text{res}}\mathbf{r}_{\underline{\text{inj}}}}{\partial \dot{\mathbf{q}}_{\underline{\text{v}}}^T} \\
\frac{\partial^{\text{res}}\mathbf{u}_{\underline{\text{vr}}}^T}{\partial \dot{\mathbf{d}}^T} & \frac{\partial^{\text{res}}\mathbf{u}_{\underline{\text{vr}}}^T}{\partial \dot{\mathbf{d}}_{\underline{\text{r}}}^T} & \frac{\partial^{\text{res}}\mathbf{u}_{\underline{\text{vr}}}^T}{\partial \dot{\mathbf{p}}^T} & \frac{\partial^{\text{res}}\mathbf{u}_{\underline{\text{vr}}}^T}{\partial \dot{\mathbf{p}}_{\underline{\text{inj}}}^T} & \frac{\partial^{\text{res}}\mathbf{u}_{\underline{\text{vr}}}^T}{\partial \dot{\mathbf{q}}_{\underline{\text{v}}}^T}
\end{bmatrix}
\begin{Bmatrix}
\delta\dot{\mathbf{d}} \\ \delta\dot{\mathbf{d}}_{\underline{\text{r}}} \\ \delta\dot{\mathbf{p}} \\ \delta\dot{\mathbf{p}}_{\underline{\text{inj}}} \\ \delta\dot{\mathbf{q}}_{\underline{\text{v}}}
\end{Bmatrix} +
$$

$$
\begin{bmatrix}
\frac{\partial^{\text{res}}\mathbf{f}}{\partial \mathbf{d}^T} & \frac{\partial^{\text{res}}\mathbf{f}}{\partial \mathbf{d}_{\underline{\text{r}}}^T} & \frac{\partial^{\text{res}}\mathbf{f}}{\partial \mathbf{p}^T} & \frac{\partial^{\text{res}}\mathbf{f}}{\partial \mathbf{p}_{\underline{\text{inj}}}^T} & \frac{\partial^{\text{res}}\mathbf{f}}{\partial \mathbf{q}_{\underline{\text{v}}}^T} \\
\frac{\partial^{\text{res}}\mathbf{f}_{\underline{\text{r}}}}{\partial \mathbf{d}^T} & \frac{\partial^{\text{res}}\mathbf{f}_{\underline{\text{r}}}}{\partial \mathbf{d}_{\underline{\text{r}}}^T} & \frac{\partial^{\text{res}}\mathbf{f}_{\underline{\text{r}}}}{\partial \mathbf{p}^T} & \frac{\partial^{\text{res}}\mathbf{f}_{\underline{\text{r}}}}{\partial \mathbf{p}_{\underline{\text{inj}}}^T} & \frac{\partial^{\text{res}}\mathbf{f}_{\underline{\text{r}}}}{\partial \mathbf{q}_{\underline{\text{v}}}^T} \\
\frac{\partial^{\text{res}}\mathbf{r}}{\partial \mathbf{d}^T} & \frac{\partial^{\text{res}}\mathbf{r}}{\partial \mathbf{d}_{\underline{\text{r}}}^T} & \frac{\partial^{\text{res}}\mathbf{r}}{\partial \mathbf{p}^T} & \frac{\partial^{\text{res}}\mathbf{r}}{\partial \mathbf{p}_{\underline{\text{inj}}}^T} & \frac{\partial^{\text{res}}\mathbf{r}}{\partial \mathbf{q}_{\underline{\text{v}}}^T} \\
\frac{\partial^{\text{res}}\mathbf{r}_{\underline{\text{inj}}}}{\partial \mathbf{d}^T} & \frac{\partial^{\text{res}}\mathbf{r}_{\underline{\text{inj}}}}{\partial \mathbf{d}_{\underline{\text{r}}}^T} & \frac{\partial^{\text{res}}\mathbf{r}_{\underline{\text{inj}}}}{\partial \mathbf{p}^T} & \frac{\partial^{\text{res}}\mathbf{r}_{\underline{\text{inj}}}}{\partial \mathbf{p}_{\underline{\text{inj}}}^T} & \frac{\partial^{\text{res}}\mathbf{r}_{\underline{\text{inj}}}}{\partial \mathbf{q}_{\underline{\text{v}}}^T} \\
\frac{\partial^{\text{res}}\mathbf{u}_{\underline{\text{vr}}}^T}{\partial \mathbf{d}^T} & \frac{\partial^{\text{res}}\mathbf{u}_{\underline{\text{vr}}}^T}{\partial \mathbf{d}_{\underline{\text{r}}}^T} & \frac{\partial^{\text{res}}\mathbf{u}_{\underline{\text{vr}}}^T}{\partial \mathbf{p}^T} & \frac{\partial^{\text{res}}\mathbf{u}_{\underline{\text{vr}}}^T}{\partial \mathbf{p}_{\underline{\text{inj}}}^T} & \frac{\partial^{\text{res}}\mathbf{u}_{\underline{\text{vr}}}^T}{\partial \mathbf{q}_{\underline{\text{v}}}^T}
\end{bmatrix}
\begin{Bmatrix}
\delta\mathbf{d} \\ \delta\mathbf{d}_{\underline{\text{r}}} \\ \delta\mathbf{p} \\ \delta\mathbf{p}_{\underline{\text{inj}}} \\ \delta\mathbf{q}_{\underline{\text{v}}}
\end{Bmatrix} =
\begin{Bmatrix}
\delta\mathbf{f} \\ \delta\mathbf{f}_{\underline{\text{r}}} \\ \delta\mathbf{r} \\ \delta\mathbf{r}_{\underline{\text{inj}}} \\ \delta\mathbf{u}_{\underline{\text{vr}}}
\end{Bmatrix} \tag{2.86}
$$

where $\delta$ denotes a small perturbation. This amounts to

$$
\begin{bmatrix}
\mathbf{M}_{\underline{\text{s}}} & & & \\
& \mathbf{M}_{\underline{\text{r}}} & & \\
& & & \\
& & & \mathbf{M}_{\underline{\text{q-q}}}
\end{bmatrix}
\begin{Bmatrix}
\delta\ddot{\mathbf{d}} \\ \delta\ddot{\mathbf{d}}_{\underline{\text{r}}} \\ \delta\ddot{\mathbf{p}} \\ \delta\ddot{\mathbf{p}}_{\underline{\text{inj}}} \\ \delta\ddot{\mathbf{q}}_{\underline{\text{v}}}
\end{Bmatrix} +
\begin{bmatrix}
 & \mathbf{D}_{\underline{\text{r}}} & & \\
\frac{\partial^{\text{res}}\mathbf{r}}{\partial \dot{\mathbf{d}}^T} & \frac{\partial^{\text{res}}\mathbf{r}}{\partial \dot{\mathbf{d}}_{\underline{\text{r}}}^T} & & \\
 & & & \\
 & \mathbf{G}_{\underline{\text{D}}} & & \mathbf{D}_{\underline{\text{q-q}}}
\end{bmatrix}
\begin{Bmatrix}
\delta\dot{\mathbf{d}} \\ \delta\dot{\mathbf{d}}_{\underline{\text{r}}} \\ \delta\dot{\mathbf{p}} \\ \delta\dot{\mathbf{p}}_{\underline{\text{inj}}} \\ \delta\dot{\mathbf{q}}_{\underline{\text{v}}}
\end{Bmatrix} +
$$

$$
\begin{bmatrix}
\mathbf{K}_{\underline{\text{s}}} & & \frac{\partial^{\text{res}}\mathbf{f}}{\partial \mathbf{p}^T} & & \\
 & \mathbf{K}_{\underline{\text{r}}} & \frac{\partial^{\text{res}}\mathbf{f}_{\underline{\text{r}}}}{\partial \mathbf{p}^T} & & \\
\frac{\partial^{\text{res}}\mathbf{r}}{\partial \mathbf{d}^T} & \frac{\partial^{\text{res}}\mathbf{r}}{\partial \mathbf{d}_{\underline{\text{r}}}^T} & \mathbf{A} & \mathbf{W} & \\
 & & \mathbf{W}^T & \mathbf{Q} & \frac{\partial^{\text{res}}\mathbf{r}_{\underline{\text{inj}}}}{\partial \mathbf{q}_{\underline{\text{v}}}^T} \\
 & \mathbf{G}_{\underline{\text{P}}} & & & \mathbf{K}_{\underline{\text{q-q}}}
\end{bmatrix}
\begin{Bmatrix}
\delta\mathbf{d} \\ \delta\mathbf{d}_{\underline{\text{r}}} \\ \delta\mathbf{p} \\ \delta\mathbf{p}_{\underline{\text{inj}}} \\ \delta\mathbf{q}_{\underline{\text{v}}}
\end{Bmatrix} =
\begin{Bmatrix}
\delta\mathbf{f} \\ \delta\mathbf{f}_{\underline{\text{r}}} \\ \delta\mathbf{r} \\ \delta\mathbf{r}_{\underline{\text{inj}}} \\ \delta\mathbf{u}_{\underline{\text{vr}}}
\end{Bmatrix} \tag{2.87}
$$

Some terms we recognise from previous derivations. Others must be investigated to yield explicit expressions. These are

$$\frac{\partial^{\underline{\text{res}}}\mathbf{r}}{\partial \mathbf{d}^T} = \frac{\partial^{\underline{\text{res}}} r_m}{\partial d_i} = \sum_{n\in\mathbb{F}} \frac{\partial A_{mn}}{\partial d_i} p_n - \frac{\partial r_m}{\partial d_i}, \quad m \in \mathbb{F}, \quad i \in \mathbb{S}^3 \tag{2.88}$$

$$\frac{\partial^{\underline{\text{res}}}\mathbf{r}}{\partial \mathbf{d}_{\underline{\mathbf{r}}}^T} = \frac{\partial^{\underline{\text{res}}} r_m}{\partial d_{\underline{\mathbf{r}}i}} = \sum_{n\in\mathbb{F}} \frac{\partial A_{mn}}{\partial d_{\underline{\mathbf{r}}i}} p_n - \frac{\partial r_m}{\partial d_{\underline{\mathbf{r}}i}}, \quad m \in \mathbb{F}, \quad i = 1,2,3 \tag{2.89}$$

$$\frac{\partial^{\underline{\text{res}}}\mathbf{r}}{\partial \dot{\mathbf{d}}^T} = \frac{\partial^{\underline{\text{res}}} r_m}{\partial \dot{d}_i} = -\frac{\partial r_m}{\partial \dot{d}_i}, \quad m \in \mathbb{F}, \quad i \in \mathbb{S}^3 \tag{2.90}$$

$$\frac{\partial^{\underline{\text{res}}}\mathbf{r}}{\partial \dot{\mathbf{d}}_{\underline{\mathbf{r}}}^T} = \frac{\partial^{\underline{\text{res}}} r_m}{\partial \dot{d}_{\underline{\mathbf{r}}i}} = -\frac{\partial r_m}{\partial \dot{d}_{\underline{\mathbf{r}}i}}, \quad m \in \mathbb{F}, \quad i = 1,2,3 \tag{2.91}$$

$$\frac{\partial^{\underline{\text{res}}}\mathbf{f}}{\partial \mathbf{p}^T} = \frac{\partial f_n}{\partial p_i}, \quad n \in \mathbb{S}^3, \quad i \in \mathbb{F} \tag{2.92}$$

$$\frac{\partial^{\underline{\text{res}}}\mathbf{f}_{\underline{\mathbf{r}}}}{\partial \mathbf{p}^T} = \frac{\partial f_{\underline{\mathbf{r}}k}}{\partial p_i}, \quad k = 1,2,3, \quad i \in \mathbb{F} \tag{2.93}$$

$$\frac{\partial^{\underline{\text{res}}}\mathbf{r}_{\underline{\text{inj}}}}{\partial \mathbf{q}_{\underline{\mathbf{v}}}^T} = -\frac{\partial r_{\underline{\text{inj}}j}}{\partial q_{\underline{\mathbf{v}}i}} \quad i,j = 1,2,...\underline{\text{Number of valves}} \tag{2.94}$$

The derivative of the right hand side of the Reynolds equation with respect to nodal displacements is

$$\frac{\partial r_m}{\partial d_i} = \frac{\partial}{\partial d_i}\left(-\int_\Phi \frac{U}{2}\left(\sum_{n=1}^N h_n \frac{\partial \phi_n}{\partial \chi_2}\right)\phi_m d\Phi - \int_\Phi \left(\sum_{n=1}^N \dot{h}_n \phi_n\right)\phi_m d\Phi\right) =$$
$$-\int_\Phi \frac{U}{2}\left(\sum_{n=1}^N \frac{\partial h_n}{\partial d_i}\frac{\partial \phi_n}{\partial \chi_2}\right)\phi_m d\Phi \tag{2.95}$$

Note that we have invoked the Reynolds condition a priori. As such, the above expression is only valid for cases where this applies. Similarly we get

$$\frac{\partial r_m}{\partial d_{\underline{\mathbf{r}}i}} = -\int_\Phi \frac{U}{2}\left(\sum_{n=1}^N \frac{\partial h_n}{\partial d_{\underline{\mathbf{r}}i}}\frac{\partial \phi_n}{\partial \chi_2}\right)\phi_m d\Phi \tag{2.96}$$

$$\frac{\partial r_m}{\partial \dot{d}i} = -\int_\Phi \left(\sum_{n=1}^N \frac{\partial \dot{h}_n}{\partial \dot{d}_i}\phi_n\right)\phi_m d\Phi = -\int_\Phi \left(\sum_{n=1}^N \frac{\partial h_n}{\partial d_i}\phi_n\right)\phi_m d\Phi \tag{2.97}$$

$$\frac{\partial r_m}{\partial \dot{d}_{\underline{\mathbf{r}}i}} = -\int_\Phi \left(\sum_{n=1}^N \frac{\partial \dot{h}_n}{\partial \dot{d}_{\underline{\mathbf{r}}i}}\phi_n\right)\phi_m d\Phi = -\int_\Phi \left(\sum_{n=1}^N \frac{\partial h_n}{\partial d_{\underline{\mathbf{r}}i}}\phi_n\right)\phi_m d\Phi \tag{2.98}$$

$$\tag{2.99}$$

All of these equations require computation of the derivative of oil film thickness with respect to nodal or rotor displacement. This is a purely kinematic quantity, see figure 2.12 for a schematic of the concept.

Similarly, the derivation of the Reynolds equation system matrix is

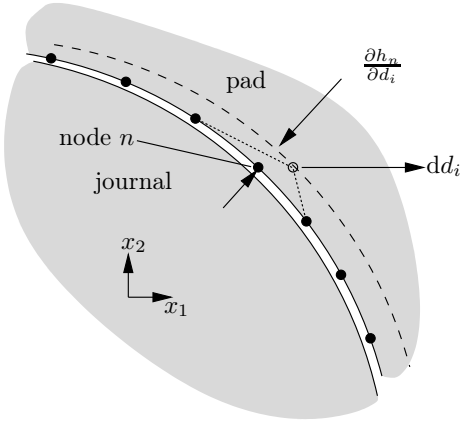


Figure 2.12: Schematic showing the kinematic relation between film thickness and nodal displacement.

$$\frac{\partial A_{mn}}{\partial d_j} = \int_\Phi \frac{1}{12} \sum_{i=1}^{2} \frac{\partial \phi_m}{\partial \chi_i} 3 \frac{\left(\sum_{n\in\mathbb{F}} h_n \phi_n\right)^2}{\mu} \frac{\partial \phi_n}{\partial \chi_i} \left( \sum_{n\in\mathbb{F}} \frac{\partial h_n}{\partial d_j} \phi_n \right) d\Phi \tag{2.100}$$

$$\frac{\partial A_{mn}}{\partial \underline{d}_{\underline{r}j}} = \int_\Phi \frac{1}{12} \sum_{i=1}^{2} \frac{\partial \phi_m}{\partial \chi_i} 3 \frac{\left(\sum_{n\in\mathbb{F}} h_n \phi_n\right)^2}{\mu} \frac{\partial \phi_n}{\partial \chi_i} \left( \sum_{n\in\mathbb{F}} \frac{\partial h_n}{\partial \underline{d}_{\underline{r}j}} \phi_n \right) d\Phi \tag{2.101}$$

where the chain rule has been applied. The nodal force derived with respect to the pressure is essentially an inward projection and integration of a unit pressure, i.e.

$$\frac{\partial^{\underline{\mathrm{res}}}\mathbf{f}}{\partial \mathbf{p}^T} = \frac{\partial f_n}{\partial p_i} = \frac{\partial}{\partial p_i} \left( \sum_{j=1}^{3} \int_\Lambda \sum_{m\in\mathbb{S}^3} T_{jm} \phi_m \psi_{jn} d\Lambda \right) =$$

$$\sum_{j=1}^{3} \int_\Lambda \sum_{m\in\mathbb{S}^3} \frac{\partial T_{jm}}{\partial p_i} \phi_m \psi_{jn} d\Lambda = -\sum_{j=1}^{3} \int_\Lambda \sum_{m\in\mathbb{S}^3} a_{im} \phi_m \psi_{jn} d\Phi \tag{2.102}$$

where $a_{im}$ is the outward normal of node $m$. For the purpose of force projection, the error from assuming pads and rotor surfaces parallel is vanishing. Thus, we may write for the rotor force

$$\frac{\partial^{\underline{\mathrm{res}}}\mathbf{f}_{\underline{\mathrm{r}}}}{\partial \mathbf{p}^T} = \frac{\partial f_{\underline{\mathrm{r}}k}}{\partial p_i} = -\sum_{n\in\mathbb{S}^3} a_{kn} \frac{\partial f_n}{\partial p_i} \tag{2.103}$$

With this, the system matrices in Eq. (2.87) may be computed.

## 2.8 Pseudo modal reduction

Since the solid typically contains a large number of degrees of freedom, there may be situations where solution time is prohibitive, for instance in a parameter study. For these situations, it may be useful to

implement a pseudo modal reduction. We approximate the nodal displacements in terms of the pseudo modal vector $\mathbf{b}$ as

$$\mathbf{d} = \mathbf{V}_{\underline{\mathrm{s}}}\mathbf{b} \tag{2.104}$$

The matrix $\mathbf{V}_{\underline{\mathrm{s}}}$ contains in its columns some of the eigenmodes of vibration of the solid, thus it satisfies

$$\mathbf{K}_{\underline{\mathrm{s}}}\mathbf{V}_{\underline{\mathrm{s}}} = \mathbf{M}_{\underline{\mathrm{s}}}\mathbf{V}_{\underline{\mathrm{s}}}\Lambda \tag{2.105}$$

where $\Lambda_{\underline{\mathrm{s}}}$ contains the squares of the corresponding solid eigenfrequencies in its diagonal and zeros elsewhere. Also, we pre-multiply the solid equations by $\mathbf{V}_{\underline{\mathrm{s}}}^T$. With this, the linear augmented system (2.87) becomes

$$\begin{bmatrix} \mathbf{V}_{\underline{\mathrm{s}}}^T\mathbf{M}_{\underline{\mathrm{s}}}\mathbf{V}_{\underline{\mathrm{s}}} & & \\ & \mathbf{M}_{\underline{\mathrm{r}}} & \\ & & \mathbf{M}_{\underline{\mathrm{q\text{-}q}}} \end{bmatrix} \begin{Bmatrix} \delta\ddot{\mathbf{b}} \\ \delta\ddot{\mathbf{d}}_{\underline{\mathrm{r}}} \\ \delta\ddot{\mathbf{p}} \\ \delta\ddot{\mathbf{p}}_{\underline{\mathrm{inj}}} \\ \delta\ddot{\mathbf{q}}_{\underline{\mathrm{v}}} \end{Bmatrix} +$$
$$\begin{bmatrix} & \mathbf{D}_{\underline{\mathrm{r}}} & \\ \frac{\partial^{\underline{\mathrm{res}}}\mathbf{r}}{\partial\dot{\mathbf{d}}^T}\mathbf{V}_{\underline{\mathrm{s}}} & \frac{\partial^{\underline{\mathrm{res}}}\mathbf{r}}{\partial\dot{\mathbf{d}}_{\underline{\mathrm{r}}}^T} & \\ & \mathbf{G}_{\underline{\mathrm{D}}} & \mathbf{D}_{\underline{\mathrm{q\text{-}q}}} \end{bmatrix} \begin{Bmatrix} \delta\dot{\mathbf{b}} \\ \delta\dot{\mathbf{d}}_{\underline{\mathrm{r}}} \\ \delta\dot{\mathbf{p}} \\ \delta\dot{\mathbf{p}}_{\underline{\mathrm{inj}}} \\ \delta\dot{\mathbf{q}}_{\underline{\mathrm{v}}} \end{Bmatrix} +$$
$$\begin{bmatrix} \mathbf{V}_{\underline{\mathrm{s}}}^T\mathbf{K}_{\underline{\mathrm{s}}}\mathbf{V}_{\underline{\mathrm{s}}} & & \mathbf{V}_{\underline{\mathrm{s}}}^T\frac{\partial^{\underline{\mathrm{res}}}\mathbf{f}}{\partial\mathbf{p}^T} & & \\ & \mathbf{K}_{\underline{\mathrm{r}}} & \frac{\partial^{\underline{\mathrm{res}}}\mathbf{f}_{\underline{\mathrm{r}}}}{\partial\mathbf{p}^T} & & \\ \frac{\partial^{\underline{\mathrm{res}}}\mathbf{r}}{\partial\mathbf{d}^T}\mathbf{V}_{\underline{\mathrm{s}}} & \frac{\partial^{\underline{\mathrm{res}}}\mathbf{r}}{\partial\mathbf{d}_{\underline{\mathrm{r}}}^T} & \mathbf{A} & \mathbf{W} & \\ & & \mathbf{W}^T & \mathbf{Q} & \frac{\partial^{\underline{\mathrm{res}}}\mathbf{r}_{\underline{\mathrm{inj}}}}{\partial\mathbf{q}_{\underline{\mathrm{v}}}^T} \\ & \mathbf{G}_{\underline{\mathrm{P}}} & & & \mathbf{K}_{\underline{\mathrm{q\text{-}q}}} \end{bmatrix} \begin{Bmatrix} \delta\mathbf{b} \\ \delta\mathbf{d}_{\underline{\mathrm{r}}} \\ \delta\mathbf{p} \\ \delta\mathbf{p}_{\underline{\mathrm{inj}}} \\ \delta\mathbf{q}_{\underline{\mathrm{v}}} \end{Bmatrix} = \begin{Bmatrix} \mathbf{V}_{\underline{\mathrm{s}}}^T\delta\mathbf{f} \\ \delta\mathbf{f}_{\underline{\mathrm{r}}} \\ \delta\mathbf{r} \\ \delta\mathbf{r}_{\underline{\mathrm{inj}}} \\ \delta\mathbf{u}_{\underline{\mathrm{vr}}} \end{Bmatrix} \tag{2.106}$$

The approximation can be applied to the original nonlinear augmented form (2.84) with equal simplicity. Generally, the more modes included, the more accurate the reduction is. Later in this thesis, a convergence study is performed, so as to determine a sensible compromise in terms of the number of modes to use.

## 2.9 Condensation

Although the fluid system contains less degrees of freedom than the solid, its size is still substantial. In the linear case, the fluid may be condensed away with no loss of accuracy, i.e. with no assumptions.

Consider the linear augmented equations (2.87). Generally only the force vector will be perturbed, thus much of the right hand side can be set to zero as

$$\begin{Bmatrix} \delta\mathbf{f} \\ \delta\mathbf{f}_{\underline{\mathrm{r}}} \\ \delta\mathbf{r} \\ \delta\mathbf{r}_{\underline{\mathrm{inj}}} \\ \delta\mathbf{u}_{\underline{\mathrm{vr}}} \end{Bmatrix} = \begin{Bmatrix} \delta\mathbf{f} \\ \delta\mathbf{f}_{\underline{\mathrm{r}}} \\ \mathbf{0} \\ \mathbf{0} \\ \mathbf{0} \end{Bmatrix} \tag{2.107}$$

With this, let us write the pressure expression

$$\frac{\partial^{\mathrm{res}}\mathbf{r}}{\partial\dot{\mathbf{d}}^T}\delta\ddot{\mathbf{d}} + \frac{\partial^{\mathrm{res}}\mathbf{r}}{\partial\dot{\mathbf{d}}_{\underline{\mathrm{r}}}^T}\delta\ddot{\mathbf{d}}_{\underline{\mathrm{r}}} + \frac{\partial^{\mathrm{res}}\mathbf{r}}{\partial\mathbf{d}^T}\delta\dot{\mathbf{d}} + \frac{\partial^{\mathrm{res}}\mathbf{r}}{\partial\mathbf{d}_{\underline{\mathrm{r}}}^T}\delta\dot{\mathbf{d}}_{\underline{\mathrm{r}}} + \mathbf{A}\delta\mathbf{p} + \mathbf{W}\delta\mathbf{p}_{\underline{\mathrm{inj}}} = \mathbf{0} \tag{2.108}$$

Now, solving for the pressure increment

$$\delta\mathbf{p} = -\mathbf{A}^{-1}\left(\frac{\partial^{\mathrm{res}}\mathbf{r}}{\partial\dot{\mathbf{d}}^T}\delta\ddot{\mathbf{d}} + \frac{\partial^{\mathrm{res}}\mathbf{r}}{\partial\dot{\mathbf{d}}_{\underline{\mathrm{r}}}^T}\delta\ddot{\mathbf{d}}_{\underline{\mathrm{r}}} + \frac{\partial^{\mathrm{res}}\mathbf{r}}{\partial\mathbf{d}^T}\delta\dot{\mathbf{d}} + \frac{\partial^{\mathrm{res}}\mathbf{r}}{\partial\mathbf{d}_{\underline{\mathrm{r}}}^T}\delta\dot{\mathbf{d}}_{\underline{\mathrm{r}}} + \mathbf{W}\delta\mathbf{p}_{\underline{\mathrm{inj}}}\right) \tag{2.109}$$

Substituting this expression for the pressure increment into (2.87) we get the condensed system

$$\begin{Bmatrix} \delta\mathbf{f} \\ \delta\mathbf{f}_{\underline{\mathrm{r}}} \\ \mathbf{0} \\ \mathbf{0} \end{Bmatrix} = \left[\begin{array}{c|c|c|c} \mathbf{M}_{\underline{\mathrm{s}}} & & & \\ \hline & \mathbf{M}_{\underline{\mathrm{r}}} & & \\ \hline & & & \\ \hline & & & \mathbf{M}_{\underline{\mathrm{q\text{-}q}}} \end{array}\right] \begin{Bmatrix} \delta\ddot{\mathbf{d}} \\ \delta\ddot{\mathbf{d}}_{\underline{\mathrm{r}}} \\ \delta\ddot{\mathbf{p}}_{\underline{\mathrm{inj}}} \\ \delta\ddot{\mathbf{q}}_{\underline{\mathrm{v}}} \end{Bmatrix} +$$

$$\left[\begin{array}{c|c|c|c} -\frac{\partial^{\mathrm{res}}\mathbf{f}}{\partial\mathbf{p}^T}\mathbf{A}^{-1}\frac{\partial^{\mathrm{res}}\mathbf{r}}{\partial\dot{\mathbf{d}}^T} & -\frac{\partial^{\mathrm{res}}\mathbf{f}}{\partial\mathbf{p}^T}\mathbf{A}^{-1}\frac{\partial^{\mathrm{res}}\mathbf{r}}{\partial\dot{\mathbf{d}}_{\underline{\mathrm{r}}}^T} & & \\ \hline -\frac{\partial^{\mathrm{res}}\mathbf{f}_{\underline{\mathrm{r}}}}{\partial\mathbf{p}^T}\mathbf{A}^{-1}\frac{\partial^{\mathrm{res}}\mathbf{r}}{\partial\dot{\mathbf{d}}^T} & \mathbf{D}_{\underline{\mathrm{r}}} - \frac{\partial^{\mathrm{res}}\mathbf{f}_{\underline{\mathrm{r}}}}{\partial\mathbf{p}^T}\mathbf{A}^{-1}\frac{\partial^{\mathrm{res}}\mathbf{r}}{\partial\dot{\mathbf{d}}_{\underline{\mathrm{r}}}^T} & & \\ \hline -\mathbf{W}^T\mathbf{A}^{-1}\frac{\partial^{\mathrm{res}}\mathbf{r}}{\partial\dot{\mathbf{d}}^T} & -\mathbf{W}^T\mathbf{A}^{-1}\frac{\partial^{\mathrm{res}}\mathbf{r}}{\partial\dot{\mathbf{d}}_{\underline{\mathrm{r}}}^T} & & \\ \hline & \mathbf{G}_{\underline{\mathrm{D}}} & & \mathbf{D}_{\underline{\mathrm{q\text{-}q}}} \end{array}\right] \begin{Bmatrix} \delta\dot{\mathbf{d}} \\ \delta\dot{\mathbf{d}}_{\underline{\mathrm{r}}} \\ \delta\dot{\mathbf{p}}_{\underline{\mathrm{inj}}} \\ \delta\dot{\mathbf{q}}_{\underline{\mathrm{v}}} \end{Bmatrix} +$$

$$\left[\begin{array}{c|c|c|c} \mathbf{K}_{\underline{\mathrm{s}}} - \frac{\partial^{\mathrm{res}}\mathbf{f}}{\partial\mathbf{p}^T}\mathbf{A}^{-1}\frac{\partial^{\mathrm{res}}\mathbf{r}}{\partial\mathbf{d}^T} & -\frac{\partial^{\mathrm{res}}\mathbf{f}}{\partial\mathbf{p}^T}\mathbf{A}^{-1}\frac{\partial^{\mathrm{res}}\mathbf{r}}{\partial\mathbf{d}_{\underline{\mathrm{r}}}^T} & -\frac{\partial^{\mathrm{res}}\mathbf{f}}{\partial\mathbf{p}^T}\mathbf{A}^{-1}\mathbf{W} & \\ \hline -\frac{\partial^{\mathrm{res}}\mathbf{f}_{\underline{\mathrm{r}}}}{\partial\mathbf{p}^T}\mathbf{A}^{-1}\frac{\partial^{\mathrm{res}}\mathbf{r}}{\partial\mathbf{d}^T} & \mathbf{K}_{\underline{\mathrm{r}}} - \frac{\partial^{\mathrm{res}}\mathbf{f}_{\underline{\mathrm{r}}}}{\partial\mathbf{p}^T}\mathbf{A}^{-1}\frac{\partial^{\mathrm{res}}\mathbf{r}}{\partial\mathbf{d}_{\underline{\mathrm{r}}}^T} & -\frac{\partial^{\mathrm{res}}\mathbf{f}_{\underline{\mathrm{r}}}}{\partial\mathbf{p}^T}\mathbf{A}^{-1}\mathbf{W} & \\ \hline -\mathbf{W}^T\mathbf{A}^{-1}\frac{\partial^{\mathrm{res}}\mathbf{r}}{\partial\mathbf{d}^T} & -\mathbf{W}^T\mathbf{A}^{-1}\frac{\partial^{\mathrm{res}}\mathbf{r}}{\partial\mathbf{d}_{\underline{\mathrm{r}}}^T} & \mathbf{Q} - \mathbf{W}^T\mathbf{A}^{-1}\mathbf{W} & \frac{\partial^{\mathrm{res}}\mathbf{r}_{\underline{\mathrm{inj}}}}{\partial\mathbf{q}_{\underline{\mathrm{v}}}^T} \\ \hline & \mathbf{G}_{\underline{\mathrm{P}}} & & \mathbf{K}_{\underline{\mathrm{q\text{-}q}}} \end{array}\right] \begin{Bmatrix} \delta\mathbf{d} \\ \delta\mathbf{d}_{\underline{\mathrm{r}}} \\ \delta\mathbf{p}_{\underline{\mathrm{inj}}} \\ \delta\mathbf{q}_{\underline{\mathrm{v}}} \end{Bmatrix} \tag{2.110}$$

Note how the pressure is no longer explicitly a part of the problem. It manifests itself purely as a force on the solid and the rotor. If we only consider the passive part of the system, the condensed equations are simplified to

$$\left[\begin{array}{c|c} \mathbf{M}_{\underline{\mathrm{s}}} & \\ \hline & \mathbf{M}_{\underline{\mathrm{r}}} \end{array}\right] \begin{Bmatrix} \delta\ddot{\mathbf{d}} \\ \delta\ddot{\mathbf{d}}_{\underline{\mathrm{r}}} \end{Bmatrix} + \left[\begin{array}{c|c} -\frac{\partial^{\mathrm{res}}\mathbf{f}}{\partial\mathbf{p}^T}\mathbf{A}^{-1}\frac{\partial^{\mathrm{res}}\mathbf{r}}{\partial\dot{\mathbf{d}}^T} & -\frac{\partial^{\mathrm{res}}\mathbf{f}}{\partial\mathbf{p}^T}\mathbf{A}^{-1}\frac{\partial^{\mathrm{res}}\mathbf{r}}{\partial\dot{\mathbf{d}}_{\underline{\mathrm{r}}}^T} \\ \hline -\frac{\partial^{\mathrm{res}}\mathbf{f}_{\underline{\mathrm{r}}}}{\partial\mathbf{p}^T}\mathbf{A}^{-1}\frac{\partial^{\mathrm{res}}\mathbf{r}}{\partial\dot{\mathbf{d}}^T} & \mathbf{D}_{\underline{\mathrm{r}}} - \frac{\partial^{\mathrm{res}}\mathbf{f}_{\underline{\mathrm{r}}}}{\partial\mathbf{p}^T}\mathbf{A}^{-1}\frac{\partial^{\mathrm{res}}\mathbf{r}}{\partial\dot{\mathbf{d}}_{\underline{\mathrm{r}}}^T} \end{array}\right] \begin{Bmatrix} \delta\dot{\mathbf{d}} \\ \delta\dot{\mathbf{d}}_{\underline{\mathrm{r}}} \end{Bmatrix} +$$

$$\left[\begin{array}{c|c} \mathbf{K}_{\underline{\mathrm{s}}} - \frac{\partial^{\mathrm{res}}\mathbf{f}}{\partial\mathbf{p}^T}\mathbf{A}^{-1}\frac{\partial^{\mathrm{res}}\mathbf{r}}{\partial\mathbf{d}^T} & -\frac{\partial^{\mathrm{res}}\mathbf{f}}{\partial\mathbf{p}^T}\mathbf{A}^{-1}\frac{\partial^{\mathrm{res}}\mathbf{r}}{\partial\mathbf{d}_{\underline{\mathrm{r}}}^T} \\ \hline -\frac{\partial^{\mathrm{res}}\mathbf{f}_{\underline{\mathrm{r}}}}{\partial\mathbf{p}^T}\mathbf{A}^{-1}\frac{\partial^{\mathrm{res}}\mathbf{r}}{\partial\mathbf{d}^T} & \mathbf{K}_{\underline{\mathrm{r}}} - \frac{\partial^{\mathrm{res}}\mathbf{f}_{\underline{\mathrm{r}}}}{\partial\mathbf{p}^T}\mathbf{A}^{-1}\frac{\partial^{\mathrm{res}}\mathbf{r}}{\partial\mathbf{d}_{\underline{\mathrm{r}}}^T} \end{array}\right] \begin{Bmatrix} \delta\mathbf{d} \\ \delta\mathbf{d}_{\underline{\mathrm{r}}} \end{Bmatrix} = \begin{Bmatrix} \delta\mathbf{f} \\ \delta\mathbf{f}_{\underline{\mathrm{r}}} \end{Bmatrix} \tag{2.111}$$

For clarity, we split the system into solid and fluid contributions, thus

$$
\underbrace{\left[\begin{array}{c|c} \mathbf{M}_{\underline{\mathrm{s}}} & \\ \hline & \mathbf{M}_{\underline{\mathrm{r}}} \end{array}\right]}_{\text{structural mass matrix}} \left\{\begin{array}{c} \delta\ddot{\mathbf{d}} \\ \delta\ddot{\mathbf{d}}_{\underline{\mathrm{r}}} \end{array}\right\} +
$$

$$
\left( \underbrace{\left[\begin{array}{c|c} & \\ \hline & \mathbf{D}_{\underline{\mathrm{r}}} \end{array}\right]}_{\text{structural damping matrix}} + \underbrace{\left[\begin{array}{c|c} -\frac{\partial^{\mathrm{res}}\mathbf{f}}{\partial\mathbf{p}^T}\mathbf{A}^{-1}\frac{\partial^{\mathrm{res}}\mathbf{r}}{\partial\dot{\mathbf{d}}^T} & -\frac{\partial^{\mathrm{res}}\mathbf{f}}{\partial\mathbf{p}^T}\mathbf{A}^{-1}\frac{\partial^{\mathrm{res}}\mathbf{r}}{\partial\dot{\mathbf{d}}_{\underline{\mathrm{r}}}^T} \\ \hline -\frac{\partial^{\mathrm{res}}\mathbf{f}_{\underline{\mathrm{r}}}}{\partial\mathbf{p}^T}\mathbf{A}^{-1}\frac{\partial^{\mathrm{res}}\mathbf{r}}{\partial\dot{\mathbf{d}}^T} & -\frac{\partial^{\mathrm{res}}\mathbf{f}_{\underline{\mathrm{r}}}}{\partial\mathbf{p}^T}\mathbf{A}^{-1}\frac{\partial^{\mathrm{res}}\mathbf{r}}{\partial\dot{\mathbf{d}}_{\underline{\mathrm{r}}}^T} \end{array}\right]}_{\text{fluid damping matrix}} \right) \left\{\begin{array}{c} \delta\dot{\mathbf{d}} \\ \delta\dot{\mathbf{d}}_{\underline{\mathrm{r}}} \end{array}\right\} +
$$

$$
\left( \underbrace{\left[\begin{array}{c|c} \mathbf{K}_{\underline{\mathrm{s}}} & \\ \hline & \mathbf{K}_{\underline{\mathrm{r}}} \end{array}\right]}_{\text{structural stiffness matrix}} + \underbrace{\left[\begin{array}{c|c} -\frac{\partial^{\mathrm{res}}\mathbf{f}}{\partial\mathbf{p}^T}\mathbf{A}^{-1}\frac{\partial^{\mathrm{res}}\mathbf{r}}{\partial\mathbf{d}^T} & -\frac{\partial^{\mathrm{res}}\mathbf{f}}{\partial\mathbf{p}^T}\mathbf{A}^{-1}\frac{\partial^{\mathrm{res}}\mathbf{r}}{\partial\mathbf{d}_{\underline{\mathrm{r}}}^T} \\ \hline -\frac{\partial^{\mathrm{res}}\mathbf{f}_{\underline{\mathrm{r}}}}{\partial\mathbf{p}^T}\mathbf{A}^{-1}\frac{\partial^{\mathrm{res}}\mathbf{r}}{\partial\mathbf{d}^T} & -\frac{\partial^{\mathrm{res}}\mathbf{f}_{\underline{\mathrm{r}}}}{\partial\mathbf{p}^T}\mathbf{A}^{-1}\frac{\partial^{\mathrm{res}}\mathbf{r}}{\partial\mathbf{d}_{\underline{\mathrm{r}}}^T} \end{array}\right]}_{\text{fluid stiffness matrix}} \right) \left\{\begin{array}{c} \delta\mathbf{d} \\ \delta\mathbf{d}_{\underline{\mathrm{r}}} \end{array}\right\} = \left\{\begin{array}{c} \delta\mathbf{f} \\ \delta\mathbf{f}_{\underline{\mathrm{r}}} \end{array}\right\} \tag{2.112}
$$

### 2.9.1 Pseudo modal reduction of the condensed system

Just as we can perform a pseudo modal reduction of the augmented linear and nonlinear equations, we can perform one on the condensed system. Following the same methodology as in section 2.8 the pseudo modal reduction of Eq. (2.110) becomes.

$$
\left\{\begin{array}{c} \delta\mathbf{f} \\ \delta\mathbf{f}_{\underline{\mathrm{r}}} \\ \mathbf{0} \\ \mathbf{0} \end{array}\right\} = \left[\begin{array}{c|c|c|c} \mathbf{V}_{\underline{\mathrm{s}}}^T\mathbf{M}_{\underline{\mathrm{s}}}\mathbf{V}_{\underline{\mathrm{s}}} & & & \\ \hline & \mathbf{M}_{\underline{\mathrm{r}}} & & \\ \hline & & & \\ \hline & & & \mathbf{M}_{\underline{\mathrm{q\text{-}q}}} \end{array}\right] \left\{\begin{array}{c} \delta\ddot{\mathbf{b}} \\ \delta\ddot{\mathbf{d}}_{\underline{\mathrm{r}}} \\ \delta\ddot{\mathbf{p}}_{\underline{\mathrm{inj}}} \\ \delta\ddot{\mathbf{q}}_{\underline{\mathrm{v}}} \end{array}\right\} +
$$

$$
\left[\begin{array}{c|c|c|c} -\mathbf{V}_{\underline{\mathrm{s}}}^T\frac{\partial^{\mathrm{res}}\mathbf{f}}{\partial\mathbf{p}^T}\mathbf{A}^{-1}\frac{\partial^{\mathrm{res}}\mathbf{r}}{\partial\dot{\mathbf{d}}^T}\mathbf{V}_{\underline{\mathrm{s}}} & -\mathbf{V}_{\underline{\mathrm{s}}}^T\frac{\partial^{\mathrm{res}}\mathbf{f}}{\partial\mathbf{p}^T}\mathbf{A}^{-1}\frac{\partial^{\mathrm{res}}\mathbf{r}}{\partial\dot{\mathbf{d}}_{\underline{\mathrm{r}}}^T} & & \\ \hline -\frac{\partial^{\mathrm{res}}\mathbf{f}_{\underline{\mathrm{r}}}}{\partial\mathbf{p}^T}\mathbf{A}^{-1}\frac{\partial^{\mathrm{res}}\mathbf{r}}{\partial\dot{\mathbf{d}}^T}\mathbf{V}_{\underline{\mathrm{s}}} & \mathbf{D}_{\underline{\mathrm{r}}} - \frac{\partial^{\mathrm{res}}\mathbf{f}_{\underline{\mathrm{r}}}}{\partial\mathbf{p}^T}\mathbf{A}^{-1}\frac{\partial^{\mathrm{res}}\mathbf{r}}{\partial\dot{\mathbf{d}}_{\underline{\mathrm{r}}}^T} & & \\ \hline -\mathbf{W}^T\mathbf{A}^{-1}\frac{\partial^{\mathrm{res}}\mathbf{r}}{\partial\dot{\mathbf{d}}^T}\mathbf{V}_{\underline{\mathrm{s}}} & -\mathbf{W}^T\mathbf{A}^{-1}\frac{\partial^{\mathrm{res}}\mathbf{r}}{\partial\dot{\mathbf{d}}_{\underline{\mathrm{r}}}^T} & & \\ \hline & \mathbf{G}_{\underline{\mathrm{D}}} & & \mathbf{D}_{\underline{\mathrm{q\text{-}q}}} \end{array}\right] \left\{\begin{array}{c} \delta\dot{\mathbf{b}} \\ \delta\dot{\mathbf{d}}_{\underline{\mathrm{r}}} \\ \delta\dot{\mathbf{p}}_{\underline{\mathrm{inj}}} \\ \delta\dot{\mathbf{q}}_{\underline{\mathrm{v}}} \end{array}\right\} +
$$

$$
\left[\begin{array}{c|c|c|c} \mathbf{V}_{\underline{\mathrm{s}}}^T(\mathbf{K}_{\underline{\mathrm{s}}} - \frac{\partial^{\mathrm{res}}\mathbf{f}}{\partial\mathbf{p}^T}\mathbf{A}^{-1}\frac{\partial^{\mathrm{res}}\mathbf{r}}{\partial\mathbf{d}^T})\mathbf{V}_{\underline{\mathrm{s}}} & -\mathbf{V}_{\underline{\mathrm{s}}}^T\frac{\partial^{\mathrm{res}}\mathbf{f}}{\partial\mathbf{p}^T}\mathbf{A}^{-1}\frac{\partial^{\mathrm{res}}\mathbf{r}}{\partial\mathbf{d}_{\underline{\mathrm{r}}}^T} & -\mathbf{V}_{\underline{\mathrm{s}}}^T\frac{\partial^{\mathrm{res}}\mathbf{f}}{\partial\mathbf{p}^T}\mathbf{A}^{-1}\mathbf{W} & \\ \hline -\frac{\partial^{\mathrm{res}}\mathbf{f}_{\underline{\mathrm{r}}}}{\partial\mathbf{p}^T}\mathbf{A}^{-1}\frac{\partial^{\mathrm{res}}\mathbf{r}}{\partial\mathbf{d}^T}\mathbf{V}_{\underline{\mathrm{s}}} & \mathbf{K}_{\underline{\mathrm{r}}} - \frac{\partial^{\mathrm{res}}\mathbf{f}_{\underline{\mathrm{r}}}}{\partial\mathbf{p}^T}\mathbf{A}^{-1}\frac{\partial^{\mathrm{res}}\mathbf{r}}{\partial\mathbf{d}_{\underline{\mathrm{r}}}^T} & -\frac{\partial^{\mathrm{res}}\mathbf{f}_{\underline{\mathrm{r}}}}{\partial\mathbf{p}^T}\mathbf{A}^{-1}\mathbf{W} & \\ \hline -\mathbf{W}^T\mathbf{A}^{-1}\frac{\partial^{\mathrm{res}}\mathbf{r}}{\partial\mathbf{d}^T}\mathbf{V}_{\underline{\mathrm{s}}} & -\mathbf{W}^T\mathbf{A}^{-1}\frac{\partial^{\mathrm{res}}\mathbf{r}}{\partial\mathbf{d}_{\underline{\mathrm{r}}}^T} & \mathbf{Q} - \mathbf{W}^T\mathbf{A}^{-1}\mathbf{W} & \frac{\partial^{\mathrm{res}}\mathbf{r}_{\underline{\mathrm{inj}}}}{\partial\mathbf{q}_{\underline{\mathrm{v}}}^T} \\ \hline & \mathbf{G}_{\underline{\mathrm{P}}} & & \mathbf{K}_{\underline{\mathrm{q\text{-}q}}} \end{array}\right] \left\{\begin{array}{c} \delta\mathbf{b} \\ \delta\mathbf{d}_{\underline{\mathrm{r}}} \\ \delta\mathbf{p}_{\underline{\mathrm{inj}}} \\ \delta\mathbf{q}_{\underline{\mathrm{v}}} \end{array}\right\} \tag{2.113}
$$

Equally, the pseudo modal reduction of the passive system in Eq. (2.112) becomes

$$
\left\{ \begin{array}{c} \mathbf{V}_{\underline{\mathrm{s}}}^T \delta\mathbf{f} \\ \delta\mathbf{f}_{\underline{\mathrm{r}}} \end{array} \right\} = \underbrace{\left[ \begin{array}{c|c} \mathbf{V}_{\underline{\mathrm{s}}}^T \mathbf{M}_{\underline{\mathrm{s}}} \mathbf{V}_{\underline{\mathrm{s}}} & \\ \hline & \mathbf{M}_{\underline{\mathrm{r}}} \end{array} \right]}_{\text{structural mass matrix}} \left\{ \begin{array}{c} \delta\ddot{\mathbf{b}} \\ \delta\ddot{\mathbf{d}}_{\underline{\mathrm{r}}} \end{array} \right\} +
$$

$$
\left( \underbrace{\left[ \begin{array}{c|c} & \\ \hline & \mathbf{D}_{\underline{\mathrm{r}}} \end{array} \right]}_{\text{structural damping matrix}} + \underbrace{\left[ \begin{array}{c|c} -\mathbf{V}_{\underline{\mathrm{s}}}^T \frac{\partial^{\mathrm{res}}\mathbf{f}}{\partial\mathbf{p}^T} \mathbf{A}^{-1} \frac{\partial^{\mathrm{res}}\mathbf{r}}{\partial\dot{\mathbf{d}}^T} \mathbf{V}_{\underline{\mathrm{s}}} & -\mathbf{V}_{\underline{\mathrm{s}}}^T \frac{\partial^{\mathrm{res}}\mathbf{f}}{\partial\mathbf{p}^T} \mathbf{A}^{-1} \frac{\partial^{\mathrm{res}}\mathbf{r}}{\partial\dot{\mathbf{d}}_{\underline{\mathrm{r}}}^T} \\ \hline -\frac{\partial^{\mathrm{res}}\mathbf{f}_{\underline{\mathrm{r}}}}{\partial\mathbf{p}^T} \mathbf{A}^{-1} \frac{\partial^{\mathrm{res}}\mathbf{r}}{\partial\dot{\mathbf{d}}^T} \mathbf{V}_{\underline{\mathrm{s}}} & -\frac{\partial^{\mathrm{res}}\mathbf{f}_{\underline{\mathrm{r}}}}{\partial\mathbf{p}^T} \mathbf{A}^{-1} \frac{\partial^{\mathrm{res}}\mathbf{r}}{\partial\dot{\mathbf{d}}_{\underline{\mathrm{r}}}^T} \end{array} \right]}_{\text{fluid damping matrix}} \right) \left\{ \begin{array}{c} \delta\dot{\mathbf{b}} \\ \delta\dot{\mathbf{d}}_{\underline{\mathrm{r}}} \end{array} \right\} +
$$

$$
\left( \underbrace{\left[ \begin{array}{c|c} \mathbf{V}_{\underline{\mathrm{s}}}^T \mathbf{K}_{\underline{\mathrm{s}}} \mathbf{V}_{\underline{\mathrm{s}}} & \\ \hline & \mathbf{K}_{\underline{\mathrm{r}}} \end{array} \right]}_{\text{structural stiffness matrix}} + \underbrace{\left[ \begin{array}{c|c} -\mathbf{V}_{\underline{\mathrm{s}}}^T \frac{\partial^{\mathrm{res}}\mathbf{f}}{\partial\mathbf{p}^T} \mathbf{A}^{-1} \frac{\partial^{\mathrm{res}}\mathbf{r}}{\partial\mathbf{d}^T} \mathbf{V}_{\underline{\mathrm{s}}} & -\mathbf{V}_{\underline{\mathrm{s}}}^T \frac{\partial^{\mathrm{res}}\mathbf{f}}{\partial\mathbf{p}^T} \mathbf{A}^{-1} \frac{\partial^{\mathrm{res}}\mathbf{r}}{\partial\mathbf{d}_{\underline{\mathrm{r}}}^T} \\ \hline -\frac{\partial^{\mathrm{res}}\mathbf{f}_{\underline{\mathrm{r}}}}{\partial\mathbf{p}^T} \mathbf{A}^{-1} \frac{\partial^{\mathrm{res}}\mathbf{r}}{\partial\mathbf{d}^T} \mathbf{V}_{\underline{\mathrm{s}}} & -\frac{\partial^{\mathrm{res}}\mathbf{f}_{\underline{\mathrm{r}}}}{\partial\mathbf{p}^T} \mathbf{A}^{-1} \frac{\partial^{\mathrm{res}}\mathbf{r}}{\partial\mathbf{d}_{\underline{\mathrm{r}}}^T} \end{array} \right]}_{\text{fluid stiffness matrix}} \right) \left\{ \begin{array}{c} \delta\mathbf{b} \\ \delta\mathbf{d}_{\underline{\mathrm{r}}} \end{array} \right\} \tag{2.114}
$$

If $\mathbf{V}_{\underline{\mathrm{s}}}$ contains only the first mode of each pad, the rigid body mode, then the equations in (2.114) are equivalent to the equations presented by [21]. As mentioned, Eqs. (2.113) and (2.114) (for the ascive and passive cases, respectively) are the most compact form, which still serves to evaluate rotor-bearing local stability. Note that they do not assume stationary harmonic motion. Thus, they shall be the starting point of the stability analyses later in this thesis.

## 2.10 Time domain analysis

Generally, time domain analysis has its merits when solving the nonlinear equations, as it handles nonlinearity in a straight forward manner. Thus time domain analysis applies to either the augmented equations (2.84) or the corresponding pseudo modal reduction. There are many ways to perform time domain analysis, depending on the specific situation. The explicit form of the Newmark algorithm is well known and widely used in time domain analysis. If the explicit form of the Newmark method is implemented to Eqs. (2.84), the pseudo algorithm is

| | | |
|---|---|---|
| set | $\mathbf{d},\quad \dot{\mathbf{d}},\quad \mathbf{d}_{\underline{r}},\quad \dot{\mathbf{d}}_{\underline{r}},\quad \mathbf{q}_{\underline{v}},\quad \dot{\mathbf{q}}_{\underline{v}}$ | |
| solve | $\begin{bmatrix} \mathbf{A} & \mathbf{W} \\ \mathbf{W}^T & \mathbf{Q}+\mathbf{K}_{\underline{pq}} \end{bmatrix} \begin{Bmatrix} \mathbf{p} \\ \mathbf{p}_{\underline{inj}} \end{Bmatrix} = \begin{Bmatrix} \mathbf{r} \\ \mathbf{r}_{\underline{inj}} \end{Bmatrix}$ | |
| compute | $\mathbf{f},\quad \mathbf{f}_{\underline{r}},\quad \mathbf{u}_{\underline{v}}$ | |
| solve for $\ddot{\mathbf{d}}$ : | $\mathbf{M}_{\underline{s}}\ddot{\mathbf{d}} = \mathbf{f} - \mathbf{K}_{\underline{s}}\mathbf{d}$ | |
| solve for $\ddot{\mathbf{d}}_{\underline{r}}$ : | $\mathbf{M}_{\underline{r}}\ddot{\mathbf{d}}_{\underline{r}} = \mathbf{f}_{\underline{r}} - \mathbf{D}_{\underline{r}}\dot{\mathbf{d}}_{\underline{r}} - \mathbf{K}_{\underline{r}}\mathbf{d}_{\underline{r}}$ | |
| solve for $\ddot{\mathbf{q}}_{\underline{v}}$ : | $\mathbf{M}_{\underline{q\text{-}q}}\ddot{\mathbf{q}}_{\underline{v}} = \mathbf{u}_{\underline{v}} - \mathbf{G}_{\underline{D}}\dot{\mathbf{d}}_{\underline{r}} - \mathbf{G}_{\underline{P}}\mathbf{d}_{\underline{r}}$ | |
| for t<T | | |
| | update | $\mathbf{d} = \mathbf{d} + \Delta t\dot{\mathbf{d}} + \frac{1}{2}\Delta t^2\ddot{\mathbf{d}}$ |
| | update | $\dot{\mathbf{d}} = \dot{\mathbf{d}} + \frac{1}{2}\Delta t\ddot{\mathbf{d}}$ |
| | solve | $\begin{bmatrix} \mathbf{A} & \mathbf{W} \\ \mathbf{W}^T & \mathbf{Q}+\mathbf{K}_{\underline{pq}} \end{bmatrix} \begin{Bmatrix} \mathbf{p} \\ \mathbf{p}_{\underline{inj}} \end{Bmatrix} = \begin{Bmatrix} \mathbf{r} \\ \mathbf{r}_{\underline{inj}} \end{Bmatrix}$ |
| | compute | $\mathbf{f},\quad \mathbf{f}_{\underline{r}},\quad \mathbf{u}_{\underline{v}}$ |
| | solve for $\ddot{\mathbf{d}}$ : | $\mathbf{M}_{\underline{s}}\ddot{\mathbf{d}} = \mathbf{f} - \mathbf{K}_{\underline{s}}\mathbf{d}$ |
| | solve for $\ddot{\mathbf{d}}_{\underline{r}}$ : | $\mathbf{M}_{\underline{r}}\ddot{\mathbf{d}}_{\underline{r}} = \mathbf{f}_{\underline{r}} - \mathbf{D}_{\underline{r}}\dot{\mathbf{d}}_{\underline{r}} - \mathbf{K}_{\underline{r}}\mathbf{d}_{\underline{r}}$ |
| | solve for $\ddot{\mathbf{q}}_{\underline{v}}$ : | $\mathbf{M}_{\underline{q\text{-}q}}\ddot{\mathbf{q}}_{\underline{v}} = \mathbf{u}_{\underline{v}} - \mathbf{G}_{\underline{D}}\dot{\mathbf{d}}_{\underline{r}} - \mathbf{G}_{\underline{P}}\mathbf{d}_{\underline{r}}$ |
| | update | $\dot{\mathbf{d}} = \dot{\mathbf{d}} + \frac{1}{2}\Delta t\ddot{\mathbf{d}}$ |
| | update | $t = t + \Delta t$ |
| end | | |

Of course, the algorithm can equally well be applied to the pseudo modal reduced version of the nonlinear equations (2.84). In fact, in doing this, the maximum allowable timestep is increased substantially, since this is limited by the largest frequency in the system. By applying the pseudo modal reduction, the highest frequencies are removed. This reduces CPU time for a given simulation. It falls outside the scope of the thesis to investigate CPU time requirements and maximum time step sizes. As a rule of thumb, the time step is set to which ever is smallest of the two values

$$\Delta t = 0.05/|\lambda|_{\underline{\max}} \quad \text{, or} \quad \Delta t = 0.05/\omega \tag{2.115}$$

where $\omega$ is the frequency of the excitation force and $\lambda$ is a system eigenvalue. It is unpractical to compute system eigenvalues for the system without prior pseudo modal reduction. If a time series solution is run for the unreduced system, a rough estimate of the maximum allowable time step can be made as the time it takes a dilatational wave to pass through a solid element. See [68] for details.

## 2.11 Frequency domain analysis

When performing frequency domain analysis, we are confined to the linearised augmented system of equations. It may be subject to a pseudo modal reduction or not. Let us write it as the generic system of equations

$$\mathbf{M}\ddot{\mathbf{y}} + \mathbf{D}\dot{\mathbf{y}} + \mathbf{K}\mathbf{y} = \mathbf{j} \tag{2.116}$$

where

$$\mathbf{y} = \left\{ \begin{array}{c} \delta\mathbf{d} \\ \delta\mathbf{d}_{\underline{\mathrm{r}}} \\ \delta\mathbf{p} \\ \delta\mathbf{p}_{\underline{\mathrm{inj}}} \\ \delta\mathbf{q}_{\underline{\mathrm{v}}} \end{array} \right\}, \quad \mathbf{j} = \left\{ \begin{array}{c} \delta\mathbf{f} \\ \delta\mathbf{f}_{\underline{\mathrm{r}}} \\ \delta\mathbf{r} \\ \delta\mathbf{r}_{\underline{\mathrm{inj}}} \\ \delta\mathbf{u}_{\underline{\mathrm{vr}}} \end{array} \right\} \tag{2.117}$$

in the case of a system that has not been reduced, or

$$\mathbf{y} = \left\{ \begin{array}{c} \delta\mathbf{b} \\ \delta\mathbf{d}_{\underline{\mathrm{r}}} \\ \delta\mathbf{p} \\ \delta\mathbf{p}_{\underline{\mathrm{inj}}} \\ \delta\mathbf{q}_{\underline{\mathrm{v}}} \end{array} \right\}, \quad \mathbf{j} = \left\{ \begin{array}{c} \mathbf{V}_{\underline{\mathrm{s}}}^T \delta\mathbf{f} \\ \delta\mathbf{f}_{\underline{\mathrm{r}}} \\ \delta\mathbf{r} \\ \delta\mathbf{r}_{\underline{\mathrm{inj}}} \\ \delta\mathbf{u}_{\underline{\mathrm{vr}}} \end{array} \right\} \tag{2.118}$$

for the case of a pseudo modal reduction, or

$$\mathbf{y} = \left\{ \begin{array}{c} \delta\mathbf{b} \\ \delta\mathbf{d}_{\underline{\mathrm{r}}} \\ \delta\mathbf{p}_{\underline{\mathrm{inj}}} \\ \delta\mathbf{q}_{\underline{\mathrm{v}}} \end{array} \right\}, \quad \mathbf{j} = \left\{ \begin{array}{c} \mathbf{V}_{\underline{\mathrm{s}}}^T \delta\mathbf{f} \\ \delta\mathbf{f}_{\underline{\mathrm{r}}} \\ \delta\mathbf{r}_{\underline{\mathrm{inj}}} \\ \delta\mathbf{u}_{\underline{\mathrm{vr}}} \end{array} \right\} \tag{2.119}$$

for the case of a pseudo modal reduction and a condensation.

The considerations in the following apply to all three cases.

As we know $\mathbf{D}$ and $\mathbf{K}$ are functionals of the state, i.e., also of a given equilibrium position. To determine whether or not a given equilibrium position is locally stable, we consider the homogeneous case

$$\mathbf{M}\ddot{\mathbf{y}} + \mathbf{D}\dot{\mathbf{y}} + \mathbf{K}\mathbf{y} = \mathbf{0} \tag{2.120}$$

This has the solution

$$\left\{ \begin{array}{c} \dot{\mathbf{y}} \\ \mathbf{y} \end{array} \right\} = \mathbf{v}e^{\lambda t}, \quad \lambda \in \mathbb{C}, \quad \mathbf{v} \in \mathbb{C}^{2\dim(\mathbf{y})} \tag{2.121}$$

where $\mathbf{v}$ and $\lambda$ are unknown a priori and are functionals of $\mathbf{M}$, $\mathbf{D}$ and $\mathbf{K}$ only. There are as many solutions $(\lambda, \mathbf{v})$ as the dimension of $\mathbf{v}$. The solutions appear as the solutions to the generalised eigenvalue problem

$$\left[ \begin{array}{cc} \mathbf{0} & \mathbf{K} \\ \mathbf{I} & \mathbf{0} \end{array} \right] \mathbf{v} = \lambda \left[ \begin{array}{cc} -\mathbf{M} & -\mathbf{D} \\ \mathbf{0} & \mathbf{I} \end{array} \right] \mathbf{v} \tag{2.122}$$

If the real part of any eigenvalue $\lambda$ is larger than zero, the equilibrium position in question is unstable.

For realistic system parameters, there are typically two static equilibria of the system of equations, but only one which is physically meaningful. Thus there is only one equilibrium that should be checked for stability. In Fig. 2.13 is seen the pressure profile for the physically meaningful static equilibrium of a bearing with a preload factor of 0.5 and a rotational speed of 6000rpm. The corresponding displacements are shown in Fig. 2.14. Primarily, note two things. (i) Firstly, the pads tilt in the same direction as the rotor rotation. This creates the well known wedge effect [66]. (ii) Secondly, the pressure on the entire surface of the pads is positive. The physically meaningless equilibrium is characterised by pads that tilt in the opposite direction of the rotor rotation, resulting in negative pressures. Here we are outside the domain of validity of our mathematical model. Any negative pressure ($p < 1$atm, since zero is defined

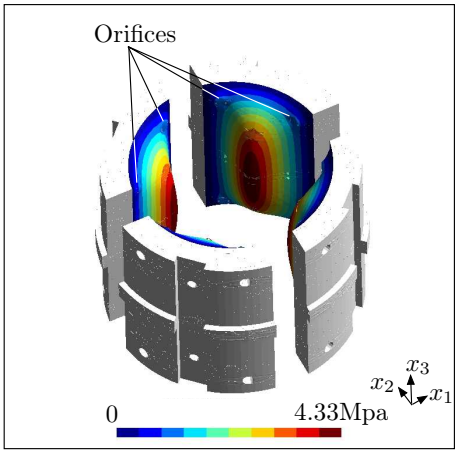


Figure 2.13: The pressure field over the pads at static equilibrium for 6000rpm and zero radial rotor load. Maximum pressure is 4.33MPa. Post processing was done with Gmsh [69].

as 1atm) is an artefact of the Reynolds equation, which assumes an incompressible fluid; it has nothing to do with physics. The model could be generalised by introduction of a more advanced fluid cavitation model or contact between rotor and pads. In the present investigation however, we shall focus on the local behaviour around the nominal operating condition. Here, neither cavitation nor contact occurs [4]. Henceforth, let us refer to the stability of the physically meaningful equilibrium position simply as "rotor-bearing stability".

If we wish to compute the response to a given excitation, we consider the inhomogeneous case

$$\mathbf{M}\ddot{\mathbf{y}} + \mathbf{D}\dot{\mathbf{y}} + \mathbf{K}\mathbf{y} = \mathbf{j}_{\underline{0}} e^{i\omega t}, \quad \omega \in \mathbb{R} \tag{2.123}$$

This has the solution

$$\mathbf{y} = \mathbf{y}_{\underline{0}} e^{i\omega t}, \quad \mathbf{y}_{\underline{0}} \in \mathbb{C}^{\dim(\mathbf{y})} \tag{2.124}$$

where $\mathbf{y}_{\underline{0}}$ is unknown a priori and is a functional of $\mathbf{M}$, $\mathbf{D}$, $\mathbf{K}$ and $\omega$. Note that $\omega$ is known a priori. The solution $\mathbf{y}_{\underline{0}}$ is the vector of frequency response functions for the system. Particularly the components of $\mathbf{y}_{\underline{0}}$ related to the rotor degrees of freedom shall be investigated in the following.

### 2.11.1 Harmonic response and dynamic coefficients

When computing the harmonic response and dynamic coefficients of the bearing itself, we set the rotor impedance to zero. That is,

$$\mathbf{M}_{\underline{\mathrm{r}}} = \mathbf{0}, \quad \mathbf{D}_{\underline{\mathrm{r}}} = \mathbf{0}, \quad \mathbf{K}_{\underline{\mathrm{r}}} = \mathbf{0} \tag{2.125}$$

we then define two force increment vectors

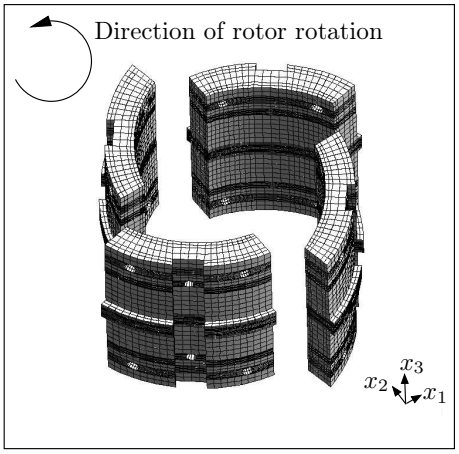


Figure 2.14: Displacement field of the pads at static equilibrium for 6000rpm and zero radial rotor load. Displacement is dominated by rigid body tilting, but also note the slight deformation of the pads. Maximum displacement is 28.9$\mu$m.

$$\mathbf{j} = \begin{Bmatrix} \delta\mathbf{f} \\ \delta\mathbf{f}_{\underline{\mathrm{r}}} \\ \delta\mathbf{r} \\ \delta\mathbf{r}_{\underline{\mathrm{inj}}} \\ \delta\mathbf{u}_{\underline{\mathrm{vr}}} \end{Bmatrix} = \begin{Bmatrix} \mathbf{0} \\ \delta\mathbf{f}_{\underline{\mathrm{r0}}} \\ \mathbf{0} \\ \mathbf{0} \\ \mathbf{0} \end{Bmatrix} e^{i\omega t} = \begin{Bmatrix} \mathbf{0} \\ \left\{ \begin{matrix} \delta f_{\underline{\mathrm{r0}}1} \\ 0 \end{matrix} \right\} \\ \mathbf{0} \\ \mathbf{0} \\ \mathbf{0} \end{Bmatrix} e^{i\omega t} \tag{2.126}$$

and

$$\mathbf{j} = \begin{Bmatrix} \delta\mathbf{f} \\ \delta\mathbf{f}_{\underline{\mathrm{r}}} \\ \delta\mathbf{r} \\ \delta\mathbf{r}_{\underline{\mathrm{inj}}} \\ \delta\mathbf{u}_{\underline{\mathrm{vr}}} \end{Bmatrix} = \begin{Bmatrix} \mathbf{0} \\ \delta\mathbf{f}_{\underline{\mathrm{r0}}} \\ \mathbf{0} \\ \mathbf{0} \\ \mathbf{0} \end{Bmatrix} e^{i\omega t} = \begin{Bmatrix} \mathbf{0} \\ \left\{ \begin{matrix} 0 \\ \delta f_{\underline{\mathrm{r0}}2} \end{matrix} \right\} \\ \mathbf{0} \\ \mathbf{0} \\ \mathbf{0} \end{Bmatrix} e^{i\omega t} \tag{2.127}$$

Also, let us write the displacement increment vector resulting from the first force increment vector as

$$\mathbf{y} = \begin{Bmatrix} \delta\mathbf{d} \\ \delta\mathbf{d}_{\underline{\mathrm{r}}} \\ \delta\mathbf{p} \\ \delta\mathbf{p}_{\underline{\mathrm{inj}}} \\ \delta\mathbf{q}_{\underline{\mathrm{v}}} \end{Bmatrix} = \begin{Bmatrix} \delta\mathbf{d}_{\underline{0}} \\ \delta\mathbf{d}_{\underline{\mathrm{r0}}} \\ \delta\mathbf{p}_{\underline{0}} \\ \delta\mathbf{p}_{\underline{\mathrm{inj}}} \\ \delta\mathbf{q}_{\underline{\mathrm{v0}}} \end{Bmatrix} e^{i\omega t} = \begin{Bmatrix} \delta\mathbf{d}_{\underline{0}} \\ \delta d_{\underline{\mathrm{r0}}11} \\ \delta d_{\underline{\mathrm{r0}}21} \\ \delta\mathbf{p}_{\underline{0}} \\ \delta\mathbf{p}_{\underline{\mathrm{inj}}} \\ \delta\mathbf{q}_{\underline{\mathrm{v0}}} \end{Bmatrix} e^{i\omega t} \tag{2.128}$$

and the one resulting from the second force increment vector as

$$\mathbf{y} = \left\{ \begin{array}{c} \delta\mathbf{d} \\ \delta\mathbf{d}_{\underline{\mathrm{r}}} \\ \delta\mathbf{p} \\ \delta\mathbf{p}_{\underline{\mathrm{inj}}} \\ \delta\mathbf{q}_{\underline{\mathrm{v}}} \end{array} \right\} = \left\{ \begin{array}{c} \delta\mathbf{d}_{\underline{0}} \\ \delta\mathbf{d}_{\underline{\mathrm{r}0}} \\ \delta\mathbf{p}_{\underline{0}} \\ \delta\mathbf{p}_{\underline{\mathrm{inj}}} \\ \delta\mathbf{q}_{\underline{\mathrm{v}0}} \end{array} \right\} e^{i\omega t} = \left\{ \begin{array}{c} \delta\mathbf{d}_{\underline{0}} \\ \delta d_{\underline{\mathrm{r}0}12} \\ \delta d_{\underline{\mathrm{r}0}22} \\ \delta\mathbf{p}_{\underline{0}} \\ \delta\mathbf{p}_{\underline{\mathrm{inj}}} \\ \delta\mathbf{q}_{\underline{\mathrm{v}0}} \end{array} \right\} e^{i\omega t} \tag{2.129}$$

the bearing dynamic stiffness matrix is then defined as

$$\left[ \begin{array}{cc} K_{\underline{\mathrm{b}}11} & K_{\underline{\mathrm{b}}12} \\ K_{\underline{\mathrm{b}}21} & K_{\underline{\mathrm{b}}22} \end{array} \right] = \mathrm{Re}\left( - \left[ \begin{array}{cc} \frac{\delta f_{\underline{\mathrm{r}}01}}{\delta d_{\underline{\mathrm{r}}011}} & \frac{\delta f_{\underline{\mathrm{r}}01}}{\delta d_{\underline{\mathrm{r}}021}} \\ \frac{\delta f_{\underline{\mathrm{r}}02}}{\delta d_{\underline{\mathrm{r}}012}} & \frac{\delta f_{\underline{\mathrm{r}}02}}{\delta d_{\underline{\mathrm{r}}022}} \end{array} \right] \right) \tag{2.130}$$

and the dynamic damping matrix is defined as

$$\left[ \begin{array}{cc} D_{\underline{\mathrm{b}}11} & D_{\underline{\mathrm{b}}12} \\ D_{\underline{\mathrm{b}}21} & D_{\underline{\mathrm{b}}22} \end{array} \right] = \frac{1}{\omega}\mathrm{Im}\left( - \left[ \begin{array}{cc} \frac{\delta f_{\underline{\mathrm{r}}01}}{\delta d_{\underline{\mathrm{r}}011}} & \frac{\delta f_{\underline{\mathrm{r}}01}}{\delta d_{\underline{\mathrm{r}}021}} \\ \frac{\delta f_{\underline{\mathrm{r}}02}}{\delta d_{\underline{\mathrm{r}}012}} & \frac{\delta f_{\underline{\mathrm{r}}02}}{\delta d_{\underline{\mathrm{r}}022}} \end{array} \right] \right) \tag{2.131}$$

Similarly, the bearing transfer function matrices are

$$\mathrm{Arg}\left[ \begin{array}{cc} \frac{\delta f_{\underline{\mathrm{r}}01}}{\delta d_{\underline{\mathrm{r}}011}} & \frac{\delta f_{\underline{\mathrm{r}}01}}{\delta d_{\underline{\mathrm{r}}021}} \\ \frac{\delta f_{\underline{\mathrm{r}}02}}{\delta d_{\underline{\mathrm{r}}012}} & \frac{\delta f_{\underline{\mathrm{r}}02}}{\delta d_{\underline{\mathrm{r}}022}} \end{array} \right] \quad \text{and} \quad \left| \left[ \begin{array}{cc} \frac{\delta f_{\underline{\mathrm{r}}01}}{\delta d_{\underline{\mathrm{r}}011}} & \frac{\delta f_{\underline{\mathrm{r}}01}}{\delta d_{\underline{\mathrm{r}}021}} \\ \frac{\delta f_{\underline{\mathrm{r}}02}}{\delta d_{\underline{\mathrm{r}}012}} & \frac{\delta f_{\underline{\mathrm{r}}02}}{\delta d_{\underline{\mathrm{r}}022}} \end{array} \right] \right| \tag{2.132}$$

Whether or not one prefers the stiffness and damping format or the transfer function format is a question of taste and particular application. Both formats fit readily into rotor-bearing simulation codes. However, their use is limited to stationary harmonic analysis (frequency response analysis).

## 2.12 Chapter discussion and summary

From the principle of virtual work for the pads, the navier stokes equations for the fluid, a second order generic ODE for the servo-valves and a twodimensional particle model for the rotor, the unified equations for the coupled system were derived. The pad solution assumes small strains and rotations. The pads and the fluid can be reduced to varying degrees of detail, depending on need and available computer capacity. The highest level of generality available with the present model is a full threedimensional finite element description of the pads with the fluid described by the twodimensional reynolds equation. This system of equations will capture general pad deformations and the nonlinear oil film behaviour. Since this system of equations is nonlinear and large, it is not suited for frequency domain analysis, but it can be used for static and time domain analysis. If a pseudo modal reduction is applied to this system, the nonlinear pseudo modal reduced system results. This system is ideal for fast time domain analysis, since it captures oil film nonlinearirty, as well as the most important pad behaviour. Generation of time series is fast because the pseudo modal reduction has removed the highest system frequencies, thus allowing larger timesteps. However, the Reynolds equation must still be solved at each time step. The most compact, and least general variant of the model is obtained by applying a pseudo modal reduction to the pads and subsequently perturbing the pad mode shapes to get the condensed fluid force response. For a rigid body model, i.e., a single mode (for each pad) expansion, this will yield one equation for each pad, two for the

rotor, and one for each servo-valve. Thus a four pad bearing with two servo-valves will be represented as a 8×8 system of second order ODEs. This sort of system is ideally suited for frequency domain analysis due to its small size and linearity. It can also be used for very fast time series computations, but will not capture oil film nonlinearity, so must such use must be limited to small displacements.

# Chapter 3

# Dimensional analysis

Before actually solving the equations, we may extract fundamental and useful information from them. This is possible, partly because the equations are stated in augmented form, i.e., as in Eq. (2.84). In the following, the dimensional information is extracted from the bearing equations. To begin with, the simplest possible situation is considered, namely the passive TPJB under static conditions. The derivation is then extended to the ATPJB under dynamic conditions.

## 3.1 Static similitude of passive bearings

To begin with, let us consider the static behaviour of a passive bearing. The equations (2.84) then reduce to

$$\begin{bmatrix} \mathbf{K}_{\underline{\mathrm{s}}} & & \\ & \mathbf{K}_{\underline{\mathrm{r}}} & \\ & & \mathbf{A} \end{bmatrix} \begin{Bmatrix} \mathbf{d} \\ \mathbf{d}_{\underline{\mathrm{r}}} \\ \mathbf{p} \end{Bmatrix} = \begin{Bmatrix} \mathbf{f} \\ \mathbf{f}_{\underline{\mathrm{r}}} \\ \mathbf{r} \end{Bmatrix} \tag{3.1}$$

With the derivation process in mind, the dimensions of each submatrix and subvector can be written explicitly, such that we get

$$\begin{bmatrix} EL\tilde{\mathbf{K}}_{\underline{\mathrm{s}}} & & \\ & k_{\underline{\mathrm{r}}}\tilde{\mathbf{K}}_{\underline{\mathrm{r}}} & \\ & & \frac{L^3}{\mu}\tilde{\mathbf{A}} \end{bmatrix} \begin{Bmatrix} L\tilde{\mathbf{d}} \\ L\tilde{\mathbf{d}}_{\underline{\mathrm{r}}} \\ \frac{F}{L^2}\tilde{\mathbf{p}} \end{Bmatrix} = \begin{Bmatrix} F\tilde{\mathbf{f}} \\ F\tilde{\mathbf{f}}_{\underline{\mathrm{r}}} \\ L^3\Omega\tilde{\mathbf{r}} \end{Bmatrix} \tag{3.2}$$

Here, $EL\tilde{\mathbf{K}}_{\underline{\mathrm{s}}} = \mathbf{K}_{\underline{\mathrm{s}}}$, $F\tilde{\mathbf{f}} = \mathbf{f}$ and so on. We have introduced the characteristic length $L$. This can be chosen to be rotor diameter, fluid film thickness, or any other important measure of length, depending on convenience. Also, we have introduced the characteristic force $F$, this may be the lateral static load on the rotor, but other measures of force may be chosen. The characteristic rotor stiffness $k_{\underline{\mathrm{r}}}$ may simply be the value of the diagonal terms in the rotor stiffness matrix. If the rotor is made from the same material as the bearing, $k_{\underline{\mathrm{r}}}$ may be replaced by $EL$.

After column and row division of the relevant factors, the system of equations (3.2) becomes

$$\begin{Bmatrix} \tilde{\mathbf{f}} \\ \tilde{\mathbf{f}}_{\underline{\mathrm{r}}} \\ \tilde{\mathbf{r}} \end{Bmatrix} = \begin{bmatrix} \frac{EL^2}{F}\tilde{\mathbf{K}}_{\underline{\mathrm{s}}} & & \\ & \frac{k_{\underline{\mathrm{r}}}L}{F}\tilde{\mathbf{K}}_{\underline{\mathrm{r}}} & \\ & & \frac{F}{L^2\mu\Omega}\tilde{\mathbf{A}} \end{bmatrix} \begin{Bmatrix} \tilde{\mathbf{d}} \\ \tilde{\mathbf{d}}_{\underline{\mathrm{r}}} \\ \tilde{\mathbf{p}} \end{Bmatrix} \tag{3.3}$$

or

$$\begin{Bmatrix} \tilde{\mathbf{f}} \\ \tilde{\mathbf{f}}_{\underline{\mathrm{r}}} \\ \tilde{\mathbf{r}} \end{Bmatrix} = \begin{bmatrix} \frac{EL^2}{F} & & \\ & \frac{k_{\underline{\mathrm{r}}}L}{F} & \\ & & \frac{F}{L^2\mu\Omega} \end{bmatrix} \circ \begin{bmatrix} \tilde{\mathbf{K}}_{\underline{\mathrm{s}}} & & \\ & \tilde{\mathbf{K}}_{\underline{\mathrm{r}}} & \\ & & \tilde{\mathbf{A}} \end{bmatrix} \begin{Bmatrix} \tilde{\mathbf{d}} \\ \tilde{\mathbf{d}}_{\underline{\mathrm{r}}} \\ \tilde{\mathbf{p}} \end{Bmatrix} \tag{3.4}$$

where $\circ$ is the symbol for Hadamard (element by element) multiplication. Thus we are left with the three characteristic numbers in Tab. 3.1.

Table 3.1: Dimensionless numbers for passive static bearing.

| | | |
|---|---|---|
| $\frac{EL^2}{F}$ | $\frac{k_{\underline{\mathrm{r}}}L}{F}$ | $\frac{F}{L^2\mu\Omega}$ |

The third number in Tab. 3.1 is immediately identified as a variation of the Sommerfeld number

$$S = \frac{F}{L^2\mu\Omega} \tag{3.5}$$

i.e. the ratio of bearing load to hydrodynamic forces. Setting $F$ to the lateral static load on the rotor, the Sommerfeld number as it is defined in, E.g., [32] is

$$S = \frac{\mu\Omega L R_{\underline{\mathrm{r}}}}{\pi F}\left(\frac{R_{\underline{\mathrm{r}}}}{R_{\underline{\mathrm{p}}} - R_{\underline{\mathrm{r}}}}\right)^2 \tag{3.6}$$

For a given rotor-bearing shape, all dimensions are proportional to $L$. Thus (in dimensional terms) the expression in Eq. (3.6) reduces to that of the inverse of that in Eq. (3.5).

The first number in Tab. 3.1 is a measure of elastic forces to bearing load. Consider two similar bearings, for which

$$\frac{E_1 L_1^2}{F_1} = \frac{E_2 L_2^2}{F_2} \tag{3.7}$$

and

$$\frac{F_1}{L_1^2\mu_1\Omega_1} = \frac{F_2}{L_2^2\mu_2\Omega_2} \tag{3.8}$$

Then, multiplying Eq. (3.7) with Eq. (3.8) we arrive at a new similitude equation

$$\frac{E_1}{\mu_1\Omega_1} = \frac{E_2}{\mu_2\Omega_2} \tag{3.9}$$

Thus, Eqs. (3.9) and (3.8) now define bearing similitude in lieu of Eqs.(3.7) and (3.8). This is merely an example of the fact that ratios, products and inverses of non-dimensional characteristic numbers are

themselves non-dimensional characteristic numbers. Consider the case where the lateral static load on the rotor is zero; another measure of force must then be chosen. I.e. zero lateral static load on the rotor does not allow us to set $F$ to zero. If there are no other external loads on the rotor, we have effectively removed one parameter from the system (the load). In such cases, e.g., the viscous force $L^2\mu\Omega$ may be used as a characteristic load in lieu of $F$. The above derivation allows us to do this.

Equation (3.9) states that the ratio of elastic forces to viscous forces be the same in two similar bearings. Let us call this ratio the hydroelastic number

$$H = \frac{E}{\mu\Omega} \tag{3.10}$$

If $H$ is sufficiently high, bearing deformation may be neglected in the given analysis. The critical value of $H$ depends on the specific bearing design, i.e., the proportions of the bearing. However, when a critical $H$ value is established for a given bearing, the analyst can neglect bearing deformation with confidence when prudent. Notice that $H$ is independent of $L$, meaning that it is independent of bearing size. From this we can draw an important conclusion: If bearing deformation can be neglected in a given small-scale laboratory experiment, it can also be neglected in a full size bearing of similar design. Lund [34] has previously derived an expression for a dimensionless pad flexibility for a beam model of the pad.

The second number in Tab. 3.1 is the ratio of rotor structural (shaft) forces to rotor load. I.e. it is a measure of how much of the load is carried by the rotor itself (thus not by the bearing). When this number approaches infinity, all the load is carried by the rotor itself. When it approaches zero, the bearing carries all the load. In most of the results presented in this thesis the number will be zero, since rotor structural stiffness is neglected.

## 3.2 Static similitude of active bearings

The static similitude of active bearings can be investigated in a similar fashion to that of the passive case. We include the relevant terms in the static part of the augmented system of equations. Long hand derivation can be found in appendix B. After the relevant row and column divisions, we arrive at

$$\begin{bmatrix} \frac{EL^2}{F}\mathbf{I} & & & & & & \\ & \frac{k_{\underline{r}}L}{F}\mathbf{I} & & & & & \\ & & \frac{F}{L^2\mu\Omega}\mathbf{I} & \frac{F}{L^2\mu\Omega}\mathbf{I} & & & \\ & & \frac{FL}{\mu q_{\underline{L}}}\mathbf{I} & \frac{FL}{\mu q_{\underline{L}}}\mathbf{I} & \frac{k_{\underline{pq}}F}{L^2 q_{\underline{L}}}\mathbf{I} & & \\ & \frac{G_{\underline{P}}L}{u_{\underline{ch}}}\mathbf{I} & & & & \frac{q_{\underline{L}}}{K_{\underline{v}}u_{\underline{ch}}}\mathbf{I} & \\ & & & \mathbf{I} & \mathbf{I} & & \end{bmatrix} \circ$$

$$\begin{bmatrix} \tilde{\mathbf{K}}_{\underline{s}} & & & & & & \\ & \tilde{\mathbf{K}}_{\underline{r}} & & & & & \\ & & \tilde{\mathbf{A}} & \tilde{\mathbf{W}} & & & \\ & & \tilde{\mathbf{W}}^T & \tilde{\mathbf{Q}} & \tilde{\mathbf{K}}_{\underline{pq}} & & \\ & \tilde{\mathbf{G}}_{\underline{P}} & & & & \tilde{\mathbf{K}}_{\underline{q\text{-}q}} & \\ & & & \mathbf{I} & -\mathbf{I} & & \end{bmatrix} \begin{Bmatrix} \tilde{\mathbf{d}} \\ \tilde{\mathbf{d}}_{\underline{r}} \\ \tilde{\mathbf{p}} \\ \tilde{\mathbf{p}}_{\underline{inj}} \\ \tilde{\mathbf{p}}_{\underline{inj}} \\ \tilde{\mathbf{q}}_{\underline{v}} \end{Bmatrix} = \begin{Bmatrix} \tilde{\mathbf{f}} \\ \tilde{\mathbf{f}}_{\underline{r}} \\ \tilde{\mathbf{r}} \\ \tilde{\mathbf{r}}_{\underline{inj}} \\ \tilde{\mathbf{u}}_{\underline{vr}} \\ \mathbf{0} \end{Bmatrix} \tag{3.11}$$

where $k_{\underline{\mathrm{pq}}}$ is a characteristic flow pressure impedance of one of the valves, $G_{\underline{\mathrm{P}}}$ is a characteristic proportional gain, $K_{\underline{\mathrm{v}}}$ is a characteristic flow voltage coefficient, $u_{\underline{\mathrm{ch}}}$ is a characteristic signal voltage and $q_{\underline{\mathrm{L}}}$ is a characteristic flow. Note that the valve inlet pipe length of pipe $i$ $l_{\underline{0}i}$ is measured in terms of the characteristic length $L$. We are thus left with the seven characteristic numbers in Tab. 3.2

Table 3.2: Dimensionless numbers for active static bearing.

| Passive | | | Active | | | |
|---|---|---|---|---|---|---|
| $\frac{EL^2}{F}$ | $\frac{k_{\underline{\mathrm{r}}}L}{F}$ | $\frac{F}{L^2\mu\Omega}$ | $\frac{FL}{\mu q_{\underline{\mathrm{L}}}}$ | $\frac{k_{\underline{\mathrm{pq}}}F}{L^2 q_{\underline{\mathrm{L}}}}$ | $\frac{G_{\underline{\mathrm{P}}}L}{u_{\underline{\mathrm{ch}}}}$ | $\frac{q_{\underline{\mathrm{L}}}}{K_{\underline{\mathrm{v}}}u_{\underline{\mathrm{ch}}}}$ |

We recognise the first three numbers in Tab. 3.2 to be those we previously derived for a passive bearing. Additionally we have four numbers associated with the control system. The first control system number is the ratio of bearing load to valve flow induced forces. The second active number is the dimensionless characteristic pressure driven flow. The third active number is the ratio of the characteristic proportional gain signal to the characteristic reference signal. Finally, the fourth active number is the inverse dimensionless piston driven flow. Often, the reference signal is zero. This corresponds to sending no signal when the rotor is in the centre of the bearing. In these cases we eliminate $u_{\underline{\mathrm{ch}}}$ to produce the characteristic number

$$\frac{G_{\underline{\mathrm{P}}}LK_{\underline{\mathrm{v}}}}{q_{\underline{\mathrm{L}}}} \tag{3.12}$$

which is the dimensionless proportional gain flow. This number then replaces $\frac{G_{\underline{\mathrm{P}}}L}{u_{\underline{\mathrm{ch}}}}$ and $\frac{q_{\underline{\mathrm{L}}}}{K_{\underline{\mathrm{v}}}u_{\underline{\mathrm{ch}}}}$.

## 3.3 Dynamic similitude of passive bearings

In a dynamic similitude analysis, it is convenient to work with the equations in state space form. As it turns out, transient similitude and stationary harmonic similitude are equivalent and encompassed in the dynamic similitude considerations. This is a very powerful conclusion, as it allows us to both predict the stability properties and stationary harmonic response of, e.g. very large bearings.

The dimensionless time $\tilde{t}$ is introduced as

$$\tilde{t} = \Omega t \tag{3.13}$$

then

$$\frac{\partial}{\partial t} = \Omega\frac{\partial}{\partial \tilde{t}}, \quad \frac{\partial^2}{\partial t^2} = \Omega^2\frac{\partial^2}{\partial \tilde{t}^2} \tag{3.14}$$

That is, the dimensionless time is measured in terms of the journal rotation. This provides a sensible measure of the "speed" of system mode shapes, since the time to, e.g., damp out a transient is now given as a number of rotations of the journal, rather than seconds. Furthermore, any critical dimensionless eigenfrequency is immediately identified as being unity. If all dimensionless eigenfrequencies are larger than unity, the system is operating subsynchronously. If any dimensionless eigenfrequency is smaller than unity, the system is operating supersynchronously.

When letting the dot notation $\dot{()}$ denote derivation with respect to $\tilde{t}$, column and row division and factoring yields

$$
\begin{bmatrix} \mathbf{0} & \begin{bmatrix} \frac{EL^2}{F}\mathbf{I} & & \\ & \frac{k_{\underline{r}}L}{F}\mathbf{I} & \\ & & \frac{F}{L^2\mu\Omega}\mathbf{I} \end{bmatrix} \\ \mathbf{I} & \mathbf{0} \end{bmatrix} \circ \begin{bmatrix} \mathbf{0} & \begin{bmatrix} \tilde{\mathbf{K}}_{\underline{s}} & & \\ & \tilde{\mathbf{K}}_{\underline{r}} & \\ & & \tilde{\mathbf{A}} \end{bmatrix} \\ \mathbf{I} & \mathbf{0} \end{bmatrix} \begin{Bmatrix} \dot{\tilde{\mathbf{d}}} \\ \dot{\tilde{\mathbf{d}}}_{\underline{r}} \\ \dot{\tilde{\mathbf{p}}} \\ \tilde{\mathbf{d}} \\ \tilde{\mathbf{d}}_{\underline{r}} \\ \tilde{\mathbf{p}} \end{Bmatrix} +
$$

$$
\begin{bmatrix} \begin{bmatrix} \frac{\rho L^4\Omega^2}{F}\mathbf{I} & \\ & \frac{L\Omega^2 m_{\underline{r}}}{F}\mathbf{I} \end{bmatrix} & \begin{bmatrix} \frac{c_{\underline{r}}\Omega L}{F}\mathbf{I} \end{bmatrix} \\ \mathbf{0} & \mathbf{I} \end{bmatrix} \circ
$$

$$
\begin{bmatrix} \begin{bmatrix} \tilde{\mathbf{M}}_{\underline{s}} & \\ & \tilde{\mathbf{M}}_{\underline{r}} \end{bmatrix} & \begin{bmatrix} \tilde{\mathbf{D}}_{\underline{r}} \end{bmatrix} \\ \mathbf{0} & \mathbf{I} \end{bmatrix} \begin{Bmatrix} \ddot{\tilde{\mathbf{d}}} \\ \ddot{\tilde{\mathbf{d}}}_{\underline{r}} \\ \ddot{\tilde{\mathbf{p}}} \\ \dot{\tilde{\mathbf{d}}} \\ \dot{\tilde{\mathbf{d}}}_{\underline{r}} \\ \dot{\tilde{\mathbf{p}}} \end{Bmatrix} = \begin{Bmatrix} \tilde{\mathbf{f}} \\ \tilde{\mathbf{f}}_{\underline{r}} \\ \tilde{\mathbf{r}} \\ \mathbf{0} \end{Bmatrix} \tag{3.15}
$$

where $\rho$ is the characteristic pad density, $m_{\underline{r}}$ is the characteristic rotor mass and $c_{\underline{r}}$ is the characteristic rotor damping. Again, the reader is referred to appendix B for a long hand derivation.

We can write the equations compactly as

$$\mathbf{D} \circ \mathbf{E}\mathbf{y} + \mathbf{G} \circ \mathbf{J}\dot{\mathbf{y}} = \mathbf{j} \tag{3.16}$$

where $\mathbf{y}$ is now the total state vector, not to be confused with the incremental one. Similarly $\mathbf{j}$ is the total right hand side. All the dimensional information is contained in $\mathbf{D}$ and $\mathbf{G}$. Thus we arrive at the six characteristic numbers in Tab. 3.3.

Table 3.3: Dimensionless numbers for passive dynamic bearing.

| Static | | | Dynamic | | |
|---|---|---|---|---|---|
| $\frac{EL^2}{F}$ | $\frac{k_{\underline{r}}L}{F}$ | $\frac{F}{L^2\mu\Omega}$ | $\frac{\rho L^4\Omega^2}{F}$ | $\frac{L\Omega^2 m_{\underline{r}}}{F}$ | $\frac{c_{\underline{r}}\Omega L}{F}$ |

The first three (static) numbers in Tab. 3.3 are recognised as the hydroelastic number, the rotor force ratio and the Sommerfeld number, respectively. The first dynamic number is the dimensionless pad mass. The second dynamic number is the dimensionless rotor mass and the third dynamic number is the dimensionless rotor damping. It is deemed worthwhile assigning a symbol to the dimensionless pad mass, as it will be discussed later in this document. Also, as a characteristic load $F$ can be difficult to determine in situations where the static rotor load is zero, it seems sensible to eliminate it. Combining the Sommerfeld number and the dimensionless pad mass, to eliminate $F$, we arrive at

$$H_2 = \frac{\rho L^2 \Omega}{\mu} \tag{3.17}$$

which is the ratio of inertial to viscous forces. Note that other expressions for the dimensionless pad mass and dimensionless rotor mass have been mentioned in litterature, e.g., in [29] and [34].

## 3.4 Dynamic similitude of active bearings

Now, including both dynamic and active terms, the starting point is the full set of equations (2.84) in state space form. After row and column division and factoring in hadamard products, we arrive at

$$
\begin{bmatrix} \mathbf{I} & \mathbf{0} & \begin{bmatrix} \frac{EL^2}{F}\mathbf{I} & \frac{k_{\underline{\mathrm{r}}}L}{F}\mathbf{I} & \frac{F}{L^2\mu\Omega}\mathbf{I} & \frac{F}{L^2\mu\Omega}\mathbf{I} & \frac{k_{\mathrm{pq}}F}{L^2 q_{\mathrm{L}}}\mathbf{I} & \frac{q_{\mathrm{L}}}{K_{\underline{\mathrm{v}}}u_{\mathrm{ch}}}\mathbf{I} \\ & \frac{G_{\mathrm{D}}L}{u_{\mathrm{ch}}}\mathbf{I} & \frac{FL}{\mu q_{\mathrm{L}}}\mathbf{I} & \frac{FL}{\mu q_{\mathrm{L}}}\mathbf{I} & & \end{bmatrix} \end{bmatrix} \circ
$$

$$
\begin{bmatrix} \mathbf{I} & \mathbf{0} & \begin{bmatrix} \tilde{\mathbf{K}}_{\underline{\mathrm{s}}} & \tilde{\mathbf{K}}_{\underline{\mathrm{r}}} & \tilde{\mathbf{A}} & \tilde{\mathbf{W}} & & \\ & \tilde{\mathbf{G}}_{\underline{\mathrm{P}}} & \tilde{\mathbf{W}}^T & \tilde{\mathbf{Q}} & \tilde{\mathbf{K}}_{\underline{\mathrm{pq}}} & \tilde{\mathbf{K}}_{\underline{\mathrm{q\text{-}q}}} \end{bmatrix} \end{bmatrix} \begin{Bmatrix} \dot{\tilde{\mathbf{d}}} \\ \dot{\tilde{\mathbf{d}}}_{\underline{\mathrm{r}}} \\ \dot{\tilde{\mathbf{P}}} \\ \dot{\tilde{\mathbf{P}}}_{\underline{\mathrm{inj}}} \\ \dot{\tilde{\mathbf{P}}}_{\underline{\mathrm{inj}}} \\ \dot{\tilde{\mathbf{q}}}_{\underline{\mathrm{v}}} \\ \tilde{\mathbf{d}} \\ \tilde{\mathbf{d}}_{\underline{\mathrm{r}}} \\ \tilde{\mathbf{P}} \\ \tilde{\mathbf{P}}_{\underline{\mathrm{inj}}} \\ \tilde{\mathbf{P}}_{\underline{\mathrm{inj}}} \\ \tilde{\mathbf{q}}_{\underline{\mathrm{v}}} \end{Bmatrix} +
$$

$$
\begin{bmatrix} \mathbf{I} & \mathbf{0} & \begin{bmatrix} \frac{\rho L^4\Omega^2}{F}\mathbf{I} & & \\ & \frac{L\Omega^2 m_{\underline{\mathrm{r}}}}{F}\mathbf{I} & \\ & & \frac{\Omega^2 q_{\mathrm{L}}}{\omega_{\underline{\mathrm{v}}}^2 K_{\underline{\mathrm{v}}} u_{\mathrm{ch}}}\mathbf{I} \end{bmatrix} \end{bmatrix} \begin{bmatrix} \mathbf{I} & \begin{bmatrix} \frac{c_{\underline{\mathrm{r}}}\Omega L}{F}\mathbf{I} & \\ \frac{G_{\mathrm{D}}L\Omega}{u_{\mathrm{ch}}}\mathbf{I} & \frac{\xi_v\Omega q_{\mathrm{L}}}{\omega_{\underline{\mathrm{v}}}K_{\underline{\mathrm{v}}}u_{\mathrm{ch}}}\mathbf{I} \end{bmatrix} \end{bmatrix} \circ
$$

$$
\begin{bmatrix} \mathbf{I} & \mathbf{0} & \begin{bmatrix} \tilde{\mathbf{M}}_{\underline{\mathrm{s}}} & \tilde{\mathbf{M}}_{\underline{\mathrm{r}}} & \\ & & \tilde{\mathbf{M}}_{\underline{\mathrm{q\text{-}q}}} \end{bmatrix} \end{bmatrix} \begin{bmatrix} \mathbf{I} & \begin{bmatrix} \tilde{\mathbf{D}}_{\underline{\mathrm{r}}} & \\ \tilde{\mathbf{G}}_{\underline{\mathrm{D}}} & \tilde{\mathbf{D}}_{\underline{\mathrm{q\text{-}q}}} \end{bmatrix} \end{bmatrix} \begin{Bmatrix} \ddot{\tilde{\mathbf{d}}} \\ \ddot{\tilde{\mathbf{d}}}_{\underline{\mathrm{r}}} \\ \ddot{\tilde{\mathbf{P}}} \\ \ddot{\tilde{\mathbf{P}}}_{\underline{\mathrm{inj}}} \\ \ddot{\tilde{\mathbf{P}}}_{\underline{\mathrm{inj}}} \\ \ddot{\tilde{\mathbf{q}}}_{\underline{\mathrm{v}}} \\ \dot{\tilde{\mathbf{d}}} \\ \dot{\tilde{\mathbf{d}}}_{\underline{\mathrm{r}}} \\ \dot{\tilde{\mathbf{P}}} \\ \dot{\tilde{\mathbf{P}}}_{\underline{\mathrm{inj}}} \\ \dot{\tilde{\mathbf{P}}}_{\underline{\mathrm{inj}}} \\ \dot{\tilde{\mathbf{q}}}_{\underline{\mathrm{v}}} \end{Bmatrix} = \begin{Bmatrix} \tilde{\mathbf{f}} \\ \tilde{\mathbf{f}}_{\underline{\mathrm{r}}} \\ \tilde{\mathbf{r}} \\ \tilde{\mathbf{r}}_{\mathrm{inj}} \\ \tilde{\mathbf{u}}_{\underline{\mathrm{vr}}} \\ \mathbf{0} \\ \mathbf{0} \end{Bmatrix} \tag{3.18}
$$

Where $\omega_{\underline{\mathrm{v}}}$ is the characteristic valve eigenfrequency $\xi_v$ is the characteristic valve damping ratio, and $G_{\underline{\mathrm{D}}}$ is the characteristic derivative gain. As before, this is written in compact form as

$$\mathbf{D} \circ \mathbf{E}\mathbf{y} + \mathbf{G} \circ \mathbf{J}\dot{\mathbf{y}} = \mathbf{j} \tag{3.19}$$

with all the dimensional information contained in $\mathbf{D}$ and $\mathbf{G}$, thus leaving us with the dimensionless numbers in Tab. 3.4.

Apart from numbers that we have seen in the previous sections, we have six new ones. That is, those belonging to the dynamic part of the system (bottom row of Tab. 3.4). Consider first the numbers for the passive system. The first of these is the dimensionless pad inertia. The second and third are the

Table 3.4: Dimensionless numbers for active dynamic bearing.

| | Passive | | | Active | | | |
|---|---|---|---|---|---|---|---|
| Static | $\frac{EL^2}{F}$ | $\frac{k_{\mathrm{r}}L}{F}$ | $\frac{F}{L^2\mu\Omega}$ | $\frac{FL}{\mu q_{\mathrm{L}}}$ | $\frac{k_{\mathrm{pq}}F}{L^2 q_{\mathrm{L}}}$ | $\frac{G_{\mathrm{P}}L}{u_{\mathrm{ch}}}$ | $\frac{q_{\mathrm{L}}}{K_{\mathrm{v}}u_{\mathrm{ch}}}$ |
| Dynamic | $\frac{\rho L^4\Omega^2}{F}$ | $\frac{L\Omega^2 m_{\mathrm{r}}}{F}$ | $\frac{c_{\mathrm{r}}\Omega L}{F}$ | $\frac{\Omega^2 q_{\mathrm{L}}}{\omega_{\mathrm{v}}^2 K_{\mathrm{v}}u_{\mathrm{ch}}}$ | $\frac{G_{\mathrm{D}}L\Omega}{u_{\mathrm{ch}}}$ | $\frac{\xi_v\Omega q_{\mathrm{L}}}{\omega_{\mathrm{v}}K_{\mathrm{v}}u_{\mathrm{ch}}}$ | |

dimensionless rotor inertia and damping, respectively. Now consider the numbers for the active system. The first of these is the inverse of the dimensionless valve inertia, the second is the dimensionless derivative gain signal and the third is the dimensionless valve damping. As in the static active case, the absence of a reference signal will yield different dimensionless numbers. That is,

$$\frac{G_{\mathrm{P}}L}{u_{\mathrm{ch}}}, \quad \frac{q_{\mathrm{L}}}{K_{\mathrm{v}}u_{\mathrm{ch}}}, \quad \frac{\Omega^2 q_{\mathrm{L}}}{\omega_{\mathrm{v}}^2 K_{\mathrm{v}}u_{\mathrm{ch}}}, \quad \frac{G_{\mathrm{D}}L\Omega}{u_{\mathrm{ch}}} \quad \text{and} \quad \frac{\xi_v\Omega q_{\mathrm{L}}}{\omega_{\mathrm{v}}K_{\mathrm{v}}u_{\mathrm{ch}}}$$

are replaced by

$$\frac{G_{\mathrm{P}}LK_{\mathrm{v}}}{q_{\mathrm{L}}}, \quad \frac{\Omega^2}{\omega_{\mathrm{v}}^2}, \quad \frac{G_{\mathrm{D}}L\Omega K_{\mathrm{v}}}{q_{\mathrm{L}}} \quad \text{and} \quad \frac{\xi_v\Omega}{\omega_{\mathrm{v}}} \tag{3.20}$$

Details of the derivation are given in appendix B. Furthermore, as before mentioned, in cases where the lateral static load on the rotor is zero it can be difficult to determine a characteristic force in the system. It is then convenient to perform the same operations that were used to derive Eqs (3.7) from Eq. (3.9). That is, we exploit that products and ratios of dimensionless numbers are themselves dimensionless numbers. Basically the operation constitutes substituting $L^2\mu\Omega$ for $F$. Thus, we may replace the dimensionless numbers

| | Passive | | | Active | |
|---|---|---|---|---|---|
| Static | $\frac{EL^2}{F}$ | $\frac{k_{\mathrm{r}}L}{F}$ | $\frac{F}{L^2\mu\Omega}$ | $\frac{FL}{\mu q_{\mathrm{L}}}$ | $\frac{k_{\mathrm{pq}}F}{L^2 q_{\mathrm{L}}}$ |
| Dynamic | $\frac{\rho L^4\Omega^2}{F}$ | $\frac{L\Omega^2 m_{\mathrm{r}}}{F}$ | $\frac{c_{\mathrm{r}}\Omega L}{F}$ | | |

(3.21)

with

| | Passive | | | Active | |
|---|---|---|---|---|---|
| Static | $\frac{E}{\mu\Omega}$ | $\frac{k_{\mathrm{r}}}{L\mu\Omega}$ | $\frac{F}{L^2\mu\Omega}$ | $\frac{L^3\Omega}{q_{\mathrm{L}}}$ | $\frac{k_{\mathrm{pq}}\mu\Omega}{q_{\mathrm{L}}}$ |
| Dynamic | $\frac{\rho L^2\Omega}{\mu}$ | $\frac{\Omega m_{\mathrm{r}}}{L\mu}$ | $\frac{c_{\mathrm{r}}}{L\mu}$ | | |

(3.22)

The latter set of numbers is far more convenient in cases where the lateral rotor load is zero or unknown.

## 3.5 Chapter discussion and summary

The non dimensional version of the rotor-bearing-valve system of equations has been derived. Key dimensionless numbers have been identified. The cases of static similitude of passive bearings, static similitude of active bearings, dynamic similitude of passive bearings and dynamic similitude of active bearings have been investigated. The three former cases can be considered special cases of the latter. Some of the dimensionless numbers are known in the literature, while others are novel. The dimensionless groups are useful

for experiment planning, since they allow extrapolation of experimental data to situations which may be hard to reproduce in a laboratory. For instance, it may be challenging to reproduce extreme rotational speeds or heavy rotors, both of which are found frequently in industrial machinery. With knowledge of the scaling of different effects, representative experiments may be planned with confidence. Examples of similitude across bearing sizes are shown in section 5.3. Furthermore, simulations are run so as to determine the critical hydroelastic number for a given bearing design.

# Chapter 4

# Model validation

There are no published studies of active bearings of the type studied in this thesis, which include pad deformations. However, some experimental data is available. There are several theroetical rigid pad studies of passive bearings, as well as a few studies of passive bearings which include pad deformations. In this chapter the present model will be compared to a selection of these studies. Furthermore, a mesh density convergence study is conducted. Calculations of the Reynolds number as well as a thermal error estimate are provided in chapter 5.

## 4.1 Mesh density convergence

The required mesh density varies from analysis to analysis. Generally, higher frequencies entail higher mesh density requirements. Also, if derived fields, such as stress and strain fields are of interest, mesh refinement should be increased. Here, the fields of displacement and pressure are in focus, thus the mesh density requirements are modest.

A mesh convergence study of eigenvalues is performed on a generic pad for varying mesh densities. For the convergence study only a single pad need be investigated. The rotor diameter is 0.0998m and the bearing inner radius of curvature is 0.05m, so the machined clearance is 100$\mu$m. The preload factor is 0.25. The pad thickness is 10mm with an extension of 80°. The pad is pivoted along its centreline at a radial distance of 70mm from the bearing centre. The rotor is thus fixed laterally, but rotating at a speed of 100Hz. The lubricant viscosity is 0.013Ns/m$^2$, the elastic modulus is 100GPa, the Poisson ratio is 0.3 and the pad density is 8400kg/m$^3$.

Meshes with 1×2×3, 2×4×6, 3×6×9 and 4×8×12 elements are utilised. The elements are twenty node serendipity elements. Key data for the meshes is shown in Tab. 4.1.

Figure 4.1 shows mesh #2. As indicated in Tab. 4.1 this mesh consists of 48 elements. The mesh connectivity is such that the total number of nodes is 349 and the total number of degrees of freedom for the deformation problem is 1047.

For each mesh, four different pseudo modal reductions are applied, starting with a rigid body reduction and ending with a four-mode reduction. Note that the computed pseudo mode shapes themselves depend on the mesh density. Again, in general, the lower the mode shape, the less severe are the mesh density requirements.

Figures 4.2 and 4.3 show the two first eigenvalues of the pad as a function of mesh density for the

Table 4.1: Mesh overview.

| | Number of elements in * direction | | | | |
|---|---|---|---|---|---|
| Mesh # | *Radial | *Axial | *Circumferential | Elements | Nodes |
| 1 | 1 | 2 | 3 | 6 | 70 |
| 2 | 2 | 4 | 6 | 48 | 349 |
| 3 | 3 | 6 | 9 | 162 | 982 |
| 4 | 4 | 8 | 12 | 384 | 2113 |

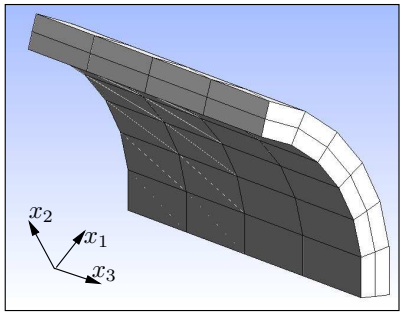


Figure 4.1: The pad under investigation. The shown mesh is mesh #2, with 2×4×6 elements. Each element is a twenty node serendipity element. Nodes are not shown.

four different pseudo modal reductions. Notice that the eigenvalues are real, i.e., the first two modes of the isolated pad are overdamped. Secondly notice the magnitude of the eigenvalues. The first and second eigenvalues are one and two orders of magnitude larger than the rotational speed, respectively. Thus, for all practical purposes, no more eigenvalues need be considered. Consider Fig. 4.2. The rigid body model seems to be largely independent of mesh refinement. Thus we may conclude that the rigid body motion, the pressure field as well as the pressure response to the rigid body motion converge very quickly. This may well be in part due to the use of higher order elements. Furthermore, we observe that the two-, three- and four mode reductions behave quite similarly with only minor differences. In deed, the two mode reduction of mesh #2 comes within 5% of the four mode reduction of the finest mesh. Finally notice that the rigid body model never fully reaches the other reductions. From this we may conclude that even the first mode of pad motion contains some pad deformation. Now consider Fig. 4.3. Notice that the rigid body model is not in the plot, i.e., this mode is dominated by pad deformation with tilting playing a minor role. Secondly, there is only very little difference between the two- three- and four mode reductions. So pad deformation is dominated by the second mode. The difference between mesh #2 and mesh #4 is roughly 15%. However, considering the magnitude of the eigenvalue this error is acceptable, as the error will not be relevant under any practical circumstances.

The combined observations of Figs. 4.2 and 4.3 lead os to conclude that for the applications relevant to this work, a two mode reduction of a mesh comparable to mesh #2 is adequate. All meshes used for the analyses presented in this thesis make use of meshes that are significantly finer.

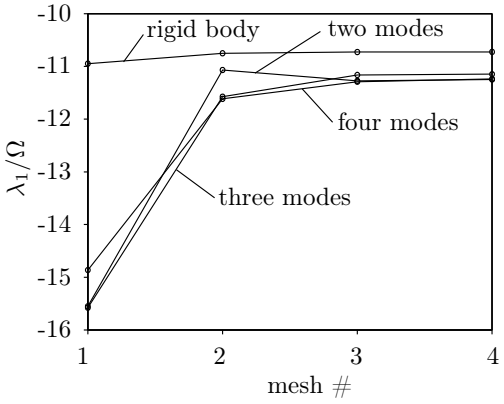


Figure 4.2: Convergence behaviour of first eigenvalue.

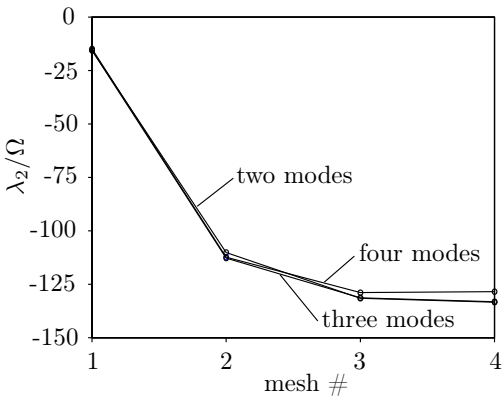


Figure 4.3: Convergence behaviour of second eigenvalue.

## 4.2 Benchmarking against Someya

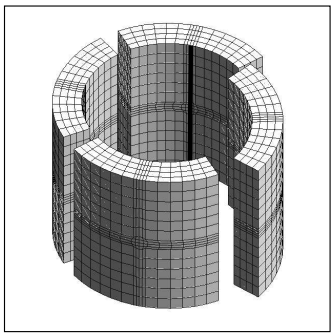

Figure 4.4: Mesh of bearing corresponding to calculation # 29 in Someya's book [32]. The mesh as shown consists of 7248 nodes and 1024 solid elements. Exploiting symmetry cuts this number in half.

As mentioned, Someya's journal-bearing databook is widely cited, and a valuable source of journal bearing data. Here, a comparison to one of Someya's results shall be made. A bearing with the same properties as the bearing in calculation # 29 in Someya's book [32] is considered. The bearing under investigation has four pads, and is in a load between pad configuration. Each pad extends 80 degrees and is pivoted on the middle. The rotor radius is 49.8mm and the pad inner surface radius of curvature is 50mm. The bearing length is 0.1m, thus the length to diameter ratio is 1. The preload factor is 0.5, thus the assembled clearance is 100$\mu$m. The journal rotational speed is 100Hz and the lubricant viscosity is 0.00937Ns/m$^2$. These parameters do not reflect what is considered to be good bearing design. Rather they are chosen solely so as to match the parameters in Someya's calculations. The pad inertia is neglected, thus pad density is set to zero. A single mode pseudo modal reduction is employed, so as to mimic the rigid body model of Someya. Each pad is pivoted about the centreline on its inner surface at a radius of

50mm. The pad thickness is 17mm, but is unimportant due to the rigid body assumption. The mesh is shown in Fig. 4.4 with indication of the pivot line on one pad and the pivoting mode of another pad.

Figure 4.5 shows fields of displacement and pressure for the static equilibrium, when the rotor is at 0.2 eccentricity, corresponding to a displacement of 20$\mu$m. The rotor is displaced in the $x_1$ direction.

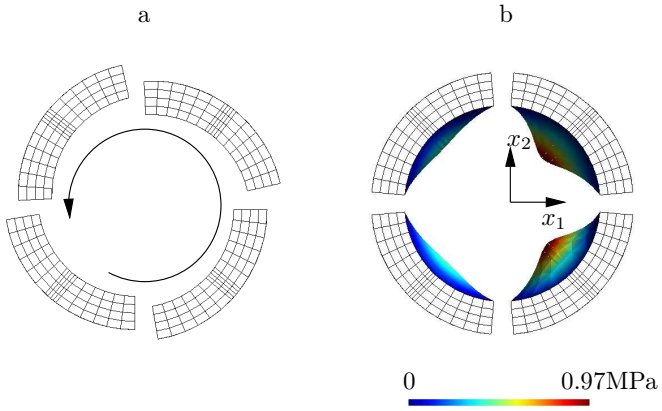


Figure 4.5: Fields for the static equilibrium when the rotor is displaced 20$\mu$m in the $x_1$ direction. a: Pad displacements (scaled). Maximum displacement of any node in the pad is 61.8$\mu$m. b: Pressure.

Figure 4.6 shows a plot of Sommerfeld number as a function of eccentricity. The graph is compared to Someya's data. A near perfect match is made. The Sommerfeld number $S$ is defined as in [32]. Thus,

$$S = \frac{\mu \Omega L R_{\underline{\mathrm{r}}}}{\pi f_{\underline{\mathrm{r}}1}} \left( \frac{R_{\underline{\mathrm{r}}}}{R_{\underline{\mathrm{p}}} - R_{\underline{\mathrm{r}}}} \right)^2 \tag{4.1}$$

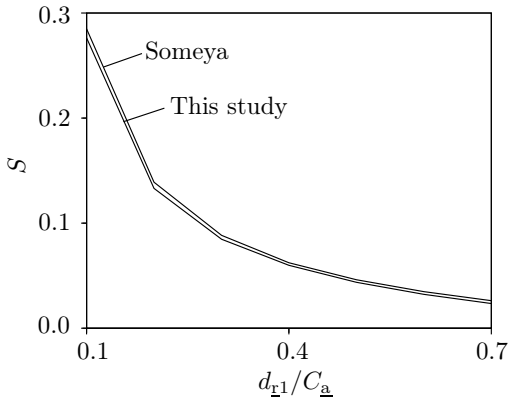


Figure 4.6: Comparison with calculation # 29 in Someya's book [32].

where L is bearing length and $f_{\underline{r}1}$ is the total static bearing load, since no load is applied in the $x_2$ direction in this case. Figures 4.7 and 4.8 show plots of synchronously reduced dimensionless stiffness and damping, respectively. Again, comparison is made to Someya's data, showing good agreement.

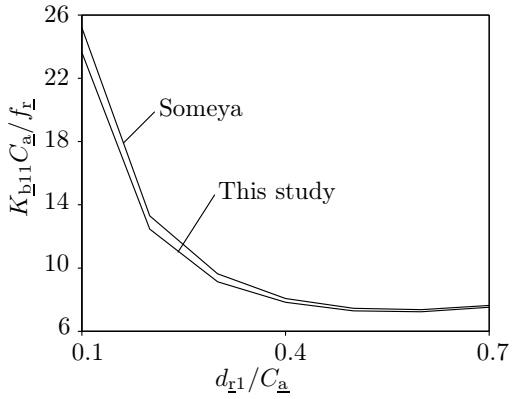


Figure 4.7: Comparison with calculation # 29 in Someya's book [32].

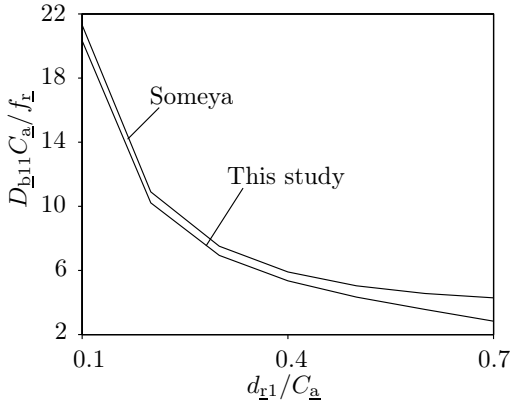


Figure 4.8: Comparison with calculation # 29 in Someya's book [32].

## 4.3 Benchmarking against Desbordes, Fillon and Frêne

Desbordes, Fillon and Frêne pioneered the introduction of pad compliance into TPJB modelling and used their model to compute journal orbits. Here we shall make a comparison between journal orbits as computed by the present code, and the journal orbits from [37]. The bearing is a three pad bearing, with steel pads. The journal radius is 60mm with a pad thickness of 30mm. The bearing length is 72mm. Machined clearance is 120$\mu$m with a preload factor of 0.5. Lubricant viscosity is 0.013Ns/m$^2$, pad elastic modulus is 210GPa and Poisson's ratio is 0.3. Rotor mass is 1000kg, and rotor speed is 3000rpm, corresponding to 50Hz or 100$\pi$rad/s. The static load is 30000N in the negative $x_2$ direction.

Here, we adopt a two mode pseudo modal reduction to account for the pad deformations. The pad modes are shown in Fig. 4.9. The pivots are located at 0.56 along the pad arc, that is, they are offset in the direction of rotor rotation. This is clearly visible in the rigid body modes. In [37] pad inertia was neglected by iterating to static pad equilibrium for every new journal position. Here, this is emulated by setting pad density to a low value. Since this lowers the time step limit, a reasonable (not too small) value must be chosen. Pad density is set to 1000kg/m$^3$ which is small enough to virtually eliminate the effect of pad inertia, while still allowing for a reasonable time step.

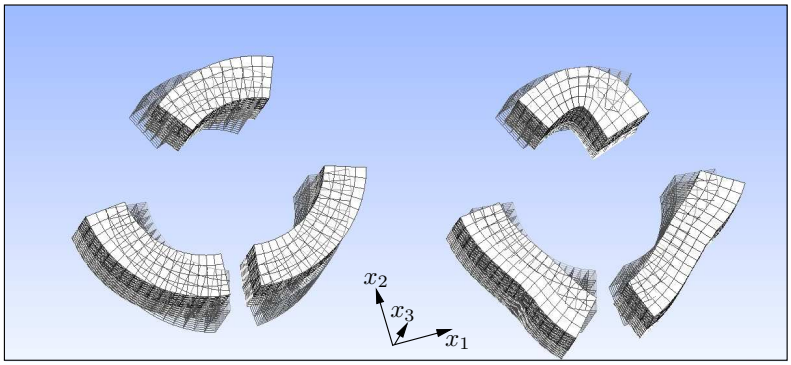


Figure 4.9: The first two pad modeshapes of each pad with wireframes indicating the undisplaced pads.

Various values of unbalance are applied to the journal. In [37] they are given as unbalance eccentricities varying from 100$\mu$m through 500$\mu$m. This corresponds to 4935N through 24674N, such that for the 100$\mu$m case, the rotor is subjected to

$$\begin{aligned} f_{\underline{r}1} &= 4935\text{N}\cos(100\pi s^{-1}t + 4\pi/3) \\ f_{\underline{r}2} &= -30000\text{N} + 4935\text{N}\sin(100\pi s^{-1}t + 4\pi/3) \end{aligned} \tag{4.2}$$

Note the $4\pi/3$ phase shift owing to the different coordinate system used in [37]. The orbits from the present calculation are compared to [37] in Fig. 4.10. They are virtually identical, with only minor differences.

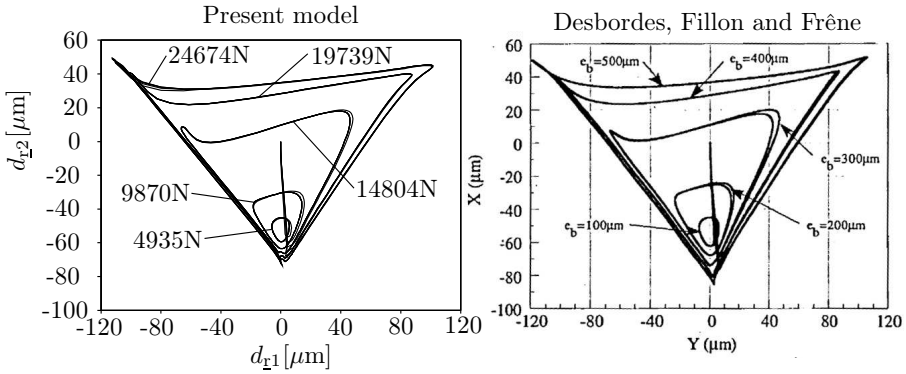


Figure 4.10: Comparison with Desbordes and Fillon [37]. The figure on the right is taken from [37]. The unbalance force amplitude is given as an unbalance eccentricity in the figure from [37], while it is given directly as a force in the present study. The mass of the eccentricity is such that the force amplitudes are identical.

## 4.4 Benchmarking against Allaire, Parsell and Barrett

Allaire, Parsell and Barrett [21] introduced a pad perturbation method with no assumption on pad motion in time. Their model could thus be used for bearing stability analysis. This set their work apart from previous TPJB models. Despite this, they did not present any stability analyses, but proceeded to present curves of bearing coefficients. As mentioned in the theory section, the present model reduces to that of [21] for a passive bearing with rigid pads, i.e., when a single mode reduction (per pad) is used.

The bearing in [21] was a five pad bearing with zero preload and centrally located pivots. Each pad arced 55°. Journal radius was 3.5 inches (88.9mm) with a clearance of 0.0055 inches (139.7$\mu$m) and a length of 4.0 inches (101.6mm). Oil viscosity was $2.03{\cdot}10^{-6}$Reyn (0.0140Ns/m$^2$) and pad inertia was neglected. We adopt the same parameters here, and compute the synchronously reduced bearing coefficients for comparison. As was reported in [21] the two top pads cavitate completely. In [21] results for fixed and non-fixed pivots were presented. The present model corresponds to the fixed pivot case, since the pivots are not allowed to move. This effect disappears when the preload is increased [21]. Figure 4.12 shows curves of the dimensionless synchronously reduced bearing coefficients. A near perfect match with [21] is observed. Figure 4.11 shows the pad modes used for the pseudo modal reduction.

## 4.5 Consistency between time series and frequency domain analyses

A good check of whether the model is consistent or not, is to compare the amplitudes of time series solutions to the predicted amplitudes from a linear frequency domain analysis. For small excitations around the equilibrium state, the the amplitudes should be predicted precisely. Figure 4.13 shows time series solutions as well as predicted amplitudes. The bearing is identical to that of the previous investigations in Fig. 4.5 and 4.6. The static load on the bearing is 2000N in the $x_1$ direction. This produces a rotor displacement of 201$\mu$m. Thus the static equilibrium position corresponds to that of Fig. 4.5. Now the bearing transfer

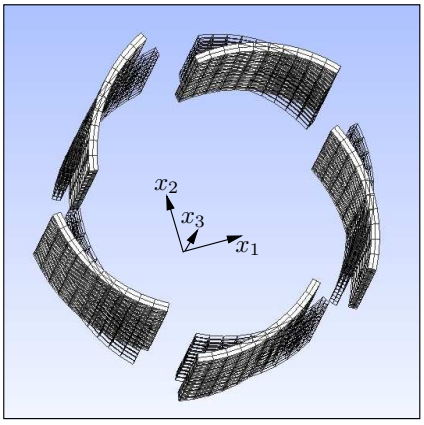


Figure 4.11: The rigid body modes of the bearing pads with wireframes indicating the undisplaced pads.

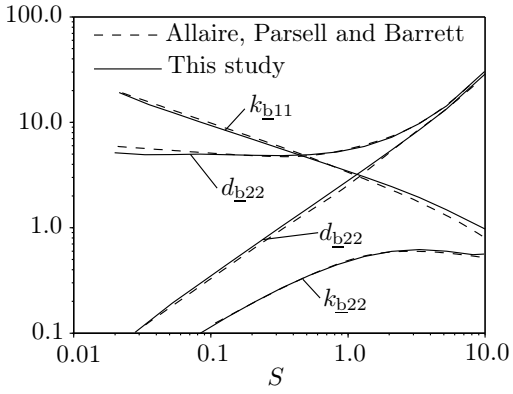


Figure 4.12: Comparison with [21].

function at this equilibrium position is computed, according to the expression in Eq. (2.132). The rotor stiffness and damping are set to zero. The rotor mass is 200kg. Thus, now, for a given harmonic force of known amplitude and excitation frequency, the linear amplitudes of vibration can be determined. Figure 4.13 shows results for a harmonic force amplitudes of 200N and 2000N, respectively. In both cases the frequency of excitation is 100rad/s, i.e., 15.9Hz. That is, the excitation force is given as

$$f_{\underline{r}1} = 2000\text{N} + 200\text{N}\cos(100s^{-1}t), \text{ or } f_{\underline{r}1} = 2000\text{N} + 2000\text{N}\cos(100s^{-1}t)$$
$$f_{\underline{r}2} = 0 \tag{4.3}$$

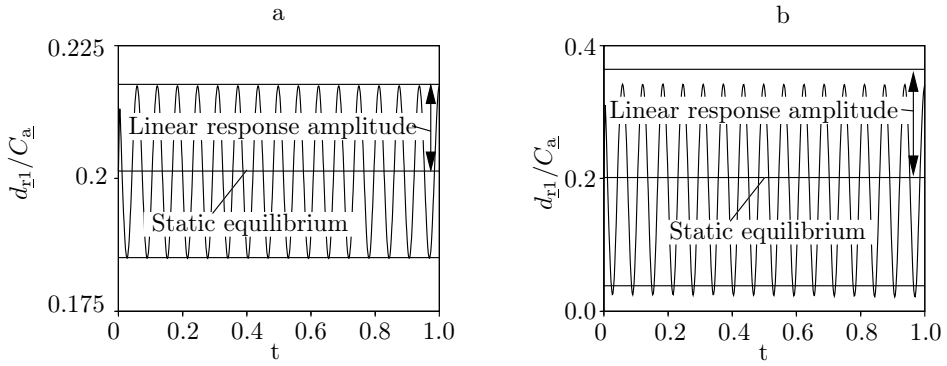


Figure 4.13: Comparison between predicted amplitude and nonlinear time domain solution for rotor position. a: Low excitation force amplitude of 200N. b: High excitation force amplitude of 2000N.

The initial condition for the nonlinear time series computation is that of a system at rest at the static equilibrium position. The low force case shows a near perfect correspondence between the linear

frequency domain amplitude prediction and the amplitude of the nonlinear time series. When comparing the results, it is clear that the low amplitude case produces a very good correlation between the linear frequency domain result and the time domain solution. For the high amplitude case, nonlinear effects have gained influence, and thus the prediction is less accurate.

## 4.6 Benchmarking against Santos

Not much experimental data exists in the literature for ATPJBs of the type under investigation in this thesis. In the 2004 paper by Santos, Nicolletti and Scalabrin [70], experiments were conducted on a ATPJB with 5 orifices per pad. The control system was kept off for 0.5 seconds of operation, and then switched on. The bearing was a four pad bearing with a journal radius of 50.80mm and a pad inner radius of curvature of 50.921mm. The assembled clearance was 76$\mu$m, thus the preload factor was 0.37. The pads were offset pivoted with an offset of 0.6. The pad width was 44.45mm and each orifice had a diameter of 5mm. The radial pivot position was 68.253mm placing them 17.377mm from the pad surface. The lubricant dynamic viscosity was $\mu$ =0.015Ns/m$^2$. The servo-valve had an eigenfrequency of $\omega_{\underline{\mathrm{v}}}$ =320.0Hz, damping ratio $\xi_{\underline{\mathrm{v}}}$ =0.48, static amplification $K_{\underline{\mathrm{v}}}$ =16.7$\cdot 10^{-6}$m$^3$/(sV) and flow-pressure constant $K_{\underline{\mathrm{pq}}}$ =1.13$\cdot 10^{-12}$m$^3$/(sPa). The rotational speed was 650rpm, corresponding to 10.8Hz. When the control system is on, the control gains are $G_{\underline{\mathrm{P}}}$ =62992V/m and $G_{\underline{\mathrm{D}}}$ =314Vs/m. These gains respond to vertical movements of the journal inside the bearing, which is in a load on pad configuration. Turning off the control system corresponds to setting the gains to zero.

To test the mathematical model against the experimental test case, we set the parameters so as to best represent the physical bearing. The concept of leak flow is not considered in [70]. In stead the pressure supply value is given. Here we set the leak flow to $q_{\underline{\mathrm{L}}}$ =6ml/s. In [70] the total rotor mass is not given for the test rig, a value of 20kg is assumed, judging from the test rig photo in [70]. With a gravity of 9.81m/s$^2$, the static bearing load on the bearing becomes 196.2N. Similarly, the diagonal entries of the rotor mass matrix become $m_{\underline{\mathrm{r}}}$ =20kg. Now, considering the load on pad configuration with pad # 4 as the loaded pad, this corresponds to a static load in the $x_1$ direction of 138.7N and in the $x_2$ direction of -138.7N. For the pads, the two-mode pseudo modal reduction is employed. The modes are shown in Fig. 4.14, which also depicts the used mesh and the orifice arrangement. The orifice configuration is not explicitly defined in [70], i.e., a detailed drawing is not provided. However, it is clear that the arrangement consists of a central orifice and orifices in each corner, totalling five orifices. Here we adopt an arrangement with one orifice in the centre of the pad, and corner orifices at $\underline{+}25^\circ$ and $\underline{+}15$mm from the pad centreline and bearing plane of symmetry, respectively. Each pad consists of 1158 nodes and 182 solid elements.

Figure 4.15 shows a comparison between the experimentally obtained rotor motion [70] and the computed one. In both cases the control system is turned on after 0.5 seconds of passive hybrid lubrication. The value of the excitation force amplitude is unknown, so the comparison serves only to evaluate the relative drop in the vibration amplitude after the control system is turned on. The curve in Fig. 4.15a is obtained by applying a synchronous excitation with a magnitude of 1000N, and a frequency of 18Hz i.e,

$$f_{\underline{\mathrm{r}}1} = 138.7\mathrm{N} + 1000\mathrm{N}\cos(113.1s^{-1}t) \tag{4.4}$$

$$f_{\underline{\mathrm{r}}2} = -138.7\mathrm{N} + 1000\mathrm{N}\sin(113.1s^{-1}t) \tag{4.5}$$

The frequency was chosen to match the dominant frequency in the results from [70], although it is evident that more frequencies are present in the experimentally obtained plot in [70].

As seen from the comparison, there is a fair correspondence between the experimental curve and the

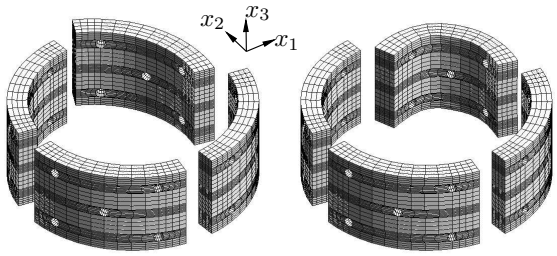


Figure 4.14: Bearing mesh, with indication of modes used for pseudo modal reduction.

computed one. The computation is stopped after 1 second of operation, since the transient has been damped out at that stage.

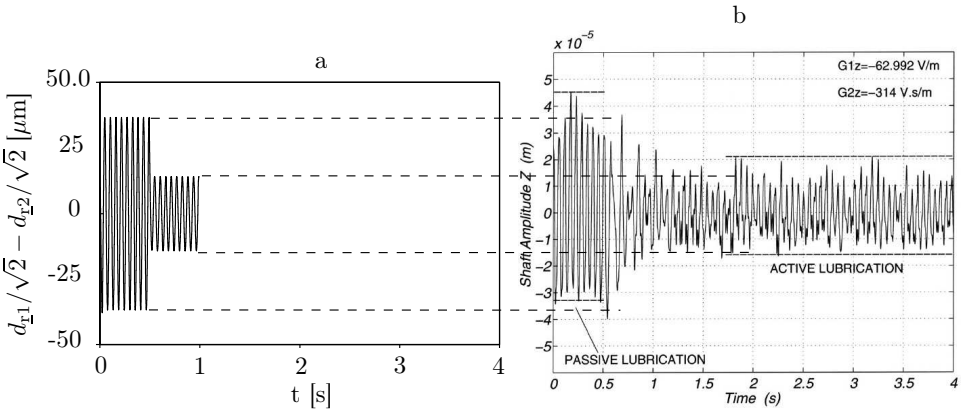


Figure 4.15: Journal vibration in the loaded direction. a: Computed. b: Experimental (figure taken from [70]). Zero is defined as the static equilibrium position.

# Chapter 5

# Selected results

In this chapter, analyses for selected bearing parameters shall be presented. The analyses complement, and in some cases, are identical to analyses from the papers by Haugaard and Santos [2, 3, 4]. Results from both nonlinear time domain analyses and linear frequency domain analyses are shown. While the bearing parameters generally vary from case to case, the fundamental bearing design and pad geometry remains the same and is described in the following section.

## 5.1 The bearing

In the present investigation, focus shall lie on four-pad TPJBs. Analyses for passive, hybrid, and active bearings shall be presented. In the case of hybrid and active bearings, two servo-valves are connected to a bearing. They couple the pads in pairs of master and slave. A sketch of such a configuration is shown in Fig. 5.1. The bearing to be analysed is a four pad bearing designed by Bo Bjerregaard Nielsen at the Technical University of Denmark. A simplified version of his design is adopted for numerical simulation. A single pad of the simplified design is sketched in Fig. 5.2.

The way the regulator is implemented is to connect the pads in pairs with servo-valves. Pad #1 is connected to pad #3 with a servo-valve. Also, pad #4 is connected to pad #2 with a servo-valve. Pads #1 and #4 are chosen as master pads, with pads #3 and #2 as their respective slave counterparts. Both servo-valves respond to rotor movement in the $x_1$ direction and $x_2$ direction. The software written for the bearing analysis takes a vector as input, so as to define what direction of rotor movement, that each servo-valve shall respond to. This vector is normalised inside the program. Here, we set the first valve to respond to (1,1) and the second valve to respond to (1,-1). Thus, after normalisation, the two servo-valve signals are computed as

$$u_{\underline{\mathrm{v}}1} = G_{\underline{\mathrm{D}}}(\dot{d}_{\underline{\mathrm{r}}1} + \dot{d}_{\underline{\mathrm{r}}2})/\sqrt{2} + G_{\underline{\mathrm{P}}}(d_{\underline{\mathrm{r}}1} + d_{\underline{\mathrm{r}}2})/\sqrt{2} \tag{5.1}$$

$$u_{\underline{\mathrm{v}}2} = G_{\underline{\mathrm{D}}}(\dot{d}_{\underline{\mathrm{r}}1} - \dot{d}_{\underline{\mathrm{r}}2})/\sqrt{2} + G_{\underline{\mathrm{P}}}(d_{\underline{\mathrm{r}}1} - d_{\underline{\mathrm{r}}2})/\sqrt{2} \tag{5.2}$$

where $G_{\underline{\mathrm{D}}}$ is the derivative gain and $G_{\underline{\mathrm{P}}}$ is the proportional gain. This makes for an active bearing which still almost decouples the $x_1$ and $x_2$ coordinate directions, just as a passive tilting-pad journal bearing. An explanation of why this is the case is given in [3, 4].

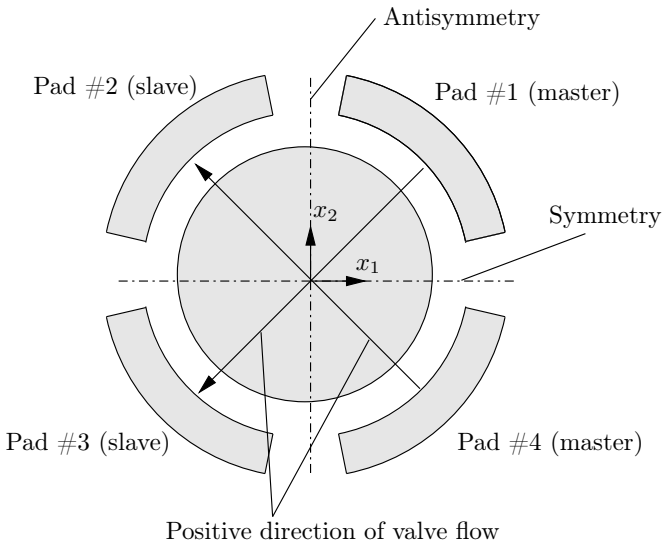


Figure 5.1: Schematic of a bearing showing the coordinate system, pad numbering and valve orientation. Figure taken from [3].

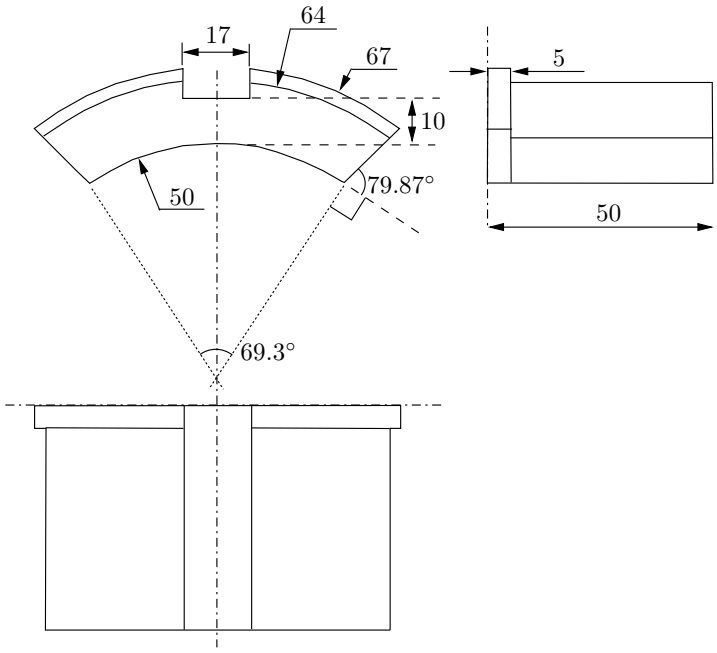


Figure 5.2: Detailed sketch of a pad with indication of dimensions in mm. The pad is for a passive bearing with no orifices. Note that only half of the pad is sketched due to symmetry.

The preload factor is well known in the tribology community, and is an important bearing parameter since it describes the unloaded oil film shape. It is defined as

$$m_{\underline{\mathrm{p}}} = 1 - \frac{C_{\underline{\mathrm{a}}}}{C_{\underline{\mathrm{m}}}} \tag{5.3}$$

where $C_{\underline{\mathrm{a}}}$ is the assembled clearance of the bearing, and $C_{\underline{\mathrm{m}}}$ is the machined clearance, defined as

$$C_{\underline{\mathrm{m}}} = R_{\underline{\mathrm{p}}} - R_{\underline{\mathrm{r}}} \tag{5.4}$$

$R_{\underline{\mathrm{r}}}$ is the radius of curvature of the rotor and $R_{\underline{\mathrm{p}}}$ is the radius of curvature of the inner pad surface. These geometrical measures are depicted in Fig. 5.3.

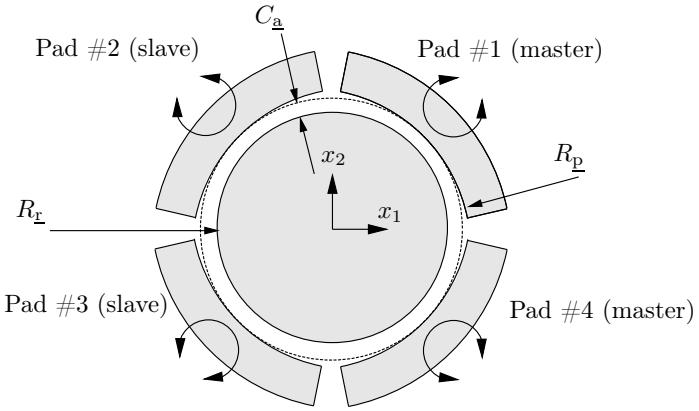


Figure 5.3: Schematic showing key geometric features of the bearing. Figure taken from [4].

Several combinations of parameters shall be investigated. The nominal bearing and servo-valve parameters are given in Tab. 5.1 and Tab. 5.2, respectively. Unless otherwise stated, these parameters apply.

Simulations will be run at a range of rotational speeds. For the model to remain valid, the rotational speed must be low enough to ensure that the onset of turbulence in the lubricant is not reached. For flow between parallel plates, the Reynolds number may be defined as [67]

$$Re = \frac{\rho U C_{\underline{\mathrm{m}}}}{\mu} \tag{5.5}$$

The expression in Eq. (5.5) is pessimistic, since $C_{\underline{\mathrm{m}}}$ is larger than the maximum oil film thickness (at rest) and $U$ is very likely to be larger than the average lubricant velocity, which is the characteristic velocity used in [67]. Hydraway HVXA 22 oil has a dynamic viscosity of 0.019 Ns/m$^2$s at 38.5°C and a density of 860kg/m$^3$ at 15°C, which is taken to apply to the 38.5°C case. The critical reynolds number is 1400 [67]. Thus with the parameters in Tab. 5.1, the limit tangential speed is $U = 309$m/s, corresponding to $\Omega = 6186$Hz. We shall stay far below this limit in all simulations. Furthermore, the limit speed in terms of thermal effects is expected to be much lower. Thermal effects will be discussed in section 5.7. As stated

in Hamrocks book [66], one can also define the modified Reynolds number

$$Re = \frac{\rho U C_{\underline{\mathrm{m}}}^2}{\mu \pi D_{\underline{\mathrm{r}}}} \tag{5.6}$$

Hamrock [66] recommends the limiting value of the modified Reynolds to be unity. With the given parameters, this results in a limiting rotational speed of $\Omega = 1105$Hz. Again, since $C_{\underline{\mathrm{m}}}$ is larger than the maximum oil film thickness (at rest), this is a pessimistic limiting value.

Table 5.1: Bearing data.

| Property | Unit | Value(s) |
|---|---|---|
| Pad radius of curvature | mm | 50 |
| Rotor radius | mm | 49.9 |
| Rotor mass | Kg | 200.0 |
| Static radial load | N | 0.0 |
| Pad extension | ° | 69.3 |
| Angular pivot locations | ° | 45, 135, 225 and 315 (at pad centres) |
| Radial pivot location | mm | 64 |
| Pad length | mm | 100 |
| Nominal pad thickness | mm | 14 |
| Pad Young's modulus | GPa | 100.0 |
| Pad Poisson's ratio | - | 0.3 |
| Pad density | $\mathrm{Kg/m^3}$ | 8400 |
| Lubricant dynamic viscosity | $\mathrm{Ns/m^2}$ | 0.019 |
| Preload factor | - | 0.5 |

Table 5.2: Servo-valve data.

| Property | Unit | Value(s) |
|---|---|---|
| Valve flow-pressure coefficient | $\mathrm{m^3/(sPa)}$ | $1.13{\cdot}10^{-12}$ |
| Valve flow-voltage coefficient | $\mathrm{m^3/(sV)}$ | $33.4{\cdot}10^{-6}$ |
| Valve damping ratio | - | 0.48 |
| Valve eigenfrequency | Hz | 320.16 |
| Valve leak flow | $\mathrm{m^3/s}$ | $6{\cdot}10^{-6}$ |
| Valve inlet length | m | 1.0 |

A pseudo modal reduction is implemented as described in section 2.8. Some of the results in this thesis will make use of a four-mode (per pad) reduction, while some will make use of a two-mode reduction. In this authors experience, for all practical purposes, the extra precision from a four mode reduction is negligible. Thus, results for two-mode reductions may be compared to those of four-mode reductions and vice versa. Figure 5.4 shows the first four modes of pad deformation. Also, from this figure, the pad design can be seen. The pad in Fig. 5.4 has six orifices with placement corresponding to configuration # 3 in [3]. The modes are largely independent of the orifice configuration, hence the ones shown in Fig. 5.4 shall be used for all orifice configurations. The used mesh consists of 3905 nodes per pad and 686 elements per pad and exploits symmetry. The image in Fig. 5.4 depicts two times the number of nodes and elements

since the whole pad is shown. I.e. 7810 nodes and 1372 elements. Note that the post-processing program connects all mid-nodes with lines.

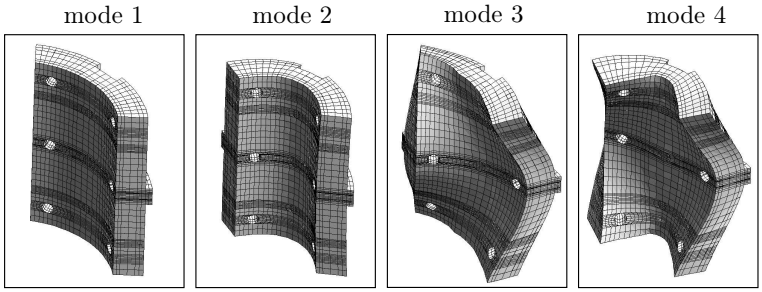


Figure 5.4: The first four pad mode shapes. The first modeshape is a rigid body modeshape consisting of pure pad pivoting. The shown orifice configuration corresponds to the six-orifice configuration described in [3]. A variation of this figure also appears in [3].

## 5.2 Stability

As explained in section 2.11, the local rotor-bearing stability is assessed by evaluation of the largest real part of any system eigenvalue. If any real part is larger than zero, the rotor-bearing system is unstable. A map of stable gain selections can be produced by computing the eigenvalues for a large number of combinations of gain. That is, the computations create a mesh in the gain plane. This mesh is then used to create isolines. The isoline corresponding to the largest real part equal to zero defines the threshold of stability. After each computation, the largest real part of any eigenvalue is investigated. If it is below zero, the rotor-bearing system is stable. In the following, we shall see that the stable domain depends on bearing operating conditions.

In all the analyses in this section, the lubricant viscosity is $0.019\text{Ns}/\text{m}^2$, the bearing length and diameter are both 0.1m, the static load is zero, the rotor structural damping and stiffness are zero, the servo-valve leak flow is $6.0 \cdot 10^{-6}\text{m}^3/\text{s}$, the flow-voltage coefficient is $16.7 \cdot 10^{-6}\text{m}^3/(\text{sV})$, the flow-pressure coefficient is $1.13 \cdot 10^{-12}\text{m}^5/(\text{sN})$, the orifice inlet length is 1.0m, the pad elastic modulus is 100GPa and the Poisson ratio is 0.3. The two first mode shapes are included for each pad. There are four injection orifices on each pad, corresponding to configuration #2 in [3]. Figure 5.5 shows stability thresholds for pseudo modal reductions using one through four modes for each pad. Clearly, convergence has been reached with the two-mode reduction. Thus henceforth the two-mode reduction is utilised.

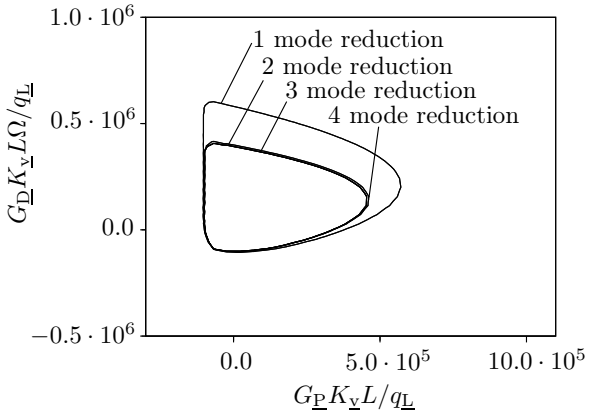


Figure 5.5: Comparison of stable domains in the gain-plane for pseudo modal reductions of one to four modes. The rotational speed is $\Omega = 100\text{Hz}$, rotor mass is $m_{\underline{\text{r}}} = 200\text{kg}$ and assembled clearance is $C_{\underline{\text{a}}} = 75\mu\text{m}$ corresponding to a preload factor of 0.25.

Figures 5.6-5.17 show stable domains in the gain-plane. That is, domains where the rotor-bearing system is stable. These domains are shaded. The results in Figs. 5.14 and 5.15 are also found in [4]. In addition to the curve of marginal stability, there are curves where the maximum real part of any eigenvalue is equal to $0.1\Omega$ (outside the stable domain) and $-0.1\Omega$ (inside the stable domain). The distance between the curve of marginal stability, and these curves, gives an impression of the bearings sensitivity to changes in the gains. The closer the curves are, the more significant is the influence of changes in gains on the rotor-bearing stability. The point where the gains are both zero is where the dotted lines cross. This point indicates the passive hybrid bearing - or open loop controlled bearing.

Figures 5.6 and 5.7 show stable domains for a 200kg rotor, with a rotational speed of 25Hz. The

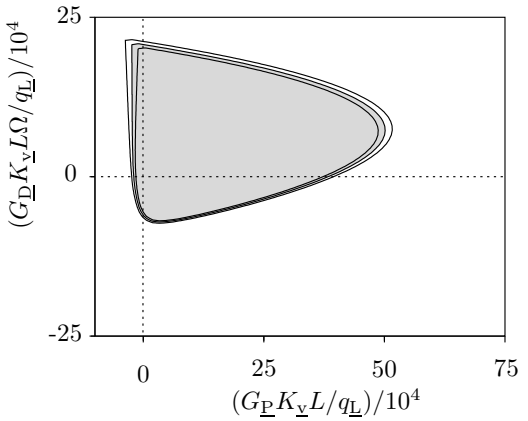


Figure 5.6: The stable domain in the gain plane for $\Omega = 25$Hz, $m_{\underline{r}} = 200$kg and $C_{\underline{a}} = 75\mu$m corresponding to a preload factor of 0.25.

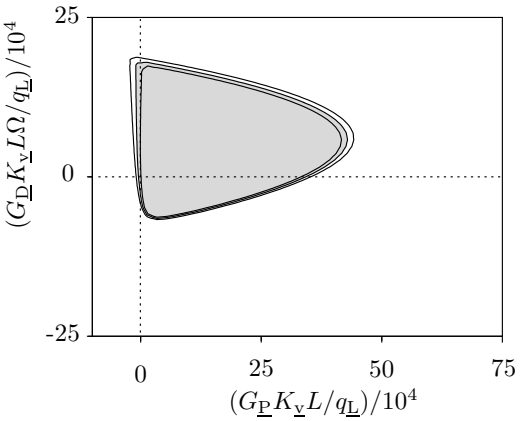


Figure 5.7: The stable domain in the gain plane for $\Omega = 25$Hz, $m_{\underline{r}} = 200$kg and $C_{\underline{a}} = 95\mu$m corresponding to a preload factor of 0.05.

preload is 0.05 and 0.25 for Figs. 5.6 and 5.7, respectively. Comparing Fig. 5.6 to Fig. 5.7, i.e., the effect of reducing preload, we immediately identify a modest decrease in the size of the stable domain. Also, the lower bound on the proportional gain moves quite close to zero, thus limiting the use of negative proportional gains. The lower bound on the proportional gain is almost constant, while the upper bound depends on the derivative gain.

Figures 5.8 and 5.9 show stable domains for a 2000kg rotor, with a rotational speed of 25Hz. The preload is 0.05 and 0.25 for Figs. 5.8 and 5.9, respectively. With the larger rotor mass, the effect of reducing the preload is much more substantial, as the stable domain grows much more than in the lighter rotor case. On the other hand, the lower bound on the proportional gain seems to be only modestly affected by the preload decrease. For both the light rotor and heavy rotor cases at 25Hz (Figs.5.6 through 5.9), the lower left corner of the stable domain seems to be insensitive to changes in preload.

Figures 5.10 and 5.11 show stable domains for a 200kg rotor, with a rotational speed of 50Hz. The preload is 0.05 and 0.25 for Figs. 5.10 and 5.11, respectively. The first thing we notice, is that the higher rotational speed has had the effect of rounding off the lower left corner of the stable domain, where it was relatively sharply defined for the lower speed. The increased rotational speed increases the bearings tolerance to negative proportional gains, as the stronger hydrodynamic effects will keep the bearing stable. Decreasing the preload factor from 0.25 (Fig. 5.10) to 0.05 (Fig. 5.11) causes the lower left corner of the stable domain to move close to the origin. Thus, the passive hybrid bearing is close to being unstable. On the other hand, the size of the stable domain is largely unaffected by the reduced preload.

Figures 5.12 and 5.13 show stable domains for a 2000kg rotor, with a rotational speed of 50Hz. The preload is 0.05 and 0.25 for Figs. 5.12 and 5.13, respectively. Consider Fig. 5.13. The low preload and absence of eccentricity have made the passive hybrid bearing unstable. That is, this bearing under the given operating conditions needs a control system to remain stable. Apart from this observation, Figs. 5.12 and 5.13 demonstrate tendencies that are similar to what we have seen previously; the reduction of preload increases the stable domain of gains with the effect being most evident in the upper bound of

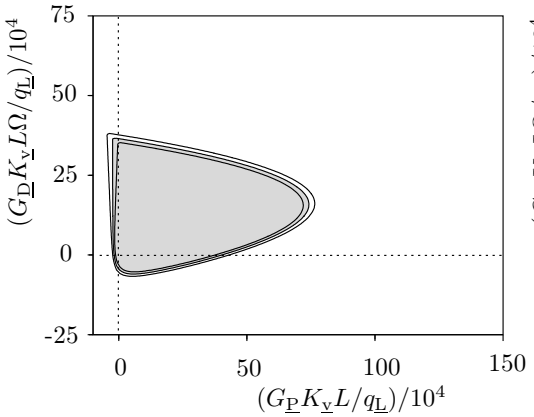


Figure 5.8: The stable domain in the gain plane for $\Omega = 25$Hz, $m_{\underline{r}} = 2000$kg and $C_{\underline{a}} = 75\mu$m corresponding to a preload factor of 0.25.

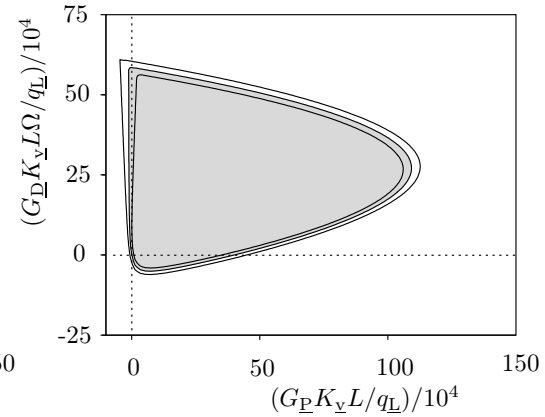


Figure 5.9: The stable domain in the gain plane for $\Omega = 25$Hz, $m_{\underline{r}} = 2000$kg and $C_{\underline{a}} = 95\mu$m corresponding to a preload factor of 0.05.

proportional and derivative gains.

Now, let us compare Fig. 5.14 to Fig. 5.15. That is, let us compare a situation with a moderate preload factor of 0.25 to a situation with a very small preload factor of 0.05. In both cases the rotational speed is 100Hz and the rotor mass is 200kg. At this rotational speed, the reduction in preload has the effect of curving the lower left corner of the stable domain. While the lower bound on the proportional gain tends to be a straight vertical line in the moderate preload case, it curves in the gain plane in the low preload case. A comparison between Figs. 5.16 and Fig. 5.17 reveals a similar conclusion. In both figures, the rotor mass is 2000kg. However here, additionally, the magnitude of the stable domain increases with the preload reduction, as was seen before. Also, the reduction in preload has made the passive hybrid bearing unstable, so that non-zero gains must be chosen to produce a stable bearing. Also note, that in addition to the large stable domain, a small stable island has appeared to the south west in fig. 5.16. However, for all practical purposes, this island should be ignored because of its small size.

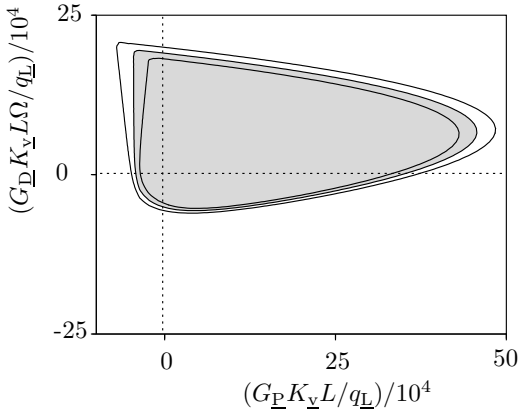


Figure 5.10: The stable domain in the gain plane for $\Omega = 50$Hz, $m_{\underline{\mathrm{r}}} = 200$kg and $C_{\underline{\mathrm{a}}} = 75\mu$m corresponding to a preload factor of 0.25.

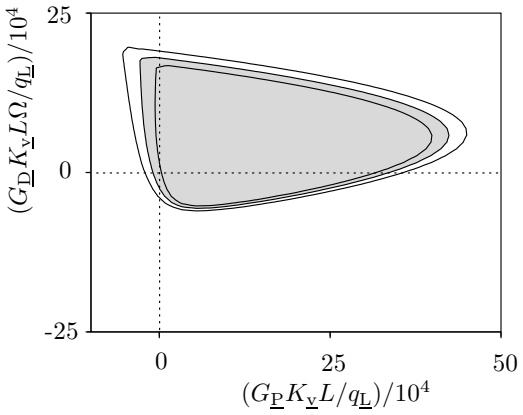


Figure 5.11: The stable domain in the gain plane for $\Omega = 50$Hz, $m_{\underline{\mathrm{r}}} = 200$kg and $C_{\underline{\mathrm{a}}} = 95\mu$m corresponding to a preload factor of 0.05.

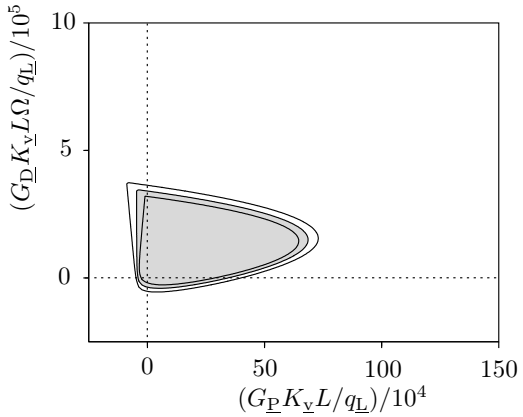


Figure 5.12: The stable domain in the gain plane for $\Omega = 50$Hz, $m_{\underline{\mathrm{r}}} = 2000$kg and $C_{\underline{\mathrm{a}}} = 75\mu$m corresponding to a preload factor of 0.25.

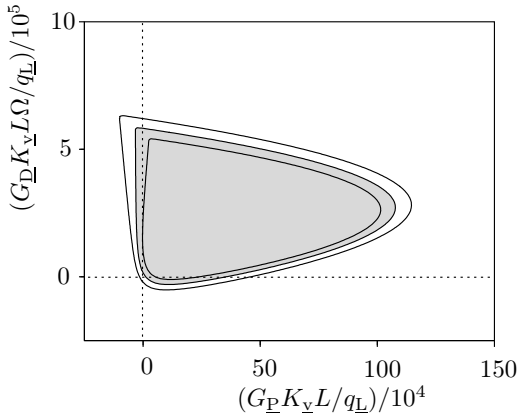


Figure 5.13: The stable domain in the gain plane for $\Omega = 50$Hz, $m_{\underline{\mathrm{r}}} = 2000$kg and $C_{\underline{\mathrm{a}}} = 95\mu$m corresponding to a preload factor of 0.05.

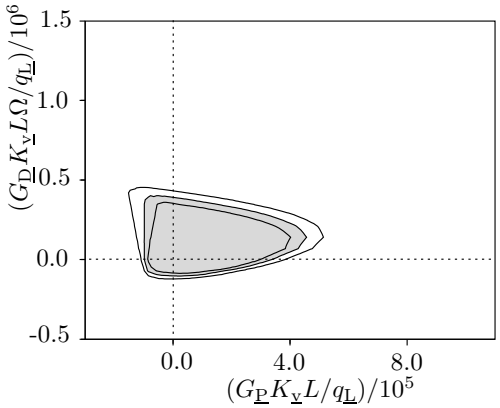


Figure 5.14: The stable domain in the gain plane for $\Omega = 100$Hz, $m_{\underline{\mathrm{r}}} = 200$kg and $C_{\underline{\mathrm{a}}} = 75\mu$m corresponding to a preload factor of 0.25.

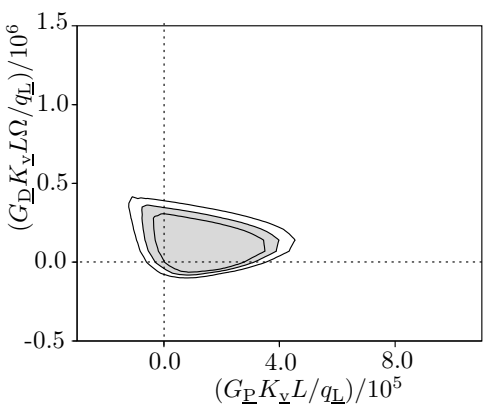


Figure 5.15: The stable domain in the gain plane for $\Omega = 100$Hz, $m_{\underline{\mathrm{r}}} = 200$kg and $C_{\underline{\mathrm{a}}} = 95\mu$m corresponding to a preload factor of 0.05.

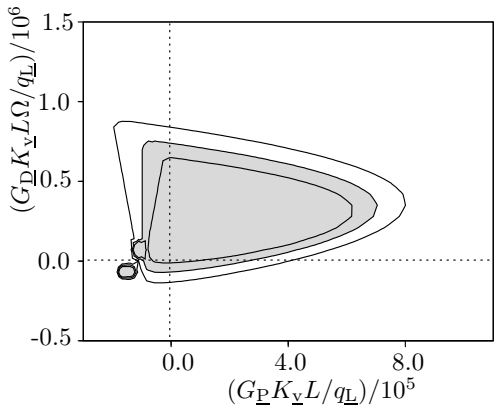


Figure 5.16: The stable domain in the gain plane for $\Omega = 100$Hz, $m_{\underline{\mathrm{r}}} = 2000$kg and $C_{\underline{\mathrm{a}}} = 75\mu$m corresponding to a preload factor of 0.25.

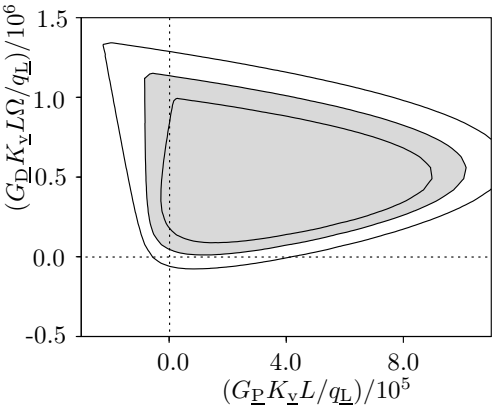


Figure 5.17: The stable domain in the gain plane for $\Omega = 100$Hz, $m_{\underline{\mathrm{r}}} = 2000$kg and $C_{\underline{\mathrm{a}}} = 95\mu$m corresponding to a preload factor of 0.05.

## 5.3 Dimensional analysis

The dimensionless numbers derived in chapter 3 are useful in several ways. Firstly, they provide experimentalists with information on how to interpret and scale experimental data to full size bearings. Secondly, they provide insight into the relative importance of phenomena. Potentially, they aid the analyst in neglecting certain effects, thus simplifying the modelling procedure and shortening analysis time. This shall be the focus in the following where the critical value of the hydroelastic number is determined for a passive bearing.

### 5.3.1 The hydroelastic number

Consider the hydroelastic number which was defined in Eq. 3.10. Let us restate it here

$$H = \frac{E}{\mu\Omega}$$

Now, let us conduct a parameter study, where $H$ is varied for all other parameters (dimensionless numbers) kept constant. At a critical value of $H$, we expect the effect of pad compliance to virtually disappear. The critical value will depend on the specific bearing design. That is, it will depend on the other dimensionless numbers, as well as the bearing geometric proportions. But the skilled engineer will be able to apply knowledge of critical $H$ value across different designs. The bearing inner radius of curvature is 0.0499m and the machined clearance is 100$\mu$m with a preload factor of 0.5 and pivots placed centrally on the pads at a radial distance of 70mm from the bearing centre. Pad thickness is 10mm and the length to diameter ratio is 1. The pad Poisson ratio is 0.3. Lubricant viscosity is 0.019Ns/m$^2$. The journal rotates at 100Hz and is assigned a mass of 400kg with zero rotor stiffness. The bearing is shown in Fig. 5.18 along with the first four modes of one of the pads.

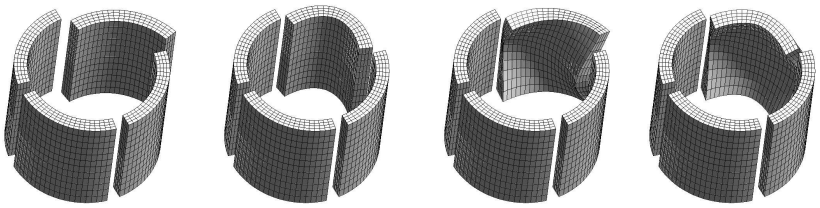

Figure 5.18: The bearing with the first four modes of one pad shown.

We employ the set of dimensionless numbers in Eq. (3.22) and use the lateral rotor load as the characteristic force $F$ and the journal diameter as the characteristic length $L$. The lateral load on the rotor is set to zero to begin with. We thus have

$$\frac{k_{\underline{r}}}{L\mu\Omega} = 0 \qquad \frac{F}{L\mu\Omega} = 0 \quad (S = \infty) \qquad \frac{\rho L^2\Omega}{\mu} = 277 \cdot 10^4 \qquad \frac{\Omega m_{\underline{r}}}{L\mu} = 132 \cdot 10^6 \qquad \frac{c_{\underline{r}}}{L\mu} = 0 \qquad (5.7)$$

Now, we vary the hydroelastic number. For each value, we solve for the static equilibrium and then for the eigenvalues. This is done for a four mode (per pad) pseudo modal reduction. When the eigenvalues converge to those of the corresponding one mode (per pad) pseudo modal reduction, i.e., the rigid body

model, the critical value of the hydroelastic number has been reached. For values of $H$ above the critical value, pad deformation may be neglected. Figures 5.19 and 5.20 show the system eigenvalues for values of

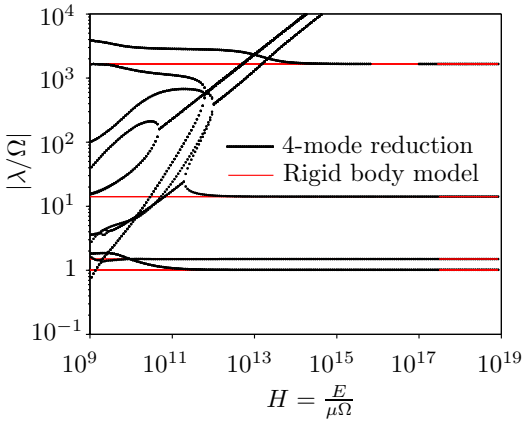


Figure 5.19: Magnitude of system eigenvalues for varying $H$ and no lateral bearing load.

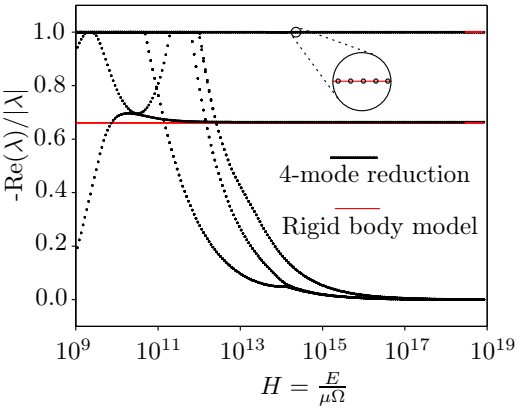


Figure 5.20: Normalised real part (modal damping ratio) of system eigenvalues for varying $H$ and no lateral bearing load.

the hydroelastic number across ten orders of magnitude. It is observed that some eigenvalues converge to those of the rigid body model, while the magnitudes of others diverge and go to infinity. This reflects that as the pads become stiffer certain modes will begin to resemble those of the pure rigid body model, while those containing pad deformation will become faster due to the stiffer pads. In other words, the very high frequency behaviour will never be captured by the rigid body model. However, the very high frequency behaviour is hardly relevant to the bearing designer. Thus, the loss of information from replacing a flexible pad model with a rigid pad model is irrelevant for high enough $H$. Note that the order of the system of equations for a four mode pseudo modal reduction of a passive bearing is 18×18, since there are four pseudo modes for each pad and the rotor has two degrees of freedom. Thus there are 36 solutions to the characteristic polynomial (second order eigenvalue problem). From looking at Figs. 5.19 and 5.20 we observe ten distinct eigenvalues for low values of $H$. Thus one or more of the eigenvalues have algebraic multiplicity larger than unity. Some simple observations can explain this. The bearing consists of four identical pads, and the rotor is centred in the bearing. Thus, for symmetry reasons, all the pads move in the same way through time, and the rotor motion in the $x_1$ and $x_2$ directions must be identical. Since we have four pads, and each pad contributes with four (second order) equations, there are eight eigenvalues with algebraic multiplicity of four. The rotor contributes with two (second order) equations, resulting in two eigenvalue with algebraic multiplicity of two. This amounts to ten distinct eigenvalues. Considering Fig. 5.20, it appears that the argument of some eigenvalues goes zero for increasing $H$, leading us to suspect that the system is becoming critically damped. However, this is merely the effect of an increasing imaginary part for an almost constant (negative) real part. That is, some modes are becoming faster, but their ability to dissipate energy is largely unaltered. Investigation of the real/imaginary parts of the eigenvalues has confirmed this.

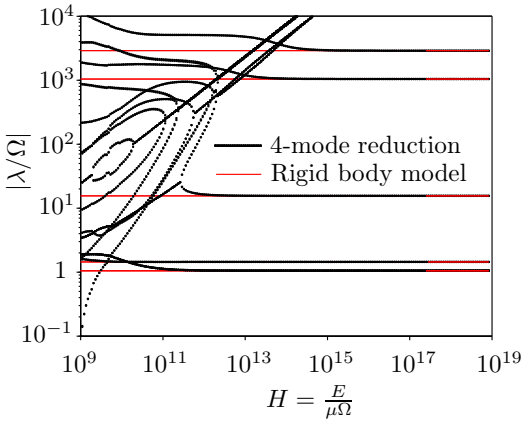


Figure 5.21: Magnitude of system eigenvalues for varying $H$ and a lateral bearing load of 20000N.

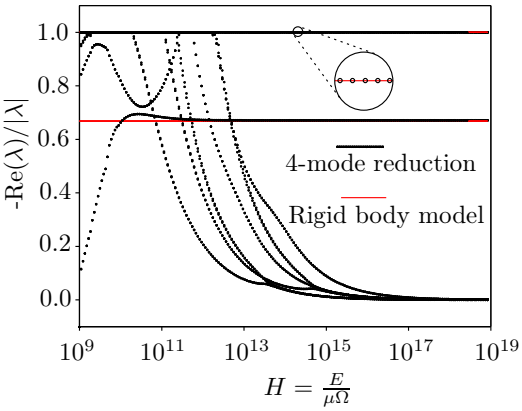


Figure 5.22: Normalised real part (modal damping ratio) of system eigenvalues for varying $H$ and a lateral bearing load of 20000N.

We now repeat the analysis for a static lateral load of 20000N. Thus now

$$\frac{F}{L\mu\Omega} = 8377 \quad (S = 0.238) \tag{5.8}$$

While the rest of the dimensionless numbers are as in the previous analysis. Figures 5.21 and 5.22 show the system eigenvalues. Again, the range of $H$ is ten orders of magnitude. The first thing we notice when observing the figures is that some of the symmetry is lost, since the rotor is not centred in the bearing. Thus, we have more distinct eigenvalues than for the unloaded case. Apart from this, Figs. 5.21 and 5.22 resemble Figs. 5.19 and 5.20. In fact, it seems that the critical value of $H$ is not significantly influenced by the bearing load. This is good news, since it allows us to define a critical $H$ independently of the bearing operating condition, albeit only for this bearing design. In both the loaded and unloaded case, for $\lambda/\Omega < 10$, the eigenvalues converge for $H > 2 \cdot 10^{11}$. For the given rotational speed (100Hz), and viscosity (0.019Ns/m$^2$), this means that the requirement is for the pads to have a minimum elastic modulus of roughly $E = 2000$GPa, which is far beyond the elastic modulus of conventional materials. Thus, for this bearing design at given rotational speed, the pad deformation should be included. A steel pad ($E = 210$GPa) would result in $H = 1.76 \cdot 10^10$. It has been shown before that pad deformation is an important effect for realistic bearing parameters, for instance in [37, 36, 2, 3, 4].

### 5.3.2 Similitude

In the following, the usefulness and relevance of similitude is illustrated. Imagine that we are designing a large bearing for an industrial application. For example for a hydropowerplant. Shaft diameters for such applications can reach 1 meter and beyond. For machines of this magnitude, producing a prototype is prohibitively expensive. Furthermore, if a prototype is manufactured, it can be very challenging to subject it to operating conditions and loads of sufficient severity to test its performance. E.g., how would

one replicate the load of thousands of cubic meters of water per hour powering the turbine? One solution could be to rely entirely on computer simulations to predict the behaviour of the real system. This is obviously not recommended, since no mathematical model can completely capture all relevant effects. If experimental data is desired, but the costs of building a prototype are too high, a scaled down experimental test rig is a good compromise. However, if this test rig is to behave like the real system, care must be taken in its design to ensure similitude. Clearly, it is paramount to run the two systems at identical Sommerfeld numbers but, as we shall see, other dimensionless numbers are relevant.

Let us investigate the similitude of active bearings under dynamic conditions. Consider a design requirement for a large bearing with two servo-valves attached for control. The active bearing has an orifice configuration corresponding to the four-orifice configuration described in [3]. The journal diameter is 0.999m and the machined clearance is 1mm. The pads are preloaded to a preload factor of 0.25. The static load on the journal is 20kN in the $x_1$ direction. The lubricant is quite viscous at 0.19Ns/m$^2$. The journal rotates at 15.915Hz or 100s$^{-1}$. The pad material has elastic modulus 100GPa and Poisson ratio 0.3. Rotor structural stiffness and damping are neglected. Rotor mass is 200 metric tons. The servo-valve is underlapped, and leaks lubricant at a rate of $6.0{\cdot}10^{-4}$m$^3$/s or 600ml per second. The linear valve flow-pressure constant is $1.13 \cdot 10^{-10}$m$^5$/sN or $11.3\frac{\text{ml/s}}{\text{atm}}$. In other words the valve will yield a considerable flow, for a relatively low pressure (it is a big valve). The linear flow-voltage coefficient is $33.4{\cdot}10^{-4}$m$^3$/(sV). Thus, in the hypothetical situation of zero impedance, a signal voltage of 1V would correspond to a flow of 3340ml per second. We set the proportional gain to 10000V/m or 10V/mm, thus the maximum theoretical voltage from a static load on pad deflection of the journal would be 7.5V, corresponding to the assembled clearance. The derivative gain is set to 500Vs/m or 0.5Vs/mm. Thus, for zero proportional gain, a synchronous journal vibration of 0.75mm amplitude, corresponding to the machined clearance, at 100s$^{-1}$ would produce a maximum voltage of 37.5V. The servo-valve eigenfrequency is 32.016Hz. Since the reference signal is zero we eliminate it as described in section 3.2. We now seek to represent this large bearing with a smaller bearing, thus paving the way for experiment planning. There are many ways to scale down the large bearing to a smaller test-rig, while obeying the rules of similitude. An option is the following

- Use same pad material.
- Decrease characteristic length by factor of 10.
- Reduce static load by factor of 100.
- Reduce lubricant viscosity by factor of 10.
- Increase rotational speed by factor of 10.
- Reduce rotor mass by factor of 1000.
- Reduce linear valve flow-pressure constant by factor of 100 (smaller valve).
- Increase valve eigenfrequency by factor of 10 (smaller valve).
- Decrease valve leak flow by factor of 100 (smaller valve).
- Decrease valve inlet length by factor of 10 (smaller valve).
- Reduce static amplification by factor of 100.
- Increase proportional gain by factor of 10.
- Leave derivative gain unaltered.

Table 5.3 shows parameters for the big bearing (case #1) as well as two smaller bearings (cases #2 and #3). While case #2 is similar to the large bearing, case #3 is not, since we have not adjusted the proportional gain according to the rules of similitude. This is a very likely mistake to make. Since the derivative gain should not be changed, it is easy to make the (wrong) assumption that the same holds for

the proportional gain. In other words, the problem is that

$$\frac{G_{\underline{\mathrm{P}}3} L_3 K_{\underline{\mathrm{v}}3}}{q_{\underline{\mathrm{L}}3}} \neq \frac{G_{\underline{\mathrm{P}}1} L_1 K_{\underline{\mathrm{v}}1}}{q_{\underline{\mathrm{L}}1}} \tag{5.9}$$

Table 5.3: Bearings parameters. Cases #1 and #2 are similar. Case #3 is not similar to the other two, since its proportional gain has not been adjusted.

| | case | #1 | #2 | #3 |
|---|---|---|---|---|
| $E$ | [GPa] | 100 | 100 | 100 |
| $L$ | [m] | 1 | 0.1 | 0.1 |
| $F$ | [kN] | 20 | 0.2 | 0.2 |
| $k_{\underline{\mathrm{r}}}$ | [N/m] | 0 | 0 | 0 |
| $\mu$ | [Ns/m$^2$] | 0.19 | 0.019 | 0.019 |
| $\Omega$ | [Hz] | 15.915 | 159.15 | 159.15 |
| $\rho$ | [kg/m$^3$] | 8400 | 8400 | 8400 |
| $m_{\underline{\mathrm{r}}}$ | [kg] | 200000 | 200 | 200 |
| $c_{\underline{\mathrm{r}}}$ | [Ns/m] | 0 | 0 | 0 |
| $k_{\underline{\mathrm{pq}}}$ | [m$^5$/(sN)] | $1.13 \cdot 10^{-10}$ | $1.13 \cdot 10^{-12}$ | $1.13 \cdot 10^{-12}$ |
| $k_{\underline{\mathrm{v}}}$ | [m$^3$/(sV)] | $33.4 \cdot 10^{-4}$ | $33.4 \cdot 10^{-6}$ | $33.4 \cdot 10^{-6}$ |
| $\xi_{\underline{\mathrm{v}}}$ | – | 0.48 | 0.48 | 0.48 |
| $\omega_{\underline{\mathrm{v}}}$ | [Hz] | 32.016 | 320.16 | 320.16 |
| $q_{\underline{\mathrm{L}}}$ | [m$^3$/s] | $6.0 \cdot 10^{-4}$ | $6.0 \cdot 10^{-6}$ | $6.0 \cdot 10^{-6}$ |
| $l_{\underline{0}}$ | [m] | 10.0 | 1.0 | 1.0 |
| $G_{\underline{\mathrm{P}}}$ | [V/m] | $10^4$ | $10^5$ | $10^4$ |
| $G_{\underline{\mathrm{D}}}$ | [Vs/m] | 500 | 500 | 500 |

(5.10)

Figure 5.23 shows non-dimensionalised orbits of rotor motion for cases #1 through #3. As expected, the similar cases #1 and #2 almost overlap, while case #3 is distinct. Here, the effect can be largely attributed to the stationary harmonic part of the motion, i.e., the amplitude of stationary vibration. However, as was seen in the previous stability analysis, a high proportional gain can destabilise the rotor-bearing system. Indeed, setting the gain a factor of ten too high, may result in unpredicted bearing behaviour.

While much of the knowledge that is gained from a dimensional analysis is common sense, the large number of parameters defining an ATPJB makes experiment planning error prone. While one dimensional effect is considered, another may be forgotten. Thus, the ATPJB dimensionless numbers are useful. The present investigation shows a case where the lack of similitude has only moderate effects on the rotor-bearing behaviour. As such, it does not warn about the dangers of extrapolating results in blindness, which may be significant.

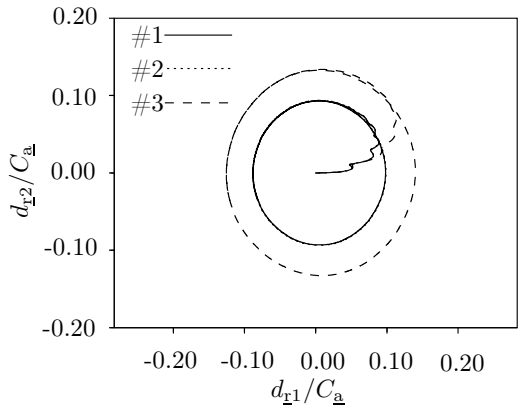


Figure 5.23: Journal orbits for cases #1, #2 and #3. Note that case #1 and #2 are similar, while case #3 is not similar to the other two.

## 5.4 Stationary harmonic response

The amplitude of the rotor vibration in the bearing can often be critical to a given design. To evaluate this, typically a linear model is sufficient [19]. In the following, we shall compute force responses for a passive, a hybrid, and an active bearing, respectively. Only one set of gains is investigated here.

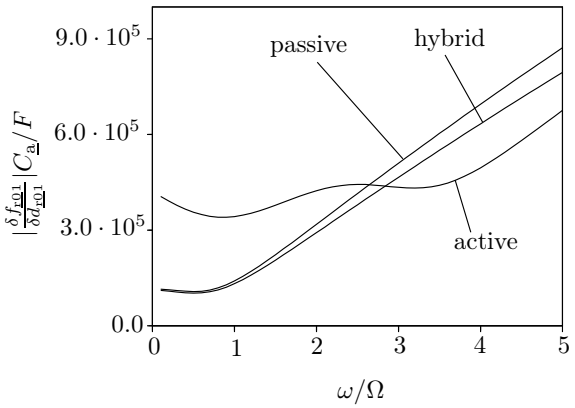


Figure 5.24: Amplitude of linear bearing force responses for the passive, hybrid and active bearing, respectively.

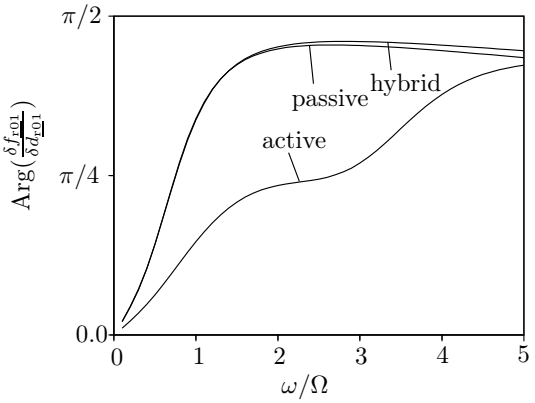


Figure 5.25: Phase of linear bearing force responses for the passive, hybrid and active bearing, respectively.

Figure 5.24 shows amplitudes of bearing force responses in the $x_1$ direction for a unit rotor amplitude in the $x_1$ direction. Curves are shown for a passive bearing, a hybrid bearing and an active bearing. The journal rotational speed is 6000rpm and the journal diameter is 0.1m. The machined clearance is 100$\mu$m and the assembled clearance is 75$\mu$m, which corresponds to a preload factor of 0.25. The lubricant viscosity is 0.019Ns/m$^2$. The pad density is 8400kg/m$^3$, the elastic modulus is 100GPa and the first two modeshapes of each pad are included in the computation. The static load on the bearing is 2000N

in the $x_1$ direction. The hybrid and active bearings incorporate two servo-valves each. The servo-valve eigenfrequency is 320.16Hz, the flow-voltage coefficient is $33.4{\cdot}10^{-6}\mathrm{m}^3/\mathrm{sV}$, the flow pressure coefficient is $1.13 \cdot 10^{-12}\mathrm{m}^5/\mathrm{sN}$, the valve damping ratio is 0.48, the leak flow is $6.0 \cdot 10^{-4}$ and the inlet pipe length is 1.0m. For the active bearing the proportional and derivative gains are 500V/mm and 0.5Vs/mm, respectively. For the hybrid bearing both the proportional and derivative gains are zero. Thus the hybrid bearing is essentially an open loop controlled bearing with a constant flow of fluid through the orifices into the bearing gap. The passive bearing has an uninterrupted wetted surface, while the active and hybrid bearings have orifice configurations corresponding to the four-orifice configuration described in [3]. The corresponding phase plots between rotor movement and bearing force responses are seen in Fig. 5.25. As mentioned, the curves in 5.24 and 5.25 are for displacement perturbations and force perturbations in the $x_1$ direction. The corresponding plots for the $x_2$ direction are almost identical, while the bearing cross coupling is neglected, as is most often reasonable with TPJBs.

With the curves in Figs. 5.24 and 5.25 the force from the bearing on a rotor for a given rotor movement is given. Then, for known rotor parameters, the forces from the structural stiffness, the damping, and the inertia of the rotor can be computed. Subsequently the rotor and bearing forces can be superimposed to produce the total force. If the rotor motion is of unit amplitude, the inverse of the total force is the frequency response function of the rotor-bearing system. Neglecting the structural stiffness and damping of the rotor, the rotor force response is simply $-m_{\underline{\mathrm{r}}}\Omega^2$. This force is superimposed on the bearing force of Fig. 5.24 and 5.25 for different values of the rotor mass $m_{\underline{\mathrm{r}}}$. Values of 2000kg, 1000kg and 200kg are investigated. The resulting frequency response functions are presented in Figs. 5.26, 5.27 and 5.28. The frequency range is 0 to $5\Omega$, corresponding to 500Hz. The servo-valve eigenfrequency thus corresponds to roughly $3\Omega$.

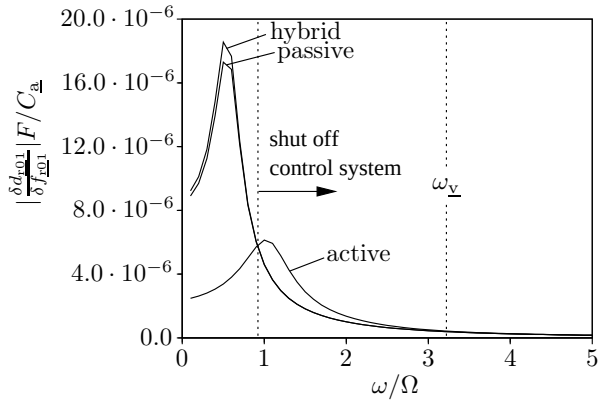


Figure 5.26: Amplitude of journal frequency response function for a rotor mass of 2000kg. The static load is 2000N in the $x_1$ direction, the rotational speed is 6000rpm and the lubricant viscosity is $0.019\mathrm{Ns/m}^2$. The assembled clearance is $75\mu$m and the machined clearance is $100\mu$m.

Consider Fig. 5.26, which is the frequency response function for the heavy rotor case. The control system is seen to damp out the first primary resonance peak considerably, while also increasing the resonance frequency. In both the active and passive cases there is only one significant resonance peak. Coincidentally, the control system reduces vibration amplitude for frequencies below the synchronous (rotational) frequency. So whether or not it is beneficial to activate the control system depends on which

frequencies dominate the forcing. Henceforth, let us denote the frequency where the amplitude curves cross each other the "shut-off frequency". One always has the option of reverting from the active bearing to the hybrid bearing. This simply requires setting the control gains to zero. The hybrid bearing is seen to perform roughly as the passive bearing, in particular for higher frequencies. Possibly, for higher valve leak values, this would not be true.

Keep in mind that the shown frequency response function is for the case of constant rotational speed $\Omega$. Thus it is not suited for investigation of the vibrational amplitude during start-up of a rotor. Its merit is in the investigation of a rotor operation at nominal operating conditions.

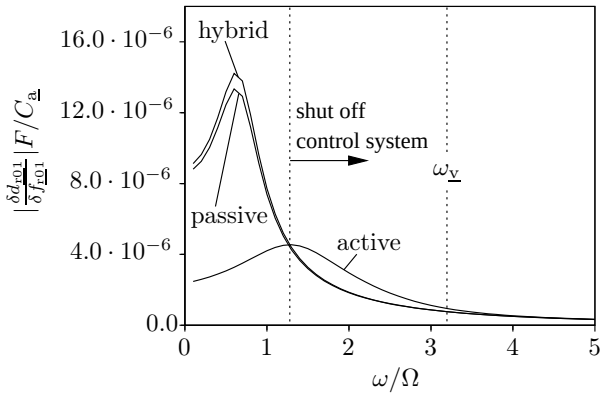


Figure 5.27: Amplitude of frequency response function for a rotor mass of 1000kg. The static load is 2000N in the $x_1$ direction, the rotational speed is 6000rpm and the lubricant viscosity is 0.019Ns/m$^2$. The assembled clearance is 75$\mu$m and the machined clearance is 100$\mu$m.

Figure 5.27 shows the frequency response functions for the moderate rotor mass. The study of these curves yields similar conclusions to that of Fig. 5.28 except perhaps, that all relevant frequencies have increased slightly. That is, the resonance frequencies for all cases, as well as the shut-off frequency.

The frequency response function for a light rotor of 200kg is shown in Fig. 5.28. The light rotor means that even for relatively high frequencies, the bearings force response is significant. Thus, for the active bearing, apart from the first resonance peak, a second peak is identified close to the servo-valve eigenfrequency. Also, as before, reducing rotor mass has had the effect of increasing the resonance and shut-off frequencies.

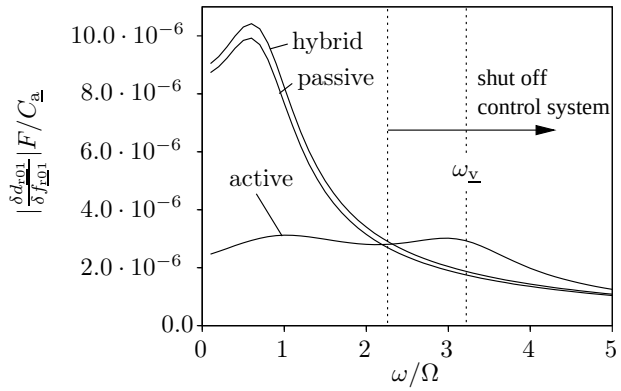


Figure 5.28: Amplitude of frequency response function for a rotor mass of 200kg. The static load is 2000N in the $x_1$ direction, the rotational speed is 6000rpm and the lubricant viscosity is 0.019Ns/m$^2$. The assembled clearance is 75$\mu$m and the machined clearance is 100$\mu$m.

## 5.5 Simple adaptive control

In recognition of the fact that rotor-bearing system behaviour depends heavily on rotational speed, it seems that control gain choice should be made accordingly. That is, the choice of control gain should also depend on the rotational speed. A few preliminary reflections are in order here. Firstly, the mission of the control system should be clarified. In optimization terms, we would refer to the objective function. Secondly, any constraints should be identified. For instance, it is quite possible that control gains, which result in small stationary harmonic amplitude of vibration actually make the bearing unstable. Furthermore, there are limits as to how high control gains can be chosen, since the capacity of the control system is limited. That is, we must keep the risk of control system saturation in mind. Saturation is a nonlinear phenomenon, and cannot readily be included in a linear frequency domain analysis. Whether it be a stability analysis or a stationary linear harmonic response analysis. The easiest way to tackle the issue, is to impose sensible limits on the magnitude of the control gains. In optimization terms, we would refer to such limits as the constraint function(s).

In the following analyses, the results are normalised with the fundamental frequency $\Omega_0$. As it is difficult to choose one relevant frequency for normalisation in both the passive and active cases, we set $\Omega_0$ to the quite arbitrary value

$$\Omega_0 = 100\text{Hz} \tag{5.11}$$

In the active cases, the implemented servo-valve has an eigenfrequency of 320.16Hz, so in those cases one may substitute this as the fundamental frequency, if it is useful.

The rotational speed, $\Omega$, is varied from almost zero to $\Omega_0$, i.e., 100Hz. The assembled clearance is $75\mu$m and the machined clearance is $100\mu$m. A two mode reduction is utilised for the pads. Rotor mass is 2000kg with zero structural rotor stiffness and damping. The static load is zero as is the rotor structural damping and stiffness. The flow-voltage coefficient is $16.7 \cdot 10^{-6}\text{m}^3/(\text{sV})$. Apart from this, the parameters are as in Tabs. 5.1 and 5.2. The orifice array is that of configuration #2 in [3].

The external force on the rotor is defined as that of an unbalance and set to

$$\omega = \Omega \tag{5.12}$$

$$f_{\underline{r}1} = 8000\text{N}(\omega/\Omega_0)^2 \cos(\omega t)$$

$$f_{\underline{r}2} = 8000\text{N}(\omega/\Omega_0)^2 \sin(\omega t) \tag{5.13}$$

The proportional gain is confined to the interval $\pm$4MV/m and the derivative gain is confined to the interval $\pm$6kVs/m. Each interval is divided into 20 segments. Thus at each rotational speed, there are 400 discrete combinations of gains, which can be selected. The passive hybrid bearing still has the valves attached, but the gains are set to zero. Thus the flow into the bearing gap is constant and equal to the leak flow. We test three different control strategies. The first (I) is to select the gains so as to produce the minimum stationary amplitude of vibration, subject to a synchronous unbalance. As a constraint, all real parts of system eigenvalues must be negative. The second (II) is to minimize the largest real part of any system eigenvalue. The third (III) is to again select the gains so as to produce the minimum stationary amplitude of vibration, subject to a synchronous unbalance. But now with the constraint, that the largest real part of any eigenvalue must be smaller than that of the passive hybrid bearing (with zero gains). The gains are selected through brute force trial and error calculations.

The adoption of the three strategies results in the gain selections shown in Figs. 5.29 and 5.30. We note that none of the selected gains are negative. The curve of selected gains for strategy II seems to be quite erratic, in particular for the lower rotational speeds. As the rotational speed increases, the curve

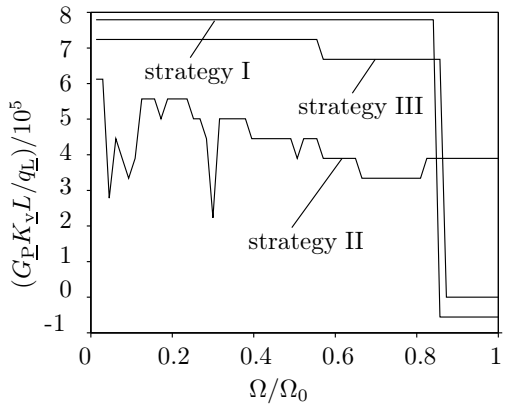


Figure 5.29: Selected proportional gains as a function of rotational speed.

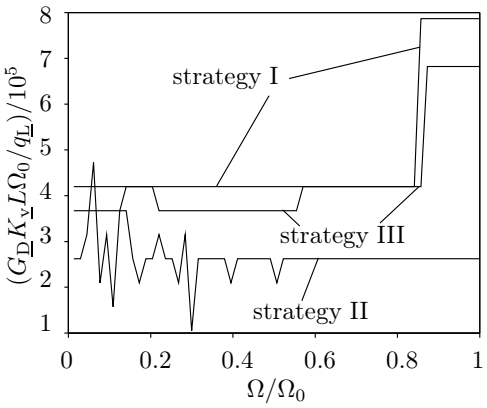


Figure 5.30: Selected derivative gains as a function of rotational speed.

straightens. In contrast, strategies I and III produce much simpler curves, with less features. It is worth noting, that strategy III tends to select smaller proportional gains than strategy I throughout most of the range of rotational speeds.

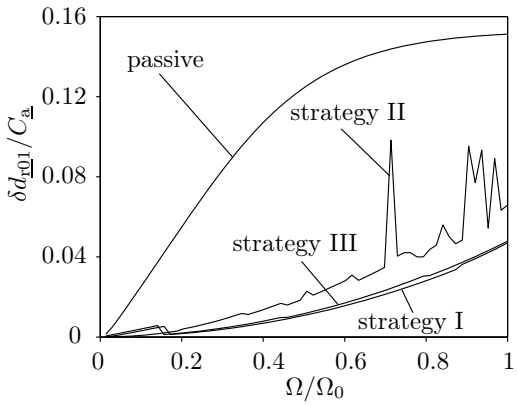


Figure 5.31: Amplitudes of stationary vibration from the unbalance force in Eq. (5.13) for the different control strategies.

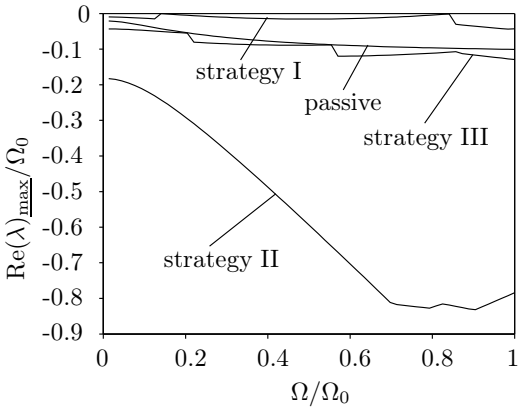


Figure 5.32: Maximum real part for the three different control strategies.

Figure 5.31 shows the amplitudes of stationary vibration for the different control strategies. While strategy I produces a large drop in amplitude across the range of rotational speed, the behaviour of strategy II is more erratic, although it too results in amplitude drops as a secondary effect. The hybrid strategy II performs almost as well as strategy I in reducing the amplitude.

Figure 5.32 shows the maximum real part of any system eigenvalue for the range of rotational speeds and the three control strategies. As seen, all cases are stable. However, the real parts of strategy I

come very close to the zero line. Thus, it is likely, that this strategy will produce a bearing with poor performance in terms of dissipation of energy. That is, it will perform poorly in the transient vibration regime. Furthermore, a small change or uncertainty in any system parameter may cause the bearing to become unstable. Thus, strategy I is rejected. Naturally, strategy II has the lowest maximum real parts across the whole range of rotational speeds. The maximum real part of strategy II stays fairly close to that of the passive case, indicating the the constraint is influencing the choice of gains.

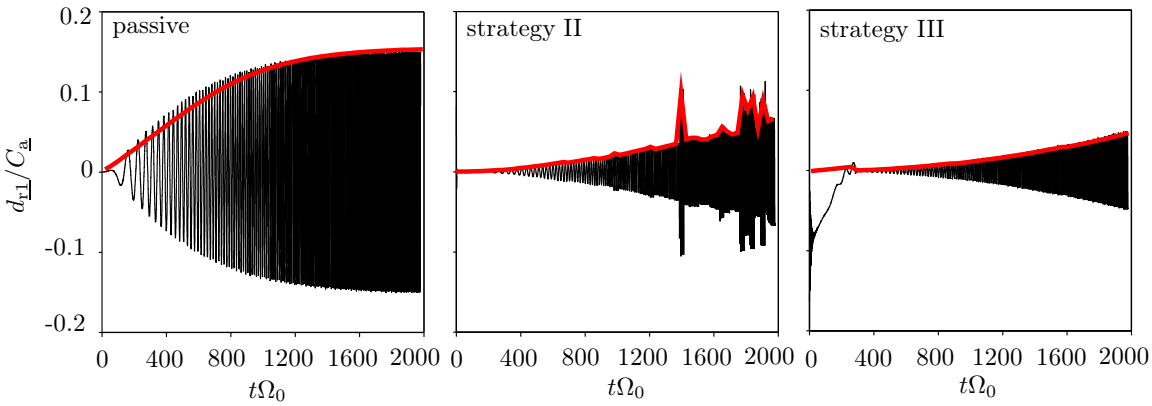


Figure 5.33: Timeseries for the passive case along with two of the control strategies.

Figure 5.33 shows timeseries for the passive case, as well as control strategies II and III. The rotational speed, $\Omega$, is increased in 63 equal steps from zero to 100Hz over a time interval of 3.18 seconds. The unbalance force is defined by Eq. 5.13. The predicted stationary vibration amplitude (from Fig. 5.31) is overlaid as a red curve. As the speed (hence the magnitude of the unbalance force) is increased in abrupt steps, each speed increase will introduce a small amount of energy into the system. Thus, the system will vibrate transiently throughout the analysis, after each step. However, the magnitude of the transient part is modest, as the curves of stationary vibration amplitude almost perfectly predict the response. One exception is the very beginning of the analysis for strategy III, where substantial transient vibrations take place. Also, keep in mind, that changing the gains abruptly is in itself a transient event, which may adversely affect the system response. In terms of vibration response, however, both strategies outperform the passive case across the range of rotational speeds.

## 5.6 Stability calculation with dynamic coefficients

As a final analysis. We investigate the possible error from applying frequency dependent bearing dynamic coefficients to stability analysis of ATPJBs. That is, dynamic coefficients from a dynamic, synchronous (or asynchronous) motion perturbation. As previously mentioned, such use is not recommended. We shall see selected examples of why this is true in the following.

The procedure for a stability analysis is

1. Find the static equilibrium of the TPJB, considering pad, rotor and valve degrees of freedom.
2. Considering the pad, rotor and valve degrees of freedom, solve for the eigenvalues.

The procedure for a synchronous motion stability analysis is

1. Find the static equilibrium of the TPJB, considering pad, rotor and valve degrees of freedom.
2. Perform dynamic condensation, considering the pad, rotor and valve degrees of freedom. This results in the 2×2 system of the rotor, with frequency dependent coefficients. The bearing contributions are defined by Eq. (2.130) and Eq. (2.131).
3. Considering only the rotor degrees of freedom, solve for the eigenvalues.

Let us use one of the test cases from section 5.2 as an example. The mass is set to $m_{\underline{\mathrm{r}}} = 200\text{kg}$ and the assembled clearance to $C_{\underline{\mathrm{a}}} = 75\mu\text{m}$ corresponding to a preload factor of 0.25. Two rotational speeds are investigated $\Omega = 100\text{Hz}$ and $\Omega = 10\text{Hz}$. A two-mode pseudo modal reduction is employed (pad tilt and bending). The 100Hz case previously produced the stable domain in Fig. 5.14. Now, in stead of performing a true stability analysis, we perform a dynamic condensation to produce the 2×2 system of equation for the journal. The condensation frequency is the synchronous value, i.e., $\omega = 100\text{Hz}$ or $\omega = 10\text{Hz}$. The bearings contribution to the stiffness and damping matrices are given by Eq. (2.130) and Eq. (2.131), respectively. The rotor structural stiffness and damping are set to zero, and the mass matrix is diagonal with $m_{\underline{\mathrm{r}}}$ in the diagonal entries. The resulting stable domain is shown in Fig. 5.36 and Fig. 5.37 for 100Hz and 10Hz, respectively. The corresponding actual stable domain is also shown for comparison. Clearly, the error is unacceptable. However, note that in the low frequency case, the lower left corner of the stable domain is predicted fairly accurately by the synchronously reduced method, as is the lower bound on the proportional gain. However, information on the rest of the stability threshold is lost, as the upper bounds on both gains are not seen at all.

Since the synchronously (or asynchronously) reduced dynamic coefficients for a passive plain (no pads) journal bearing are frequency independent, and may be used for stability analysis, it is tempting to use them for stability analysis of said bearings with active servo-valves [65]. However, as mentioned, such use is not recommended, since the addition of the control system adds degrees of freedom to the system, and thus makes the condensed system frequency dependent. Firstly, such use constitutes a mathematical error. Secondly, as we shall see, the error can be significant. To make the analysis as simple and clear and reproducible as possible, it is desirable to investigate a bearing in which cavitation does not occur. A straight forward way of doing this is to simply define the bearing surface as that of a TPJB at static equilibrium. It is straight forward to create a plain journal bearing from a tilting pad journal bearing; simply fix the pads. Figure 5.34 illustrates the idea. It shows the generic system of equations for a rigid body model of an ATPJB with indication of components. The pads are fixed in a position that corresponds to static equilibrium of the corresponding bearing with rigid pad degrees of freedom. That is, the pads are allowed to tilt into the static equilibrium position and are subsequently fixed. This ensures that cavitation does not occur. The generic geometry of the active plain bearing is illustrated in Fig. 5.35.

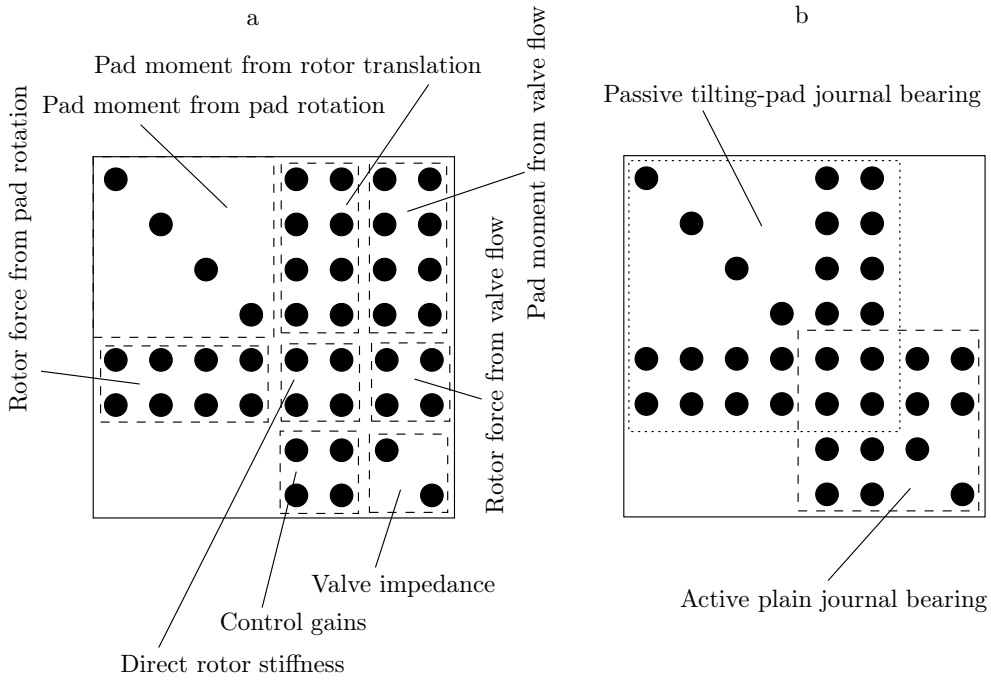


Figure 5.34: a: Illustration of the structure of the system of equations for a rigid body model of an ATPJB with indication of the individual contributions. b: Indication of the corresponding system of equations for an active plain journal bearing and a passive TPJB.

Now, for the stability analysis, the procedure is as follows.

1. Find the static equilibrium of the TPJB, considering pad, rotor and valve degrees of freedom.
2. Considering only the rotor and valve degrees of freedom (active plain journal bearing), solve for the eigenvalues.

The procedure for a synchronous motion coefficient stability analysis is

1. Find the static equilibrium of the TPJB, considering pad, rotor and valve degrees of freedom.
2. Perform dynamic condensation, considering only the rotor and valve degrees of freedom. This results in the 2×2 system of the rotor, with frequency dependent coefficients. The bearing contributions are defined by Eq. (2.130) and Eq. (2.131).
3. Considering only the rotor degrees of freedom, solve for the eigenvalues.

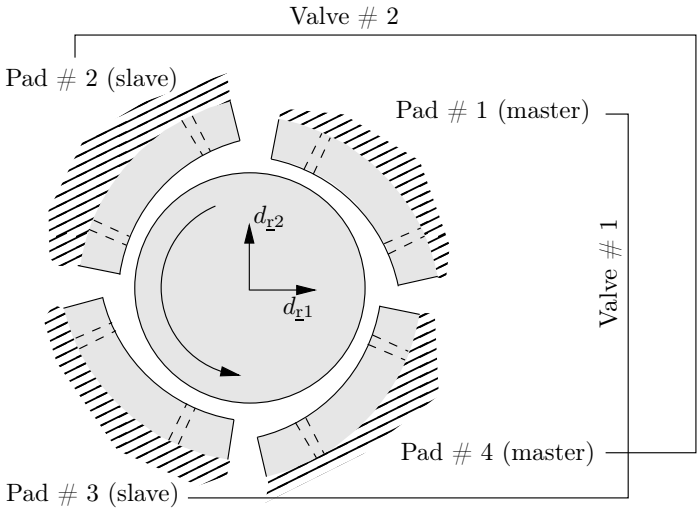


Figure 5.35: Schematic representation of the active journal bearing. The four pads are fixed, leaving only the degrees of freedom of the rotor and the servo-valve. Effectively, this makes the bearing an active plain journal bearing. The incline of the pads is greatly exaggerated.

As before, the mass is set to $m_{\underline{r}} = 200$kg and the assembled clearance to $C_{\underline{a}} = 75\mu$m corresponding to a preload factor of 0.25. Two rotational speeds are investigated $\Omega = 100$Hz and $\Omega = 10$Hz. Also, as before, the condensation frequency is the synchronous value, i.e., $\omega = 100$Hz or $\omega = 10$Hz. The rotor structural stiffness and damping are set to zero, and the mass matrix is diagonal with $m_{\underline{r}}$ in the diagonal entries. The resulting stable domains are shown in Fig. 5.38 and Fig. 5.39 for 100Hz and 10Hz, respectively. The corresponding actual stable domain is also shown for comparison. Again, we note that in the low frequency case, the lower left corner of the stable domain is predicted accurately by the synchronously reduced method. Also, the lower bound on the proportional gain is in agreement with that of the actual stability analysis. However, as before, the rest of the stability threshold is not captured.

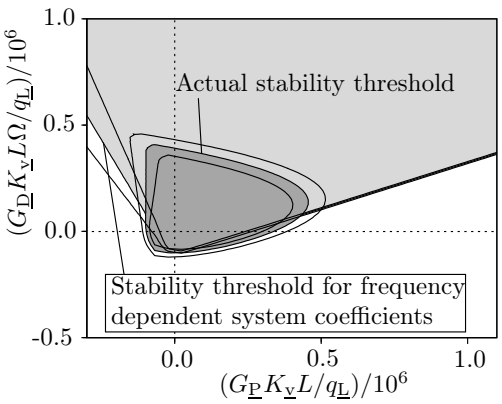


Figure 5.36: Stable domains for an AT-PJB. The stable domain, as predicted by the dynamic coefficient method, is shaded. The actual stable domain is shaded even darker. In addition to the curve of marginal stability, there are curves where the maximum real part of any eigenvalue is equal to $0.1\Omega$ (outside the stable domain) and $-0.1\Omega$ (inside the stable domain). The distance between the curve of marginal stability, and these curves, gives an impression of the bearings sensitivity to changes in the gains. Rotational speed is $\Omega = 100$Hz.

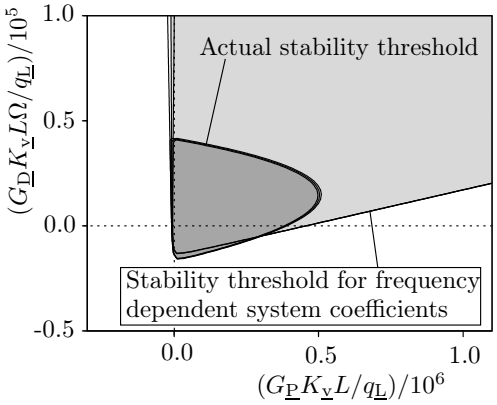


Figure 5.37: Stable domains for an AT-PJB. The stable domain, as predicted by the dynamic coefficient method, is shaded. The actual stable domain is shaded even darker. In addition to the curve of marginal stability, there are curves where the maximum real part of any eigenvalue is equal to $0.1\Omega$ (outside the stable domain) and $-0.1\Omega$ (inside the stable domain). The distance between the curve of marginal stability, and these curves, gives an impression of the bearings sensitivity to changes in the gains. Rotational speed is $\Omega = 10$Hz.

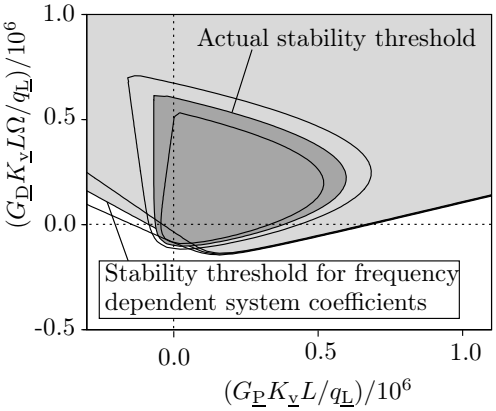


Figure 5.38: Stable domains for an active journal bearing (no pads). The pads are fixed. The stable domain, as predicted by the dynamic coefficient method, is shaded. The actual stable domain is shaded even darker. In addition to the curve of marginal stability, there are curves where the maximum real part of any eigenvalue is equal to $0.1\Omega$ (outside the stable domain) and $-0.1\Omega$ (inside the stable domain). The distance between the curve of marginal stability, and these curves, gives an impression of the bearings sensitivity to changes in the gains. Rotational speed is $\Omega = 100$Hz.

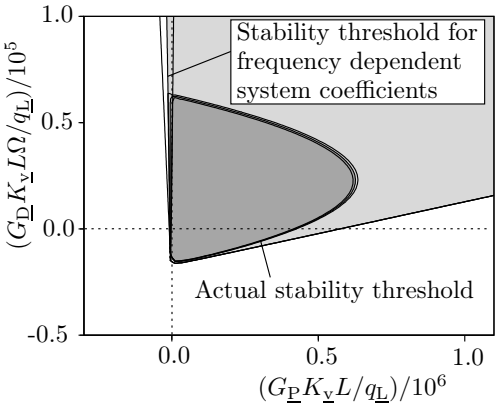


Figure 5.39: Stable domains for an active journal bearing (no pads). The pads are fixed. The stable domain, as predicted by the dynamic coefficient method, is shaded. The actual stable domain is shaded even darker. In addition to the curve of marginal stability, there are curves where the maximum real part of any eigenvalue is equal to $0.1\Omega$ (outside the stable domain) and $-0.1\Omega$ (inside the stable domain). The distance between the curve of marginal stability, and these curves, gives an impression of the bearings sensitivity to changes in the gains. Rotational speed is $\Omega = 10$Hz.

## 5.7 Thermal error estimate

To gain insight into the magnitude of the error from neglecting thermal effects, a simplified thermal study is conducted. The study adopts an engineering approach and is by no means exact. But it will serve to effectively estimate how sensitive the previously presented results are with respect to thermal influences. For this investigation we shall assume the bearing infinitely long. Also, while the study does not assume isothermal conditions, it does rely on averaged system parameters.

Assuming the pad and rotor surfaces parallel, then the oil film shear stress is constant across the film thickness and is given as

$$\tau = \mu \frac{U}{h} \left[ \frac{\mathrm{N}}{\mathrm{m}^2} \right] \tag{5.14}$$

furthermore, the average area specific power dissipated in the oil film shear is given as

$$P = \tau U \left[ \frac{\mathrm{W}}{\mathrm{m}^2} \right] \tag{5.15}$$

For a four pad bearing, the maximum arc length of a pad is $\pi D/4$. A rough estimate of the average lubricant velocity is $U/2$. Thus the average time that a lubricant particle spends in the gap is given as

$$\Delta t = \frac{\pi D/4}{U/2} \, [s] \tag{5.16}$$

Assuming no heat transfer through the pad and rotor, then all the shear dissipation is stored in the lubricant as thermal energy. Thus the area specific energy absorbed by the lubricant through its motion past one pad is given as

$$E_{\underline{\text{shear}}} = P \Delta t = \mu \frac{U \pi D/2}{h} \left[ \frac{\mathrm{J}}{\mathrm{m}^2} \right] \tag{5.17}$$

The average area specific heat capacity is given as

$$c_{\underline{\text{a}}} = c_{\underline{\text{p}}} \rho_{\underline{\text{oil}}} h \left[ \frac{\mathrm{J}}{\mathrm{m}^2 \mathrm{K}} \right] \tag{5.18}$$

where $c_{\underline{\text{p}}}$ is the lubricant heat capacity and $\rho_{\underline{\text{oil}}}$ is the density. The temperature change of the lubricant through its motion past one pad is computed as

$$\Delta T = T_{\underline{\text{out}}} - T_{\underline{\text{in}}} = \frac{E_{\underline{\text{shear}}}}{c_{\underline{\text{a}}}} = \frac{\mu U \pi D/2}{c_{\underline{\text{p}}} \rho_{\underline{\text{oil}}} h^2} \tag{5.19}$$

Thus now we have one equation linking temperature and viscosity change to rotational speed. That is, we have one equation with two unknowns. As a constitutive relation between temperature and viscosity we make use of the following empirical relation [66]

$$\mu = 10^{G_{\underline{0}}(1+\frac{T}{135})^{-S_{\underline{0}}}-4.2} \quad [\mathrm{Ns/m^2}] \tag{5.20}$$

where $G_{\underline{0}}$ and $S_{\underline{0}}$ are determined from experiment. Thus with two datapoints, the temperature-viscosity relation can be established. Note that $T$ is measured in °C. The equation (5.20) has been rewritten slightly

from the expression in [66] so as to define $\mu$ in SI units. We set the temperature to the median over the pad. Thus

$$T = (T_{\underline{\text{out}}} + T_{\underline{\text{in}}})/2 = T_{\underline{\text{in}}} + \Delta T/2 \tag{5.21}$$

Thus Eq. (5.20) with Eq. (5.21) produces

$$\mu = 10^{G_{\underline{0}}(1+\frac{T_{\underline{\text{in}}}+\Delta T/2}{135})^{-S_{\underline{0}}}-4.2} \quad [\text{Ns/m}^2] \tag{5.22}$$

Equations (5.19) and (5.22) can be solved iteratively for $\Delta T$ and $\mu$. We combine them to define the residual equation

$$r_{\underline{\mu}} = \frac{c_{\underline{\text{p}}}\rho_{\underline{\text{oil}}}h^2\Delta T}{U\pi D/2} - 10^{G_{\underline{0}}(1+\frac{T_{\underline{\text{in}}}+\Delta T/2}{135})^{-S_{\underline{0}}}-4.2} = 0 \tag{5.23}$$

which is a single nonlinear equation in $\Delta T$. We solve this equation with the Newton-Raphson method. Deriving with respect to $\Delta$T yields

$$\frac{\partial r_{\underline{\mu}}}{\partial \Delta T} = \frac{2c_{\underline{\text{p}}}\rho_{\underline{\text{oil}}}h^2}{U\pi D/2} + \ln(10)G_{\underline{0}}S_{\underline{0}}\left(1+\frac{T_{\underline{\text{in}}}+\Delta T/2}{135}\right)^{-S_{\underline{0}}-1} 10^{G_{\underline{0}}(1+\frac{T_{\underline{\text{in}}}+\Delta T/2}{135})^{-S_{\underline{0}}}-4.2}/270 \tag{5.24}$$

Hydraway HVXA 22 oil has a kinematic viscosity of 21.2 mm$^2$/s at 40°C and 4.8 mm$^2$/s at 100°C. The density at 15°C is 860kg/m$^3$ and assumed constant. The heat capacity is taken to be $1900\frac{\text{J}}{\text{kgK}}$ which is a realistic value. Figure 5.40 shows the dynamic viscosity as a function of temperature for the oil in question. The curve follows the expression in Eq. (5.20). Figure 5.41 shows the temperature change over

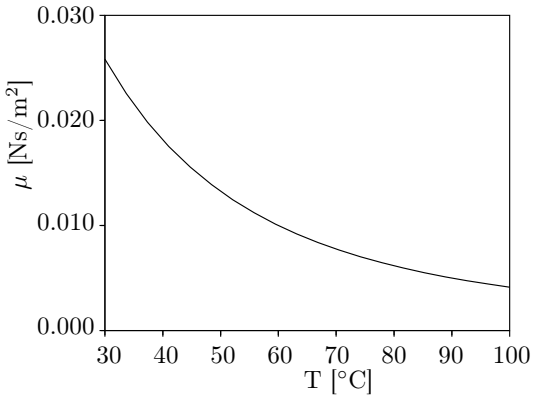


Figure 5.40: Dynamic viscosity as a function of temperature for Hydraway HVXA 22.

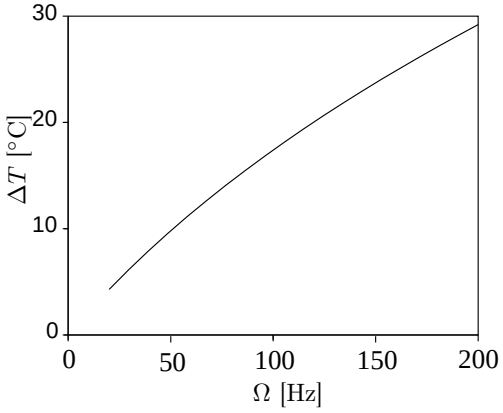


Figure 5.41: Temperature change as a function of rotational speed.

one pad as a function of rotational speed as computed from Eq. (5.23). The inlet temperature $T_{\underline{\text{in}}}$ is set to 38.5°C. This temperature produces a viscosity of 0.019Ns/m$^2$, which is the value adopted in many of the analyses in this thesis. The other system parameters are chosen to correspond to the analyses in 5.2. Here a 0.1m journal is rotating at speeds up to 100Hz in a bearing with a machined clearance of 100$\mu$m. There is no static load on the bearing. A thin oil film will produce higher shear stresses, so the worst case

is that of the high preload factor, which is 0.25. As a worst case scenario for the thermal computation, the film thickness is set to $50\mu$m. In Fig. 5.42 the resulting relative change in average viscosity over the pad is shown. The effect is substantial, with the error reaching 36% for the 200Hz case. At 150Hz the reduction is 32%. To investigate the impact on the results of such a decrease in viscosity, we compute the stable domain of gains with a 32% reduction in viscosity (from 0.019Ns/m$^2$ to 0.0129Ns/m$^2$). This is taken to represent a more severe thermal error than that of any result presented, as the rotational speed is 150Hz, compared to the 100Hz speed of, e.g., Fig. 5.14. The effect of the viscosity drop is presented in Fig. 5.43. The effect is noticeable, but would not impact any drawn conclusions. Note that asserting that the computation with a reduced viscosity is more accurate than the original would be false. For this, the thermal correction is too simple. What the thermal correction allows us to do is merely evaluate the sensitivity of the results with respect to the thermal influence. As it is seen, the control system is not severely affected by changes in the viscosity. Also, note that the effect may be even more modest, if the control system is taken to inject oil at the inlet temperature and viscosity. As such, the presented thermal computation constitutes a worst case investigation.

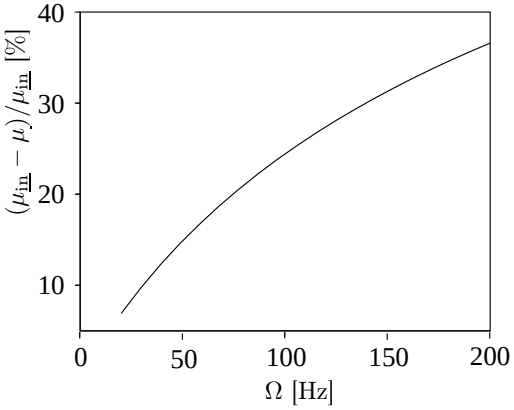


Figure 5.42: Relative change in average viscosity as a function of rotational speed.

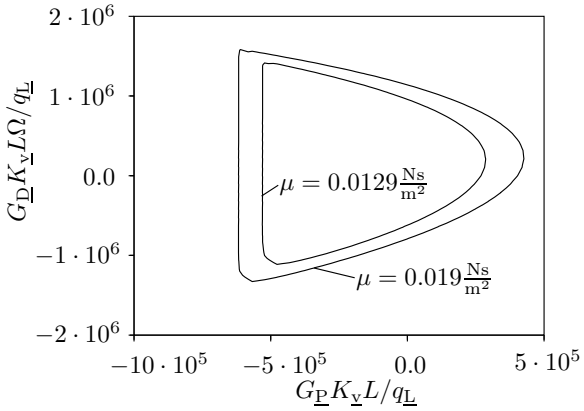


Figure 5.43: Effect on stability threshold by change in viscosity.

## 5.8 Chapter discussion and summary

In the present chapter, the mathematical model has been validated inexhaustibly against selected results from literature.

The model has been checked for consistency through comparison between linear stationary harmonic analysis and nonlinear time domain analysis. Also a convergence check with respect to spacial resolution has been performed, by comparing pseudo modal reductions with different numbers of modes.

A large study on the influence of model parameters on stability has been performed. Most notably, stability limits on control parameters have been established. The results from the dimensional analysis have been put to use, as all stable domains are non-dimensional.

The critical hydroelastic number for a given bearing design has been established. Also, a small study on the implications of similitude and the lack thereof is also included. This serves as a guide to the safe

extrapolation of results to bearings of other dimensions.

A linear frequency response analysis has been performed. This is useful for the limitation of the amplitude of stationary harmonic non-synchronous vibrations. The analysis is performed for three values of rotor mass. Generally, the lighter the rotor, the higher is the frequency at which it is beneficial to shut off the control system. At low frequencies the control system should be on, since hydrodynamic load carrying capacity is low.

Finally, it has been shown that a $2\times2$ system of equations with frequency dependent matrix entries is not suitable for ATPJB stability predictions, nor for stability predictions of active plain journal bearings without moving pads.

# Chapter 6

# Conclusions and future aspects

A mathematical modelling procedure for active tilting-pad journal bearings has been presented. The resulting model can be used for local stability analysis, stationary harmonic vibration analysis, and nonlinear time series analysis. All three analysis types are combined to evaluate specific bearing designs at given operating conditions. The conclusions in the following draw from the results of this thesis as well as the candidates recent publications [2, 3, 4, 5, 6, 7, 8].

It is seen that placement of radial injection orifices is important. Placement far from the pad pivot line is recommended, as passive hydrodynamic pressure in this region is small. Thus, all other things being equal, orifice placement far from the pivot line will amount to a more effective control system than one with centrally placed orifices. Secondly, it has been demonstrated that, while pad deformation has modest influence on the static equilibrium and oil film thickness of the bearing, it is of great importance to the dynamics. This is particularly relevant for active tilting-pad journal bearings, as use of a rigid body model can lead to miss-tuning of the bearing. Miss-tuning can lead to bearing instability and failure.

Stable domains in the proportional-derivative gain planes have been identified. These depend on operating conditions and bearing parameters. Increased rotor mass is seen to increase the size of the domain. The effect of reducing the pad preload factor is less obvious, but the effect of rounding off the south-west corner of the stable domain seems to prevail across the range of simulations. This round off effect can in some cases destabilise the passive bearing. That small preload can lead to an unstable bearing is well known, so this is not surprising in itself. However, the same analyses reveal, that the control system can stabilise the bearing when the small preload makes the passive bearing unstable.

A dimensional analysis has been performed. A total of twelve dimensionless parameters are identified for the dynamic behaviour of active tilting-pad journal bearings. A few of these have already been known for many years, namely the Sommerfeld number and the dimensionless rotor mass. These are also, by far, the most important. However, as active tilting-pad journal bearings are not yet fully understood, the dimensionless numbers related to the control system, will aid greatly in future experiment planning. An example of a representative scaled down test-rig bearing design process is presented. Furthermore, simulations have revealed the value of the critical hydroelastic number for a given bearing design. Future research should aim to produce tables of critical values for a range of bearing designs.

Initial attempts at simple adaptive control have been made. These reveal that the concept of "ideal" rotor-bearing behaviour poses ambiguous requirements on the control gains. That is, ideal stationary vibration performance is in conflict with transient performance. Thus, the designer must consider carefully what the role of the control system is. Is it to minimise vibration inside the bearing for reduced wear and

long bearing service life? Or is it to dissipate mechanical transients from other machine elements on the rotating shaft? These roles will lead to different gain selections.

It has been illustrated through theoretical argumentation and selected examples, that frequency dependent dynamic coefficients are not suited for stability predictions of active journal bearings of the type investigated here. This holds, whether the bearings are of the tilting-pad type or not.

Finally, it cannot be overemphasised that all the presented simulations assume isothermal conditions. Once a sound thermoelastohydrodynamic model of an active tilting-pad journal bearing is developed, many conclusions in this thesis become subject to possible revision.

# Bibliography


[1] A. Rosenblueth, N. Wiener, The Role of Models in Science, Philosophy of Science 12 (4) (1945) 316–321.

[2] A. M. Haugaard, I. F. Santos, Elastohydrodynamics Applied to Active Tiliting-Pad Journal Bearings, ASME Journal of Tribology 132 (2) (2009) 1–10.

[3] A. M. Haugaard, I. F. Santos, Multi Orifice Active Tilting-Pad Journal Bearings - Harnessing of Synergetic Coupling Effects, Tribology International 43 (8) (2010) 1374–1391.

[4] A. M. Haugaard, I. F. Santos, Stability of Multi Orifice Active Tilting-Pad Journal Bearings, Tribology International 43 (9) (2010) 1742–1750.

[5] A. M. Haugaard, I. F. Santos, Flexibility Effects in Tilting-Pad Journal Bearings with Radial Oil Injection, in: EURODYN 2008, 7. European Conference on Structural Dynamics, Southampton, UK, 2008, pp. 1–12, paper ID: E187.

[6] A. M. Haugaard, I. F. Santos, Flexibility Effects in Tilting-Pad Journal Bearings with Controllable Radial Oil Injection, in: NORDTRIB 2008, 13. Nordic Symposium in Tribology (ISBN: 978-952-15-1959-8), Tampere, Finland, 2008, pp. 1–17, paper ID: NT2008-43-4.

[7] A. M. Haugaard, I. F. Santos, Modeling of Flexible Tilting Pad Journal Bearings with Radial Oil Injection, in: 2008 Proceedings of the STLE/ASME International Joint Tribology Conference (ISBN: 978-0-7918-3837-2), Miami, Florida, USA, 2008, pp. 335–337.

[8] A. M. Haugaard, I. F. Santos, Fast Solution of Fluid Structure Interaction Problems in the Frequency Domain - with an Application (in print), in: 11th Pan-American Congress of Applied Mechanics - PACAM XI, Foz do Iguaçu, Paraná - BRAZIL, 2010, pp. 1–6.

[9] G. C. Brito, E. Andreoli, D. C. de Oliveira, K. A. Brol, K. B. Brol, Dynamic Behaviour of Hydrogenerators During Mechanical Transients, in: 11th Pan-American Congress of Applied Mechanics - PACAM XI, Foz do Iguaçu, Paraná - BRAZIL, 2010, pp. 1–6.

[10] R. D. Flack, C. J. Zuck, Experiments on the Stability of Two Flexible Rotor in Tilting-pad Journal Bearing, Tribology Transactions 31 (2) (1988) 251–257.

[11] Y. Lie, Z. J. You-Bai, Q. Damou, Experiments on the Destabilizing Factors in Tilting-Pad Journal Bearings, Tribology International 22 (5) (1989) 329–334.

[12] E. Pollman, H. Shcwerdtfeger, H. Termuehlen, Flow Excited Vibrations in High-Pressure Turbines (Steam Whirl), ASME Journal of Engineering for Power 100 (1978) 219–228.

[13] A. Stodola, Critical Frequencies in Shafts due to Elasticity of Oil Film in Bearing, Schweizerische Bauzeitung (1925) 265–266.

[14] H. H. Jeffcott, The Lateral Vibration Loaded Shafts in the Neighborhood of a Whirling Speed. - The Effect of Want of Balance, Philosophical Magazine 37 (1) (1919) 304–314.

[15] F. K. Orcutt, E. B. Arwas, The Steady-State and Dynamic Characteristics of a Full Circular Bearing and a Partial Arc Bearing in the Laminar and Turbulent Flow Regimes, Journal of Lubrication Technology 2 (89) (1967) 143–153.

[16] D. Reynolds, On the Theory of Lubrication and Its Application to Mr. Beauchamp Tower's Experiments, Including an Experimental Determination of the Viscosity of Olive Oil, Philosophical transactions of the Royal Society of London 177 (1886) 157–234.

[17] J. Boyd, A. A. Raimondi, Analysis of Pivoted-Pad Journal Bearing, ASME Transactions 75 (5) (1953) 380–386.

[18] A. A. Raimondi, J. Boyd, Applying Bearing Theory to the Analysis and Design of Pad-Type Bearings, ASME Transactions 77 (3) (1955) 287–309.

[19] J. W. Lund, Spring and Damping Coefficients for the Tilting Pad Journal Bearing, Trans. ASLE 7 (1964) 342–352.

[20] C. M. M. Ettles, The Analysis and Performance of Pivoted Pad Journal Bearings Considering Thermal and Elastic Effects, ASME Journal of Lubrication Technology 102 (1980) 182–192.

[21] P. E. Allaire, J. A. Parsell, L. E. Barrett, A Perturbation Method for the Dynamic Coefficients of Tilting-Pad Journal Bearings, Wear 72 (1981) 29–44.

[22] T. S. Brockett, L. E. Barrett, Exact Dynamic Reduction of Tilting-Pad Bearing Models for Stability Analyses, Tribology Transactions 36 (4) (1993) 581–588.

[23] J. C. Nicholas, E. J. Gunter, L. E. Barrett, Topics in Fluid Film Bearing and Rotor Bearing System Design and Optimization, ASME, 1978, Ch. The Influence of Tilting Pad Bearing Characteristics on the Stability of High Speed Rotor-Bearing Systems, pp. 55–78.

[24] J. C. Nicholas, Lund's Tilting-Pad Journal Bearing Pad Assembly Method, ASME Journal of Vibration and Acoustics 125 (4) (2003) 448–454.

[25] J. C. Nicholas, E. J. Gunter, P. E. Allaire, Stiffness and Damping Coefficients for the Five-Pad Tilting-Pad Bearing, ASLE Transactions 22 (2) (1979) 113–124.

[26] L. E. Rodriguez, D. W. Childs, Frequency Dependency of Measured and Predicted Rotordynamic Coefficients for a Load-on-Pad Flexible-Pivot Tilting-Pad Bearing, ASME Journal of Tribology 128 (2006) 388–395.

[27] J. K. Parsell, P. E. Allaire, L. E. Barrett, Frequency Effects in Tilting-Pad Journal Bearing Dynamic Coefficients, ASLE Trans. 26 (2) (1983) 222–227.

[28] J. Thomsen, Vibrations and Stability - Advanced Theory, Analysis and Tools, Springer, Berlin, Germany, 2003.

[29] J. W. Lund, Review of the Concept of Dynamic Coefficients for Fluid Film Journal Bearings, ASME Journal of Tribology 109 (1987) 37–41.

[30] L. L. Earles, A. B. Palazzolo, R. W. Armentrout, A Finite Element Approach to Pad Flexibility Effects in Tilt Pad Journal Bearings: Part II - Assembled Bearing and System Analysis, ASME Journal of Tribology 112 (1990) 178–182.

[31] Z. Yan, L. Wang, G. Qiao, T. Zheng, An Analytical Model for Complete Dynamical Coefficients of a Tilting-Pad Journal Bearing, Tribology International 43 (2010) 7–15.

[32] T. Someya, Journal Bearing Databook, Springer Verlag, Berlin, Germany, 1989.

[33] M. F. White, S. H. Chan, The Subsynchronous Dynamic Behaviour of Tilting-Pad Journal Bearings, ASME Journal of Tribology 114 (1) (1992) 167–173.

[34] J. W. Lund, L. B. Pedersen, The Influence of Pad Flexibility on the Dynamic Coefficients of a Tilting-Pad Journal Bearing, ASME Journal of Tribology 109 (1987) 65–70.

[35] L. L. Earles, A. B. Palazzolo, R. W. Armentrout, A Finite Element Approach to Pad Flexibility Effects in Tilt Pad Journal Bearings: Part I - Single Pad Analysis, ASME Journal of Tribology 112 (1990) 169–177.

[36] H. Desbordes, M. Fillon, C. Chan Hew Wai, J. Frêne, Dynamic Analysis of Tilting-Pad Journal Bearings - Influence of Pad Deformations, ASME Journal of Tribology 116 (1994) 621–627.

[37] H. Desbordes, M. Fillon, J. Frêne, The Effects of Three-Dimensional Pad Deformations on Tilting-Pad Journal Bearings Under Dynamic Loading, ASME Journal of Tribology 117 (1995) 389–384.

[38] R. K. Gadangi, A. B. Palazzolo, Transient Analysis of Tilt Pad Journal Bearings Including Effects of Pad Flexibility and Fluid Film Temperature, ASME Journal of Tribology 117 (1995) 302–307.

[39] P. Monmousseau, M. Fillon, Frequency Effects on the TEHD Behavior of a Tilting-Pad Journal Bearing Under Dynamic Loading, Journal of Tribology 121 (2) (1999) 321–326.

[40] R. Brancati, E. Rocca, R. Russo, Non-linear Stability Analysis of a Rigid Rotor on Tilting Pad Journal Bearings, Tribology International 29 (7) (1996) 571–578.

[41] G. Qiao, L. Wang, T. Zheng, Linear Stability Analysis of a Tilting-Pad Journal Bearing System, ASME Journal of Tribology 129 (2007) 348–353.

[42] R. Klumpp, Die Eigenschaften von Kippsegment-Radiallagern, Konstruktion 28 (8) (1976) 320–324.

[43] W. Dmockowski, Dynamic Properties of Tilting-Pad Journal Bearings: Experimental and Theoretical Investigation of Frequency Effects due to Pivot Flexibility, ASME Journal of Engineering for Gas Turbines and Power 129 (2007) 865–869.

[44] I. F. Santos, A. Scalabrin, Control System Design for Active Lubrication with Theoretical and Experimental Examples, ASME Journal of Engineering for Gas Turbine and Power 125 (2003) 75–80.

[45] R. Stanway, C. R. Burrows, Active Vibration Control of a Flexible Rotor on Flexibly-Mounted Journal Bearings, Journal of Dynamic Systems, Measurement, and Control 103 (1981) 383–388.

[46] H. Ulbrich, J. Althaus, Actuator Design for Rotor Control, in: 12th Biennial ASME Conference on Vibration and Noise, 1989, pp. 17–22.

[47] J. Althaus, S. Fürst, H. Ulbrich, Aktive lagerabstützung zur dämpfung biegeelastischer rotoren, in: VDI-Berichte, Nr. 787, 1989, pp. 201–218.

[48] H. Ulbrich, J. Althaus, Active Chamber System as Adjusting Element for Controlling Rotors, Zeitschrift fur Angewandte Mathematik und Mechanik 70 (4) (1990) 148–150.

[49] I. F. Santos, Active Tilting-Pad Bearings - Theory and Experiment, VDI-Verlag, Düsseldorf, Germany, 1993.

[50] A. B. Palazzolo, R. R. Lin, R. M. Alexander, A. F. Kascak, J. Montague, Test and Theory for Piezoelectric Actuators - Active Vibration Control of Rotating Machinery, Trans. Of ASME, Journal of Vibration and Accoustics 113 (1991) 167–175.

[51] D. C. Deckler, R. J. Veillette, M. J. Braun, F. K. Choy, Simulation and Control of an Active Tilting-Pad Journal Bearing, STLE Tribology Trans. 47 (2004) 440–458.

[52] A. Wu, Z. Cai, M. S. de Queiroz, Model-Based Control of Active Tilting-Pad Bearings, IEEE/ASME Transactions on Mechatronics 12 (6) (2007) 689–695.

[53] L. Sun, J. M. Krodkiewski, Experimental Investigation of Dynamic Properties of an Active Journal Bearing, Journal of Sound and Vibration 230 (5) (2000) 1103–1117.

[54] S. Glavatskih, E. Höglund, Tribotronics - Towards Active Tribology, Tribology International 41 (2008) 934–939.

[55] I. F. Santos, F. H. Russo, Tilting-Pad Journal Bearings with Electronic Radial Oil Injection, ASME Journal of Tribology 120 (1998) 583–594.

[56] I. F. Santos, Design and Evaluation of Two Types of Active Tilting-Pad Journal Bearings, in: IUTAM Symposium - The Active Control of Vibration, Mechanical Engineering Publications Limited, 1995, pp. 79–87.

[57] P. Klit, J. W. Lund, Calculation of the Dynamic Coefficients of a Journal Bearing, Using a Variational Approach, ASME Journal of Tribology 108 (1986) 421–424.

[58] N. Heinrichson, I. F. Santos, Reducing Friction in Tilting-Pad Bearings by the Use of Enclosed Recesses, ASME Journal of Tribology 130 (1) (2008) 1–9.

[59] M. J. Braun, Y. M. Zhou, F. K. Choy, Transient Flow Patterns and Pressures Characteristics in a Hydrostatic Pocket, ASME Journal of Tribology 116 (1994) 139–146.

[60] M. J. Braun, Dzodzo, Three-Dimensional Flow and Pressure Patterns in a Hydrostatic Journal Bearing Pocket, ASME Journal of Tribology 119 (1997) 711–719.

[61] I. F. Santos, R. Nicoletti, THD Analysis in Tilting-Pad Journal Bearings with Hybrid Lubrication., ASME Journal of Tribology 121 (4) (1998) 892–900.

[62] I. F. Santos, R. Nicoletti, Influence of Orifice Distribution on the Thermal and Static Properties of Hybridly Lubricated Bearings., International Journal of Solids and Structures 38 (2001) 2069–2081.

[63] R. Nicoletti, I. F. Santos, Linear and Non-Linear Control Techniques Applied to Actively-Lubricated Journal Bearings, Journal of Sound and Vibration 260 (2003) 927–947.

[64] I. F. Santos, F. Y. Watanabe, Compensation of Cross-Coupling Stiffness and Increase of Direct Damping in Multirecess Journal Bearings Using Active Hybrid Lubrication: Part I - Theory, ASME Journal of Tribology 126 (1) (2004) 146–155.

[65] R. Nicoletti, I. F. Santos, Control System Design for Flexible Rotors Supported by Actively Lubricated Bearings, Journal of Vibration and Control 14 (3) (2008) 347–374.

[66] B. J. Hamrock, Fundamentals of Fluid Film Lubrication, McGraw-Hill Higher Education, New York, USA, 1994.

[67] R. W. Fox, A. T. McDonald, Introduction to Fluid Mechanics, J. Wiley & Sons., New York, USA, 1998.

[68] R. D. Cook, D. S. Malkus, M. E. Plesha, R. J. Witt, Concepts and Applications of Finite Element Analysis, J. Wiley & Sons., New York, USA, 2001.

[69] C. Geuzaine, J.-F. Remacle, Gmsh: a Three-Dimensional Finite Element Mesh Generator with Built-In Pre- and Post-Processing Facilities, International Journal for Numerical Methods in Engineering 79 (11) (2009) 1309–1311.

[70] I. F. Santos, R. Nicoletti, A. Scalabrin, Feasibility of Applying Active Lubrication to Reduce Vibration in Industrial Compressors, ASME Journal of Engineering for Gas Turbine and Power 126 (4) (2004) 888–894.

# Appendices

# Appendix A

# Software implementation

Numerical simulations with tilting pad journal bearings may require many different operations in different sequences. Furthermore, they require direct access to details in the model, which are generally not accessible in commercial software. In recognition of this, a scripting language has been developed specifically for bearing simulations. Subroutines may be called in a user defined sequence, and the results may be post processed as the user sees fit. Generally, the output consists of a nodal result file with ending ".nsol" along with several output files containing data such as rotor position and valve flow. The ".nsol" files are post-processed[1] and subsequently read by Gmsh [69] for production of nodal solution plots, e.g., plots of pressure and nodal displacement.

To run a bearing simulation, the user must create a mesh file and an input file. The mesh file contains nodal positions and connectivity information. The input file contains a reference to the mesh file, as well as the commands for the program. Per default, when the program is run, a proprietary variable file is created. This file stores variables that are declared when running the program. Each variable is assigned a line in the variable file. This feature is inspired from the .php language, and brings the advantage that a variables type and size does not need to be know a priori. In addition to the mandatory files, the user may include auxiliary files. For instance, it may be useful to compute the mode-shapes for the pads in one simulation, and then save them for re-use in other simulations. Also, it may be useful to save the static equilibrium state in a file for later use.

Figure A.1 shows a schematic of the flow of information. The user created script file "myscript.scr" contains call to subroutines, as well as references to the mesh file "mymesh.i" and the proprietary variable file "myscript.scr.vars". Also, in this case, it refers to two auxiliary variable files; "aux1.vars" and "aux2.vars".

## A.1 Example input files

An example of an input file is shown below. The script file computes synchronously reduced dynamic coefficients for a range of rotational speeds and control gains. The condensation frequency is set to match the rotational speed. Also, the eigenvalues are computed at each rotational speed and set of control gains. Again, it is stressed that the eigenvalues have nothing to do with the condensation frequency. The rotors structural stiffness and damping matrices are set to nil, but a diagonal mass matrix is defined.

[1] Post processing is done with a simple command line tool developed by the author.

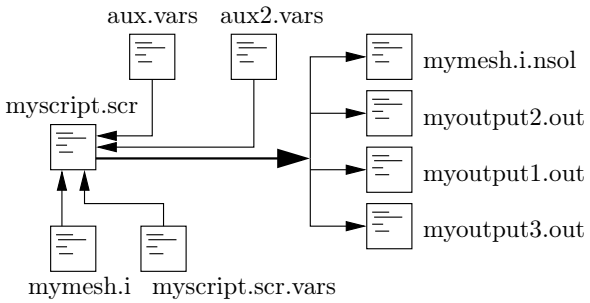


Figure A.1: A simple flowchart, illustrating the flow of information.

```
READ mekmulti_mg.i !Read mesh file for one pad, including nodal boundary conditions
RUN COPYPAD 4      !Copy the pad to generate a total of four pads
RUN INIT           !Initialise
RUN INITFLUID      !Initialise fluid
RUN INITSTRUCT     !Initialise solid
RUN SOLIDBC PERMANENT !Impose permanent boundary conditions
SET NEWMARK OUTPUT NSOL NFR 5 !Output 5 nodal frames in the newmark algorithm.
SET NEWMARK OUTPUT ORBIT NFR 100 !Output 5 orbit frames in the newmark algorithm.
SET NEWMARK OUTPUT SERVO NFR 100 !Output 5 servo-valve frames in the newmark algorithm.
SET NR OUTPUT NSOL ON !Toggle nodal output on for newton-raphson iterations
SET NR OUTPUT ORBIT ON !Toggle rotor output on for newton-raphson iterations
SET NR OUTPUT SERVO ON !Toggle servo-valve output on for newton-raphson iterations
CLEARFILE response.out !Clear or create file
CLEARFILE frequency.out !Clear or create file
CLEARFILE eigvals_01_re.out !Clear or create file
CLEARFILE eigvals_01_im.out !Clear or create file
CLEARFILE eigvals_01_TVEL_re.out !Clear or create file
CLEARFILE eigvals_01_TVEL_im.out !Clear or create file

RUN WRITEHEADER !Write header in mekmulti.i.nsol

SET ROTOR LOAD STATIC 0.0 0.0 !Set static lateral rotor load to nil
SET ROTOR K 1 1 0.0 !Set rotor 2X2 stiffness matrix to zero
SET ROTOR K 1 2 0.0
SET ROTOR K 2 1 0.0
SET ROTOR K 2 2 0.0

SET ROTOR M 1 1 100.0 !Set rotor 2X2 mass matrix
SET ROTOR M 1 2   0.0
SET ROTOR M 2 2   0.0
SET ROTOR M 2 2 100.0

SET ROTOR C 1 1   0.0 !Set rotor 2X2 damping matrix
SET ROTOR C 1 2   0.0
SET ROTOR C 2 2   0.0
SET ROTOR C 2 2   0.0


INCLUDEVAR mekmulti_mg_modeshapes_16modes.vars !Include file with previously computed solid modeshapes

SET TVEL 31.415926535 !Set the tangential velocity of the journal

RUN PRELOAD 25.0E-6 !Preload the pads

!Define pads (i.e., relate elements to a pad number)
SET PAD 1 0   90
SET PAD 2 90  180
SET PAD 3 180 270
```

```
SET PAD 4 270 360

!Declare variables...

VAR $FR
VAR $COUNTER
VAR $PRELOAD
VAR $EQ
VAR $TVEL
VAR $RUNME
VAR $RUNME2
VAR $RUNME3
VAR $NN
VAR $RESIDUAL
VAR $MAXREAL
VAR $MODSOL1
VAR $MODSOL2
VAR $MODSOL3
VAR $MODSOL4
VAR $EIGVALS_REAL
VAR $EIGVALS_IMAG
VAR $VGAIN
VAR $DGAIN
VAR $SHAPES_REAL
VAR $SHAPES_IMAG

!These variables are already declared and defined in mekmulti_mg_modeshapes_16modes.vars,
!so we do not declare them here.
!VAR $PAD_1_MODES
!VAR $PAD_1_FREQS
!VAR $PAD_2_MODES
!VAR $PAD_2_FREQS
!VAR $PAD_3_MODES
!VAR $PAD_3_FREQS
!VAR $PAD_4_MODES
!VAR $PAD_4_FREQS
VAR $PADMODES
VAR $STOP
VAR $STOP2
VAR $INDEX1
VAR $INDEX2
VAR $INDEX3
VAR $INDEX4
VAR $ROTOR_D_X

$INDEX1 = 1
$INDEX2 = 46860
$INDEX3 = $INDEX2 + 1
$INDEX4 = $INDEX2 * 2

!If we didn't have the solid mode shapes from mekmulti_mg_modeshapes_16modes.vars, we could
!compute them here.
!RUN MODAL 4 1 $PAD_1_FREQS $PAD_1_MODES
!RUN MODAL 4 2 $PAD_2_FREQS $PAD_2_MODES
!RUN MODAL 4 3 $PAD_3_FREQS $PAD_3_MODES
!RUN MODAL 4 4 $PAD_4_FREQS $PAD_4_MODES

!Generate vector with all modeshapes, pad after pad.
$PADMODES = $PAD_1_MODES(1:93720) & $PAD_2_MODES(1:93720)
$PADMODES = $PADMODES & $PAD_3_MODES(1:93720)
$PADMODES = $PADMODES & $PAD_4_MODES(1:93720)


!Set boolean variable
$RUNME = T

!Set integer variable
$COUNTER = 0
```

```
!We already have a good initial guess for the NR algorithm, but if we needed it, we could get it here.
!RUN COMBINATORICS 5 2 $PAD_1_MODES 50E-6 5E-6 $RESIDUAL 0 $MAXREAL $MODSOL1
!RUN COMBINATORICS 5 2 $PAD_2_MODES 50E-6 5E-6 $RESIDUAL 0 $MAXREAL $MODSOL2
!RUN COMBINATORICS 5 2 $PAD_3_MODES 50E-6 5E-6 $RESIDUAL 0 $MAXREAL $MODSOL3
!RUN COMBINATORICS 5 2 $PAD_4_MODES 50E-6 5E-6 $RESIDUAL 0 $MAXREAL $MODSOL4

!Initial guess for NR algorithm (modal coordinates)
$MODSOL1 = [-5.5E-4;9.5E-5]
$MODSOL2 = [-5.5E-4;-9.5E-5]
$MODSOL3 = [-5.5E-4;-9.5E-5]
$MODSOL4 = [5.5E-4;-9.5E-5]

!Apply initial guess
SET D MODAL $PAD_1_MODES $INDEX1 $INDEX2 $MODSOL1(1) 0
SET D MODAL $PAD_1_MODES $INDEX3 $INDEX4 $MODSOL1(2) 1
SET D MODAL $PAD_2_MODES $INDEX1 $INDEX2 $MODSOL2(1) 1
SET D MODAL $PAD_2_MODES $INDEX3 $INDEX4 $MODSOL2(2) 1
SET D MODAL $PAD_3_MODES $INDEX1 $INDEX2 $MODSOL3(1) 1
SET D MODAL $PAD_3_MODES $INDEX3 $INDEX4 $MODSOL3(2) 1
SET D MODAL $PAD_4_MODES $INDEX1 $INDEX2 $MODSOL4(1) 1
SET D MODAL $PAD_4_MODES $INDEX3 $INDEX4 $MODSOL4(2) 1

!Set variables
$TVEL = 0.0
$FR = 0.0

!Begin while loop
WHILE $RUNME3

    !Increment variables
    $TVEL = $TVEL + 0.031415926535
    $FR = $FR + 0.62831853

    !Set tangential velocity
    SET TVEL $TVEL

    !Find equilibrium for pseudo modal reduced model.
    !Static lateral load is nil, so equilibrium does not depend on displacement gain.

    RUN NRMODAL 10 $EQ 8 $PADMODES

    !Set variable
    $DGAIN = -2000000.0

    !Set boolean variable
    $RUNME = T

    !Begin while loop
    WHILE $RUNME

       !Set variable
       $VGAIN = -2000.00

       !Set displacement (proportional) gains
       SET SERVOVALVE 1 DGAIN $DGAIN
       SET SERVOVALVE 2 DGAIN $DGAIN

       !Set boolean variable
       $RUNME2 = T

       !Begin while loop
       WHILE $RUNME2

           !Set velocity (derivative) gains
           SET SERVOVALVE 1 VGAIN $VGAIN
           SET SERVOVALVE 2 VGAIN $VGAIN
```

```
         !Allow rotor motion
          SET ROTOR FREE

         !Compute eigenvalues for pseudo modal reduced system
          RUN EIGMODAL 8 $PADMODES $EIGVALS_REAL $EIGVALS_IMAG $SHAPES_REAL $SHAPES_IMAG $MAXREAL
          SET ROTOR LOCK

          !FIRST MODESHAPE IS IN SHAPES_REAL(13:24), second is in SHAPES_REAL(37:48) and so on

          !Write the computed eigenvalues to files
          WRITE $EIGVALS_REAL eigvals_01_TVEL_re.out
          WRITE $EIGVALS_IMAG eigvals_01_TVEL_im.out

          !Set frequency for dynamic condensation
          SET DC FREQUENCY $FR !0Hz

          !Perform harmonic dynamic condensation for pseudo modal reduced system
          RUN DCMODAL 1 8 $PADMODES

         !Write harmonic response to file
          WRITE DC RESPONSE  response.out

          !Increment variable
          $VGAIN = $VGAIN + 500.0

         !Evaluate boolean variable
          $STOP2 = $VGAIN > 4001

         !Evaluate boolean variable. Stop loop?
          IF $STOP2
            $RUNME2 = F
          END_IF

         !End of while loop
       END_WHILE

       !Increment variables
       $COUNTER = $COUNTER + 1
       $DGAIN = $DGAIN + 200000.0

       !Evaluate boolean variable
       $STOP = $DGAIN > 2000001.0
       IF $STOP
         $RUNME = F
       END_IF

       !Write text to file
       WRITE TEXT DGAIN_INCREMENT eigvals.out

       !End of while loop
   END_WHILE

   !Evaluate boolean variable
   $STOP = $TVEL > 0.3141

   !Set boolean variable
   $RUNME3 = T

   !Evaluate boolean variable. Stop loop?
   IF $STOP
      $RUNME3 = F
   END_IF

   !End of while loop
END_WHILE

!Finish script
FINISH
```

# Appendix B

# Detailed derivation of dimensionless numbers

## B.1 The solid

Let us restate the expressions for the solid stiffness and mass matrices, as well as the force vector.

$$
\begin{aligned}
K_{\underline{s}nm} &= \sum_{i,j,k,l=1}^{3} \int_{\Pi} L_{ijkl} \frac{1}{4} \left( \frac{\partial \psi_{km}}{\partial x_l} + \frac{\partial \psi_{lm}}{\partial x_k} \right) \left( \frac{\partial \psi_{in}}{\partial x_j} + \frac{\partial \psi_{jn}}{\partial x_i} \right) d\Pi, \quad m, n \in \mathbb{S}^3 \\
M_{\underline{s}nm} &= \sum_{i=1}^{3} \int_{\Pi} \rho \psi_{im} \psi_{in} d\Pi, \quad m, n \in \mathbb{S}^3 \\
f_n &= \sum_{i=1}^{3} \int_{\Lambda} \sum_{m \in \mathbb{S}^3} T_{im} \phi_m \psi_{in} d\Lambda, \quad n \in \mathbb{S}^3
\end{aligned}
$$

We shall seek to write these in a form, where the dimensional information is contained in a scalar factor. We introduce dimensionless space

$$
\begin{aligned}
& x_i = L \tilde{x}_i, \quad i = 1, 2, 3 \\
& \frac{\partial}{\partial x_i} = \frac{\partial \tilde{x}_i}{\partial x_i} \frac{\partial}{\partial \tilde{x}_i} = \frac{1}{L} \frac{\partial}{\partial \tilde{x}_i} \\
& \frac{\partial^2}{\partial x_i \partial x_j} = \frac{1}{L^2} \frac{\partial^2}{\partial \tilde{x}_i \partial \tilde{x}_j}, \quad i, j = 1, 2, 3 \\
& d\Pi = L^3 d\tilde{\Pi} \\
& d\Lambda = L^2 d\tilde{\Lambda}
\end{aligned} \tag{B.1}
$$

Similarly we introduce dimensionless time.

$$\begin{aligned}\Omega t &= \tilde{t} \\ \frac{\partial}{\partial t} &= \frac{\partial \tilde{t}}{\partial t}\frac{\partial}{\partial \tilde{t}} = \Omega\frac{\partial}{\partial \tilde{t}} \\ \frac{\partial^2}{\partial t^2} &= \Omega^2\frac{\partial^2}{\partial \tilde{t}^2}\end{aligned} \tag{B.2}$$

Thus, now space is measured in fractions of a characteristic length $L$, and speed is measured in terms of the rotational speed of the rotor $\Omega$. Furthermore, we write the dimensionless surface traction as

$$T_{im} = \frac{F}{L^2}\tilde{T}_{im}, \quad i = 1,2,3, \quad m \in \mathbb{S} \tag{B.3}$$

$$\tag{B.4}$$

So traction is measured in terms of a characteristic force $F$, and the characteristic length $L$. Restating the expression for the constitutive tensor for the solid, the dimensional information is readily available

$$L_{ijkl} = E\frac{1}{2(1+\nu)}\left(\delta_{ik}\delta_{jl} + \delta_{il}\delta_{jk} + \frac{2\nu}{1-2\nu}\delta_{ij}\delta_{kl}\right)$$

i.e.

$$L_{ijkl} = E\tilde{L}_{ijkl} \tag{B.5}$$

Now, substituting spatial derivatives with their dimensionless counterparts and by use of Eq. B.5, we may write

$$K_{\underline{s}nm} = \sum_{i,j,k,l=1}^{3}\int_{\Pi} E\tilde{L}_{ijkl}\frac{1}{4}\frac{1}{L^2}\left(\frac{\partial\psi_{km}}{\partial\tilde{x}_l} + \frac{\partial\psi_{lm}}{\partial\tilde{x}_k}\right)\left(\frac{\partial\psi_{in}}{\partial\tilde{x}_j} + \frac{\partial\psi_{jn}}{\partial\tilde{x}_i}\right)L^3 d\tilde{\Pi}, \quad m,n \in \mathbb{S}^3 \tag{B.6}$$

or simply

$$K_{\underline{s}nm} = EL\tilde{K}_{\underline{s}nm} \tag{B.7}$$

with

$$\tilde{K}_{\underline{s}nm} = \sum_{i,j,k,l=1}^{3}\int_{\Pi} \tilde{L}_{ijkl}\frac{1}{4}\left(\frac{\partial\psi_{km}}{\partial\tilde{x}_l} + \frac{\partial\psi_{lm}}{\partial\tilde{x}_k}\right)\left(\frac{\partial\psi_{in}}{\partial\tilde{x}_j} + \frac{\partial\psi_{jn}}{\partial\tilde{x}_i}\right)d\tilde{\Pi}, \quad m,n \in \mathbb{S}^3 \tag{B.8}$$

Similarly we may write the mass matrix as

$$M_{\underline{s}nm} = \rho L^3\tilde{M}_{\underline{s}nm}, \quad m,n \in \mathbb{S}^3 \tag{B.9}$$

where

$$\tilde{M}_{\underline{s}nm} = \sum_{i=1}^{3}\int_{\Pi}\psi_{im}\psi_{in}d\tilde{\Pi}, \quad m,n \in \mathbb{S}^3 \tag{B.10}$$

The force vector is readily written as fractions of the characteristic force $F$, so that

$$f_n = F\tilde{f}_n, \quad n \in \mathbb{S}^3 \tag{B.11}$$

where

$$\tilde{f}_n = \sum_{i=1}^{3} \int_\Lambda \sum_{m\in\mathbb{S}^3} \tilde{T}_{im}\phi_m\psi_{in}d\tilde{\Lambda}, \quad n \in \mathbb{S}^3 \tag{B.12}$$

Furthermore, through substitution of dimensionless time and space, the dimensionless displacement, velocity and acceleration can be written as

$$\begin{aligned} d_n &= L\tilde{d}_n, \quad n \in \mathbb{S}^3 \\ \dot{d}_n &= L\Omega\frac{\partial\tilde{d}_n}{\partial\tilde{t}} \\ \ddot{d}_n &= L\Omega^2\frac{\partial^2\tilde{d}_n}{\partial\tilde{t}^2} \end{aligned} \tag{B.13}$$

## B.2 The fluid

Now, let us restate the expressions for the fluid system matrices and right hand side.

$$A_{mn} = \int_\Phi \frac{1}{12}\sum_{i=1}^{2}\frac{\partial\phi_m}{\partial\chi_i}\frac{\left(\sum_{n\in\mathbb{F}}h_n\phi_n\right)^3}{\mu}\frac{\partial\phi_n}{\partial\chi_i}d\Phi + \int_\Phi \sum_{i=1}^{N_{\underline{o}}}\frac{\sum_{k\in\mathbb{F}}g_{ik}\phi_k}{4\mu l_{\underline{0}i}}\phi_n\phi_m d\Phi$$

,

$$W_{mi} = -\int_\Phi \frac{\sum_{n\in\mathbb{F}}g_{in}\phi_n}{4\mu l_{\underline{0}i}}\phi_m d\Phi, \quad i = 1, 2, ..., N_{\underline{o}}$$

and with the Reynolds boundary condition invoked a priori

$$r_m = -\int_\Phi \frac{U}{2}\left(\sum_{n\in\mathbb{F}}h_n\frac{\partial\phi_n}{\partial\chi_2}\right)\phi_m d\Phi - \int_\Phi\left(\sum_{n\in\mathbb{F}}\dot{h}_n\phi_n\right)\phi_m d\Phi$$

Again, we introduce dimensionless space, but now in the curvilinear coordinates

$$\begin{aligned} &\chi_i = L\tilde{\chi}_i, \quad i = 1, 2, 3 \\ &\frac{\partial}{\partial\chi_i} = \frac{\partial\tilde{\chi}_i}{\partial\chi_i}\frac{\partial}{\partial\tilde{\chi}_i} = \frac{1}{L}\frac{\partial}{\partial\tilde{\chi}_i} \\ &\frac{\partial^2}{\partial\chi_i\partial\chi_j} = \frac{1}{L^2}\frac{\partial^2}{\partial\tilde{\chi}_i\partial\tilde{\chi}_j}, \quad i, j = 1, 2, 3 \\ &d\Phi = L^2 d\tilde{\Phi} \qquad\qquad h = L\tilde{h} \end{aligned} \tag{B.14}$$

We introduce the dimensionless film thickness, pipe inlet length and flow profile shape function as

$$\begin{aligned} h &= L\tilde{h} \\ l_{\underline{0}i} &= L\tilde{l}_{\underline{0}i}, \quad i = 1, 2, ..., N_{\underline{o}} \\ g_{ik} &= L^2\tilde{g}_{ik}, \quad i = 1, 2, ..., N_{\underline{o}}, \quad k \in \mathbb{F} \end{aligned} \tag{B.15}$$

Now, applying these substitutions, the pressure system matrix can be written as

$$A_{mn} = \int_\Phi \frac{1}{12}\sum_{i=1}^{2}\frac{1}{L}\frac{\partial\phi_m}{\partial\tilde{\chi}_i}\frac{\left(\sum_{n\in\mathbb{F}} L\tilde{h}_n\phi_n\right)^3}{\mu}\frac{1}{L}\frac{\partial\phi_n}{\partial\tilde{\chi}_i}L^2 d\tilde{\Phi} + \int_\Phi \sum_{i=1}^{N_{\underline{o}}}\frac{\sum_{k\in\mathbb{F}} L^2\tilde{g}_{ik}\phi_k}{4\mu L\tilde{l}_{\underline{0}i}}\phi_n\phi_m L^2 d\tilde{\Phi} \tag{B.16}$$

Or simply

$$A_{mn} = \frac{L^3}{\mu}\tilde{A}_{mn} \tag{B.17}$$

where

$$A_{mn} = \int_\Phi \frac{1}{12}\sum_{i=1}^{2}\frac{\partial\phi_m}{\partial\tilde{\chi}_i}\left(\sum_{n\in\mathbb{F}}\tilde{h}_n\phi_n\right)^3\frac{\partial\phi_n}{\partial\tilde{\chi}_i}d\tilde{\Phi} + \int_\Phi \sum_{i=1}^{N_{\underline{o}}}\frac{\sum_{k\in\mathbb{F}}\tilde{g}_{ik}\phi_k}{4\tilde{l}_{\underline{0}i}}\phi_n\phi_m d\tilde{\Phi} \tag{B.18}$$

Likewise we may write the injection pressure matrix as

$$W_{mi} = \frac{L^3}{\mu}\tilde{W}_{mi} \tag{B.19}$$

where

$$\tilde{W}_{mi} = -\int_\Phi \frac{\sum_{n\in\mathbb{F}}\tilde{g}_{in}\phi_n}{4\tilde{l}_{\underline{0}i}}\phi_m d\tilde{\Phi}, \quad i = 1, 2, ..., N_{\underline{o}} \tag{B.20}$$

Furthermore the right hand side can be written as

$$r_m = L^3\Omega\tilde{r}_m \tag{B.21}$$

where

$$r_m = -\int_\Phi \frac{\tilde{U}}{2}\left(\sum_{n\in\mathbb{F}}\tilde{h}_n\frac{\partial\phi_n}{\partial\tilde{\chi}_2}\right)\phi_m d\Phi - \int_\Phi\left(\sum_{n\in\mathbb{F}}\frac{\partial\tilde{h}_n}{\partial\tilde{t}}\phi_n\right)\phi_m d\tilde{\Phi} \tag{B.22}$$

We measure the flow and its time derivatives in fractions of the leak flow as

$$\begin{aligned} q_{\underline{v}} &= q_{\underline{L}}\tilde{q}_{\underline{v}} \\ \dot{q}_{\underline{v}} &= q_{\underline{L}}\frac{\partial\tilde{q}_{\underline{v}}}{\partial\tilde{t}} \\ \ddot{q}_{\underline{v}} &= q_{\underline{L}}\frac{\partial^2\tilde{q}_{\underline{v}}}{\partial\tilde{t}^2} \end{aligned} \tag{B.23}$$

With this, we rewrite the right hand side of the injection equations as

$$r_{\underline{\underline{\text{inj}}}m} = q_{\underline{\text{L}}}\tilde{r}_{\underline{\underline{\text{inj}}}m}, \quad m = 1, 2, ...N_{\underline{\text{o}}} \tag{B.24}$$

where, if the leak flow is the same for all valves, we have

$$\tilde{r}_{\underline{\underline{\text{inj}}}m} = \left\{ \begin{array}{c} 1 + \tilde{q}_{\underline{\text{v}}1} \\ 1 - \tilde{q}_{\underline{\text{v}}1} \\ 1 + \tilde{q}_{\underline{\text{v}}2} \\ 1 - \tilde{q}_{\underline{\text{v}}2} \\ ... \end{array} \right\} \tag{B.25}$$

if this is not the case, we can write the vector components as fractions of the leak flow of one of the valves, e.g., the first one as

$$\tilde{r}_{\underline{\underline{\text{inj}}}m} = \left\{ \begin{array}{c} 1 + \tilde{q}_{\underline{\text{v}}1} \\ 1 - \tilde{q}_{\underline{\text{v}}1} \\ q_{\underline{\text{L}}2}/q_{\underline{\text{L}}1} + \tilde{q}_{\underline{\text{v}}2} \\ q_{\underline{\text{L}}2}/q_{\underline{\text{L}}1} - \tilde{q}_{\underline{\text{v}}2} \\ ... \end{array} \right\} \tag{B.26}$$

The dimensionless pressure and its time derivatives can be written in terms of the characteristic force and length as

$$\begin{aligned} p_m &= \frac{F}{L^2}\tilde{p}_m, \quad m \in \mathbb{F} \\ p_m &= \frac{F}{L^2}\Omega\frac{\partial\tilde{p}_m}{\partial\tilde{t}}, \quad m \in \mathbb{F} \\ p_m &= \frac{F}{L^2}\Omega^2\frac{\partial^2\tilde{p}_m}{\partial\tilde{t}^2}, \quad m \in \mathbb{F} \end{aligned} \tag{B.27}$$

Similarly, the injection pressure is written as

$$\begin{aligned} p_{\underline{\underline{\text{inj}}}m} &= \frac{F}{L^2}\tilde{p}_{\underline{\underline{\text{inj}}}m}, \quad m \in \mathbb{F} \\ p_{\underline{\underline{\text{inj}}}m} &= \frac{F}{L^2}\Omega\frac{\partial\tilde{p}_{\underline{\underline{\text{inj}}}m}}{\partial\tilde{t}}, \quad m \in \mathbb{F} \\ p_{\underline{\underline{\text{inj}}}m} &= \frac{F}{L^2}\Omega^2\frac{\partial^2\tilde{p}_{\underline{\underline{\text{inj}}}m}}{\partial\tilde{t}^2}, \quad m \in \mathbb{F} \end{aligned} \tag{B.28}$$

## B.3 The rotor

Let us restate the rotor equations

$$\left[ \begin{array}{cc} k_{\underline{\text{r}}11} & k_{\underline{\text{r}}12} \\ k_{\underline{\text{r}}21} & k_{\underline{\text{r}}22} \end{array} \right] \left\{ \begin{array}{c} d_{\underline{\text{r}}1} \\ d_{\underline{\text{r}}2} \end{array} \right\} + \left[ \begin{array}{cc} c_{\underline{\text{r}}11} & c_{\underline{\text{r}}12} \\ c_{\underline{\text{r}}21} & c_{\underline{\text{r}}22} \end{array} \right] \left\{ \begin{array}{c} \dot{d}_{\underline{\text{r}}1} \\ \dot{d}_{\underline{\text{r}}2} \end{array} \right\} + \left[ \begin{array}{cc} m_{\underline{\text{r}}} & 0 \\ 0 & m_{\underline{\text{r}}} \end{array} \right] \left\{ \begin{array}{c} \ddot{d}_{\underline{\text{r}}1} \\ \ddot{d}_{\underline{\text{r}}2} \end{array} \right\} = \left\{ \begin{array}{c} f_{\underline{\text{r}}1} \\ f_{\underline{\text{r}}2} \end{array} \right\}$$

or less explicitly as

$$\mathbf{K}_{\underline{\text{r}}}\mathbf{d}_{\underline{\text{r}}} + \mathbf{C}_{\underline{\text{r}}}\dot{\mathbf{d}}_{\underline{\text{r}}} + \mathbf{M}_{\underline{\text{r}}}\ddot{\mathbf{d}}_{\underline{\text{r}}} = \mathbf{f}_{\underline{\text{r}}} \tag{B.29}$$

We introduce dimensionless rotor displacement, velocity and acceleration as

$$\begin{aligned} d_{\underline{\mathrm{r}}n} &= L\tilde{d}_{\underline{\mathrm{r}}n}, \quad n \in \mathbb{S}^3 \\ \dot{d}_{\underline{\mathrm{r}}n} &= L\Omega\frac{\partial\tilde{d}_{\underline{\mathrm{r}}n}}{\partial\tilde{t}} \\ \ddot{d}_{\underline{\mathrm{r}}n} &= L\Omega^2\frac{\partial^2\tilde{d}_{\underline{\mathrm{r}}n}}{\partial\tilde{t}^2} \end{aligned} \tag{B.30}$$

which allows us to rewrite the rotor equations as

$$k_{\underline{\mathrm{r}}}\tilde{\mathbf{K}}_{\underline{\mathrm{r}}}L\tilde{\mathbf{d}}_{\underline{\mathrm{r}}} + c_{\underline{\mathrm{r}}}\tilde{\mathbf{C}}_{\underline{\mathrm{r}}}L\Omega\frac{\partial\tilde{\mathbf{d}}_{\underline{\mathrm{r}}}}{\partial\tilde{t}} + m_{\underline{\mathrm{r}}}\tilde{\mathbf{M}}_{\underline{\mathrm{r}}}L\Omega^2\frac{\partial^2\tilde{\mathbf{d}}_{\underline{\mathrm{r}}}}{\partial\tilde{t}^2} = F\tilde{\mathbf{f}}_{\underline{\mathrm{r}}} \tag{B.31}$$

In all of the simulations presented in this thesis $k_{\underline{\mathrm{r}}11} = k_{\underline{\mathrm{r}}22} = k_{\underline{\mathrm{r}}}$, $k_{\underline{\mathrm{r}}12} = k_{\underline{\mathrm{r}}21} = 0$ and $c_{\underline{\mathrm{r}}11} = c_{\underline{\mathrm{r}}12} = c_{\underline{\mathrm{r}}21} = c_{\underline{\mathrm{r}}22} = 0$, so

$$\tilde{\mathbf{K}}_{\underline{\mathrm{r}}} = \begin{bmatrix} 1 & 0 \\ 0 & 1 \end{bmatrix}, \quad \tilde{\mathbf{D}}_{\underline{\mathrm{r}}} = \begin{bmatrix} 0 & 0 \\ 0 & 0 \end{bmatrix}, \quad \tilde{\mathbf{M}}_{\underline{\mathrm{r}}} = \begin{bmatrix} 1 & 0 \\ 0 & 1 \end{bmatrix} \tag{B.32}$$

## B.4 The valve

Let us restate the equations for the valves

$$\sum_{m\in\mathbb{F}} W_{mi}p_m + \sum_{m=1}^{N_{\underline{\mathrm{o}}}} Q_{im}p_{\underline{\mathrm{inj}}m} + \sum_{m=1}^{N_{\underline{\mathrm{o}}}} K_{\underline{\mathrm{pq}}im}p_{\underline{\mathrm{inj}}m} = r_{\underline{\mathrm{inj}}i}, \quad i = 1, 2, ...N_{\underline{\mathrm{o}}}$$

where, for the case of two coupled orifice arrays (pads), the pipe flow impedance matrix is defined as

$$Q_{in} = \begin{bmatrix} Q_{11} & Q_{12} \\ Q_{21} & Q_{22} \end{bmatrix} = \begin{bmatrix} \int_\Phi \frac{\sum_{n\in\mathbb{F}} g_{1n}\phi_n}{4\mu l_{\underline{\mathrm{o}}1}}d\Phi & \\ & \int_\Phi \frac{\sum_{n\in\mathbb{F}} g_{2n}\phi_n}{4\mu l_{\underline{\mathrm{o}}2}}d\Phi \end{bmatrix},$$

and the valve flow impedance matrix is defined as

$$K_{\underline{\mathrm{pq}}in} = \begin{bmatrix} K_{\underline{\mathrm{pq}}11} & K_{\underline{\mathrm{pq}}12} \\ K_{\underline{\mathrm{pq}}21} & K_{\underline{\mathrm{pq}}22} \end{bmatrix} = \begin{bmatrix} K_{\underline{\mathrm{pq}}} & -K_{\underline{\mathrm{pq}}} \\ -K_{\underline{\mathrm{pq}}} & K_{\underline{\mathrm{pq}}} \end{bmatrix} \tag{B.33}$$

and the right hand side consists of valve flows

$$r_{\underline{\mathrm{inj}}i} = \{r\}_{\underline{\mathrm{inj}}} = \begin{Bmatrix} q_{\underline{\mathrm{v}}} + q_{\underline{\mathrm{L}}} \\ -q_{\underline{\mathrm{v}}} + q_{\underline{\mathrm{L}}} \end{Bmatrix} \tag{B.34}$$

Considering the expression for the pipe flow impedance matrix, we may write

$$Q_{in} = \frac{L^3}{\mu}\tilde{Q}_{in} \tag{B.35}$$

where, for the case of two orifice arrays

$$\tilde{Q}_{in} = \begin{bmatrix} \tilde{Q}_{11} & \tilde{Q}_{12} \\ \tilde{Q}_{21} & \tilde{Q}_{22} \end{bmatrix} = \begin{bmatrix} \int_\Phi \frac{\sum_{n\in\mathbb{F}} \tilde{g}_{1n}\phi_n}{4\tilde{l}_{\underline{01}}} d\tilde{\Phi} & \\ & \int_\Phi \frac{\sum_{n\in\mathbb{F}} \tilde{g}_{2n}\phi_n}{4\tilde{l}_{\underline{02}}} d\tilde{\Phi} \end{bmatrix}, \tag{B.36}$$

and, readily,

$$K_{\underline{\mathrm{pq}}in} = K_{\underline{\mathrm{pq}}} \tilde{K}_{\underline{\mathrm{pq}}in}, \quad i = 1, 2, \quad n = 1, 2 \tag{B.37}$$

where, for the case of two orifice arrays

$$\tilde{K}_{\underline{\mathrm{pq}}in} = \begin{bmatrix} 1 & -1 \\ -1 & 1 \end{bmatrix} \tag{B.38}$$

Not that Eqs. (B.36) and (B.37) may be readily extended to cases with many orifice arrays, as the orifice arrays couple in pairs, and produce block diagonal matrices.

Consider the valve dynamic equation for valve $i$

$$\ddot{q}_{\underline{\mathrm{v}}i} + 2\xi_{\underline{\mathrm{v}}i}\omega_{\underline{\mathrm{v}}i}\dot{q}_{\underline{\mathrm{v}}i} + \omega^2_{\underline{\mathrm{v}}i} q_{\underline{\mathrm{v}}i} = \omega^2_{\underline{\mathrm{v}}i} K_{\underline{\mathrm{v}}i} u_{\underline{\mathrm{v}}i}$$

If the the valves are identical, the index $i$ on the parameters $\xi_{\underline{\mathrm{v}}i}$, $\omega_{\underline{\mathrm{v}}i}$ and $K_{\underline{\mathrm{v}}i}$ may be dropped.

As before, we define the control signal as that of a P-D controller with a constant reference signal. Thus for two valves responding to twodimensional lateral rotor movement, we have

$$\mathbf{u}_{\underline{\mathrm{v}}} = -\underbrace{\mathbf{G}_{\underline{\mathrm{P}}}}_{N_{\underline{\mathrm{v}}}\times 2} \mathbf{d}_{\underline{\mathrm{r}}} - \underbrace{\mathbf{G}_{\underline{\mathrm{D}}}}_{N_{\underline{\mathrm{v}}}\times 2} \dot{\mathbf{d}}_{\underline{\mathrm{r}}} + \mathbf{u}_{\underline{\mathrm{vr}}} \tag{B.39}$$

all results presented in this thesis apply te same control strategy, namely that of Eq. (5.2), thus

$$\mathbf{G}_{\underline{\mathrm{P}}} = G_{\underline{\mathrm{P}}} \begin{bmatrix} 1/\sqrt{2} & 1/\sqrt{2} \\ 1/\sqrt{2} & -1/\sqrt{2} \end{bmatrix} \tag{B.40}$$

and

$$\mathbf{G}_{\underline{\mathrm{D}}} = G_{\underline{\mathrm{D}}} \begin{bmatrix} 1/\sqrt{2} & 1/\sqrt{2} \\ 1/\sqrt{2} & -1/\sqrt{2} \end{bmatrix} \tag{B.41}$$

In general, we write

$$\begin{aligned} \mathbf{G}_{\underline{\mathrm{P}}} &= G_{\underline{\mathrm{P}}} \tilde{\mathbf{G}}_{\underline{\mathrm{P}}} \\ \mathbf{G}_{\underline{\mathrm{D}}} &= G_{\underline{\mathrm{D}}} \tilde{\mathbf{G}}_{\underline{\mathrm{D}}} \end{aligned} \tag{B.42}$$

where, in this special case,

$$\tilde{\mathbf{G}}_{\underline{\mathrm{P}}} = \tilde{\mathbf{G}}_{\underline{\mathrm{D}}} = \begin{bmatrix} 1/\sqrt{2} & 1/\sqrt{2} \\ 1/\sqrt{2} & -1/\sqrt{2} \end{bmatrix} \tag{B.43}$$

We write the reference signal vector as fractions of a characteristic voltage $u_{\underline{\mathrm{ch}}}$

$$\mathbf{u}_{\underline{\mathrm{vr}}} = u_{\underline{\mathrm{ch}}} \tilde{\mathbf{u}}_{\underline{\mathrm{vr}}} \tag{B.44}$$

with Eq. (B.42) and the introduction of dimensionless time, flow and rotor displacement, we get

$$\Omega^2 q_{\underline{\mathrm{L}}} \frac{\partial^2 \tilde{\mathbf{q}}_{\underline{\mathrm{v}}}}{\partial \tilde{t}^2} + 2\xi_{\underline{\mathrm{v}}}\omega_{\underline{\mathrm{v}}}\Omega \frac{\partial \tilde{\mathbf{q}}_{\underline{\mathrm{v}}}}{\partial \tilde{t}} + \omega^2_{\underline{\mathrm{v}}} q_{\underline{\mathrm{L}}} \tilde{\mathbf{q}}_{\underline{\mathrm{v}}} = -\omega^2_{\underline{\mathrm{v}}} K_{\underline{\mathrm{v}}} L G_{\underline{\mathrm{P}}} \tilde{\mathbf{G}}_{\underline{\mathrm{P}}} \tilde{\mathbf{d}}_{\underline{\mathrm{r}}} - \omega^2_{\underline{\mathrm{v}}} K_{\underline{\mathrm{v}}} \Omega L G_{\underline{\mathrm{D}}} \tilde{\mathbf{G}}_{\underline{\mathrm{D}}} \frac{\partial \tilde{\mathbf{d}}_{\underline{\mathrm{r}}}}{\partial \tilde{t}} + \omega^2_{\underline{\mathrm{v}}} K_{\underline{\mathrm{v}}} u_{\underline{\mathrm{ch}}} \tilde{\mathbf{u}}_{\underline{\mathrm{vr}}} \tag{B.45}$$

## B.5 The global system

Let us restate Eq. (2.84) in state space form.

$$\begin{bmatrix} \mathbf{0} & \begin{bmatrix} \mathbf{K}_{\underline{s}} & & & & \\ & \mathbf{K}_{\underline{r}} & & & \\ & & \mathbf{A} & \mathbf{W} & \\ & \mathbf{G}_{\underline{P}} & \mathbf{W}^T & \mathbf{Q}+\mathbf{K}_{\underline{pq}} & \mathbf{K}_{\underline{q\text{-}q}} \end{bmatrix} \\ \mathbf{I} & \begin{bmatrix} & & & \mathbf{0} & \end{bmatrix} \end{bmatrix} \begin{Bmatrix} \dot{\mathbf{d}} \\ \dot{\mathbf{d}}_{\underline{r}} \\ \dot{\mathbf{p}} \\ \dot{\mathbf{p}}_{\underline{inj}} \\ \dot{\mathbf{q}}_{\underline{v}} \\ \mathbf{d} \\ \mathbf{d}_{\underline{r}} \\ \mathbf{p} \\ \mathbf{p}_{\underline{inj}} \\ \mathbf{q}_{\underline{v}} \end{Bmatrix} + \begin{bmatrix} \begin{bmatrix} \mathbf{M}_{\underline{s}} & & \\ & \mathbf{M}_{\underline{r}} & \\ & & \mathbf{M}_{\underline{q\text{-}q}} \end{bmatrix} & \begin{bmatrix} \mathbf{D}_{\underline{r}} & \\ \mathbf{G}_{\underline{D}} & \\ & \mathbf{D}_{\underline{q\text{-}q}} \end{bmatrix} \\ \mathbf{0} & \begin{bmatrix} & \\ & -\mathbf{I} \end{bmatrix} \end{bmatrix} \begin{Bmatrix} \ddot{\mathbf{d}} \\ \ddot{\mathbf{d}}_{\underline{r}} \\ \ddot{\mathbf{p}} \\ \ddot{\mathbf{p}}_{\underline{inj}} \\ \dot{\mathbf{q}}_{\underline{v}} \\ \dot{\mathbf{d}} \\ \dot{\mathbf{d}}_{\underline{r}} \\ \dot{\mathbf{p}} \\ \dot{\mathbf{p}}_{\underline{inj}} \\ \dot{\mathbf{q}}_{\underline{v}} \end{Bmatrix} = \begin{Bmatrix} \mathbf{f} \\ \mathbf{f}_{\underline{r}} \\ \mathbf{r} \\ \mathbf{r}_{\underline{inj}} \\ \mathbf{u}_{\underline{vr}} \\ \mathbf{0} \end{Bmatrix}$$

$$\begin{bmatrix} \mathbf{0} & \begin{bmatrix} \mathbf{K}_{\underline{s}} & & & & & \\ & \mathbf{K}_{\underline{r}} & & & & \\ & & \mathbf{A} & \mathbf{W} & & \\ & & \mathbf{W}^T & \mathbf{Q} & \mathbf{K}_{\underline{pq}} & \\ & \mathbf{G}_{\underline{P}} & & & & \mathbf{K}_{\underline{q\text{-}q}} \end{bmatrix} \\ \mathbf{I} & \begin{bmatrix} & & & \mathbf{I} & -\mathbf{I} & \\ & & & \mathbf{0} & & \end{bmatrix} \end{bmatrix} \begin{Bmatrix} \dot{\mathbf{d}} \\ \dot{\mathbf{d}}_{\underline{r}} \\ \dot{\mathbf{p}} \\ \dot{\mathbf{p}}_{\underline{inj}} \\ \dot{\mathbf{p}}_{\underline{inj}} \\ \dot{\mathbf{q}}_{\underline{v}} \\ \mathbf{d} \\ \mathbf{d}_{\underline{r}} \\ \mathbf{p} \\ \mathbf{p}_{\underline{inj}} \\ \mathbf{p}_{\underline{inj}} \\ \mathbf{q}_{\underline{v}} \end{Bmatrix} + \begin{bmatrix} \begin{bmatrix} \mathbf{M}_{\underline{s}} & & \\ & \mathbf{M}_{\underline{r}} & \\ & & \mathbf{M}_{\underline{q\text{-}q}} \end{bmatrix} & \begin{bmatrix} \mathbf{D}_{\underline{r}} & \\ \mathbf{G}_{\underline{D}} & \\ & \mathbf{D}_{\underline{q\text{-}q}} \end{bmatrix} \\ \mathbf{0} & \begin{bmatrix} & \\ \mathbf{I} & \end{bmatrix} \end{bmatrix} \begin{Bmatrix} \ddot{\mathbf{d}} \\ \ddot{\mathbf{d}}_{\underline{r}} \\ \ddot{\mathbf{p}} \\ \ddot{\mathbf{p}}_{\underline{inj}} \\ \ddot{\mathbf{p}}_{\underline{inj}} \\ \dot{\mathbf{q}}_{\underline{v}} \\ \dot{\mathbf{d}} \\ \dot{\mathbf{d}}_{\underline{r}} \\ \dot{\mathbf{p}} \\ \dot{\mathbf{p}}_{\underline{inj}} \\ \dot{\mathbf{p}}_{\underline{inj}} \\ \dot{\mathbf{q}}_{\underline{v}} \end{Bmatrix} = \begin{Bmatrix} \mathbf{f} \\ \mathbf{f}_{\underline{r}} \\ \mathbf{r} \\ \mathbf{r}_{\underline{inj}} \\ \mathbf{u}_{\underline{vr}} \\ \mathbf{0} \\ \mathbf{0} \end{Bmatrix} \tag{B.46}$$

now, applying Eqs. (B.7), (B.9), (B.11), (B.13), (B.17), (B.19), (B.21), (B.27), (B.28) (B.31), (B.35), (B.45), (B.38) and redefining the dot-notation to mean

$$\dot{\cdot} = \frac{\partial}{\partial \tilde{t}} \tag{B.47}$$

we can write Eq. (B.46) as

$$\begin{bmatrix} \mathbf{0} & \begin{bmatrix} EL\tilde{\mathbf{K}}_{\underline{s}} & & & & & \\ & k_{\underline{r}}\tilde{\mathbf{K}}_{\underline{r}} & & & & \\ & & \frac{L^3}{\mu}\tilde{\mathbf{A}} & \frac{L^3}{\mu}\tilde{\mathbf{W}} & & \\ & & \frac{L^3}{\mu}\tilde{\mathbf{W}}^T & \frac{L^3}{\mu}\tilde{\mathbf{Q}} & K_{\underline{pq}}\tilde{\mathbf{K}}_{\underline{pq}} & \\ & G_{\underline{P}}\omega_{\underline{v}}^2 K_{\underline{v}}\tilde{\mathbf{G}}_{\underline{P}} & & & & \omega_{\underline{v}}^2\tilde{\mathbf{K}}_{\underline{q\text{-}q}} \end{bmatrix} \\ \mathbf{I} & \begin{bmatrix} & & & \mathbf{I} & -\mathbf{I} & \\ & & & \mathbf{0} & & \end{bmatrix} \end{bmatrix} \begin{Bmatrix} L\Omega\dot{\tilde{\mathbf{d}}} \\ L\Omega\dot{\tilde{\mathbf{d}}}_{\underline{r}} \\ \Omega\frac{F}{L^2}\dot{\tilde{\mathbf{p}}} \\ \Omega\frac{F}{L^2}\dot{\tilde{\mathbf{p}}}_{\underline{inj}} \\ \Omega\frac{F}{L^2}\dot{\tilde{\mathbf{p}}}_{\underline{inj}} \\ q_{\underline{L}}\Omega\dot{\tilde{\mathbf{q}}}_{\underline{v}} \\ L\tilde{\mathbf{d}} \\ L\tilde{\mathbf{d}}_{\underline{r}} \\ \frac{F}{L^2}\tilde{\mathbf{p}} \\ \frac{F}{L^2}\tilde{\mathbf{p}}_{\underline{inj}} \\ \frac{F}{L^2}\tilde{\mathbf{p}}_{\underline{inj}} \\ q_{\underline{L}}\tilde{\mathbf{q}}_{\underline{v}} \end{Bmatrix} +$$

$$\begin{bmatrix} \begin{bmatrix} \rho L^3\tilde{\mathbf{M}}_{\underline{s}} & & \\ & m_{\underline{r}}\tilde{\mathbf{M}}_{\underline{r}} & \\ & & \tilde{\mathbf{M}}_{\underline{q\text{-}q}} \end{bmatrix} & \begin{bmatrix} c_{\underline{r}}\tilde{\mathbf{D}}_{\underline{r}} & \\ G_{\underline{D}}\omega_{\underline{v}}^2 K_{\underline{v}}\tilde{\mathbf{G}}_{\underline{D}} & \\ & \xi_{\underline{v}}\omega_{\underline{v}}\tilde{\mathbf{D}}_{\underline{q\text{-}q}} \end{bmatrix} \\ \mathbf{0} & \begin{bmatrix} & \\ \mathbf{I} & \end{bmatrix} \end{bmatrix} \begin{Bmatrix} L\Omega^2\ddot{\tilde{\mathbf{d}}} \\ L\Omega^2\ddot{\tilde{\mathbf{d}}}_{\underline{r}} \\ \Omega^2\frac{F}{L^2}\ddot{\tilde{\mathbf{p}}} \\ \Omega^2\frac{F}{L^2}\ddot{\tilde{\mathbf{p}}}_{\underline{inj}} \\ \Omega^2\frac{F}{L^2}\ddot{\tilde{\mathbf{p}}}_{\underline{inj}} \\ q_{\underline{L}}\Omega^2\ddot{\tilde{\mathbf{q}}}_{\underline{v}} \\ L\Omega\dot{\tilde{\mathbf{d}}} \\ L\Omega\dot{\tilde{\mathbf{d}}}_{\underline{r}} \\ \Omega\frac{F}{L^2}\dot{\tilde{\mathbf{p}}} \\ \Omega\frac{F}{L^2}\dot{\tilde{\mathbf{p}}}_{\underline{inj}} \\ \Omega\frac{F}{L^2}\dot{\tilde{\mathbf{p}}}_{\underline{inj}} \\ q_{\underline{L}}\Omega\dot{\tilde{\mathbf{q}}}_{\underline{v}} \end{Bmatrix} = \begin{Bmatrix} F\tilde{\mathbf{f}} \\ F\tilde{\mathbf{f}}_{\underline{r}} \\ L^3\Omega\tilde{\mathbf{r}} \\ q_{\underline{L}}\tilde{\mathbf{r}}_{\underline{inj}} \\ u_{\underline{ch}}\omega_{\underline{v}}^2 K_{\underline{v}}\tilde{\mathbf{u}}_{\underline{vr}} \\ \mathbf{0} \\ \mathbf{0} \end{Bmatrix} \tag{B.48}$$

Now, multiplying the factors of the state vectors into the matrices, we arrive at

$$\begin{bmatrix} \mathbf{0} & \begin{bmatrix} EL^2\tilde{\mathbf{K}}_{\underline{\mathrm{s}}} & & \frac{FL}{\mu}\tilde{\mathbf{A}} & \frac{FL}{\mu}\tilde{\mathbf{W}} & & \\ & Lk_{\underline{\mathrm{r}}}\tilde{\mathbf{K}}_{\underline{\mathrm{r}}} & \frac{FL}{\mu}\tilde{\mathbf{W}}^T & \frac{FL}{\mu}\tilde{\mathbf{Q}} & \frac{F}{L^2}K_{\underline{\mathrm{pq}}}\tilde{\mathbf{K}}_{\underline{\mathrm{pq}}} & \\ & LG_{\underline{\mathrm{D}}}\omega_{\underline{\mathrm{v}}}^2K_{\underline{\mathrm{v}}}\tilde{\mathbf{G}}_{\underline{\mathrm{D}}} & & \frac{F}{L^2}\mathbf{I} & -\frac{F}{L^2}\mathbf{I} & q_{\underline{\mathrm{L}}}\omega_{\underline{\mathrm{v}}}^2\tilde{\mathbf{K}}_{\underline{\mathrm{q\text{-}q}}} \end{bmatrix} \\ \mathbf{I} & & \mathbf{0} & & & \end{bmatrix} \begin{Bmatrix} \dot{\tilde{\mathbf{d}}} \\ \dot{\tilde{\mathbf{d}}}_{\underline{\mathrm{r}}} \\ \dot{\tilde{\mathbf{p}}} \\ \dot{\tilde{\mathbf{p}}}_{\underline{\mathrm{inj}}} \\ \dot{\tilde{\mathbf{p}}}_{\underline{\mathrm{inj}}} \\ \dot{\tilde{\mathbf{q}}}_{\underline{\mathrm{v}}} \\ \tilde{\mathbf{d}} \\ \tilde{\mathbf{d}}_{\underline{\mathrm{r}}} \\ \tilde{\mathbf{p}} \\ \tilde{\mathbf{p}}_{\underline{\mathrm{inj}}} \\ \tilde{\mathbf{p}}_{\underline{\mathrm{inj}}} \\ \tilde{\mathbf{q}}_{\underline{\mathrm{v}}} \end{Bmatrix} +$$

$$\begin{bmatrix} \begin{bmatrix} \rho L^4\Omega^2\tilde{\mathbf{M}}_{\underline{\mathrm{s}}} & & \\ & L\Omega^2 m_{\underline{\mathrm{r}}}\tilde{\mathbf{M}}_{\underline{\mathrm{r}}} & \\ & & q_{\underline{\mathrm{L}}}\Omega^2\tilde{\mathbf{M}}_{\underline{\mathrm{q\text{-}q}}} \end{bmatrix} & \begin{bmatrix} L\Omega c_{\underline{\mathrm{r}}}\tilde{\mathbf{D}}_{\underline{\mathrm{r}}} & \\ L\Omega G_{\underline{\mathrm{D}}}\omega_{\underline{\mathrm{v}}}^2K_{\underline{\mathrm{v}}}\tilde{\mathbf{G}}_{\underline{\mathrm{D}}} & q_{\underline{\mathrm{L}}}\Omega\xi_{\underline{\mathrm{v}}}\omega_{\underline{\mathrm{v}}}\tilde{\mathbf{D}}_{\underline{\mathrm{q\text{-}q}}} \end{bmatrix} \\ \mathbf{0} & \mathbf{I} \end{bmatrix} \begin{Bmatrix} \ddot{\tilde{\mathbf{d}}} \\ \ddot{\tilde{\mathbf{d}}}_{\underline{\mathrm{r}}} \\ \ddot{\tilde{\mathbf{p}}} \\ \ddot{\tilde{\mathbf{p}}}_{\underline{\mathrm{inj}}} \\ \ddot{\tilde{\mathbf{p}}}_{\underline{\mathrm{inj}}} \\ \ddot{\tilde{\mathbf{q}}}_{\underline{\mathrm{v}}} \\ \dot{\tilde{\mathbf{d}}} \\ \dot{\tilde{\mathbf{d}}}_{\underline{\mathrm{r}}} \\ \dot{\tilde{\mathbf{p}}} \\ \dot{\tilde{\mathbf{p}}}_{\underline{\mathrm{inj}}} \\ \dot{\tilde{\mathbf{p}}}_{\underline{\mathrm{inj}}} \\ \dot{\tilde{\mathbf{q}}}_{\underline{\mathrm{v}}} \end{Bmatrix} = \begin{Bmatrix} F\tilde{\mathbf{f}} \\ F\tilde{\mathbf{f}}_{\underline{\mathrm{r}}} \\ L^3\Omega\tilde{\mathbf{r}} \\ q_{\underline{\mathrm{L}}}\tilde{\mathbf{r}}_{\underline{\mathrm{inj}}} \\ u_{\underline{\mathrm{ch}}}\omega_{\underline{\mathrm{v}}}^2K_{\underline{\mathrm{v}}}\tilde{\mathbf{u}}_{\underline{\mathrm{vr}}} \\ \mathbf{0} \\ \mathbf{0} \end{Bmatrix} \tag{B.49}$$

Dividing rows, so as to get dimensionless right hand side vectors and matrix components, we get

$$\begin{bmatrix} \mathbf{0} & \begin{bmatrix} \frac{EL^2}{F}\tilde{\mathbf{K}}_{\underline{\mathrm{s}}} & & \frac{F}{L^2\mu\Omega}\tilde{\mathbf{A}} & \frac{F}{L^2\mu\Omega}\tilde{\mathbf{W}} & & \\ & \frac{L}{F}k_{\underline{\mathrm{r}}}\tilde{\mathbf{K}}_{\underline{\mathrm{r}}} & \frac{FL}{\mu q_{\underline{\mathrm{L}}}}\tilde{\mathbf{W}}^T & \frac{FL}{\mu q_{\underline{\mathrm{L}}}}\tilde{\mathbf{Q}} & \frac{FK_{\underline{\mathrm{pq}}}}{L^2q_{\underline{\mathrm{L}}}}\tilde{\mathbf{K}}_{\underline{\mathrm{pq}}} & \\ & \frac{LG_{\underline{\mathrm{D}}}}{u_{\underline{\mathrm{ch}}}}\tilde{\mathbf{G}}_{\underline{\mathrm{D}}} & & \mathbf{I} & -\mathbf{I} & \frac{q_{\underline{\mathrm{L}}}}{K_{\underline{\mathrm{v}}}u_{\underline{\mathrm{ch}}}}\tilde{\mathbf{K}}_{\underline{\mathrm{q\text{-}q}}} \end{bmatrix} \\ \mathbf{I} & & \mathbf{0} & & & \end{bmatrix} \begin{Bmatrix} \dot{\tilde{\mathbf{d}}} \\ \dot{\tilde{\mathbf{d}}}_{\underline{\mathrm{r}}} \\ \dot{\tilde{\mathbf{p}}} \\ \dot{\tilde{\mathbf{p}}}_{\underline{\mathrm{inj}}} \\ \dot{\tilde{\mathbf{p}}}_{\underline{\mathrm{inj}}} \\ \dot{\tilde{\mathbf{q}}}_{\underline{\mathrm{v}}} \\ \tilde{\mathbf{d}} \\ \tilde{\mathbf{d}}_{\underline{\mathrm{r}}} \\ \tilde{\mathbf{p}} \\ \tilde{\mathbf{p}}_{\underline{\mathrm{inj}}} \\ \tilde{\mathbf{p}}_{\underline{\mathrm{inj}}} \\ \tilde{\mathbf{q}}_{\underline{\mathrm{v}}} \end{Bmatrix} +$$

$$\begin{bmatrix} \begin{bmatrix} \frac{\rho L^4\Omega^2}{F}\tilde{\mathbf{M}}_{\underline{\mathrm{s}}} & & \\ & \frac{L\Omega^2 m_{\underline{\mathrm{r}}}}{F}\tilde{\mathbf{M}}_{\underline{\mathrm{r}}} & \\ & & \frac{q_{\underline{\mathrm{L}}}\Omega^2}{\omega_{\underline{\mathrm{v}}}^2K_{\underline{\mathrm{v}}}u_{\underline{\mathrm{ch}}}}\tilde{\mathbf{M}}_{\underline{\mathrm{q\text{-}q}}} \end{bmatrix} & \begin{bmatrix} \frac{L\Omega c_{\underline{\mathrm{r}}}}{F}\tilde{\mathbf{D}}_{\underline{\mathrm{r}}} & \\ \frac{L\Omega G_{\underline{\mathrm{D}}}}{u_{\underline{\mathrm{ch}}}}\tilde{\mathbf{G}}_{\underline{\mathrm{D}}} & \frac{q_{\underline{\mathrm{L}}}\Omega\xi_{\underline{\mathrm{v}}}}{\omega_{\underline{\mathrm{v}}}K_{\underline{\mathrm{v}}}u_{\underline{\mathrm{ch}}}}\tilde{\mathbf{D}}_{\underline{\mathrm{q\text{-}q}}} \end{bmatrix} \\ \mathbf{0} & \mathbf{I} \end{bmatrix} \begin{Bmatrix} \ddot{\tilde{\mathbf{d}}} \\ \ddot{\tilde{\mathbf{d}}}_{\underline{\mathrm{r}}} \\ \ddot{\tilde{\mathbf{p}}} \\ \ddot{\tilde{\mathbf{p}}}_{\underline{\mathrm{inj}}} \\ \ddot{\tilde{\mathbf{p}}}_{\underline{\mathrm{inj}}} \\ \ddot{\tilde{\mathbf{q}}}_{\underline{\mathrm{v}}} \\ \dot{\tilde{\mathbf{d}}} \\ \dot{\tilde{\mathbf{d}}}_{\underline{\mathrm{r}}} \\ \dot{\tilde{\mathbf{p}}} \\ \dot{\tilde{\mathbf{p}}}_{\underline{\mathrm{inj}}} \\ \dot{\tilde{\mathbf{p}}}_{\underline{\mathrm{inj}}} \\ \dot{\tilde{\mathbf{q}}}_{\underline{\mathrm{v}}} \end{Bmatrix} = \begin{Bmatrix} \tilde{\mathbf{f}} \\ \tilde{\mathbf{f}}_{\underline{\mathrm{r}}} \\ \Omega\tilde{\mathbf{r}} \\ \tilde{\mathbf{r}}_{\underline{\mathrm{inj}}} \\ \tilde{\mathbf{u}}_{\underline{\mathrm{vr}}} \\ \mathbf{0} \\ \mathbf{0} \end{Bmatrix} \tag{B.50}$$

The matrices in Eq. (B.50) can be written as Hadamard products, thus yielding Eq. (3.18).

### B.5.1 Zero reference signal case

Now, let us investigate the case where the reference signal is zero, i.e., the case where the signal is zero when the rotor is at rest in the centre of the bearing. Equation (B.49) is then simplified slightly to

$$\begin{bmatrix} \mathbf{0} & \begin{bmatrix} EL^2\tilde{\mathbf{K}}_{\underline{\mathrm{s}}} & Lk_{\underline{\mathrm{r}}}\tilde{\mathbf{K}}_{\underline{\mathrm{r}}} & \frac{FL}{\mu}\tilde{\mathbf{A}} & \frac{FL}{\mu}\tilde{\mathbf{W}} & & \\ & & \frac{FL}{\mu}\tilde{\mathbf{W}}^T & \frac{FL}{\mu}\tilde{\mathbf{Q}} & \frac{F}{L^2}K_{\underline{\mathrm{pq}}}\tilde{\mathbf{K}}_{\underline{\mathrm{pq}}} & \\ & LG_{\underline{\mathrm{P}}}\omega_{\underline{\mathrm{v}}}^2K_{\underline{\mathrm{v}}}\tilde{\mathbf{G}}_{\underline{\mathrm{P}}} & & \frac{F}{L^2}\mathbf{I} & -\frac{F}{L^2}\mathbf{I} & q_{\underline{\mathrm{L}}}\omega_{\underline{\mathrm{v}}}^2\tilde{\mathbf{K}}_{\underline{\mathrm{q\text{-}q}}} \end{bmatrix} \\ \mathbf{I} & \mathbf{0} \end{bmatrix} \begin{Bmatrix} \dot{\tilde{\mathbf{d}}} \\ \dot{\tilde{\mathbf{d}}}_{\underline{\mathrm{r}}} \\ \dot{\tilde{\mathbf{p}}} \\ \dot{\tilde{\mathbf{p}}}_{\underline{\mathrm{inj}}} \\ \dot{\tilde{\mathbf{p}}}_{\underline{\mathrm{inj}}} \\ \dot{\tilde{\mathbf{q}}}_{\underline{\mathrm{v}}} \\ \tilde{\mathbf{d}} \\ \tilde{\mathbf{d}}_{\underline{\mathrm{r}}} \\ \tilde{\mathbf{p}} \\ \tilde{\mathbf{p}}_{\underline{\mathrm{inj}}} \\ \tilde{\mathbf{p}}_{\underline{\mathrm{inj}}} \\ \tilde{\mathbf{q}}_{\underline{\mathrm{v}}} \end{Bmatrix} +$$

$$\begin{bmatrix} \begin{bmatrix} \rho L^4\Omega^2\tilde{\mathbf{M}}_{\underline{\mathrm{s}}} & L\Omega^2 m_{\underline{\mathrm{r}}}\tilde{\mathbf{M}}_{\underline{\mathrm{r}}} & \\ & & q_{\underline{\mathrm{L}}}\Omega^2\tilde{\mathbf{M}}_{\underline{\mathrm{q\text{-}q}}} \\ \mathbf{0} & & \end{bmatrix} & \begin{bmatrix} L\Omega c_{\underline{\mathrm{r}}}\tilde{\mathbf{D}}_{\underline{\mathrm{r}}} & \\ L\Omega G_{\underline{\mathrm{D}}}\omega_{\underline{\mathrm{v}}}^2K_{\underline{\mathrm{v}}}\tilde{\mathbf{G}}_{\underline{\mathrm{D}}} & q_{\underline{\mathrm{L}}}\Omega\xi_{\underline{\mathrm{v}}}\omega_{\underline{\mathrm{v}}}\tilde{\mathbf{D}}_{\underline{\mathrm{q\text{-}q}}} \\ \mathbf{I} & \end{bmatrix} \end{bmatrix} \begin{Bmatrix} \ddot{\tilde{\mathbf{d}}} \\ \ddot{\tilde{\mathbf{d}}}_{\underline{\mathrm{r}}} \\ \ddot{\tilde{\mathbf{p}}} \\ \ddot{\tilde{\mathbf{p}}}_{\underline{\mathrm{inj}}} \\ \ddot{\tilde{\mathbf{p}}}_{\underline{\mathrm{inj}}} \\ \ddot{\tilde{\mathbf{q}}}_{\underline{\mathrm{v}}} \\ \dot{\tilde{\mathbf{d}}} \\ \dot{\tilde{\mathbf{d}}}_{\underline{\mathrm{r}}} \\ \dot{\tilde{\mathbf{p}}} \\ \dot{\tilde{\mathbf{p}}}_{\underline{\mathrm{inj}}} \\ \dot{\tilde{\mathbf{p}}}_{\underline{\mathrm{inj}}} \\ \dot{\tilde{\mathbf{q}}}_{\underline{\mathrm{v}}} \end{Bmatrix} = \begin{Bmatrix} F\tilde{\mathbf{f}} \\ F\tilde{\mathbf{f}}_{\underline{\mathrm{r}}} \\ L^3\Omega\tilde{\mathbf{r}} \\ q_{\underline{\mathrm{L}}}\tilde{\mathbf{r}}_{\underline{\mathrm{inj}}} \\ \mathbf{0} \\ \mathbf{0} \\ \mathbf{0} \end{Bmatrix} \tag{B.51}$$

Now, as before, dividing rows, so as to get dimensionless right hand side vectors and matrix components, we get

$$\begin{bmatrix} \mathbf{0} & \begin{bmatrix} \frac{EL^2}{F}\tilde{\mathbf{K}}_{\underline{\mathrm{s}}} & \frac{L}{F}k_{\underline{\mathrm{r}}}\tilde{\mathbf{K}}_{\underline{\mathrm{r}}} & \frac{F}{L^2\mu\Omega}\tilde{\mathbf{A}} & \frac{F}{L^2\mu\Omega}\tilde{\mathbf{W}} & & \\ & & \frac{FL}{\mu q_{\underline{\mathrm{L}}}}\tilde{\mathbf{W}}^T & \frac{FL}{\mu q_{\underline{\mathrm{L}}}}\tilde{\mathbf{Q}} & \frac{FK_{\underline{\mathrm{pq}}}}{L^2q_{\underline{\mathrm{L}}}}\tilde{\mathbf{K}}_{\underline{\mathrm{pq}}} & \\ & \frac{LG_{\underline{\mathrm{P}}}K_{\underline{\mathrm{v}}}}{q_{\underline{\mathrm{L}}}}\tilde{\mathbf{G}}_{\underline{\mathrm{P}}} & & \mathbf{I} & -\mathbf{I} & \tilde{\mathbf{K}}_{\underline{\mathrm{q\text{-}q}}} \end{bmatrix} \\ \mathbf{I} & \mathbf{0} \end{bmatrix} \begin{Bmatrix} \dot{\tilde{\mathbf{d}}} \\ \dot{\tilde{\mathbf{d}}}_{\underline{\mathrm{r}}} \\ \dot{\tilde{\mathbf{p}}} \\ \dot{\tilde{\mathbf{p}}}_{\underline{\mathrm{inj}}} \\ \dot{\tilde{\mathbf{p}}}_{\underline{\mathrm{inj}}} \\ \dot{\tilde{\mathbf{q}}}_{\underline{\mathrm{v}}} \\ \tilde{\mathbf{d}} \\ \tilde{\mathbf{d}}_{\underline{\mathrm{r}}} \\ \tilde{\mathbf{p}} \\ \tilde{\mathbf{p}}_{\underline{\mathrm{inj}}} \\ \tilde{\mathbf{p}}_{\underline{\mathrm{inj}}} \\ \tilde{\mathbf{q}}_{\underline{\mathrm{v}}} \end{Bmatrix} +$$

$$\begin{bmatrix} \begin{bmatrix} \frac{\rho L^4\Omega^2}{F}\tilde{\mathbf{M}}_{\underline{\mathrm{s}}} & \frac{L\Omega^2 m_{\underline{\mathrm{r}}}}{F}\tilde{\mathbf{M}}_{\underline{\mathrm{r}}} & \\ & & \frac{\Omega^2}{\omega_{\underline{\mathrm{v}}}^2}\tilde{\mathbf{M}}_{\underline{\mathrm{q\text{-}q}}} \\ \mathbf{0} & & \end{bmatrix} & \begin{bmatrix} \frac{L\Omega c_{\underline{\mathrm{r}}}}{F}\tilde{\mathbf{D}}_{\underline{\mathrm{r}}} & \\ \frac{L\Omega G_{\underline{\mathrm{D}}}K_{\underline{\mathrm{v}}}}{q_{\underline{\mathrm{L}}}}\tilde{\mathbf{G}}_{\underline{\mathrm{D}}} & \frac{\Omega\xi_{\underline{\mathrm{v}}}}{\omega_{\underline{\mathrm{v}}}}\tilde{\mathbf{D}}_{\underline{\mathrm{q\text{-}q}}} \\ \mathbf{I} & \end{bmatrix} \end{bmatrix} \begin{Bmatrix} \ddot{\tilde{\mathbf{d}}} \\ \ddot{\tilde{\mathbf{d}}}_{\underline{\mathrm{r}}} \\ \ddot{\tilde{\mathbf{p}}} \\ \ddot{\tilde{\mathbf{p}}}_{\underline{\mathrm{inj}}} \\ \ddot{\tilde{\mathbf{p}}}_{\underline{\mathrm{inj}}} \\ \ddot{\tilde{\mathbf{q}}}_{\underline{\mathrm{v}}} \\ \dot{\tilde{\mathbf{d}}} \\ \dot{\tilde{\mathbf{d}}}_{\underline{\mathrm{r}}} \\ \dot{\tilde{\mathbf{p}}} \\ \dot{\tilde{\mathbf{p}}}_{\underline{\mathrm{inj}}} \\ \dot{\tilde{\mathbf{p}}}_{\underline{\mathrm{inj}}} \\ \dot{\tilde{\mathbf{q}}}_{\underline{\mathrm{v}}} \end{Bmatrix} = \begin{Bmatrix} \tilde{\mathbf{f}} \\ \tilde{\mathbf{f}}_{\underline{\mathrm{r}}} \\ \tilde{\Omega\mathbf{r}} \\ \ddot{\tilde{\mathbf{r}}}_{\underline{\mathrm{inj}}} \\ \tilde{\mathbf{u}}_{\underline{\mathrm{vr}}} \\ \mathbf{0} \\ \mathbf{0} \end{Bmatrix} \tag{B.52}$$

Again, the dimensionless coefficients can be readily seen from this system of equations

# Appendix C

# Journal Papers

# Publication 1

Elastohydrodynamics Applied to Active Tilting-Pad Journal Bearings
Journal of Tribology (ASME)

# Elastohydrodynamics Applied to Active Tilting-Pad Journal Bearings

**Asger M. Haugaard**
e-mail: mah@mek.dtu.dk

**Ilmar F. Santos**
e-mail: ifs@mek.dtu.dk

Department of Mechanical Engineering,
Section for Solid Mechanics,
Technical University of Denmark,
2800 Lyngby, Denmark

*The static and dynamic properties of tilting-pad journal bearings with controllable radial oil injection are investigated theoretically. The tilting pads are modeled as flexible structures and their behavior is described using a three-dimensional finite element framework and linear elasticity. The oil film pressure and flow are considered to follow the modified Reynolds equation, which includes the contribution from controllable radial oil injection. The Reynolds equation is solved using a two-dimensional finite element mesh. The rotor is considered to be rigid in terms of shape and size, but lateral movement is permitted. The servovalve flow is governed by a second order ordinary differential equation, where the right hand side is controlled by an electronic input signal. The constitutive flow-pressure relationship of the injection orifices is that of a fully developed laminar velocity profile and the servovalve is introduced into the system of equations by a mass conservation consideration. The Reynolds equation is linearized with respect to displacements and velocities of the nodal degrees of freedom. When all nodal points satisfy static equilibrium, the system of equations is dynamically perturbed and subsequently condensed to a $2\times2$ system, keeping only the lateral motion of the rotor. As expected, bearing dynamic coefficients are heavily influenced by the control parameters and pad compliance.* [DOI: 10.1115/1.4000721]

*Keywords: tilting-pad journal bearings, control, elastohydrodynamics, vibration*

## 1 Introduction

During the last 4 decades, the dynamics of tilting-pad journal bearings have been intensively investigated by many authors worldwide using different computer models. In Lund's pioneering work [1], damping and stiffness coefficients of tilting-pad journal bearings under conventional hydrodynamic lubrication are calculated. In Ref. [2] a simplified beam-model is used to include pad flexibility and deal with an elastohydrodynamic analysis. Such an elastohydrodynamic analysis became much more sophisticated and the results much more precise in Refs. [3,4], aided by the finite element method. In 5 and 6, based on an isothermal conventional hydrodynamic analysis, a perturbation method was used to obtain the global and reduced dynamic coefficients of tilting-pad journal bearings and predict the dependency of the reduced coefficients on the perturbation frequency. Such a frequency dependency is detected and measured more easily, when pivot compliance is clearly pronounced. This is shown theoretically, as well as experimentally in Ref. [7] using a test rig, where the excitation force is applied directly to the rotating shaft. Such a frequency dependency seems to be more difficult to measure accurately when no pivot or pad compliance is present, and the excitation force is applied directly to the moving bearing housing, as it can be concluded from Refs. [8,9]. "Passive" thermoelastohydrodynamic analysis of tilting-pad journal bearings is carried out in Refs. [10,11] considering dynamic loading, where good agreements between theoretical and experimental results are reported.

Tilting-pad journal bearings (TPJBs) are frequently used in industrial applications due to their excellent stability properties. It is true that such bearings are much more stable than other types of hydrodynamic bearings, but instabilities may occur depending on the operational conditions, i.e., low preload factor and low static loading. This is thoroughly investigated theoretically, as well as experimentally, by different authors [12–17]. Moreover, TPJB direct damping is significantly smaller than that of other types of hydrodynamic bearings. TPJBs are more stable at high angular velocities than other types of hydrodynamic bearings, but the amount of direct damping at higher angular velocities is normally small. This is carefully investigated by many authors, among others by Glienicke [18]. When size and mass (inertia) of supercritical rotating machines increase, combined with small values of direct damping, rotors supported by TPJBs can face severe vibration problems, for example, when crossing critical speeds or excited by aerodynamic effects originated from the process. It is relatively common in the oil and gas industry to have squeeze-film dampers attached to TPJB housings, with the aim of increasing the amount of damping in the system. Such a design solution can be found in many industrial gas compressors, for example, radial compressors. This means that there are "rotordynamic deficiencies" to be overcome, even though TPJBs have good stability properties. Squeeze-film dampers or arc-spring dampers are possible passive solutions to the problem of lack of damping in supercritical gas compressors supported by TPJBs. Active lubrication is another feasible solution. Both technical solutions, namely, passive or "active," have advantages and drawbacks. There are many advantages in using actively lubricated TPJBs. This is thoroughly mentioned in the literature, among others in Ref. [19].

A model including radial oil injection, but disregarding pad compliance, was developed in Ref. [20]. In Ref. [20], the fundamental set of equations to describe a controllable radial oil injection into the bearing gap using servovalves and a simple feedback controller was presented. However, the procedure entailed assuming that the pressure is almost constant in the orifice region in order to allow coupling between servovalve flow and journal pressure. The formulation was not explained clearly in all details, which could lead to confusion. It is important to point out that in Ref. [20], the journal pressure in the orifice region was Taylor expanded and only the term of order zero was taken into account. The justification was based on the claim that the orifice area is much smaller than the pad surface area and the journal pressure

Contributed by the Tribology Division of ASME for publication in the JOURNAL OF TRIBOLOGY. Manuscript received March 19, 2009; final manuscript received October 21, 2009; published online March 25, 2010. Assoc. Editor: Ilya I. Kudish.

variation over this small area is almost negligible when compared with the journal pressure variation over the entire pad surface area. The control parameters were later introduced directly into the modified Reynolds equation for active lubrication [21] under such an approximation. This provided insight into the influence of the control terms since they appeared explicitly in the modified Reynolds equation. The present paper relies heavily on the ideas introduced in Ref. [20].

Theoretical and experimental contributions to conventional [22–24], hybrid [22–26], and active lubrication [22–24] applied to tilting-pad bearings can be found in the literature. The lateral dynamics of a light and rigid rotor supported by a tilting-pad journal bearing under conventional hydrodynamic and active lubrication is compared in the time [22] and frequency [23] domains. In Ref. [24], the lateral dynamics of flexible rotors is experimentally controlled by using a tilting-pad journal bearing under three different lubrication regimes, namely, hydrodynamic, hybrid (hydrodynamic+hydrostatic), and actively lubricated (using a simple PD-controller). In Refs. [25,26], the influence of the injection pockets on the steady-state performance of tilting-pad journal bearings are theoretically, as well as experimentally investigated, using two different test setups, and thermoelastohydrodynamic models validated for heavily loaded bearings.

The paper gives an original contribution to a multiphysics problem, where tribology is in the center of the different areas of expertise. The combination of solid mechanics, fluid power, control theory, and CAD is done in an original way, opening new possibilities for integrated-engineering design. Working in the field of mechatronics demands good analytical skills and a good capability of synthesis, i.e., to put together different areas of expertise and develop new products and achieve more advanced, more robust, and more efficient machines. The integration of different areas of expertise (multiphysics) is a modern trend and vision in engineering design. The main original contribution of this paper is of theoretical nature. In the present investigation, pad compliance, as well as radial oil injection, are included. The orifice flow is introduced into the model consistently as an integral of the pressure field (assuming a constitutive relation between pressures and velocities). The pressure field is not assumed constant in the orifice region, as in Ref. [20]. The equations for the fluid and solid are handled with the finite element method, which makes numerical integrals of field quantities straight forward and unambiguous. The elastohydrodynamic model is used to investigate static and dynamic properties of a tilting-pad journal bearing in a load between pads configuration under hybrid elastohydrodynamics (open loop control), as well as in controllable radial oil injection (closed loop control).

It is important to mention that all technical solutions toward achieving a more stable and more damped rotordynamic system will be associated with additional costs. Squeeze-film dampers or arc-spring dampers, passive devices to be attached to TPJB housings, also have costs related to manufacturing, pressurization, etc. Such passive solutions do not allow significant changes and adjustments. Active lubrication (a mechatronic device) obviously also entails costs. Nevertheless, such a design solution allows engineers to work with many more variables toward achieving more robustness (capability of system adjustments to different needs, at different operational conditions). Keeping our application focus on the oil and gas industry, an unexpected stop of a power plant production, due to vibration problems, will lead to much higher costs than an actively lubricated TPJB and its additional control features. For example, the control features will make feasible the temporary elimination of vibration problems and will give engineers time to plan the power plant shutdown, repair machine problems, and significantly reduce economic damages due to the unexpected stop of production.

Finally, the authors want to emphasize that the intention of the research work is not to replace active magnetic bearings by actively lubricated TPJBs, but add new features and capabilities to such a machine element. Active magnetic bearing technology is a well-established technology with a long history [27–30], while active lubricated bearings is an emerging technology, a little more than 1 decade old [24]. Both technologies have advantages and drawbacks. No bearing type can beat an active magnetic bearing in terms of friction. Comparing the two technologies in more depth, not only considering "friction," it is fair to claim that: Actively lubricated TPJBs can operate in passive and active modes, depending on situation needs. Active magnetic bearings need backup bearings while actively lubricated TPJBs do not. In case of control failure, the conventional hydrodynamic lubrication will still be supporting the rotating shaft. Active magnetic bearings operate always with control. The static and dynamic forces generated by fluid power are much higher than the forces generated by electromagnetism. Given the load capacity, an actively lubricated TPJB is significantly smaller than an active magnetic bearing.

## 2 Governing Equations

In the present paper, tensors will appear in certain places. To avoid confusion, while retaining a consistent nomenclature, summation of repeated indices is not employed, thus, all summations are stated explicitly. Underlined indices are part of variable names, and indices without underline are used for numbering, e.g., $q_{\underline{v}i}$ is the valve flow of servovalve number $i$.

Figure 1 illustrates the different coordinate frames and domains used to describe the elastic behavior of the pads, and the journal pressure distribution among the rotor and the pads. The curvilinear coordinates $(\chi_1, \chi_2)$ are used to represent the fluid film and the Cartesian coordinates $(x_1, x_2, x_3)$ are used to represent the pads.

The solid is taken to be linearly elastic and isotropic. Small strains and rotations suffice for the description of the deformed state. The governing equation is traditionally given directly in integral form as the principle of virtual work

$$\sum_{i,j,k,l=1}^{3} \int_{\Pi} L_{ijkl}\varepsilon_{kl}\delta\varepsilon_{ij}d\Pi = \sum_{i=1}^{3} \int_{\Pi} \rho\ddot{u}_i\delta u_i d\Pi + \sum_{i=1}^{3} \int_{\Lambda} T_i\delta u_i d\Lambda \tag{1}$$

From this, a stiffness and mass matrix for the solid can be derived. The pressure field in the fluid is described by the modified Reynolds equation, which becomes

$$\frac{1}{12}\sum_{i=1}^{2} \frac{\partial}{\partial\chi_i}\left(\frac{h^3}{\mu}\frac{\partial p}{\partial\chi_i}\right) = \frac{U}{2}\frac{\partial h}{\partial\chi_2} + \dot{h} + \frac{\Sigma_i g_i(p - p_{\underline{\text{inj}}i})}{4\mu l_0} \tag{2}$$

Here, the $\chi_2$ coordinate is aligned with the direction of rotation. For reasons that shall soon become obvious, the Reynolds equation has been divided by 12 on both sides, when comparing to the way that it is normally stated.

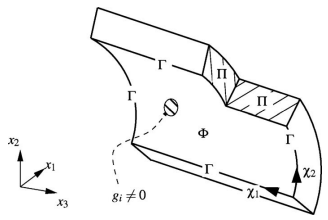


**Fig. 1 Overview of the different domains, the fluid film curvilinear coordinate system $(\chi_1, \chi_2)$, and the Cartesian coordinate system $(x_1, x_2, x_3)$. The figure depicts a generic bearing pad, with an arbitrarily placed orifice. It is to be understood as a qualitative aid.**

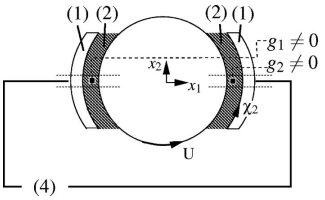


**Fig. 2 Overview of the coupled system, with denotion of the equations that govern the different parts, i.e., (2) means that that part is governed by the Reynolds equation. The first coordinates of the Cartesian coordinate system ($x_1, x_2$) are shown, the coordinate system is right handed, thus, $x_3$ points out of the plane of the paper. The curvilinear coordinate $\chi_2$ is also shown, but is better understood by regarding Fig. 1.**

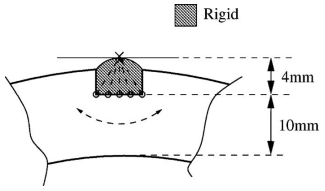


**Fig. 3 Schematic of the pivot boundary conditions. The pivot is modeled as rigid. Nodes along the surface of the pad are constrained to move tangentially relative to the pivot point.**

The flow in the servovalves is described by the second order ordinary differential equation (4)

$$\ddot{q}_{\underline{v}} + 2\xi_{\underline{v}}\omega_{\underline{v}}\dot{q}_{\underline{v}} + \omega_{\underline{v}}^2 q_{\underline{v}} = \omega_{\underline{v}}^2 K_{\underline{v}} u_{\underline{v}} \tag{3}$$

or

$$\frac{1}{\omega_{\underline{v}}^2 K_{\underline{v}}}\ddot{q}_{\underline{v}} + \frac{2\xi_{\underline{v}}}{\omega_{\underline{v}} K_{\underline{v}}}\dot{q}_{\underline{v}} + \frac{1}{K_{\underline{v}}} q_{\underline{v}} = u_{\underline{v}} \tag{4}$$

If more servovalves are included, an uncoupled system of equations results, thus

$$\mathbf{M}_{\underline{q-q}}\ddot{\mathbf{q}}_{\underline{v}} + \mathbf{D}_{\underline{q-q}}\dot{\mathbf{q}}_{\underline{v}} + \mathbf{K}_{\underline{q-q}}\mathbf{q}_{\underline{v}} = \mathbf{u}_{\underline{v}} \tag{5}$$

where the system matrices follow directly from Eq. (4). The injection orifices are connected by servovalves as pairs. Thus, the flows in an orifice pair are coupled. The linearized $2 \times 2$ system of equations for a servovalve connecting, e.g., orifices $i$ and $j$, is

$$\begin{Bmatrix} q_i \\ q_j \end{Bmatrix} = \begin{bmatrix} K_{\underline{pq}} & -K_{\underline{pq}} \\ -K_{\underline{pq}} & K_{\underline{pq}} \end{bmatrix} \begin{Bmatrix} p_{\underline{\text{inj}i}} \\ p_{\underline{\text{inj}j}} \end{Bmatrix} + \begin{Bmatrix} q_{\underline{v}} \\ -q_{\underline{v}} \end{Bmatrix} + \begin{Bmatrix} q_{\underline{L}} \\ q_{\underline{L}} \end{Bmatrix} \tag{6}$$

where $K_{\underline{pq}}$ and $q_{\underline{L}}$ are valve specific constants, i.e., they can differ from valve to valve. Here we have selected a positive direction of flow for the servovalve. The orifice associated with positive valve flow, in this case orifice $i$, is denoted as the master orifice. The orifice associated with the negative valve flow, in this case, orifice $j$, is denoted as the slave orifice.

Since the bearings are the main focus of this investigation, the rotor is described as simple as possible, however, still in a fashion that retains its qualitative behavior. The rotor is assumed to move laterally only, i.e., rotor tilting motion is not included, and its center of mass is assumed to coincide with its axis of rotation at all times. Also, since the focus of this investigation is the bearing influence on the rotor behavior, no stiffness is assigned to the rotor apart from the one coming from the oil film. In Fig. 2, a system with two pads and one servovalve is shown, with the indication of the governing equation of each body. The figure is for illustrative purposes only. The oil film thickness is greatly exaggerated, and in this investigation, bearings with four pads will be investigated.

**2.1 Boundary Conditions.** The pads are pivoted about their center. The pivoting is modeled as a radial constraint on relevant nodes, see Fig. 3. This is done by coordinate transformations back and forth between the inertial coordinate system, and systems that are aligned with the constraints. When in a constraint coordinate system, zeros can be introduced into the off diagonal components of the stiffness matrix, which couple with the degree of freedom to be constrained. One could simply introduce stiff springs between the pivot point and the surface nodes, but this would introduce high frequencies into the system, thus, possibly reducing the maximum allowable time step. The boundary condition for the Reynolds equation is the Reynolds condition, i.e., the pressure is set to zero along the boundary of the lubricated surface. In this investigation, cavitation has not been observed.

## 3 Coupling

The different governing equations cannot be coupled in a general way before they are brought into a space where they are all defined. The servovalves are not defined in space, thus, the servovalves cannot be introduced into the system in a consistent manner before the pressure field is discretized, unless some practical assumptions [20] are made, as described in the introduction. This is of course also the case for the displacement field. Once spatial discretization has been performed, a system of equations, all defined in time only, arises. These equations are straight forward to couple. This approach is more general.

It is evident that the oil pressure should be imposed as a surface load on the solid, that is

$$T_i = a_i \sum_{j \in \mathbb{F}^2} \phi_j p_j \quad \text{on} \quad \Phi \tag{7}$$

From the expression for the traction $T_i$, the nodal force of degree of freedom $n$, $f_n$ can be computed as

$$f_i = \int_\Phi \sum_{m=1}^{3} T_m e_{im} d\Phi, \quad i = 1,2,\ldots,N \tag{8}$$

When solving for the pressures, the very slight pad-rotor misalignment is of vital importance. However, for the particular purpose of obtaining the resultant force on the rotor, it is reasonable to assume rotor and pad surfaces parallel, thus, when $i$ corresponds to a rotor degree of freedom, we may write

$$f_i = -\int_\Phi T_i d\Phi \tag{9}$$

The flow through a given orifice can be written in terms of the pressure difference field over the orifice as

$$q_i = \int_\Phi g_i \frac{1}{4\mu l_0}(p(\chi_1,\chi_2) - p_{\underline{\text{inj}i}}) d\Phi \tag{10}$$

where $g_i$ are shape functions that describe the velocity profile in the orifice. Here we shall let them describe a fully developed laminar pipe velocity profile, which is reasonable, considering the dimensions and operating conditions, but in principle, any profile could be used.

In matrix form, we get

$$\begin{bmatrix} [\mathbf{A}_{\underline{p-p}}] & [\mathbf{A}_{\underline{p-\text{inj}}}] \\ [\mathbf{A}_{\underline{\text{inj}-p}}] & [\mathbf{A}_{\underline{\text{inj}-\text{inj}}}] \end{bmatrix} \begin{Bmatrix} \mathbf{p} \\ \mathbf{p}_{\underline{\text{inj}}} \end{Bmatrix} = \begin{Bmatrix} \mathbf{r} \\ \mathbf{r}_{\underline{\text{inj}}} \end{Bmatrix} \tag{11}$$

The nodal pressure to nodal pressure matrix $\mathbf{A}_{\underline{p-p}}$ is derived from Eq. (2) as

$$\mathbf{A}_{\underline{p-p}} = A_{\underline{p-p}mn} = \sum_{\text{elements}} \frac{1}{12} \sum_{i=1}^{2} \int_{\Phi} \frac{\partial \phi_n}{\partial \chi_i} \frac{\partial \phi_m}{\partial \chi_i} \frac{h^3}{\mu} d\Phi + \frac{1}{4} \sum_i \int_{\Phi} \frac{g_i \phi_m \phi_n}{\mu l_0} d\Phi \tag{12}$$

Note that $\mathbf{A}_{\underline{p-p}}$ is the matrix that contains the scalar components $A_{\underline{p-p}mn}$. This nomenclature is used throughout the paper.

The nodal pressure part of the right hand side is given by

$$\mathbf{r} = r_m = \sum_{\text{elements}} - \int_{\Phi} \frac{1}{2} U \frac{\partial h}{\partial \chi_2} \phi_m d\Phi - \int_{\Phi} \frac{\partial h}{\partial t} \phi_m d\Phi \tag{13}$$

In Eqs. (12) and (13), the fields $h=h(\chi_1, \chi_2)$ and $g_i=g_i(\chi_1, \chi_2)$ are expanded in terms of element shape functions. To retain compactness, this is not stated explicitly, nor will it be henceforth. Integration is performed with full Gauss quadrature, see, e.g., Ref. [31].

The orifices are coupled in pairs by the $\mathbf{A}_{\underline{\text{inj}-\text{inj}}}$ matrix. If the system only contains the orifices $m$ and $n$, which are coupled by a valve, the $\mathbf{A}_{\underline{\text{inj}-\text{inj}}}$ matrix becomes

$$\mathbf{A}_{\underline{\text{inj}-\text{inj}}} = A_{\underline{\text{inj}-\text{inj}}mn} = \begin{bmatrix} K_{\underline{pq}} + \int_{\Phi} \frac{g_m}{4\mu l_0} d\Phi & -K_{\underline{pq}} \\ -K_{\underline{pq}} & K_{\underline{pq}} + \int_{\Phi} \frac{g_n}{4\mu l_0} d\Phi \end{bmatrix} \tag{14}$$

Since the orifices are coupled in pairs, the $\mathbf{A}_{\underline{\text{inj}-\text{inj}}}$ matrix has a bandwidth of two, and is sparse when many orifices exist.

The injection pressure part of the right hand side of Eq. (11) is given by

$$\mathbf{r}_{\underline{\text{inj}}} = r_{\underline{\text{inj}}m} = N_m q_{\underline{v}m} - q_{\underline{L}m} \tag{15}$$

where $N_m=1$ if orifice $m$ is a master orifice and $N_m=-1$ if it is a slave orifice.

The coupling between orifice injection pressure and pressure distribution is governed by the $\mathbf{A}_{\underline{\text{inj}-p}}$ matrix

$$\mathbf{A}_{\underline{\text{inj}-p}} = A_{\underline{\text{inj}-p}mn} = -\int_{\Phi} \frac{g_m \phi_n}{4\mu l_0} d\Phi \tag{16}$$

If the Reynolds equation is in the form of Eq. (2), then

$$\mathbf{A}_{\underline{p-\text{inj}}} = \mathbf{A}^T_{\underline{\text{inj}-p}} \tag{17}$$

This is of paramount importance since it makes the system of equations (11) symmetric, thus allowing the use of fast equation solvers, like, for instance, the conjugate gradient (CG) method, which is a well known method, see, e.g., Ref. [32]. The CG method has been used in this investigation for symmetric system solution. Let us write the system of equations (12) more compactly as

$$\mathbf{A}\mathbf{p}_{\underline{g}} = \mathbf{r}_{\underline{g}}, \quad \mathbf{p}_{\underline{g}} = \begin{Bmatrix} \mathbf{p} \\ \mathbf{p}_{\underline{\text{inj}}} \end{Bmatrix}, \quad \mathbf{r}_{\underline{g}} = \begin{Bmatrix} \mathbf{r} \\ \mathbf{r}_{\underline{\text{inj}}} \end{Bmatrix} \tag{18}$$

where the index $\underline{g}$ indicates that the system of equations include the injection terms, i.e., $\mathbf{p}_{\underline{g}}$ is the vector of generalized pressures. Now, given the valve flow vector $\mathbf{q}_{\underline{v}}$, we can solve simultaneously for the nodal pressures, as well as injection pressures. With the given formulation, time series solutions can be computed by time integration schemes. Here, the explicit form of the Newmark method shall be used.

## 4 Linearization

The system of equations can be linearized with respect to displacements, so as to provide a fluid film stiffness and damping. The linearized system is derived by first order Taylor expansions of relevant quantities. Since, as before mentioned, the injection pressures are not defined in space; we may as well work directly on the discretized system. Thus

$$p_{\underline{g}n} \approx \tilde{p}_{\underline{g}n} + \sum_i \frac{\partial p_{\underline{g}n}}{\partial d_i} \delta d_i + \sum_i \frac{\partial p_{\underline{g}n}}{\partial \dot{d}_i} \delta \dot{d}_i + \sum_i \frac{\partial p_{\underline{g}n}}{\partial q_{\underline{v}i}} \delta q_{\underline{v}i} \tag{19}$$

Deriving both sides of Eq. (18) with nodal displacements, we arrive at

$$\frac{\partial p_{\underline{g}n}}{\partial d_i} = \frac{\partial \mathbf{p}_{\underline{g}}}{\partial d_i} = \mathbf{A}^{-1} \left( \frac{\partial \mathbf{r}_{\underline{g}}}{\partial d_i} - \frac{\partial \mathbf{A}}{\partial d_i} \mathbf{p}_{\underline{g}} \right) \tag{20}$$

Here, $\mathbf{A}$ depends on $d_i$ since the fluid film thickness does. Of course, expressions for velocity perturbations and flow perturbations are completely analogous

$$\frac{\partial p_{\underline{g}n}}{\partial \dot{d}_i} = \frac{\partial \mathbf{p}_{\underline{g}}}{\partial \dot{d}_i} = \mathbf{A}^{-1} \left( \frac{\partial \mathbf{r}_{\underline{g}}}{\partial \dot{d}_i} - \frac{\partial \mathbf{A}}{\partial \dot{d}_i} \mathbf{p}_{\underline{g}} \right) \tag{21}$$

Here, $\mathbf{A}$ depends on $\dot{d}_i$ since the fluid film thickness rate does

$$\frac{\partial p_{\underline{g}n}}{\partial q_{\underline{v}i}} = \frac{\partial \mathbf{p}_{\underline{g}}}{\partial q_{\underline{v}i}} = \mathbf{A}^{-1} \left( \frac{\partial \mathbf{r}_{\underline{g}}}{\partial q_{\underline{v}i}} - \cancel{\frac{\partial \mathbf{A}}{\partial q_{\underline{v}i}}}^{0} \mathbf{p}_{\underline{g}} \right) \tag{22}$$

The expression for $\partial \mathbf{r}_{\underline{g}} / \partial q_{\underline{v}i}$ is particularly simple, that is

$$\frac{\partial \mathbf{r}_{\underline{g}}}{\partial q_{\underline{v}i}} = \{0 \ \ldots \ 0 \ -1 \ 1 \ 0 \ \ldots \ 0\}^T \tag{23}$$

where the position of the nonzero components depends on the specific numbering of degrees of freedom. Now, the second order ordinary differential equation describing the dynamics of the system can be written as

$$\mathbf{M}\ddot{\mathbf{d}}_{\underline{g}} + \mathbf{D}\dot{\mathbf{d}}_{\underline{g}} + \mathbf{K}\mathbf{d}_{\underline{g}} = \mathbf{f} \tag{24}$$

If the last degrees of freedom are assigned to the flows, the structure of the system of equations is

$$\underbrace{\begin{bmatrix} [\mathbf{M}_{\underline{d-d}}] & [\mathbf{M}_{\underline{d-q}}] \\ [\mathbf{M}_{\underline{q-d}}] & [\mathbf{M}_{\underline{q-q}}] \end{bmatrix}}_{\mathbf{M}} \underbrace{\begin{Bmatrix} \ddot{\mathbf{d}} \\ \ddot{\mathbf{q}}_{\underline{v}} \end{Bmatrix}}_{\ddot{\mathbf{d}}_{\underline{g}}} + \underbrace{\begin{bmatrix} [\mathbf{D}_{\underline{d-d}}] & [\mathbf{D}_{\underline{d-q}}] \\ [\mathbf{D}_{\underline{q-d}}] & [\mathbf{K}_{\underline{q-q}}] \end{bmatrix}}_{\mathbf{D}} \underbrace{\begin{Bmatrix} \dot{\mathbf{d}} \\ \dot{\mathbf{q}}_{\underline{v}} \end{Bmatrix}}_{\dot{\mathbf{d}}_{\underline{g}}} + \underbrace{\begin{bmatrix} [\mathbf{K}_{\underline{d-d}}] & [\mathbf{K}_{\underline{d-q}}] \\ [\mathbf{K}_{\underline{q-d}}] & [\mathbf{K}_{\underline{q-q}}] \end{bmatrix}}_{\mathbf{K}} \underbrace{\begin{Bmatrix} \mathbf{d} \\ \mathbf{q}_{\underline{v}} \end{Bmatrix}}_{\mathbf{d}_{\underline{g}}} = \underbrace{\begin{Bmatrix} \mathbf{f} \\ \mathbf{u}_{\underline{v}} \end{Bmatrix}}_{\mathbf{f}_{\underline{g}}} \tag{25}$$

Note that $\mathbf{K}_{\underline{q-q}}$ is given in Eq. (5).

Since the fluid inertia is neglected, the mass matrix contains contributions only from the solid. The stiffness and damping matrices contain contributions from the fluid, as well as the solid. The displacement to displacement stiffness matrix can be shown to be

$$\mathbf{K}_{\underline{d-d}} = K_{\underline{d-d}mn} = K_{\underline{\text{solid}}mn} + K_{\underline{\text{fluid}}mn} \tag{26}$$

where

$$K_{\underline{\text{fluid}}mn} = -\int_{\Phi} \sum_{i=1}^{3} e_{mi} a_i \sum_{j \in \mathbb{P}^2} \phi_j \frac{\partial p_j}{\partial d_n} d\Phi \tag{27}$$

and

$$K_{\underline{\text{solid}}mn} = \sum_{\underline{\text{elements}}} \int_{\Pi} \sum_{i,j,k,l=1}^{3} \frac{L_{ijkl}}{4} \left( \frac{\partial V_{im}}{\partial x_j} + \frac{\partial V_{jm}}{\partial x_i} \right) \left( \frac{\partial V_{kn}}{\partial x_l} + \frac{\partial V_{ln}}{\partial x_k} \right) d\Pi \tag{28}$$

where $V_{jm}$ is the coupling between $u_j$ and $d_m$, i.e., the coupling between the displacement field in the $x_j$ direction and the displacement of degree of freedom $m$. Thus, $V_{jm}$ is either zero or equal to the shape function of the node associated to degree of freedom $m$.

Note that in the expression for the fluid part of the stiffness matrix, the inward normal of the solid $a_i$ will depend on space $(\chi_1, \chi_2)$ if higher order elements are used. Since damping is dominated by the fluid, the structural damping is neglected, leading to

$$\mathbf{D}_{\underline{d-d}} = D_{\underline{d-d}mn} = -\int_{\Phi} \sum_{i=1}^{3} e_{mi} a_i \sum_{j \in \mathbb{F}^2} \phi_j \frac{\partial p_{\underline{j}}}{\partial \dot{d}_n} d\Phi \tag{29}$$

Fluid inertia is neglected as one of the assumptions in the Reynolds equation. This assumption is valid due to the low Reynolds number of the flow. Thus, the displacement to displacement mass matrix contains only contributions from the solid

$$\mathbf{M}_{\underline{d-d}} = M_{\underline{d-d}mn} = \sum_{\underline{\text{elements}}} \int_{\Pi} \sum_{i=1}^{3} \rho V_{im} V_{in} d\Pi \tag{30}$$

The flow to displacement stiffness matrix is the nodal force produced by an incremental change in an orifice flow, thus

$$\mathbf{K}_{\underline{d-q}} = K_{\underline{d-q}mn} = \int_{\Phi} \sum_{i=1}^{3} e_{mi} a_i \sum_{j \in \mathbb{F}^2} \phi_j \frac{\partial p_{\underline{j}}}{\partial q_{\underline{v}n}} d\Phi \tag{31}$$

The displacement to flow stiffness matrix is the change in control signal, resulting from an incremental change in a nodal displacement, that is

$$\mathbf{K}_{\underline{q-d}} = K_{\underline{q-d}mn} = \frac{\partial u_{\underline{v}m}}{\partial d_n} \tag{32}$$

Note that the functionals $(u_{\underline{v}m}, m = 1,2,\ldots)$ can be chosen freely. Thus, $\mathbf{K}_{\underline{q-d}}$ constitutes an active part of the system, and can be tuned to produce desired behavior. If, for instance, a linear D-regulator was implemented, $\partial u_{\underline{v}m}/\partial d_n$ would be the displacement gain. Let us consider an example with one servovalve so that $q_{\underline{v}n} = q_{\underline{v}1} = q_{\underline{v}}$ with a P-D regulator that responds to the rotor displacement and displacement rate in the $x_2$ direction only. If we assign the last nodal degree of freedom $r$ to the rotor movement in the $x_2$ direction, then the functional $u_{\underline{v}m} = u_{\underline{v}1} = u_{\underline{v}}$ would be

$$u_{\underline{v}} = G_{\underline{P}} d_{\underline{\text{rotor2}}} + G_{\underline{D}} \dot{d}_{\underline{\text{rotor2}}} \tag{33}$$

Moving the electronic servovalve signal to the left hand side, the system matrices become

$$\mathbf{K} = \begin{bmatrix} [\mathbf{K}_{\underline{dd}}] & \int_{\Phi} \sum_{i=1}^{3} e_{mi} a_i \sum_{j \in \mathbb{F}^2} \phi_j \frac{\partial p_{\underline{j}}}{\partial q_{\underline{v}}} d\Phi \\ [0, \ldots, -G_{\underline{P}}] & 1/K_{\underline{v}} \end{bmatrix} \tag{34}$$

$$\mathbf{D} = \begin{bmatrix} [\mathbf{D}_{\underline{dd}}] & 0 \\ [0, \ldots, -G_{\underline{D}}] & \frac{2\xi_{\underline{v}}}{\omega_{\underline{v}} K_{\underline{v}}} \end{bmatrix}, \quad \mathbf{M} = \begin{bmatrix} [\mathbf{M}_{\underline{dd}}] & 0 \\ 0 & \frac{1}{\omega_{\underline{v}}^2 K_{\underline{v}}} \end{bmatrix} \tag{35}$$

The linearized system is useful for two things. First, it allows linear frequency domain analysis of the bearing; this shall be performed in Sec. 5. Second, the system stiffness matrix is exactly the Jacobian of the out of balance forces, and is thus necessary when performing Newton–Raphson iterations toward equilibrium. Since the system is nonlinear, it will potentially have more than one static equilibrium. A good way to reach a (the) stable equilibrium position is to run a Newmark time stepping solution until a given time, and use the final system state as the initial guess for Newton–Raphson iterations. Since the pads are allowed to deform, the system typically contains many thousands of degrees of freedom. The solid part of the stiffness matrix is singular because of the pivot supports, so the equations must be solved as fully coupled, which means that the fluid part of the stiffness matrix must be computed at each Newton–Raphson iteration step. This is nonsymmetric and nonsparse, which makes the solution computationally challenging. In the present investigation, the Jacobi preconditioned conjugate gradient squared method (see, e.g., Ref. [32]) was used to solve at each iteration step, exhibiting decent performance. Presumably, a more advanced preconditioner would improve performance.

## 5 Analyses

To obtain tangible information about the bearing behavior, we create a bearing superelement, i.e., we condense away all degrees of freedom, except those of the rotor. Setting rotor parameters to zero, the isolated properties of the bearing, i.e., the stiffness and the damping, are obtained. Given that the problem is dynamic in nature, the bearing properties become frequency dependent. With a time harmonic excitation of the rotor $\mathbf{f}_{\underline{s}} = \mathbf{f}_{\underline{s}0} e^{\imath\omega t}$, we can write the solution as $\mathbf{d}_{\underline{s}} = \mathbf{d}_{\underline{s}0} e^{\imath\omega t}$, where

$$(\mathbf{K} + \imath\omega\mathbf{D} - \omega^2\mathbf{M})\mathbf{d}_{\underline{s}0} = \mathbf{f}_{\underline{s}0} \tag{36}$$

Now, the bearing stiffness is defined as the real part of the force amplitude response to a unit movement of displacement amplitude. The damping is defined as the imaginary part divided by the frequency. That is, we know that the displacement of the rotor in the $x_1$ and $x_2$ direction is unity and zero, respectively, but we need to solve the system to know the value of the other roughly 29,998 (complex valued) displacements. For example, given a solution to Eq. (36) $\mathbf{d}_{\underline{s}0} = \{\ldots, 1, 0, \ldots\}^T$, where the 1 and 0 are a prescribed rotor displacements in the $x_1, x_2$ plane, and a corresponding force vector $\mathbf{f}_{\underline{s}0} = \{\ldots, f_{\underline{\text{rotor1}}}, f_{\underline{\text{rotor2}}}, \ldots\}^T$. Then

$$K_{\underline{b}11} = \text{Re}(f_{\underline{\text{rotor1}}}), \quad K_{\underline{b}21} = \text{Re}(f_{\underline{\text{rotor2}}}) \tag{37}$$

and

$$D_{\underline{b}11} = \frac{1}{\omega}\text{Im}(f_{\underline{\text{rotor1}}}), \quad D_{\underline{b}21} = \frac{1}{\omega}\text{Im}(f_{\underline{\text{rotor2}}}) \tag{38}$$

For tilting-pad journal bearings, for the special case of four pads and load between pad configurations, it is generally the case that the off diagonal stiffness and damping components are negligible, compared with the diagonal ones. Furthermore, the diagonal components are all but equal. So it is sensible to consider the bearing stiffness and damping simply as scalar values $K_{\underline{b}}$ and $D_{\underline{b}}$. Since the rotor is perturbed along the real axis, all phases between degrees of freedom of the result vector $\mathbf{d}_{\underline{s}0}$ are measured from the real axis, and are relative to the phase of the rotor (Fig. 4).

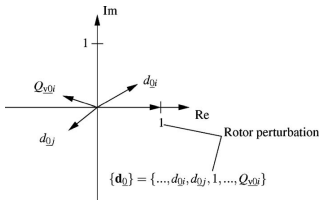


**Fig. 4 Visualization of rotor perturbation and result vector components**

**Table 1 Bearing geometrical properties**

| Property | Unit | Value |
|---|---|---|
| Pad radius of curvature | mm | 50 |
| Rotor radius | mm | 49.9 |
| Nominal clearance | $\mu$m | 100 |
| Assembled (minimum) clearance | $\mu$m | 50 |
| Preload | - | 0.5 |
| Pad extension | deg | 69.3 |
| Angular pivot location | deg | Center ofpad |
| Radial pivot location | mm | 64 |
| Pad length | mm | 100 |
| Nominal pad thickness | mm | 14 |

## 6 Computations and Results

The bearing under investigation has a length and diameter of 0.1 m, so the length/diameter ratio is 1. Each pad extends 69.3 deg. There is one orifice situated in the center of each pad. Each orifice has a diameter of 6 mm. The pads are at 45 deg angles to the $x_1$ and $x_2$ directions. Key geometrical parameters are indicated in Table 1. The rotor is loaded in the $x_1$ direction, thus, we have a load between pad configuration. Figure 5 shows the finite element mesh used for the computations. Second order elements with 20 nodes are used. The mesh may seem coarse, but we remind that in this particular investigation, derived fields (e.g., stresses and strains) are of no interest, thus, convergence is achieved rather quickly.

The mesh, as shown in Fig. 5, contains roughly 60,000 degrees of freedom. We exploit the symmetry of the problem, and thus only have to deal with half of these, although the whole structure is shown. The number of degrees of freedom is modest for, for instance, static stress analysis of a solid with a dead load. However, as mentioned, the current problem produces system matrices that have none of the usual beneficial properties that facilitate fast solution of large systems of equations. They are not symmetric/hermitian nor sparse. This makes the solution of the linearized system of equations (36) a computational challenge. In the present investigation, the conjugate gradient squared method with the Jacobi preconditioner has been used. For the given discretization, solution time for the system of equations (36) is of the order of magnitude of hours with a modern CPU, when the code (FORTRAN90) is compiled with the highest level of compiler optimization. It is expected that solution time can be significantly reduced by implementing a solver, which is more suited to the given problem. This work is underway.

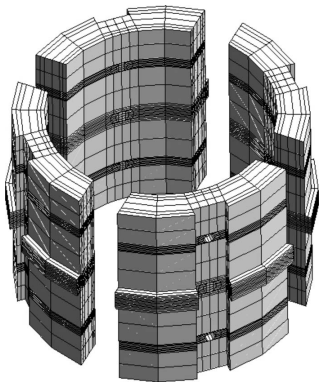

**Fig. 5 The finite element mesh used for the computations. Note that the mesh, as shown here, contains roughly 60,000 degrees of freedom. Due to symmetry, only half of these need be considered. The elements are 20 node (second order) serendipity elements. When derived fields (stresses and strains) are not of relevance, this mesh is more than adequate in terms of refinement.**

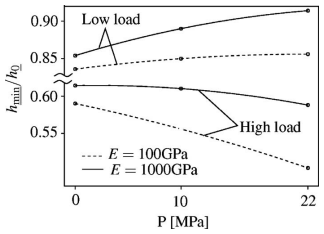


**Fig. 6 Curves of minimum film thickness for different load cases and pad elastic moduli. High load refers to a radial static bearing load of 20,000 N, and low load corresponds to 2000 N. The data are fitted by polynomials.**

First, we shall implement a hybrid lubrication system where a constant static injection pressure is specified a priori to all orifices. The value of the injection pressure is the same in all four orifices, and results for $p_{inji}=P=0$, 10 MPa, and 22 MPa are investigated. Furthermore, we select two different values of the pad modulus of elasticity, $E=100$ GPa and $E=1000$ GPa, representing bearing brass, and a quasi rigid material, respectively. Parameters for bearing brass are selected, since the authors have access to a test rig with brass pads. The Poisson's ratio is set to $\nu=0.3$ and the density to $\rho=8400$ kg/m$^3$. The rotational speed is $U=31.14$ m/s, corresponding to $\Omega=100$ Hz, and the oil viscosity is $\mu=0.019$ Ns/m$^2$. The preload factor, as defined in, e.g., Ref. [33], is 0.5. The servovalve leak flow is $q_L=3.0$ ml/s. The orifice inlet of each orifice is set to $l_0=1$ m, meaning that we specify the injection pressure 1 m of pipe before the oil reaches the journal. Unless otherwise stated, these are the relevant model parameters henceforth.

**6.1 Static Analysis.** Figure 6 shows curves of minimum film thickness for the two different load cases, and three different static injection pressure values. Table 2 gives an overview of the simulation parameters. Clearly, the value of the pad elastic modulus influences the minimum film thickness. It is worth to highlight that, where an increase in static injection pressure has a positive influence on the minimum film thickness at low load, the opposite is true for the high load case. Here, there are two oppositely acting effects playing an important role: (i) the pressure and flow effects related to the radial oil injection and (ii) the changes of oil film gradient. The pad-rotor realignment associated with an increase in static injection pressure will increase the minimum film thickness, if the oil film gradient does not drastically change, as it can be seen in Fig. 6 at low load. The oil film gradient can change due to a change in the relative equilibrium position between the rotor and tilting-pad or due to the deformation of the pad and changes in the

**Table 2 Static analysis parameters**

| Property | Unit | Value(s) |
|---|---|---|
| Static radial bearing load | N | 20,000, 2000 |
| Injection pressures | Pa | 0, 100, 220 |
| Rotational speed | rpm | 6000 |
| Viscosity | N s/m$^2$ | 0.019 |

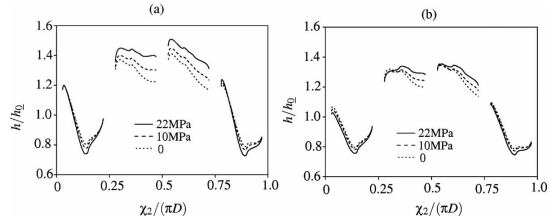


**Fig. 7 Curves of static oil film thickness as a function of $\chi_2$ measured from $(x_1, x_2)=(D/2, 0)$ for different injection pressures and pad elastic moduli; (*a*) $E=100$ GPa and (*b*) $E=1000$ GPa. The bearing is under a static radial load of 20,000 N in the $x_1$ direction, corresponding to $S=0.235$.**

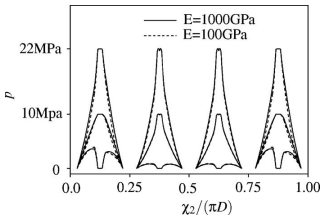


**Fig. 8 Curves of static pressure at $x_3=0$ as a function of $\chi_2$ measured from $(x_1, x_2)=(D/2, 0)$. The bearing is under a static radial load of 20,000 N in the $x_1$ direction, corresponding to $S=0.235$. Results for the three different values of static injection pressure are shown.**

pad radius. At high load, the elastic deformation of the pad, and consequently of the pad radius, strongly influences the oil film gradient. The bearing preload effect decreases due to the reduction in the pad radius. Figure 7 shows curves of static fluid film thickness at equilibrium for different injection pressures and elastic moduli, as a function of the angular position. The load is high, at 20,000 N. The loaded pads are the ones in the intervals $\chi_2/(\pi D) \in [0; 0.25]$ and $\chi_2/(\pi D) \in [0.75; 1.0]$. Considering Fig. 7(*a*), which is the computation for the flexible case. Clearly, the film thickness of the loaded pads changes with injection pressure. However, the effect is concentrated to the center of the pad, leaving the thickness practically unaltered at the edges. This constitutes the aforementioned decrease in effective pad radius. Compare this with the quasi rigid case in Fig. 7(*b*), where the effect occurs more evenly along the pad surface in a tilting motion, thus, with no change in pad effective radius.

Figure 8 shows pressure curves at $x_3=0$ for the three different static injection pressures and two different values of elastic modulus. Only results for the high load case ($S=0.235$) are presented. Notice that the pressure profiles are very similar. However, when the curves are carefully analyzed, one can see that the more compliant the material is, the narrower are the pressure profiles. The load tends to distribute itself over a smaller surface in the compliant pad case, deforming the pad, reducing the pad radius, and decreasing the bearing load capacity and minimum oil film thickness. Although the pad compliance has little effect on static pressure, it has a profound impact on fluid film thickness, as previously stated. Also, as we shall see in Sec. 6.2, it influences the bearing stiffness (i.e., the effect of the infinitesimal change in pressure due to an infinitesimal rotor movement.

**6.2 Bearing Dynamic Coefficients (Hybrid Lubrication).** In Figs. 9(*a*) and 9(*b*), curves of bearing stiffness for different values of static injection pressure and pad elastic modulus are shown. Table 3 gives an overview of the simulation parameters. In Fig. 9(*a*), the rotor is operating at low static load of $\mathbf{f}_{\underline{r}} = \{2000\ \mathrm{N}, 0\}^T$, corresponding to the Sommerfeld number $S=2.35$. In Fig. 9(*b*), the load is increased ten-fold to $S=0.235$. Primarily, it is interesting to observe that, for the low load case, increasing the static injection pressure will decrease the stiffness. For the high load case, the effect of changing the static injection pressure is the opposite. This change in the sign of the effect of hybrid lubrication corresponds well to what was observed for the minimum film thickness in Fig. 6. For higher loads, pad compliance tends to dominate, compared with the effect of static injection. This is because a given change in the static injection pressure will have a diminishing effect on pad angle as the load increases. One could conclude that, for higher loads, the effect of pad com-

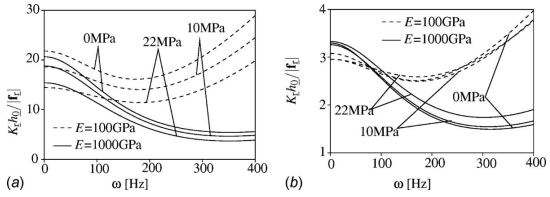


**Fig. 9 (*a*) Curves of bearing stiffens for various values of the static injection pressures in the low load case, $S=2.35$. (*b*) Curves of bearing stiffens for various values of the static injection pressures in the high load case, $S=0.235$.**

**Table 3 Dynamic analysis parameters**

| Property | Unit | Value(s) |
|---|---|---|
| Static radial bearing load | N | 20,000, 2000 |
| Proportional gain | V/m | 0, 500,000 |
| Derivative gain | V/m | 0, 50,000 |
| Valve flow-pressure coefficient | $m^3/(s\ Pa)$ | $1.13\times10^{-12}$ |
| Valve flow-voltage coefficient | $m^3/(s\ V)$ | $33.4\times10^{-6}$ |
| Valve damping ratio | - | 0.48 |
| Valve eigenfrequency | Hz | 320.16 |
| Rotational speed | rpm | 6000 |
| Viscosity | $N\ s/m^2$ | 0.019 |

pliance almost cancels out the hybrid lubrication terms. It is important to point out though, that such a conclusion is valid only for a single orifice positioned over the pivot line.

Figures 10(*a*) and 10(*b*) show curves of bearing damping for different values of static injection pressure and pad elastic modulus. The loads are $S=2.35$ and $S=0.235$, respectively. Again, the high load case shows that pad compliance almost eliminates the effect of static oil injection. Also, the dependence of frequency seems to drop.

**6.3 Bearing Dynamic Coefficients (Active Lubrication).** Now we shall implement a control system that responds to rotor displacement in the $x_1$ direction. We select two sets of gains; these sets apply to both servovalves, and the master and slave orifice of each valve is set so that the oil injection will oppose rotor motion (increase stiffness and damping). The orifices have the same dimensions and locations as before. The "proportional gains" $G_{\underline{P}}=500{,}000$ V/m, $G_{\underline{D}}=0$ Vs/m and the "derivative gains" $G_{\underline{P}}=0$ V/m, $G_{\underline{D}}=50{,}000$ Vs/m. The servovalve constants are set to $K_{\underline{pq}}=1.13\cdot10^{-12}$ $m^3/(sPa)$, $K_{\underline{v}}=33.4\times10^{-6}$ $m^3/(sV)$, $\xi_{\underline{v}}=0.48$, and $\omega_{\underline{v}}=320.16$ Hz. Note that there is no reason to believe that the coupled system will have a resonance exactly at $\omega=\omega_{\underline{v}}$. The servovalve parameters are similar to those used in Ref. [22]. The servovalve parameters are realistic in the sense that, even under severe load conditions, the assumed maximum injection pressure of 22 MPa is not exceeded.

Figures 11(*a*) and 11(*b*) show curves of bearing stiffness for proportional gains and two different values of pad elastic modulus. Note that the figures are almost identical; only a factor of 10 makes them different. This factor stems from the simple fact that the set of curves in Fig. 11(*a*) is normalized with the force $|\mathbf{f}_{\underline{r}}|=2000$ N, whereas Fig. 11(*b*) is normalized with $|\mathbf{f}_{\underline{r}}|=20{,}000$ N. In other words, the stiffness is independent of load case, i.e., independent of the state, so the system is essentially linear in behavior. This is because the controller, which is a linear controller, dominates the system almost completely. It is seen that pad compliance has an effect on bearing stiffness—in particular, for higher excitation frequencies. The first bending mode of the pads has an eigenfrequency of several kHz, so we are nowhere near pad bending resonance. Nevertheless, pad compliance has a significant effect.

Comparing the values of the stiffness coefficients for $\omega>\omega_{\underline{v}}$ in Figs. 9 and 11, one can conclude that no significant change in such coefficients is achieved. To realize this, compare the values after the point marked by $x$ in Fig. 11 to the corresponding values of Fig. 9. The curves are very similar. That is, above the servovalve eigenfrequency, the servovalves have almost no dynamic response, and the flow is almost constant in time.

Figures 12(*a*) and 12(*b*) show curves of bearing stiffness for derivative gains and two different values of pad elastic modulus. Again, the figures are almost identical, differing only by the previously mentioned factor of 10. Again, higher frequencies promote an increasing influence from pad compliance. However, where pad compliance tended to increase stiffness for the proportional gain controller, it has the opposite effect in the case of the derivative gain controller. Also note that the derivative gain controller has a much greater influence on the bearing stiffness at higher frequencies than the proportional gain controller for the given parameters. This can seem contradictory, since a propor-

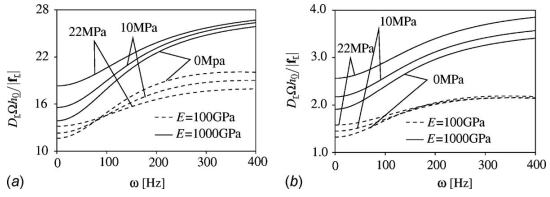


**Fig. 10 (*a*) Curves of bearing damping for various values of the static injection pressures in the low load case, $S=2.35$. (*b*) Curves of bearing damping for various values of the static injection pressures in the high load case, $S=0.235$.**

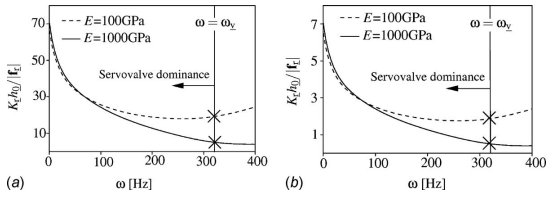


**Fig. 11 (*a*) Curves of bearing stiffness for proportional control gains in the low load case, $S=2.35$. (*b*) Curves of bearing stiffness for proportional control gains in the high load case, $S=0.235$.**

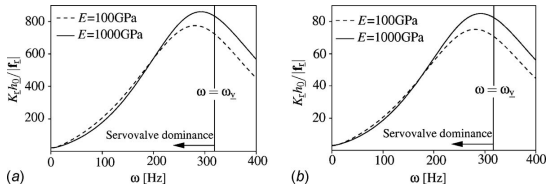


**Fig. 12 (*a*) Curves of bearing stiffness for derivative control gains in the low load case, *S*=2.35. (*b*) Curves of bearing stiffness for derivative control gains in the high load case, *S*=0.235.**

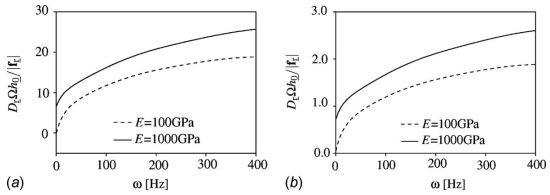


**Fig. 13 (*a*) Curves of bearing damping for proportional control gains in the low load case, *S*=2.35. (*b*) Curves of bearing damping for proportional control gains in the high load case, *S*=0.235.**

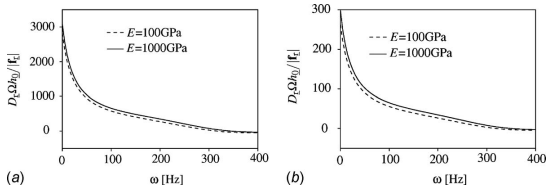


**Fig. 14 (*a*) Curves of bearing damping for derivative control gains in the low load case, *S*=2.35. (*b*) Curves of bearing damping for derivative control gains in the high load case, *S*=0.235.**

tional term is generally regarded as stiffness, and a derivative term is generally regarded as damping. What is important to remember is that the dynamic condensation process couples everything.

Figures 13(*a*) and 13(*b*) show curves of bearing damping for proportional gains and two different values of pad elastic modulus. As before, the figures are almost identical, with a factor of 10 between them. The effect of pad compliance is to reduce damping. For lower frequencies, the stiffness was only affected a little by pad compliance (see Fig. 12), but as we see, the damping is affected for all frequencies. When comparing the active case in Fig. 13 with the corresponding hybrid case in Fig. 10, we see very similar magnitudes. Thus, we must conclude that a control system with only proportional gains will not affect bearing damping. This corresponds well to the findings in Ref. [21].

Figures 14(*a*) and 14(*b*) show curves of bearing damping for derivative gains and two different values of pad elastic modulus. Again, the system shows an effectively linear behavior. Here we see little to no pad compliance effect on damping, meaning that not only does the controller make the system almost linear, it also dominates the imaginary part of the dynamic condensation process.

## 7 Conclusions

It is seen that for quasi rigid pads, static (constant pressure) oil injection significantly influences bearing coefficients, a bit less so at high load. However, when pad compliance is taken into account, this effect is dramatically reduced. One should keep this in mind when designing open loop control systems, since all real pads are flexible. We restate that the pad elastic modulus chosen for the flexible case corresponds to that of bearing brass.

The minimum oil film thickness is influenced by static oil injection. However, depending on radial load, the influence will be positive or negative. This result is explained as a shift between two effects: (i) the pressure and flow effects related to the radial oil injection and (ii) the changes of oil film gradient due to the relative equilibrium position between rotor and tilting-pad or due to the deformation of the pad and changes in the pad radius.

When closed loop control is applied to the system, either as a proportional or derivative controller (or a combination), and sensible control gains are selected, the dynamic coefficients can be significantly modified. It seems that a controller with realistic control parameters can dominate the bearing dynamics. Embracing this fact, we can design closed loop control systems, with disregard to the static load case. This greatly reduces the work of tuning a control system, since there is one less parameter to take into consideration.

## Nomenclature

$D_{\underline{b}}$ = bearing damping

$D$ = bearing diameter
$E$ = modulus of elasticity for the solid (the pads)
$\mathbb{F}$ = set containing the numbers of nodes in $\Phi$
$\mathbb{F}^2$ = set containing the degrees of freedom of nodes in $\Phi$ in two dimensions
$G_{\underline{P}}$ = proportional (displacement) gain of servovalve
$G_{\underline{D}}$ = derivative (velocity) gain of servovalve
$K_{\underline{v}}$ = servovalve electrical signal constant
$K_{\underline{pq}}$ = servovalve pressure-flow constant
$K_{\underline{b}}$ = bearing stiffness
$L_{ijkl}$ = constitutive tensor
$N$ = total number of degrees of freedom
$T_i$ = traction in direction $x_i$
$S = 1/4\mu Ul(D/h_0)^2/(\pi|\mathbf{f}_{\underline{r}}|)$ = Sommerfeld number
$U$ = tangential velocity of rotor surface
$a_i$ = inward normal of the solid
$d_i$ = displacement of degree of freedom $i$
$e_{im}$ = the unit vector of displacement component $d_i$, thus if $d_i$ points in the $x_1$ direction, then $\{e\}_i = \{1,0,0\}^T$, and so on
$f_i$ = external force on degree of freedom $i$
$f_{\underline{ri}} = \mathbf{f}_{\underline{r}}$ = rotor force vector
$g_i$ = shape function, that describes the velocity profile of the orifice $i$
$h$ = fluid film thickness
$h_{\underline{\min}}$ = minimum fluid film thickness
$h_0$ = assembled clearance
$l$ = axial length of bearing
$l_0$ = length of orifice inlet
$p$ = fluid film pressure
$p_{\underline{\text{inj}i}}$ = orifice injection pressure of orifice $i$
$q_{\underline{v}}$ = servovalve flow
$q_{\underline{L}}$ = servovalve leakage flow
$q_i$ = flow to orifice $i$
$u_i$ = field of displacements in the $x_i$ direction
$u_{\underline{v}}$ = servovalve control signal
$(x_1, x_2, x_3)$ = Cartesian coordinate system
$\Lambda$ = boundary of $\Pi$
$\Pi$ = domain of solid (the pads)
$\Phi$ = domain of lubricated surface
$\Omega$ = angular velocity
$\mu$ = absolute (dynamic) viscosity
$\xi_{\underline{v}}$ = servovalve damping factor
$\phi_i$ = shape function of node $i$
$\varepsilon_{ij}$ = strain tensor
$\delta\varepsilon_{ij}$ = tensor of virtual strain increments
$\rho$ = density of solid
$(\chi_1, \chi_2)$ = curvilinear coordinate system on lubricated surface
$\omega$ = excitation frequency
$\omega_{\underline{v}}$ = servovalve eigenfrequency

## References


[1] Lund, J., 1964, "Spring and Damping Coefficients for the Tilting Pad Journal Bearing," ASLE Trans., **7**, pp. 342–352.
[2] Lund, J., 1987, "The Influence of Pad Flexibility on the Dynamic Coefficients of a Tilting-Pad Journal Bearing," ASME J. Tribol., **109**, pp. 65–70.
[3] Earles, L. L., Palazzolo, A. B., and Armentrout, R. W., 1990, "A Finite Element Approach to Pad Flexibility Effects in Tilt Pad Journal Bearings: Part I—Single Pad Analysis," ASME J. Tribol., **112**, pp. 169–177.
[4] Earles, L. L., Palazzolo, A. B., and Armentrout, R. W., 1990, "A Finite Element Approach to Pad Flexibility Effects in Tilt Pad Journal Bearings: Part II—Assembled Bearing and System Analysis," ASME J. Tribol., **112**, pp. 178–182.
[5] Allaire, P. E., Parsell, J. A., and Barrett, L. E., 1981, "A Perturbation Method for the Dynamic Coefficients of Tilting-Pad Journal Bearings," Wear, **72**, pp. 29–44.
[6] Parsell, J. K., Allaire, P. E., and Barrett, L. E., 1983, "Frequency Effects in Tilting-Pad Journal Bearing Dynamic Coefficients," ASLE Trans., **26**, pp. 222–227.
[7] Santos, I. F., 1995, "On the Adjusting of the Dynamic Coefficients of Tilting-Pad Journal Bearings," STLE Tribol. Trans., **38**(3), pp. 700–706.
[8] Dmochowski, W., 2007, "Dynamic Properties of Tilting-Pad Journal Bearings: Experimental and Theoretical Investigation of Frequency Effects Due to Pivot Flexibility," ASME J. Eng. Gas Turbines Power, **129**, pp. 865–869.
[9] Rodriguez, L. E., and Childs, D. W., 2006, "Frequency Dependency of Measured and Predicted Rotordynamic Coefficients for a Load-on-Pad Flexible-Pivot Tilting-Pad Bearing," ASME J. Tribol., **128**, pp. 388–395.
[10] Desbordes, H., Fillon, M.,Frêne, J., and Chan Hew Wai, C.,1995, "The Effects of Three-Dimensional Pad Deformations on Tilting-Pad Journal Bearings Under Dynamic Loading," ASME J. Tribol., **117**, pp. 379–384.
[11] Monmousseau, P., and Fillon, M., 1999, "Frequency Effects on the TEHD Behavior of a Tilting-Pad Journal Bearing Under Dynamic Loading," ASME J. Tribol., **121**(2), pp. 321–326.
[12] Flack, R. D., and Zuck, C. J., 1988, "Experiments on the Stability of Two Flexible Rotor in Tilting-Pad Journal Bearing," Tribol. Trans., **31**(2), pp. 251–257.
[13] Zuck, C. J., Flack, R. D., Knight, J. D., and Barrett, L. E., 1988, "Experiments and Stability Predictions of Two Sets of Tilting-Pad Bearings on an Overhung Rotor," Tribol. Trans., **31**(4), pp. 468–475.
[14] Lie, Y., You-Bai, Z. J., and Damou, Q., 1989, "Experiments on the Destabilizing Factors in Tilting-Pad Journal Bearings," Tribol. Int., **22**(5), pp. 329–334.
[15] Olsson, K. O., 1996, "Some Fundamental Aspects on the Dynamic Properties of Journal Bearings," *Proceedings of the Sixth International Conference on Vibrations in Rotating Machinery, IMechE*, pp. 31–40.
[16] White, M. F., and Chan, S. H., 1992, "The Subsynchronous Dynamic Behaviour of Tilting-Pad Journal Bearings," ASME J. Tribol., **114**(1), pp. 167–173.
[17] Nicoletti, R., and Santos, I. F., 2003, "Linear and Non-Linear Control Techniques Applied to Actively-Lubricated Journal Bearings," J. Sound Vib., **260**, pp. 927–947.
[18] Glienicke, J., 1987, "Sem-Nr.111107, Stabilitätsprobleme bei Lagerung Schnelllaufenden Wellen—Berechnung, Konstruktion und Verhalten von Merhflächen- und Kippsegmentlagern," *Tech. Rep*, Technische Akademie Wuppertal, Germany.
[19] Santos, I. F., Nicoletti, R., and Scalabrin, A., 2004, "Feasibility of Applying Active Lubrication to Reduce Vibration in Industrial Compressors," ASME J. Eng. Gas Turbines Power, **126**(4), pp. 848–854.
[20] Santos, I. F., and Russo, F. H., 1998, "Tilting-Pad Journal Bearings With Electronic Radial Oil Injection," ASME J. Tribol., **120**, pp. 583–594.
[21] Santos, I. F., Nicoletti, R., and Scalabrin, A., 2001, "Beitrag zur Aktiven Schmierungstheorie," *Schwingungen in rotie-renden Maschinen*, Vieweg Verlag, Braunschweig, Germany, Vol. 5, pp. 21–30.
[22] Santos, I. F., and Scalabrin, A., 2003, "Control System Design for Active Lubrication With Theoretical and Experimental Examples," ASME J. Eng. Gas Turbines Power, **125**, pp. 75–80.
[23] Nicoletti, R., and Santos, I. F., 2005, "Frequency Response Analysis of an Actively Lubricated Rotor/Tilting-Pad Bearing System," ASME J. Eng. Gas Turbines Power, **127**(3), pp. 638–645.
[24] Santos, I. F., 2009, "Trends in Controllable Oil Film Bearings," *Proceedings of the IUTAM Symposium on Emerging Trends in Rotor Dynamics*, Springer, Delhi, India, pp. 1–15.
[25] Heinrichson, N., Santos, I. F., and Fuerst, A., 2007, "The Influence of Injection Pockets on the Performance of Tilting-Pad Thrust Bearings: Part I—Theory," ASME J. Tribol., **129**(4), pp. 895–903.
[26] Heinrichson, N., Fuerst, A., and Santos, I. F., 2007, "The Influence of Injection Pockets on the Performance of Tilting-Pad Thrust Bearings: Part II—Comparison Between Theory and Experiment," ASME J. Tribol., **129**(4), pp. 904–912.
[27] Earnshaw, S., 1842, "On the Nature of the Molecular Forces Which Regulate the Constitution of the Luminiferous Ether," Trans. Cambridge Philos. Soc., **7**(1), pp. 97–112.
[28] Braunbek, W., 1939, "Frei Schwebende Körper in Elektrischen und Magnetischen Feld," Z. Phys., **112**, pp. 753–763.
[29] Schweitzer, G., Bleuler, H., and Traxler, A., 1994, *Active Magnetic Bearings—Basics, Properties and Applications of Active Magnetic Bearings*, Hochschulverlag AG, Zürich, Switzerland.
[30] Dussaux, M., 1989, "Present Status of the Application of the Active Magnetic Bearings to Turbomachines," ASME, New York, Vol. 4, pp. 411–417.
[31] Cook, R., Malkus, D., Plesha, M., and Witt, R., 2001, *Concepts and Applications of Finite Element Analysis*, Wiley, New York.
[32] Greenbaum, A., 1997, *Iterative Methods for Solving Linear Systems*, Society for Industrial and Applied Mathematics, Philadelphia, PA.
[33] Someya, T., 1989, *Journal Bearing Databook*, Springer-Verlag, Berlin.

# Publication 2

Multi Orifice Active Tilting-Pad Journal Bearings - Harnessing of Synergetic Coupling Effects

Tribology International (Elsevier)

Tribology International 43 (2010) 1374–1391

Contents lists available at ScienceDirect

Tribology International

journal homepage: www.elsevier.com/locate/triboint

# Multi-orifice active tilting-pad journal bearings—Harnessing of synergetic coupling effects

Asger M. Haugaard, Ilmar F. Santos *

*Department of Mechanical Engineering, Technical University of Denmark, 2800 Lyngby, Denmark*

ARTICLE INFO

*Article history:*
Received 29 October 2009
Received in revised form
14 January 2010
Accepted 17 January 2010
Available online 25 January 2010

*Keywords:*
Tilting-pad journal bearings
Control
Elastohydrodynamics
Vibration

ABSTRACT

The dynamic performance of tilting-pad journal bearings with controllable radial oil injection is theoretically investigated, exploring the synergetic effect between passive elastohydrodynamics and active radial lubricant injection.

The flexible tilting-pads are modelled as linearly elastic using finite elements. To reduce computational work, a pseudo-modal reduction is applied.

Curves of dynamic bearing coefficients as well as the corresponding phase-magnitude plots are presented.

Strong synergy between elastohydrodynamics and active control is observed, in particular for bearings with injection orifices far from the pivot line.



## 1. Introduction

Due to the development of high performance rotating machinery, growing attention has been paid to the design of new active (mechatronic) devices able to actively control vibrations and improve dynamic behaviour, i.e. magnetic bearings [1] piezoelectric bearing pushers [2–5], hydraulic actuator journal bearings [6–8], variable impedance bearings [9], actively controlled bearing surface profiles or simply deformable bushes [10], active journal bearings with flexible sleeves [11,12], active lubricated bearings [13–15], or pressurised bearings [16,17] among others.

The active systems described in [10–12,15] belong to a special category of tribological devices where "controllable" elastohydrodynamics plays a crucial role. In such systems the bearing surface profile is intentionally modified and/or adjusted in order to control rotor vibrations and improve bearing dynamic properties. The actively controlled bearing surface profiles [10] can be generated by coupling any kind of actuator (hydraulic, electromagnetic or piezoelectric) to deformable bushes. The efficiency of such an approach will be strongly dependent on the number and type of actuators used. In [10] the unbalance response of a rigid rotor is significantly reduced using actuators in one single direction. By adapting pressure chambers to the back of one single finger-form deformable sleeves bearing profile can also be changed and subsynchronous vibration instabilities eliminated, as illustrated in [11]. The same idea is later on used to design an active journal bearing composed of three finger-form deformable sleeves [12] in the form of a tilting-pad bearing with three flexible pads clamped at one of their ends. In [15] a combined effect of active radial pressure control [12–14] and bearing surface profile is investigated. Due to the manufacturing of only a single orifice in the centre of the deformable pad, the modification of the bearing surface profile is limited.

This paper is fundamentally based on the knowledge gained in [15]. The main original theoretical contribution is the exploration of different orifice configurations over the pad surface in order to improve the dynamic properties of the bearing through the combined effect of active radial oil injection (active lubrication) and pad deformation.

In [15], dynamic coefficients for active tilting pad journal bearings were determined, but only with centrally placed orifices. It was found in [15] that, while maybe not significant for static analysis, pad compliance plays a major role in bearing response for higher frequencies, and thus must be included. In [15] this was done with a full fletched finite element model, making analysis a computationally heavy process. Though, in [18] it is shown that, under certain circumstances, computation time can be reduced significantly. Here we shall take a different approach than that of [15] to reduce computation time. The solid part of the finite element model is used to compute approximate eigenmodes of the system. These are then used for pseudo-modal reduction of the entire system. Pseudo; because the eigenmodes of the solid system will never expand the motion of the entire system (including the fluid) exactly. Nevertheless, as long as fluid forces from pad deformation are small compared to solid forces, a

* Corresponding author. Tel.: +45 45256269; fax: +45 45931475.
*E-mail address:* ifs@mek.dtu.dk (I.F. Santos).

0301-679X/$ - see front matter © 2010 Elsevier Ltd. All rights reserved.
doi:10.1016/j.triboint.2010.01.009

pseudo-modal reduction is sufficiently accurate to capture the essential behaviour of the system. In other words, fluid forces from mode shape perturbation are a measure of the error of the pseudo-modal reduction. As long as these are small, the method is accurate. In fact, many previous studies, e.g. [19–21] model the pads as rigid bodies. A rigid body model is essentially a pseudo-modal reduction containing only the first eigenmode of vibration of the solid, since the first eigenmode of vibration will be the rigid body pivoting motion.

One of the earliest studies of tilting pad journal bearings to include pad compliance is [22], where a beam model is taken to capture essential bearing deformation. Since then, more advanced models have been introduced. In [23] the fluid and solid are both discretised in two-dimensional on perpendicular surfaces. Thus the bearing is assumed "long", but only in terms of the solid deformations. This should not be confused with the "long" and "short" bearing theory of tribology literature. Furthermore, the deformations are reduced to a scalar; pad effective radius. This is a clever way of incorporating pad compliance in a compact way. The analyses are conducted for single pads only. In [24] an assembled rotor pad system is investigated. Pad compliance is seen to have a destabilising effect on the system, reducing the instability onset speed. In [25] a similar model is used to compute time series solutions for various system states. However, very prudently, pad inertia from all but the tilting motion is neglected. This reduces computation time considerably. In [26] a similar study is conducted on a model where the pads are modelled in three dimensions. A comparison is carried out, which reveals that for severely loaded bearings, a three-dimensional pad compliance model is necessary.

The present investigation does not take thermal effects into account. This is relegated to future research. In [27], thermal effects were accounted for in an active tilting-pad journal bearing, but pad compliance was neglected.

In terms of potential application of this work, one could mention steam turbine shafts, normally supported by tilting-pad journal bearings [28–31]. Instability phenomena in steam turbines may happen as a consequence of certain characteristics of the steam flow as well as of the mechanical and geometrical properties of the seals. The steam-whirl instability onsets occur generally in on-load operating conditions characterised by high values of steam pressure and flow.

## 2. Governing equations

In the present paper, tensors will appear in certain places. To avoid confusion, while retaining a consistent nomenclature, summation of repeated indices is not employed, thus all summations are stated explicitly. Underlined indices are part of variable names and indices without underline are used for numbering, e.g. $q_{\underline{v}i}$ is the $\underline{v}$alve flow of servo-valve number $i$. An overview of the nomenclature is given in Table 1.

Fig. 1 illustrates the different coordinate frames and domains used to describe the elastic behaviour of the pads, and the journal pressure distribution among the rotor and the pads. The curvilinear coordinates $(\chi_1, \chi_2)$ are used to represent the fluid film and the Cartesian coordinates $(x_1, x_2, x_3)$ are used to represent the pads.

The solid is taken to be linearly elastic and isotropic. Small strains and rotations suffice for the description of the deformed state. The governing equation is traditionally given directly in integral form as the principle of virtual work

$$\sum_{i,j,k,l=1}^{3} \int_{\Pi} L_{ijkl}\varepsilon_{kl}\delta\varepsilon_{ij}\,d\Pi = -\sum_{i=1}^{3}\int_{\Pi}\rho\ddot{u}_i\delta u_i\,d\Pi + \sum_{i=1}^{3}\int_{\Lambda} T_i\delta u_i\,d\Lambda \qquad (1)$$

**Table 1**
Nomenclature.

| | |
|---|---|
| $\mathbf{A}$ | Pressure system matrix |
| $\mathbf{D}$ | Generalised damping matrix |
| $D_{\underline{b}}$ | Bearing damping |
| $D_{\underline{q-q}}$ | Flow damping matrix |
| $E$ | Young's modulus |
| $G_{\underline{\Omega}}$ | Derivative gain |
| $G_{\underline{P}}$ | Proportional gain |
| $\mathbf{K}$ | Generalised stiffness matrix |
| $K_{\underline{b}}$ | Bearing stiffness |
| $K_{\underline{pq}}$ | Flow pressure constant |
| $K_{\underline{q-q}}$ | Flow stiffness matrix |
| $K_{\underline{s}}$ | Solid stiffness matrix |
| $K_{\underline{v}}$ | Valve static amplification |
| $L_{ijkl}$ | Solid constitutive tensor |
| $\mathbf{M}$ | Generalised mass matrix |
| $\mathbf{M}_{\underline{r}}$ | Rotor mass matrix |
| $\mathbf{M}_{\underline{q-q}}$ | Flow mass matrix |
| $\mathbf{M}_{\underline{s}}$ | Solid massmatrix |
| $U$ | Tangential rotor speed |
| $\mathbf{V}$ | Reduction matrix |
| $\mathbf{V}_{\underline{s}}$ | Matrix of solid modes of vibration |
| $\mathbf{b}$ | Modal coordinate vector |
| $\mathbf{d}_{\underline{e}}$ | Generalised displacement vector |
| $\mathbf{f}$ | Nodal forcevector |
| $\mathbf{f}_{\underline{e}}$ | Generalised force vector |
| $\mathbf{f}_{\underline{r}}$ | Rotor forcevector |
| $g_i$ | Orifice flow shape function |
| h | Fluid film thickness |
| $h_{\underline{a}}$ | Assembled clearance |
| $l_{\underline{oi}}$ | Orifice inlet length |
| $\mathbf{p}$ | Generalised pressure vector |
| $p$ | Fluid pressure |
| $p_{inji}$ | Injection pressure |
| $q_{\underline{L}}$ | Leak flow |
| $q_{\underline{v}}$ | Valve flow |
| $\mathbf{r}$ | Pressure right-hand side |
| $t$ | Time |
| $u_{\underline{i}}$ | Displacement |
| $u_{\underline{v}}$ | Valve input signal |
| $x_i$ | Inertial coordinates |
| $\Delta d_{\underline{ei}}$ | Rotor perturbation |
| $\Delta f_{\underline{ei}}$ | Rotor force response |
| $\Lambda$ | Solid boundary |
| $\Pi$ | Solid domain |
| $\varepsilon_{ij}$ | Strain tensor |
| $\xi_{\underline{v}}$ | Valve damping ratio |
| $\chi_i$ | Curvilinear coordinates |
| $\omega_{\underline{v}}$ | Valve eigenfrequency |
| $\Gamma$ | Fluid boundary |
| $\Lambda_{\underline{s}}$ | Diagonal matrix of eigenvalues |
| $\Phi$ | Fluid domain |
| $\nu$ | Poisson's ratio |
| $\rho$ | Solid density |
| $\omega$ | Excitation frequency |

where $\varepsilon_{kl}$ is the strain tensor, $\rho$ is the density of the solid, $T_i$ denotes the surface traction, $u_i$ is the displacement vector, $\delta$ denotes an increment and $L_{ijkl}$ is the constitutive tensor for the material, and is given by

$$L_{ijkl} = \frac{E}{2(1+\nu)}\left(\delta_{ik}\delta_{jl} + \delta_{il}\delta_{jk} + \frac{2\nu}{1-2\nu}\delta_{ij}\delta_{kl}\right) \qquad (2)$$

where $E$ is Young's modulus, $\nu$ is Poisson's ratio and $\delta_{ij}$ is Kronecker's delta. From Eqs. (1) and (2) the stiffness and mass matrices of the solid can be derived, refer to [15].

The pressure field in the fluid is described by the modified Reynolds equation

$$\frac{1}{12}\sum_{i=1}^{2}\frac{\partial}{\partial\chi_i}\left(\frac{h^3}{\mu}\frac{\partial p}{\partial\chi_i}\right) = \frac{U}{2}\frac{\partial h}{\partial\chi_2} + \dot{h} + \frac{\sum_i g_i(p - p_{\underline{inj}i})}{4\mu l_{\underline{0}i}} \qquad (3)$$

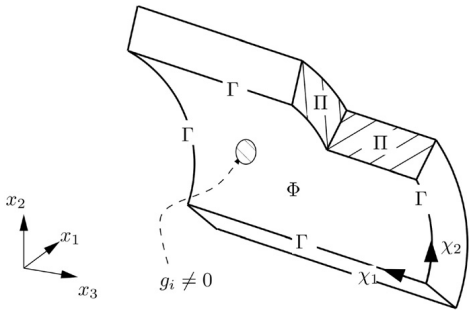


**Fig. 1.** Overview of the different domains, the fluid film curvilinear coordinate system ($\chi_1$, $\chi_2$) and the Cartesian coordinate system ($x_1$, $x_2$, $x_3$). The sub-domain where $g_i \neq 0$ is that of an orifice. The solid domain is denoted by $\Pi$ and its boundary by $\Lambda$. Note that all external surfaces are part of the solid boundary. The fluid domain is denoted by $\Phi$ and its boundary by $\Gamma$.

where $p$ is the pressure, $h$ is the oil film thickness, $U$ is the relative tangential speed of the rotor, $g_i$ is a shape function describing a laminar flow profile in orifice $i$, $p_{\underline{\text{inj}i}}$ is the injection pressure in orifice $i$, $l_{0\underline{i}}$ is the length of the orifice inlet tube $i$ and $\mu$ is the dynamic viscosity of the lubricant. The $\chi_2$ coordinate is aligned with the direction of rotation. The Reynolds equation has been divided by 12 on both sides, when comparing to the way that it is normally stated. This makes the governing matrix of the pressure problem symmetric. Refer to [15] for a more detailed explanation.

The flow in the servo-valves is described by the second order ordinary differential equation

$$\ddot{q}_{\underline{v}} + 2\xi_{\underline{v}}\omega_{\underline{v}}\dot{q}_{\underline{v}} + \omega_{\underline{v}}^2 q_{\underline{v}} = \omega_{\underline{v}}^2 K_{\underline{v}} u_{\underline{v}} \tag{4}$$

or

$$\frac{1}{\omega_{\underline{v}}^2 K_{\underline{v}}}\ddot{q}_{\underline{v}} + \frac{2\xi_{\underline{v}}}{\omega_{\underline{v}} K_{\underline{v}}}\dot{q}_{\underline{v}} + \frac{1}{K_{\underline{v}}} q_{\underline{v}} = u_{\underline{v}} \tag{5}$$

where $\omega_{\underline{v}}$ is the servo-valve eigenfrequency, $K_{\underline{v}}$ is the valve flow voltage coefficient, $\xi_{\underline{v}}$ is the valve damping ratio and $q_{\underline{v}}$ is the valve flow.

If more servo-valves are included, an uncoupled system of equations results, thus

$$\mathbf{M}_{\underline{q-q}}\ddot{\mathbf{q}}_{\underline{v}} + \mathbf{D}_{\underline{q-q}}\dot{\mathbf{q}}_{\underline{v}} + \mathbf{K}_{\underline{q-q}}\mathbf{q}_{\underline{v}} = \mathbf{u}_{\underline{v}} \tag{6}$$

where the system matrices follow directly from Eq. (4). The injection orifice arrays (pads) are connected by servo-valves as pairs. Thus the flows in a pad pair are coupled. The linearised 2 by 2 system of equations for a servo-valve connecting, e.g. pad $i$ and $j$ is

$$\begin{Bmatrix} q_i \\ q_j \end{Bmatrix} = \begin{bmatrix} K_{\underline{pq}} & -K_{\underline{pq}} \\ -K_{\underline{pq}} & K_{\underline{pq}} \end{bmatrix} \begin{Bmatrix} p_{\underline{\text{inj}i}} \\ p_{\underline{\text{inj}j}} \end{Bmatrix} + \begin{Bmatrix} q_{\underline{v}} \\ -q_{\underline{v}} \end{Bmatrix} + \begin{Bmatrix} q_{\underline{L}} \\ q_{\underline{L}} \end{Bmatrix} \tag{7}$$

where $K_{\underline{pq}}$ is the valve flow-pressure coefficient, $q_{\underline{L}}$ is the valve leak flow, $q_i$ is the flow to pad $i$ and $p_{\underline{\text{inj}i}}$ is the injection pressure at pad $i$. Here we have selected a positive direction of flow for the servo-valve. The pad associated with positive valve flow, in this case pad $i$, is denoted the master pad. The pad associated with negative valve flow, in this case pad $j$, is denoted the slave pad.

Since the bearings are the main focus of this investigation, the rotor is described as simply as possible, however, still in a fashion that retains its qualitative behaviour. The rotor is assumed to move laterally only, i.e. the axis of symmetry is assumed to align with $x_3$ at all times, also its centre of mass is assumed to coincide with its axis of rotation at all times. Since the focus of this investigation is the bearing influence on the rotor behaviour, no stiffness is assigned to the rotor apart from the one coming from the oil film. Also, as mentioned in the Introduction, this study assumes an isothermal bearing and lubricant. This greatly simplifies the modelling. Including thermal effects is the most prudent next step in the refining process of the model. In Fig. 2 a system with two pads and one servo-valve is shown, with indication of the governing equation of each body. The figure is for illustrative purposes only. The oil film thickness is greatly exaggerated, and in this investigation, bearings with four pads will be investigated.

### 2.1. Boundary conditions

The pads are pivoted about their centre. The pivoting is modelled as a radial constraint on relevant nodes, see Fig. 3. This is done by coordinate transformations back and forth between the inertial coordinate system, and systems that are aligned with the constraints. When in a constraint coordinate system, zeros can be introduced into the off diagonal components of the stiffness matrix, which couple with the degree of freedom to be constrained. One could simply introduce stiff springs between the pivot point and the surface nodes, but this would introduce high

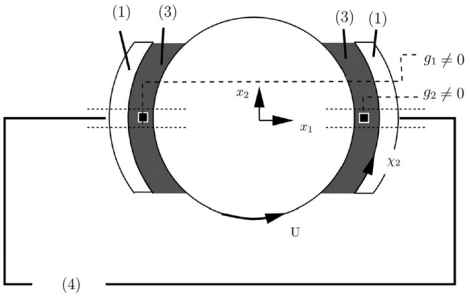


**Fig. 2.** Overview of coupled system, with denotation of the equations that govern the different parts. I.e. Eq. (3) means that part is governed by the Reynolds equation. The first coordinates of the Cartesian coordinate system ($x_1$, $x_2$) are shown, the coordinate system is right handed, thus $x_3$ points out of the plane of the paper. The curvilinear coordinate $\chi_2$ is also shown.

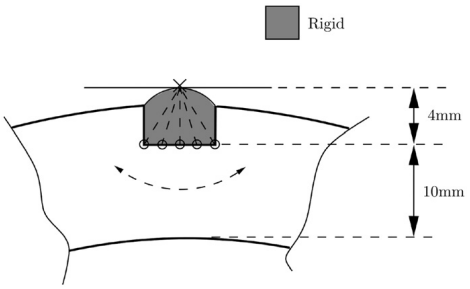


**Fig. 3.** Schematic of the pivot boundary conditions. The pivot is modelled as rigid. Nodes along the surface of the pad are constrained to move tangentially relative to the pivot point.

frequencies into the system, thus possibly reducing the maximum allowable time step for time integration procedures. The boundary condition for the Reynolds equation is the Reynolds condition, i.e. the pressure is set to zero along the boundary of the lubricated surface.

## 3. Coupling

Eqs. (1), (3) and (6) can, given a few prudent conditions, be coupled into one set of non-linear algebraic equations. Also, the rotor is included. Three conditions are applied: (i) The fluid film pressure is applied as a surface load on the solid and the rotor. (ii) The fluid film thickness is given as a function of the displacement (rigid body motion and deformation) of the solid as well as the rotor position. (iii) The flow through an orifice is set equal to the net flow into the fluid film in the domain of that orifice.

The details of the implementation of these three conditions can be found in [15]. When they are applied, we can write the system of equations compactly as

$$\mathbf{M}_{\underline{s}}\ddot{\mathbf{d}} + \mathbf{K}_{\underline{s}}\mathbf{d} = \mathbf{f}(\mathbf{p})$$

$$\mathbf{M}_{\underline{r}}\ddot{\mathbf{d}}_{\underline{r}} = \mathbf{f}_{\underline{r}}(\mathbf{p})$$

$$\mathbf{A}(\mathbf{d}, \dot{\mathbf{d}}, \mathbf{d}_{\underline{r}}, \dot{\mathbf{d}}_{\underline{r}})\mathbf{p} = \mathbf{r}(\mathbf{d}, \dot{\mathbf{d}}, \mathbf{d}_{\underline{r}}, \dot{\mathbf{d}}_{\underline{r}}, \mathbf{q}_{\underline{v}})$$

$$\mathbf{M}_{\underline{q-q}}\ddot{\mathbf{q}}_{\underline{v}} + \mathbf{D}_{\underline{q-q}}\dot{\mathbf{q}}_{\underline{v}} + \mathbf{K}_{\underline{q-q}}\mathbf{q}_{\underline{v}} = \mathbf{u}_{\underline{v}}(\mathbf{d}_{\underline{r}}, \dot{\mathbf{d}}_{\underline{r}}, \ldots) \tag{8}$$

where $\mathbf{M}_{\underline{s}}$ and $\mathbf{M}_{\underline{r}}$ are the solid mass matrix and rotor mass matrix, respectively, $\mathbf{K}_{\underline{s}}$ is the solid stiffness matrix and $\mathbf{A}$ is the system matrix for the pressure problem as derived from the modified Reynolds equation, $\mathbf{r}$ is the corresponding right-hand side, $\mathbf{d}$ is the nodal displacement vector and $\mathbf{d}_{\underline{r}}$ is the rotor displacement vector. Here $\mathbf{M}_{\underline{s}}$, $\mathbf{M}_{\underline{r}}$, $\mathbf{A}$, $\mathbf{M}_{\underline{q-q}}$, $\mathbf{D}_{\underline{q-q}}$ and $\mathbf{K}_{\underline{q-q}}$ are positive definite. $\mathbf{K}_{\underline{s}}$ is positive semidefinite on account of the rigid body mode. The bulk of the computational work lies with the solution for pressures and nodal displacements, as the number of nodes is typically in the order of thousands. Note that the generalised pressure vector $\mathbf{p}$ contains the nodal values of the pressure field as well as the pad injection pressures $p_{\underline{\mathrm{inj}i}}$. The nodal force vector $\mathbf{f}(\mathbf{p})$ depends linearly on the fluid film pressure $\mathbf{p}$. This also applies to the rotor force vector $\mathbf{f}_{\underline{r}}(\mathbf{p})$. The servo-valve signal $\mathbf{u}_{\underline{v}}$ can be any functional of any measurable quantity. In the present investigation we shall let it be a functional of lateral rotor displacement and velocity, i.e. we will implement a PD-controller.

## 4. The linear system

The system of equations can be linearised with respect to displacements, so as to provide a fluid film stiffness and damping. The linearised system is derived by first order Taylor expansions of relevant quantities. Since, the injection pressures are not defined in space, we may as well work directly on the discretised system. Thus

$$p_{\underline{g}n} \approx \tilde{p}_{\underline{g}n} + \sum_i \frac{\partial p_{\underline{g}n}}{\partial d_i}\delta d_i + \sum_i \frac{\partial p_{\underline{g}n}}{\partial \dot{d}_i}\delta \dot{d}_i + \sum_i \frac{\partial p_{\underline{g}n}}{\partial q_{\underline{v}i}}\delta q_{\underline{v}i} + \sum_i \frac{\partial p_{\underline{g}n}}{\partial d_{\underline{r}i}}\delta d_i + \sum_i \frac{\partial p_{\underline{g}n}}{\partial \dot{d}_{\underline{r}i}}\delta \dot{d}_i \tag{9}$$

where $\tilde{p}_{\underline{g}n}$ is the generalised pressure vector at static equilibrium. That is, we expand the system around static equilibrium, and assume deviations from this state to be small. To find $\tilde{p}_{\underline{g}n}$ can itself be a challenge, since it involves solving a system of non-linear equations. The process of building the discrete global linearised system of equations follows that of [15]. After some derivation, one ends with the system of equations

$$\mathbf{M}\ddot{\mathbf{d}}_{\underline{g}} + \mathbf{D}\dot{\mathbf{d}}_{\underline{g}} + \mathbf{K}\mathbf{d}_{\underline{g}} = \mathbf{f}_{\underline{g}} \tag{10}$$

where $\mathbf{d}_{\underline{g}}$ and $\mathbf{f}_{\underline{g}}$ are the vectors of generalised displacements and forces, respectively. The vector $\mathbf{d}_{\underline{g}}$ contains all nodal displacements of the solid ($\mathbf{d}$) as well as the lateral displacement of the rotor ($\mathbf{d}_{\underline{r}}$) and the flow in each servo-valve ($\mathbf{q}_{\underline{v}}$). The vector $\mathbf{f}_{\underline{g}}$ contains the corresponding forces, and the servo-valve signal. As such

$$\mathbf{d}_{\underline{g}} = \begin{Bmatrix} \mathbf{d} \\ \mathbf{d}_{\underline{r}} \\ \mathbf{q}_{\underline{v}} \end{Bmatrix}, \quad \mathbf{f}_{\underline{g}} = \begin{Bmatrix} \mathbf{f} \\ \mathbf{f}_{\underline{r}} \\ \mathbf{u}_{\underline{v}} \end{Bmatrix} \tag{11}$$

The vector of nodal displacements will typically contain thousands of degrees of freedom, and so contributes with the bulk of the computational workload. The vector of lateral rotor displacements contains only the two components of lateral rotor movement, i.e. $\mathbf{d}_{\underline{r}} = [d_{\underline{r}1}\ \ d_{\underline{r}2}]^T$. Finally, the vector of flows contains as many components as there are servo-valves. In the present investigation, this means two. Grouping $\mathbf{d}$ and $\mathbf{d}_{\underline{r}}$ together, we can write the system matrices as

$$\mathbf{M} = \begin{bmatrix} [\mathbf{M}_{\underline{d-d}}] & [\mathbf{M}_{\underline{d-q}}] \\ [\mathbf{M}_{\underline{q-d}}] & [\mathbf{M}_{\underline{q-q}}] \end{bmatrix} \tag{12}$$

,

$$\mathbf{D} = \begin{bmatrix} [\mathbf{D}_{\underline{d-d}}] & [\mathbf{D}_{\underline{d-q}}] \\ [\mathbf{D}_{\underline{q-d}}] & [\mathbf{D}_{\underline{q-q}}] \end{bmatrix} \tag{13}$$

and

$$\mathbf{K} = \begin{bmatrix} [\mathbf{K}_{\underline{d-d}}] & [\mathbf{K}_{\underline{d-q}}] \\ [\mathbf{K}_{\underline{q-d}}] & [\mathbf{K}_{\underline{q-q}}] \end{bmatrix} \tag{14}$$

Since the fluid inertia is neglected, the mass matrix contains contributions only from the solid. The stiffness and damping matrices contain contributions from the fluid as well as the solid. The matrices are derived in more detail in [15].

Note that the functionals ($u_{\underline{v}m}$, $m = 1,2,\ldots$) can be chosen freely. Thus, $\mathbf{K}_{\underline{q-d}}$ constitutes an active part of the system, and can be tuned to produce desired behaviour. Let us consider an example with one servo-valve so that $q_{\underline{v}n} = q_{\underline{v}1} = q_{\underline{v}}$ with a PD-controller that responds to rotor displacement and displacement rate in the $x_2$ direction only. If we assign the last nodal degree of freedom $r$ to the rotor movement in the $x_2$ direction, then the functional $u_{\underline{v}m} = u_{\underline{v}1} = u_{\underline{v}}$ would be

$$u_{\underline{v}} = G_{\underline{\mathrm{P}}}d_{\underline{r}2} + G_{\underline{\mathrm{D}}}\dot{d}_{\underline{r}2} \tag{15}$$

where $G_{\underline{\mathrm{P}}}$ is the proportional gain $G_{\underline{\mathrm{D}}}$ is the derivative gain and $d_{\underline{r}2}$ is the displacement of the rotor in the $x_2$ direction. Moving the electronic servo-valve signal to the left-hand side, the system matrices become

$$\mathbf{K} = \begin{bmatrix} [\mathbf{K}_{\underline{\mathrm{dd}}}] & \int_\Phi \sum_{i=1}^{3} e_{mi}a_i \sum_{j\in\mathbb{F}^2} \varphi_j \dfrac{\partial p_j}{\partial q_{\underline{v}}}\,d\Phi \\ [0,\ldots,-G_{\underline{\mathrm{P}}}] & 1/K_{\underline{v}} \end{bmatrix} \tag{16}$$

$$\mathbf{D} = \begin{bmatrix} [\mathbf{D}_{\underline{\mathrm{dd}}}] & 0 \\ [0,\ldots,-G_{\underline{\mathrm{D}}}] & \dfrac{2\xi_{\underline{v}}}{\omega_{\underline{v}}K_{\underline{v}}} \end{bmatrix}, \quad \mathbf{M} = \begin{bmatrix} [\mathbf{M}_{\underline{\mathrm{dd}}}] & 0 \\ 0 & \dfrac{1}{\omega_{\underline{v}}^2 K_{\underline{v}}} \end{bmatrix} \tag{17}$$

The linearised system is useful for two things. Firstly it allows linear frequency domain analysis of the bearing, this shall be performed in the following section. Secondly the system stiffness matrix is exactly the Jacobian of the out of balance forces, and is thus necessary when performing Newton–Raphson iterations toward equilibrium. Since the system is non-linear, it will potentially have more than one static equilibrium, though in practice only one stable equilibrium is observed. A good way to reach a stable equilibrium position is to run a Newmark time stepping solution until a given time and use the final system state as the initial guess for Newton–Raphson iterations. As mentioned, since the pads are allowed to deform, the system typically contains many thousands degrees of freedom. The solid part of the stiffness matrix is singular because of the pivot supports, so the equations must be solved as fully coupled, which means that the fluid part of the stiffness matrix must be computed at each Newton–Raphson iteration step. This matrix is non-symmetric and non-sparse, which makes solution computationally challenging. To speed up solution, while retaining reasonable precision, a pseudo-modal reduction is performed.

### 4.1. Pseudo-modal reduction

If the force from perturbing a node comes mainly from the solid, then the mode shapes of the solid only system will be very similar to those of the combined fluid–solid system. In other words: Given the assumption that the deformation forces from the solid are larger than those from the fluid, the system of equations (10) can be condensed spectrally as

$$\mathbf{V}^T\mathbf{M}\mathbf{V}\ddot{\mathbf{b}}+\mathbf{V}^T\mathbf{D}\mathbf{V}\dot{\mathbf{b}}+\mathbf{V}^T\mathbf{K}\mathbf{V}\mathbf{b}=\mathbf{V}^T\mathbf{f} \tag{18}$$

where

$$\mathbf{V}=\begin{bmatrix}[\mathbf{V}_{\underline{s}}] & [\mathbf{0}]\\ [\mathbf{0}] & [\mathbf{I}]\end{bmatrix} \tag{19}$$

Now, $\mathbf{d}_{\underline{g}}$ is approximated as

$$\mathbf{d}_{\underline{g}}=\mathbf{V}\mathbf{b} \tag{20}$$

The matrix $\mathbf{V}_{\underline{s}}$ contains in its columns some of the eigenmodes of vibration of the solid, thus it satisfies

$$\mathbf{K}_{\underline{s}}\mathbf{V}_{\underline{s}}=\mathbf{M}_{\underline{s}}\mathbf{V}_{\underline{s}}\Lambda_{\underline{s}} \tag{21}$$

and $\Lambda_{\underline{s}}$ contains the squares of the corresponding solid eigenfrequencies in its diagonal and zeros elsewhere. The identity matrix in the lower right corner of Eq. (19) transfers the rotor and servo-valve degrees of freedom untransformed. I.e. The purpose of $\mathbf{V}$ is to reduce the workload associated with the large number of degrees of freedom in the pads. The rotor and valves cannot and will not be reduced any further. In the present investigation, four modes of vibration have been considered for each pad. The system has four pads, one rotor and two servo-valves. Thus the size of the reduced system equation (18) is $20\times 20$, which is manageable by any modern computer. Fig. 4 shows the four modes considered for each pad. These figures also give an impression of the mesh refinement used in the analyses, as the meshes shown are used throughout the investigation. The elements are 20-node serendipity elements, see e.g. [32]. Since we include only four modeshapes, the mesh is more than adequate in terms of refinement.

## 5. Analyses

To obtain tangible information about the bearing behaviour, we perturb the rotor, and measure the force response, i.e. we determine the transfer function of the rotor. With a time harmonic perturbation of the rotor $\Delta\mathbf{f}_{\underline{g}}=\Delta\mathbf{f}_{\underline{g}0}e^{i\omega t}$, we can write the solution as $\Delta\mathbf{b}=\Delta\mathbf{b}_{\underline{0}}e^{i\omega t}$, where

$$\mathbf{V}^T(\mathbf{K}+i\omega\mathbf{D}-\omega^2\mathbf{M})\mathbf{V}\Delta\mathbf{b}_{\underline{0}}=\mathbf{V}^T\Delta\mathbf{f}_{\underline{g}0} \tag{22}$$

Now, the bearing stiffness is defined as the real part of the rotor force response. The damping is defined as the imaginary part divided by the frequency. We know that the displacements of the rotor in the $x_1$ and $x_2$ direction are unity and zero, respectively, but we need to solve the system to know the value of the other displacements. E.g. given a solution to Eq. (22) $\Delta\mathbf{b}_{\underline{0}}=[\ldots,\Delta d_{\underline{r}1},\Delta d_{\underline{r}2},\ldots]^T=[\ldots,1,0,\ldots]$, where the 1 and 0 are a prescribed rotor displacements in the $x_1$, $x_2$ plane, and a corresponding force vector $\Delta\mathbf{f}_{\underline{g}0}=[\ldots,\Delta f_{\underline{r}1},\Delta f_{\underline{r}2},\ldots]^T$. Then the bearing stiffness is defined as

$$K_{\underline{b}}=\mathrm{Re}(\Delta f_{\underline{r}1}) \tag{23}$$

and the bearing damping is defined as

$$D_{\underline{b}}=\frac{1}{\omega}\mathrm{Im}(\Delta f_{\underline{r}1}) \tag{24}$$

For four pad bearings in a load between pad situation, the off diagonal terms are very small. Thus the bearing stiffness and damping are considered scalar. Note that for this to hold for an active bearing, the orifices should be placed symmetrically about the pivot line. In the

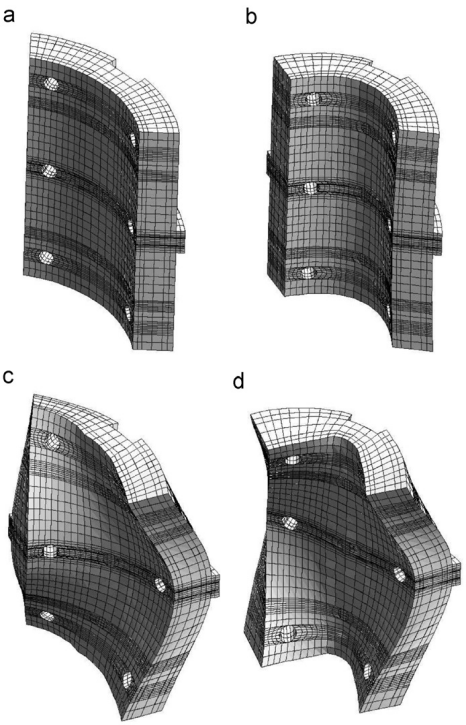


**Fig. 4.** Eigenmodes of the solid part of the system. (a) The first mode, which is a rigid body mode. (b) The second, bending, mode. (c) The third, skewing, mode. (d) The fourth, flapping, mode. Given that $E$ = 100 GPa, the eigenfrequencies for the modes are 0, 7.29 kHz, 8.34 kHz and 10.76 Hz, respectively. Note that the modeshapes are independent of $E$.

results section, the force response magnitude and phase will be presented. These quantities can be related to the stiffness and damping by the inverse of the relations in Eqs. (23) and (24), thus

$$|\Delta \underline{f}_{\underline{r}}| = |\Delta \underline{f}_{\underline{r}1}| = \sqrt{K_{\underline{b}}^2 + \omega^2 D_{\underline{b}}^2} \tag{25}$$

and

$$\mathrm{Arg}(\Delta \underline{f}_{\underline{r}}) = \mathrm{Arg}(\Delta \underline{f}_{\underline{r}1}) = \mathrm{Arg}(K_{\underline{b}} + i\omega D_{\underline{b}}) \tag{26}$$

here, one should keep in mind that both $K_{\underline{b}}$ and $D_{\underline{b}}$ are rational functions of $\omega$.

A dynamic analysis based on the stiffness and damping coefficients, Eqs. (23) and (24), gives engineers the main information about the softening/hardening effect of the bearing as a function of the excitation frequency and different lubrication regimes, i.e. an equivalent impedance. With the equivalent damping coefficients a general idea of vibration energy dissipation as a function of the excitation frequency can be achieved. Such coefficients can be directly used as input data for rotordynamic computational programs and rotor unbalance response can be performed in a straightforward manner.

A dynamic analysis based on amplitude and phase of the journal bearing forces, Eqs. (25) and (26), gives engineers insight into their maximum values depending on the different lubrication regimes and excitation frequency. Moreover, the phase between the maximum value of the journal force and the maximum rotor lateral displacement allows for the calculation of time delay between rotor response and controllable journal forces. Using the dynamic coefficients for stability analysis can seem tempting, given the naming convention of equivalent "stiffness" and "damping". This is, however, not possible, and may lead to erroneous results. An advantage of the phase and magnitude representation is that it is not prone to this error.

In this paper both dynamic analyses, based on bearing dynamic coefficients and journal forces amplitude and phase, will be presented.

## 6. Results

This section contains documentation of selected results.

The bearing under investigation has length as well as diameter 0.1 m, so the length/diameter ratio is 1. Each pad extends 69.3°. The rotational speed of the rotor is 6000 rpm. Three different orifice configurations will be investigated, the possible orifice configurations are explained in Fig. 5 and Table 2. Each orifice has a diameter of 6 mm. Key bearing data are given in Table 3. The bearing preload factor of 0.5 is high enough that passive hydrodynamic effects in themselves are substantial. The idea of the investigations is that if a bearing with a high preload factor can be improved, then so can a bearing with a low preload factor. The servo-valve constants for the active bearing are given in Table 4. These values apply to all of the discussed analyses. The bearing has four pads. The bearing pads are numbered consecutively in the counter clockwise direction from the $x_1$-axis. Thus we have pad #1 ($x_1 > 0$ and $x_2 > 0$), pad #2 ($x_1 < 0$ and $x_2 > 0$), pad #3 ($x_1 < 0$ and $x_2 < 0$) and pad #4 ($x_1 > 0$ and $x_2 < 0$). Fig. 6 shows a schematic of the bearing with indication of pad numbering.

The pivots are at 45° angles to the $x_1$ and $x_2$ directions, and the pads extend symmetrically from the pivot lines. The rotor is loaded in the $x_1$ direction, thus we have a load-between-pad configuration. The pad is pivoted about its centre.

We shall implement a control system that responds to rotor movement in the $x_1$ direction. The way we do this is to connect the pads in pairs with servo-valves. Pad #1 is connected to pad #3 with a servo-valve. Also, pad #4 is connected to pad #2 with a servo-valve. Pads #1 and #4 are chosen as master pads, with pads #3 and #2 as their respective slave counterparts. Both servo-valves respond to rotor movement in the $x_1$ direction and $x_2$ direction. The software written for the bearing analysis takes

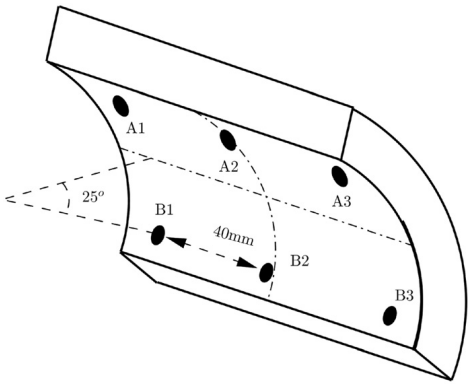


**Fig. 5.** Schematic of possible orifice placement. The orifices are denoted A1 through B3. The orifices are places symmetrically on the pad.

**Table 2**
Overview of orifice configurations.

| Configuration | Orifices |
|---|---|
| #1 | A2–B2 |
| #2 | A1–A3–B1–B3 |
| #3 | A1–A2–A3–B1–B2–B3 |

**Table 3**
Bearing and lubricant data.

| Property | Unit | Value(s) |
|---|---|---|
| Pad radius of curvature | mm | 50 |
| Rotor radius | mm | 49.9 |
| Nominal clearance | μm | 100 |
| Assembled (minimum) clearance | μm | 50 |
| Preload | – | 0.5 |
| Pad extension | ° | 69.3 |
| Angular pivot locations | ° | 45, 135, 225 and 315 (at pad centres) |
| Radial pivot location | mm | 64 |
| Pad length | mm | 100 |
| Nominal pad thickness | mm | 14 |
| Pad Young's modulus | GPa | 100 |
| Pad Poisson's ratio | - | 0.3 |
| Pad density | Kg/m^3 | 8400 |
| Static load (in $x_1$ direction) | N | 20 000 |
| Number of pads | – | 4 |
| Lubricant dynamic viscosity | N s/m$^2$ | 0.019 |

**Table 4**
Servo-valve constants.

| Property | Unit | Value(s) |
|---|---|---|
| Valve flow-pressure coefficient | m$^3$/(s Pa) | $1.13 \times 10^{-12}$ |
| Valve flow-voltage coefficient | m$^3$/(s V) | $16.7 \times 10^{-6}$ |
| Valve damping ratio | – | 0.48 |
| Valve eigenfrequency | Hz | 320.16 |

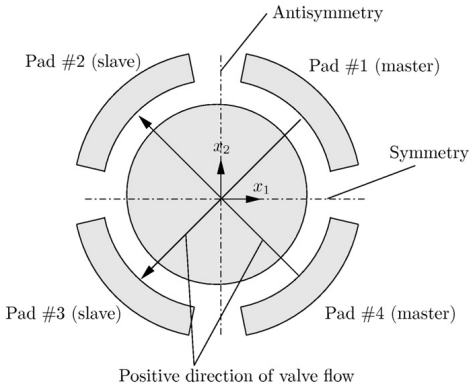


**Fig. 6.** Schematic of the bearing, showing pad numbering and valve orientation.

a vector as input, so as to define what direction of rotor movement, that each servo-valve shall respond to. This vector is normalised inside the program. Here, we set the first valve to respond to (1,1) and the second valve to respond to $(1,-1)$. Thus, after normalisation, the two servo-valve signals are computed as

$$u_{\underline{v}1} = G_{\underline{P}}(d_{\underline{r}1}+d_{\underline{r}2})/\sqrt{2}+G_{\underline{D}}(\dot{d}_{\underline{r}1}+\dot{d}_{\underline{r}2})/\sqrt{2} \tag{27}$$

$$u_{\underline{v}2} = G_{\underline{P}}(d_{\underline{r}1}-d_{\underline{r}2})/\sqrt{2}+G_{\underline{D}}(\dot{d}_{\underline{r}1}-\dot{d}_{\underline{r}2})/\sqrt{2} \tag{28}$$

This makes for an active bearing which still, for all practical purposes decouples the $x_1$ and $x_2$ coordinate directions, just as a passive tilting-pad journal bearing. Consider a movement in the $x_1$ direction. Since the two valve arrangements are symmetric about the $x_1$, $x_3$ plane, the resulting net flow from top (pad #1 and pad #2) to bottom (pad #3 and pad #4), i.e. in the $x_2$ direction is nil. Similarly, consider a movement in the $x_2$ direction. The two valve arrangements are antisymmetric about the $x_2$, $x_3$ plane. However, valve number two responds negatively to movement in the $x_2$ direction, so the net flow from left (pad #2 and pad #3) to right (pad #1 and pad #4) is nil.

### 6.1. Preliminary analysis—static load

Before embarking upon dynamic analyses, the static behaviour of the active bearing is investigated. A proportional gain of 500 V/mm is chosen. This value represents the maximum proportional gain, that will allow a substantial eccentricity of the rotor without producing excessive injection pressures, and at the same time respects the linear response range of the servo-valve (approx. 5% of the maximal voltage). The maximum injection pressure of a servo-valve is typically 22 MPa. The pressure in the oil film in the orifice domain is very close to the injection pressure. So one way of checking the injection pressure is by setting the rotor eccentricity to a given maximum value, and then evaluating the pressure field. An appropriate maximum proportional gain can then be set by trial and error. The derivative gain is irrelevant, since the analysis is static. Some results shall be compared to a corresponding passive bearing. The passive bearing is defined as a system with no orifices, i.e. the passive bearing is purely hydrodynamic in nature. Apart from this, it shares all parameters with the active bearing. Also, results for a rigid body model will be presented and compared to results of a four mode pseudo-modal reduction. The mode shapes for the four mode pseudo-modal reduction are shown in Fig. 4. The rigid body model utilises only the first of these modes. The orifices are placed according to configuration #3. That is, each pad has six orifices.

Fig. 7 shows the pressure field for the P-regulated active bearing under a static load in the $x_1$ direction of 20 000 N, producing a Sommerfeld number of 0.235. Half of the solid is cut away to enable better inspection of the pressure in the fluid film. Note how the pressure in the orifice regions is high on the loaded pads and low on the unloaded pads. This is a consequence of the response of the servo-valve.

Fig. 8 shows curves of fluid film thickness for a passive system under the same conditions as well as the mentioned P-regulated active system. The angle is measured from the $x_1$-axis, meaning that the loaded pads are in the intervals $[0;\pi/2]$ (pad #1) and $[3\pi/2;2\pi]$ (pad #4). The fluid film thicknesses are those of the static equilibrium position, on which the P-regulator has an effect. Even in the present (static) case we see an effect of pad compliance; note the difference in fluid film thickness between the four mode pseudo-modal reduction and the rigid body model.

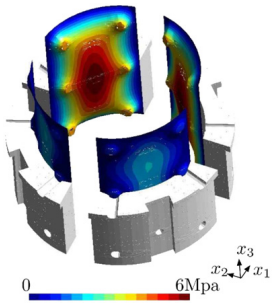


**Fig. 7.** The pressure field at static equilibrium with a P-gain of 500 V/mm and a static load of 20 000 N in the $x_1$ direction. The state is identical to that of Fig. 8. (a) The pressure field with the entire pads shown. (b) The top half of the pads is cut away. The figure is generated with the Gmsh software [36].

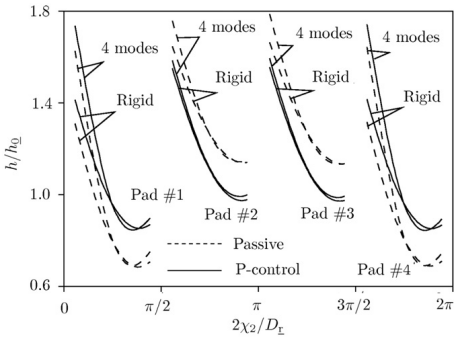


**Fig. 8.** Curves of fluid film thickness normalised with respect to the assembled clearance $h_0 = 50\,\mu$m. The state is that of static equilibrium at a static load on the rotor of 20 000 N in the $x_1$ direction. To illustrate the static effect of pad compliance, the four mode pseudo-modal reduction is compared to a rigid body model. The orifices are placed according to configuration #3. That is, each pad has six orifices. Results are shown for a passive bearing as well as for a P-controlled bearing with a P-gain of 500 V/mm.

As explained in [15], the effect of pad compliance is generally felt in dynamic analysis at higher frequencies. For a bearing like the one we investigate here, this means from 50 Hz upwards. This frequency is much lower than the eigenfrequencies of the modes that involve deformation. Yet, keep in mind that the eigenfrequencies are computed for the solid only system. The four mode pseudo-modal reduction allows for an increase of the pad effective radius, thus increasing the preload factor. This is identified as increased fluid film thickness at the edges of the loaded pads. Note the effect of the P-regulator. It resists static rotor displacement, and as such it helps increase the minimum film thickness.

### 6.2. Harmonic responses to dynamic loads

Now, dynamic analyses shall be performed. A pure proportional regulator, or "P-regulator" as well as a pure derivative regulator, or "D-regulator" will be implemented, and different gains will be chosen. This will enable us to explore the influence of a control system on the bearing, by comparison to results for a passive bearing. Typically, control systems make use of a combined PD regulator. In the present study, to keep the number of computations to a reasonably low number, we choose to investigate P-control and D-control separately. Furthermore most control systems incorporate noise filters—one such has not been modelled here. Also, note that many types of controllers exist. For instance, in [33,34] a PID controller was investigated, and deemed not suitable for application to tilting pad journal bearings. The pure P-regulator responds to changes in the lateral rotor position in the $x_1$ direction. Proportional gains are set to six different values from 50 to 500 V/mm. The pure D-regulator responds to changes in the lateral rotor velocity in the $x_1$ direction. Derivative gains are set to six different values from 0.5 to 5 V s/mm. Thus we have three configurations at 12 distinct sets of gains each, amounting to 36 different analyses. Each analysis is run at a range of frequencies between 0 and 400 Hz. The static load on the bearing is 20 000 N as for the previous static analysis. This results in a Sommerfeld number of 0.235. All perturbations are performed about the static equilibrium state. This will depend on the P gain, since the P regulator responds to static rotor motion.

Bearing responses to unit rotor perturbations are presented and discussed. All perturbations are in the $x_1$ coordinate direction, and all force responses are measured in the $x_1$ coordinate direction. Thus we denote the rotor force response simply as a scalar $\Delta f_{\bar{\mathrm{F}}}$. Since we perform a unit perturbation, the rotor force response $\Delta f_{\bar{\mathrm{F}}}$ has unit [N/m]. It is normalised with $|\mathbf{f}|_{\bar{\mathrm{F}}}/h_0$, i.e. the static rotor force (20 000 N) divided by the assembled clearance (50 μm).

Before the regulator is implemented, the corresponding passive bearing reaction force in the $x_1$ direction to a unit rotor displacement in the $x_1$ direction is computed for comparison.

#### 6.2.1. Results presented as magnitude and phase of force response

The passive bearing performance is seen in Fig. 9. Fig. 9(a) shows the magnitude of the force response and Fig. 9(b) shows the phase of the force response in the $x_1$ direction. What is meant by the phase of the force response, is the time delay between the harmonic displacement perturbation of the rotor, and the harmonic resulting force on the rotor, both in the $x_1$ direction. After around 100 Hz the magnitude grows almost linearly. The phase is that between displacement and force. It grows almost linearly, and then levels out at roughly $3\pi/8$. Both curves are typical of a heavily damped system. Given the curves for the passive bearing, we have a foundation on which to evaluate the performance of the active bearing.

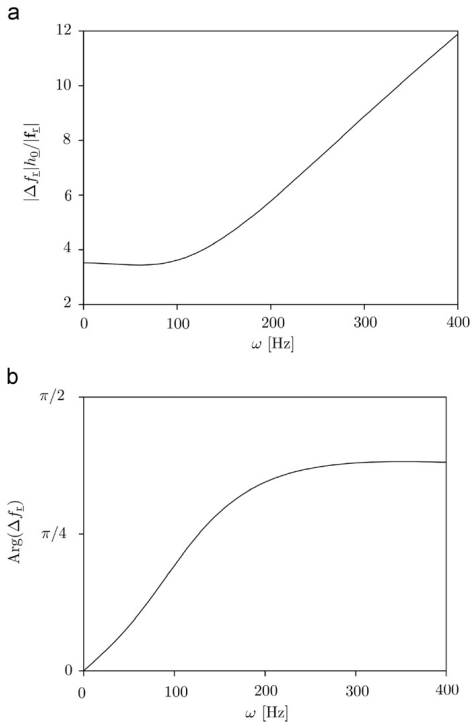


**Fig. 9.** Passive bearing force response in the $x_1$ direction to unit movement of rotor in $x_1$ direction. (a) Magnitude, (b) phase.

Note that there is no reason to believe that the coupled system will have a resonance exactly at $\omega = \omega_{\mathrm{v}}$. The servo-valve parameters are similar to those used in [35,15]. The servo-valve parameters are realistic in the sense that even under severe load conditions, the assumed maximum injection pressure of 22 MPa is not exceeded.

One may jump to the conclusion that more orifices are always better, in that more orifices will produce a greater force. This is not true for two reasons: Firstly, more orifices does not mean more valves, the flow from a given valve is distributed among the orifices. An excessive number of orifices may lead to an insufficient flow to the individual orifice, thus reducing the pressure. Secondly, passive effects are still important in active bearings. When adding an orifice, one removes a small area where the passive hydrodynamic effects would otherwise support the rotor.

Fig. 10 shows amplitudes of the bearing response for a proportional regulator. Figs. 10(a), (b) and (c) show results for configurations #1, #2 and #3, respectively. There seems to be little difference between the three configurations. In all three cases, the response tends to drop until a frequency of 100–120 Hz is reached, after which an almost linear increase is observed. Note that the quasi-static response, i.e. the response at 0 Hz,

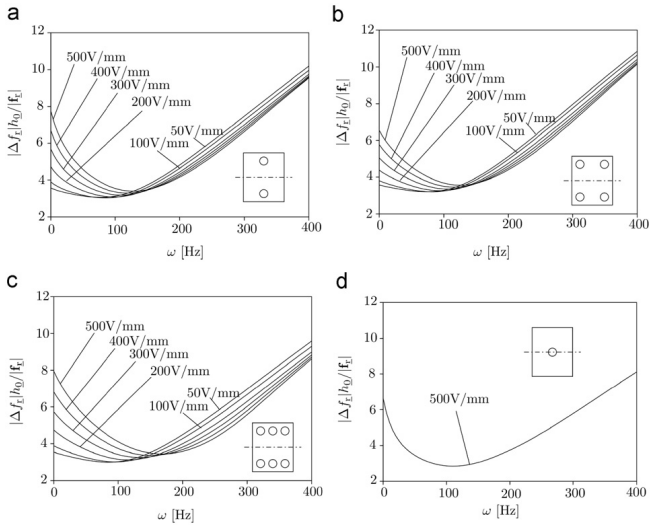


**Fig. 10.** Magnitude of the bearing force component in the $x_1$ direction in response to a unit rotor perturbation in the $x_1$ direction as a function of the excitation frequency. Curves for configuration (a) #1, (b) #2 and (c) #3 and different values of proportional gain.

of configuration #2 is somewhat lower than that of the other configurations. This is only true for the highest gains. As the frequency increases, configuration #3 exhibits a slower increase in response, although the difference is slight. Fig. 10(d) shows the corresponding curve for a centre orifice configuration, and the maximum P-gain of 500 V/mm. It is seen that all three multi-orifice configurations outperform the centre orifice configuration. That is, the amplitude of the force response from the bearing is higher with any multi-orifice configuration than that of a centre orifice configuration. Also, compare to Figs. 9(a) and (b) which show the corresponding curves for a passive bearing: Clearly, for lower frequencies, the P-regulated active bearing outperforms the passive one in terms of force response.

Fig. 11 shows phases of the bearing force response for a proportional regulator. The phase is defined as relative to the displacement. Figs. 11(a), (b) and (c) show results for configurations # 1, # 2 and # 3, respectively. All three configurations exhibit a phase shift from 0, where the bearing response is in phase with the movement of the rotor, to almost $\pi/2$. For configuration #3, the value of the P-gain seems to have more influence on the phase, although the effect is marginal. There is virtually no difference between configurations #1 and #2. Fig. 11(d) shows the corresponding curve for a centre orifice configuration, and the maximum P-gain of 500 V/mm. Again, orifice placement seems to have very little impact on the phase. Furthermore, the phase plots of Figs. 11(a)–(d) resemble that of the passive system in Fig. 9(b). This leads to the conclusion that a P-regulator on a tilting-pad journal bearing will have little influence on the phase. This knowledge can be useful in the design process of an active bearing.

Fig. 12 shows amplitudes of the bearing response for a derivative regulator. Figs. 12(a), (b) and (c) show results for configurations #1, #2 and #3, respectively. Here configuration #2 stands out, since it exhibits a large response at around 250 Hz, which the other configurations do not. The effect is most pronounced for the highest value of the gain. Note that there is a non-linear relation between the value of the gain and the value of the response. I.e. a slight increase from 4 to 5 V s/mm results in a large impact on the amplitude of the force response. This illustrates well, why active hybrid bearings cannot simply be viewed as hydrodynamic bearings in parallel with hydrostatic bearings; the coupling in the fluid film between hydrostatic and hydrodynamic terms is not trivial. That is, we cannot simply view the servo-valve as an actuator, applying a force somewhere on the system. Rather, we should think of it as a generalised spring that we build into the system; the state of this spring clearly depends on the state of the rest of the system. Even though this is the case, the bearing is virtually linear with respect to rotor load, for a given value of the gain, as long as the gain is large enough. This is demonstrated in [15]. Fig. 12(d) shows the corresponding curve for a centre orifice configuration, and the maximum D-gain of 5 V s/mm. As for the P-gain case, it is seen that all three multi-orifice configurations outperform the centre orifice configuration. That is, the amplitude of the force response from the bearing is higher with any multi-orifice configuration than that of a centre orifice configuration. Again, compare to Figs. 9(a), (b) which show the corresponding curves for a passive bearing. Under the given conditions, the D-regulated bearing provides superior performance. This is true in particular in the mid-frequency range above 50 Hz and below 300 Hz. Above 300 Hz the limited servo-valve bandwidth is felt, and force response begins to drop to that of a passive bearing.

Fig. 13 shows phases of the bearing force response for a derivative regulator. The phase is defined as relative to the displacement. Figs. 13(a), (b) and (c) show results for configurations #1, #2 and #3, respectively. It seems that configuration #3 has a profound effect on the phase for the highest of gains, and at very low and very high frequencies. Apart from this, the configuration choice seems not to affect the system too much. Compare Fig. 11 with Fig. 13. In Fig. 11 the phases intersect each other along a line. Since the P-regulator changes the static

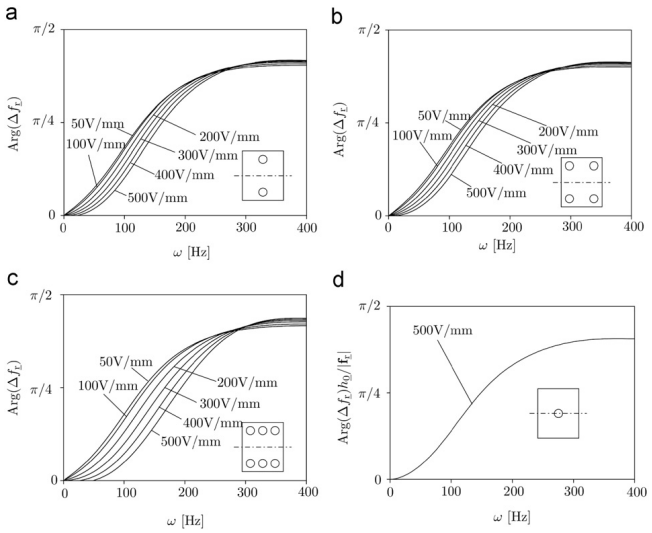


**Fig. 11.** Phase of the bearing force component in the $x_1$ direction relative to a unit rotor perturbation in the $x_1$ direction as a function of the excitation frequency. Curves for configuration (a) #1, (b) #2 and (c) #3 and different values of proportional gain.

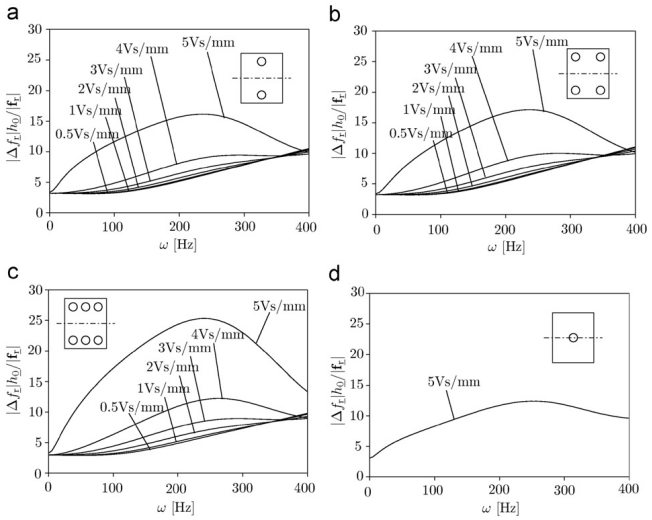


**Fig. 12.** Magnitude of the bearing force component in the $x_1$ direction in response to a unit rotor perturbation in the $x_1$ direction as a function of the excitation frequency. Curves for configuration (a) #1, (b) #2 and (c) #3 and different values of derivative gain.

equilibrium position of the system, the passive hydrodynamic pressure response depends indirectly on the value of the P-gain. On the other hand, the D-regulator has no influence on the static equilibrium position, i.e. the passive hydrodynamic pressure response does not depend on the value of the D-gain. Therefore the curves in Fig. 13 intersect each other in a very well defined point (around 140 Hz). In mathematical terms, D-control only changes the right-hand side of Eq. (22) (since the rotor motion is prescribed), where as P-control changes the system matrix as well as the right-hand side. Fig. 13(d) shows the phase

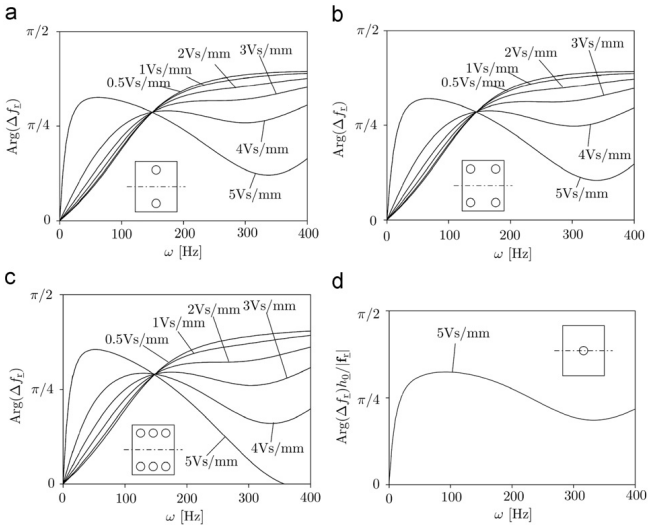


**Fig. 13.** Phase of the bearing force component in the $x_1$ direction relative to a unit rotor perturbation in the $x_1$ direction as a function of the excitation frequency. Curves for configuration (a) #1, (b) #2 and (c) #3 and different values of derivative gain.

curve for a centre orifice configuration, and the maximum D-gain of 5 V s/mm. It seems that a centre orifice configuration tends to keep the phase between rotor displacement and rotor force, close to $\pi/4$. That is, the large drop in phase that the multi-orifice configurations experience after roughly 100 Hz is less pronounced for the centre orifice configuration. Also, comparing Figs. 13(a)–(c) to the corresponding curve for the passive bearing in Fig. 9(b) one can conclude that for higher derivative gains, the phase of a bearing of configuration #1, #2 or #3 will deviate substantially from that of the passive bearing.

### 6.2.2. Results presented as dynamic coefficients

Data from the same computations as in Section 6.2.1 are here presented as dynamic coefficients.

Fig. 14 shows bearing stiffness for a proportional regulator. Figs. 14(a), (b) and (c) show results for configurations #1, #2 and #3, respectively. As concluded in Section 6.2.1, orifice configuration has very little influence, for the P-regulated case. As expected, the value of the P-gain has the biggest importance for lower frequencies.

Fig. 15 shows bearing damping for a proportional regulator. Figs. 15(a), (b) and (c) show results for configurations #1, #2 and #3, respectively. Again, no significant influence from orifice configuration is observed. The damping is observed to drop as the P-gain is increased. This effect is most pronounced for lower frequencies.

Fig. 16 shows bearing stiffness for a derivative regulator. Figs. 16(a), (b) and (c) show results for configurations #1, #2 and #3, respectively. The D-regulator has little influence for lower frequencies. But for higher frequencies its influence increases dramatically. As the servo-valve eigenfrequency of 320.16 Hz is passed, the curves begin to converge, and the regulator looses influence. It is observed that configuration #3 outperforms the other configurations in terms of stiffness magnitude.

Fig. 17 shows bearing damping for a derivative regulator. Figs. 17(a), (b) and (c) show results for configurations #1, #2 and #3, respectively. The D-regulator dramatically affects the damping for lower frequencies. But as the frequency increases the curves for different D-gain become hard to distinguish from each other. Thus a derivative regulator can greatly influence damping at lower frequencies.

### 6.2.3. Pad pivoting and deformation

Fig. 18 shows the responses of the pads at 1 Hz, for the case of a D-gain of 5 V s/mm and four orifices on each pad. Snapshots are taken at $\omega t = 0$, $\omega t = \pi/2$, $\omega t = \pi$ and $\omega t = 3\pi/2$, i.e. four times in a harmonic cycle. Because of the low frequency, the response is dominated by tilting of the pads. Fig. 19 shows the responses of the same system as Fig. 18, only the frequency is now 140 Hz. There is still tilting motion, but the higher frequency means that the response shows significant deformation of the pads. This is apparent simply from looking at Fig. 19. The maximum deflection is now 1.65, thus significantly higher than for the quasi-static case. This is not surprising, since the higher frequency means that the control system will react with a higher flow, producing high pressure responses in the corners of the pads. This result clearly confirms the assertion previously made in [15] that when implementing control systems to tilting pad journal bearings, pad compliance should be accounted for. At least this is true for heavily loaded bearings, such as is the case here, where the Sommerfeld number is 0.235.

### 6.2.4. Results in the time domain

A few combinations of parameters are selected for non-linear time domain analysis. This type of analysis is computationally heavy. Also, it is relatively time demanding to interpret the large amounts of data that it produces. On the other hand, time domain analysis handles non-linearities easily. Also, in a time domain analysis, any system will eventually end in a stable limit cycle or

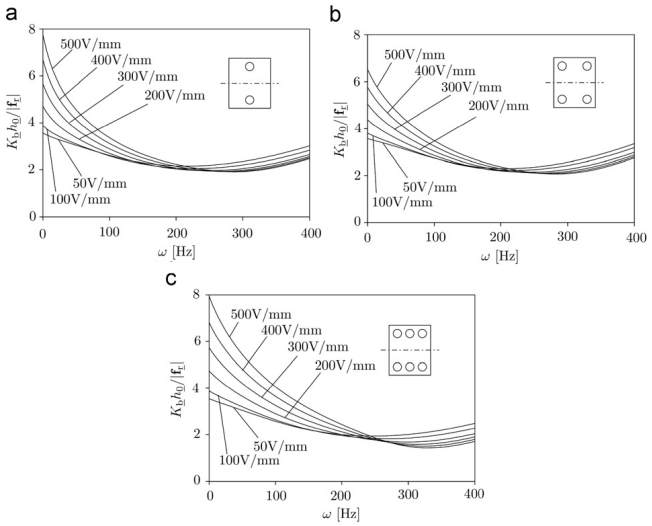


**Fig. 14.** Bearing stiffness as a function of the excitation frequency for configuration (a) #1, (b) #2 and (c) #3. Different values of proportional gain.

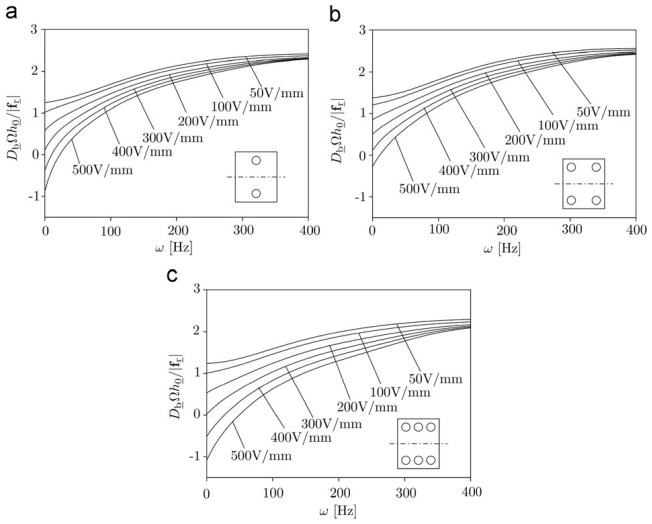


**Fig. 15.** Bearing damping as a function of the excitation frequency for configuration (a) #1, (b) #2 and (c) #3. Different values of proportional gain.

static equilibrium, if these exist and the forcing is not too hard. Bearing stability is not the focus of this study, but is relegated to future research.

Eqs. (8) are solved in the time domain by explicit Newmark time integration. Orifice configuration #2 is chosen for the analysis. All the bearing, lubricant and servo-valve parameters are as in the previous sections. The rotor mass is set to 2000 kg. This would be representative of, e.g. a steam turbine. As before, the static load is set to 20 000 N in the $x_1$ direction. In addition, a low static load of 2000 N in the $x_1$ direction is investigated. In all the time domain analyses the initial condition is that of a static equilibrium with the rotor fixed in $(x_1, x_2) = (10\,\mu\text{m}, 0)$. At $t = 0$ the rotor is set free. In addition to the static load, the rotor is loaded by a rotating asynchronous harmonic load with a magnitude of

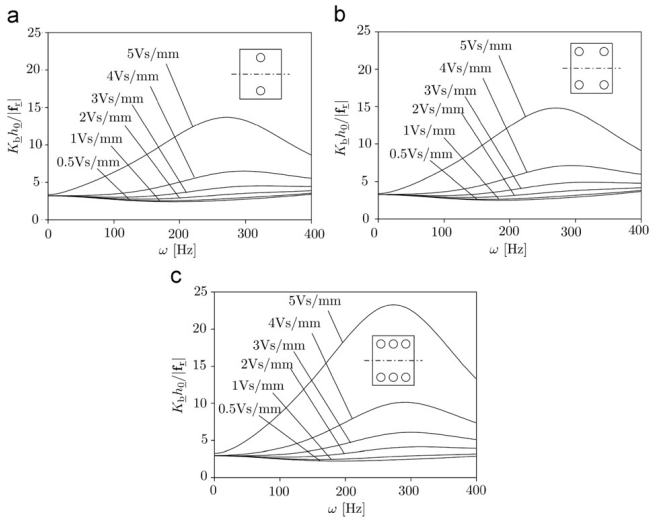


**Fig. 16.** Bearing stiffness as a function of the excitation frequency for configuration (a) #1, (b) #2 and (c) #3. Different values of derivative gain.

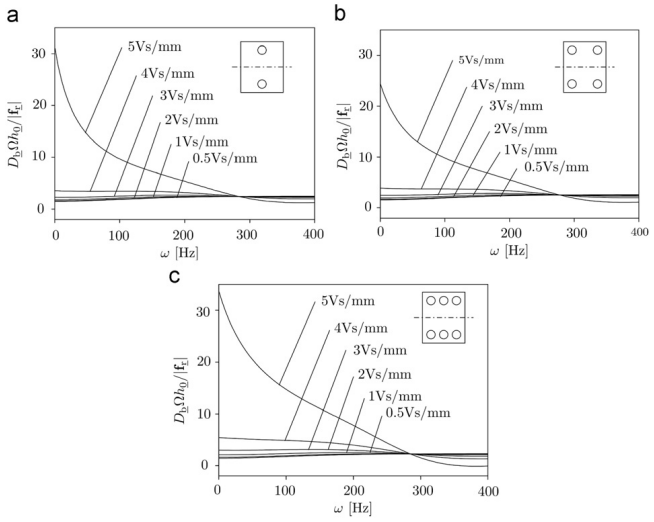


**Fig. 17.** Bearing damping as a function of the excitation frequency for configuration (a) #1, (b) #2 and (c) #3. Different values of derivative gain.

10 000 N. For the high static load case, the harmonic load frequency is set to 200 Hz. For the low static load case, two cases of harmonic load frequencies are investigated: 200 and 55.21 Hz, respectively. The latter frequency is the first undamped natural frequency of the passive system. Thus the total rotor load in the high static load case is given as

$$f_{\underline{r}1} = 20\,000\,\mathrm{N} + 10\,000\,\mathrm{N}\cos 400\pi t$$

$$f_{\underline{r}2} = 20\,000\,\mathrm{N} + 10\,000\,\mathrm{N}\sin 400\pi t \tag{29}$$

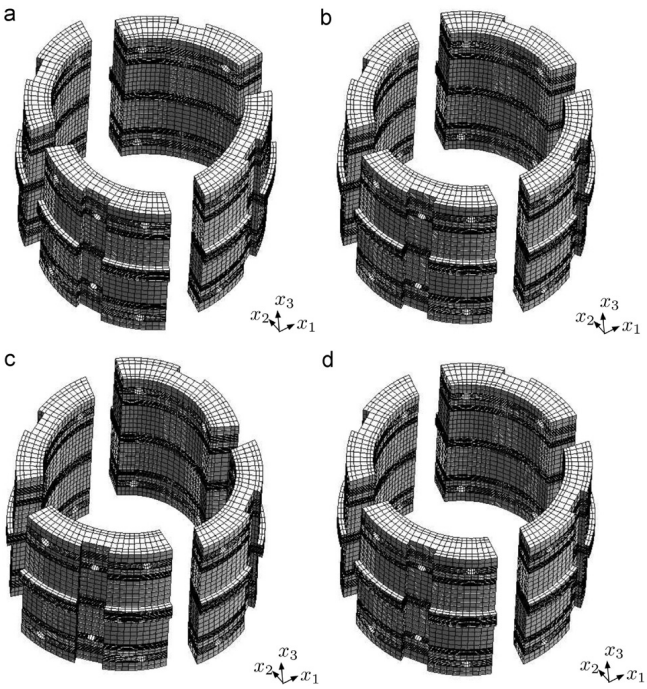


**Fig. 18.** Pad linear harmonic response to a unit movement of the rotor in the $x_1$ direction at 1 Hz. Snapshots at (a) 0, (b) $\pi/2$, (c) $\pi$ and (d) $3\pi/2$. Maximum deflection is 1.04. Note that the motion is dominated by rigid body motion.

and in the low static load case as

$$f_{\underline{r}1} = 2000\,\mathrm{N} + 10\,000\,\mathrm{N}\cos 400\pi t$$

$$f_{\underline{r}2} = 2000\,\mathrm{N} + 10\,000\,\mathrm{N}\sin 400\pi t \tag{30}$$

or

$$f_{\underline{r}1} = 2000\,\mathrm{N} + 10\,000\,\mathrm{N}\cos 110.42\pi t$$

$$f_{\underline{r}2} = 2000\,\mathrm{N} + 10\,000\,\mathrm{N}\sin 110.42\pi t \tag{31}$$

Figs. 20(a)–(d) show orbits of the rotor centre for the high static load case. In Fig. 20(a) the bearing is passive, in Fig. 20(b) the bearing is purely P-controlled with a P-gain of 100 V/mm, in Fig. 20(c) the bearing is purely D-controlled with a D-gain of 1 V s/mm, and finally in Fig. 20(d) the bearing is PD-controlled with the combination of the mentioned gains. Fig. 21 shows the limit cycles of the rotor centre for all four cases. Generally, one cannot simply superimpose the responses of controllers. However, here, this is almost the case: The P-controller has little influence on the radius of the limit cycle as compared to the passive case, however, it moves the centre of the limit cycle closer to the origo. On the other hand, the D-controller does not move the centre of the limit cycle, as compared to the passive case, but it reduces the radius. The PD-controller seems to be very close to the linear superposition of the P- and D-controllers, i.e. it moves the centre of the limit cycle closer to the origo, and reduces the radius. Even with the fairly modest control gains, a significant increase in the minimum film thickness is observed, since the extreme of the rotor eccentricity is moved closer to the origo. The benefit is shown in Fig. 21.

Figs. 22(a)–(d) show orbits of the rotor centre for the low static load case, excited harmonically at 200 Hz. In Fig. 22(a) the bearing is passive, in Fig. 22(b) the bearing is purely P-controlled with a P-gain of 100 V/mm, in Fig. 22(c) the bearing is purely D-controlled with a D-gain of 1 V s/mm, and finally in Fig. 22(d) the bearing is PD-controlled with the combination of the mentioned gains. Fig. 23 shows the corresponding limit cycles. One can make the same conclusions as for the high load case, except that the low static load means that the P-controller has a relatively small effect.

Generally, stability related problems for tilting pad journal bearings are most severe at low static loads. A theoretical investigation of this requires an eigenvalue analysis, which will not be performed here, rather it will be covered in future work. However, a hint of the stability of a bearing can be obtained by observing its transient behaviour, since this is governed by the eigenvalues. Compare the orbit of the passive bearing under low static load in Fig. 22(a) with the corresponding orbit for high static load in Fig. 20(a). In the low static load case, the rotor cycles three times before reaching the limit cycle; in the high static load case this is reduced to one and a half. Let us compare the passive bearing to the PD- and the D-controlled bearing. At high static load, the controller has little positive effect on transient

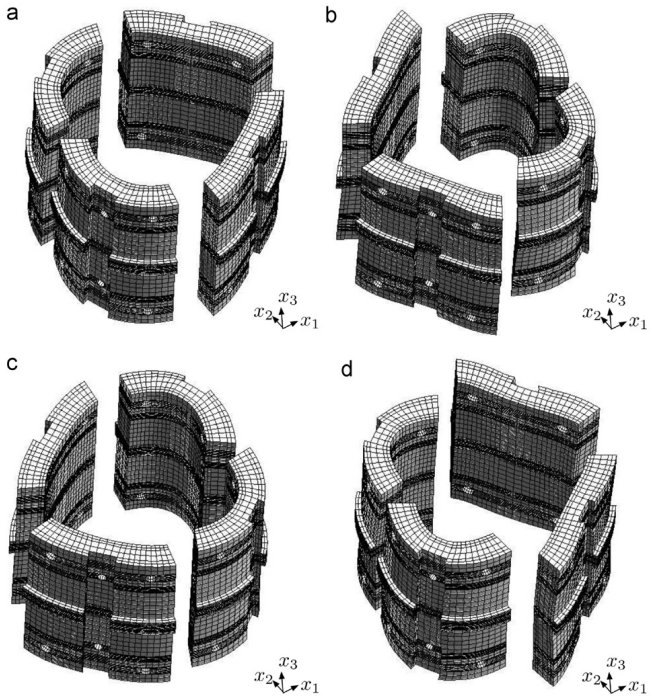


**Fig. 19.** Pad linear harmonic response to a unit movement of the rotor in the $x_1$ direction at 140 Hz. Snapshots at (a) 0, (b) $\pi/2$, (c) $\pi$ and (d) $3\pi/2$. Maximum deflection is 1.65. Note that the motion is heavily influenced by pad deformation.

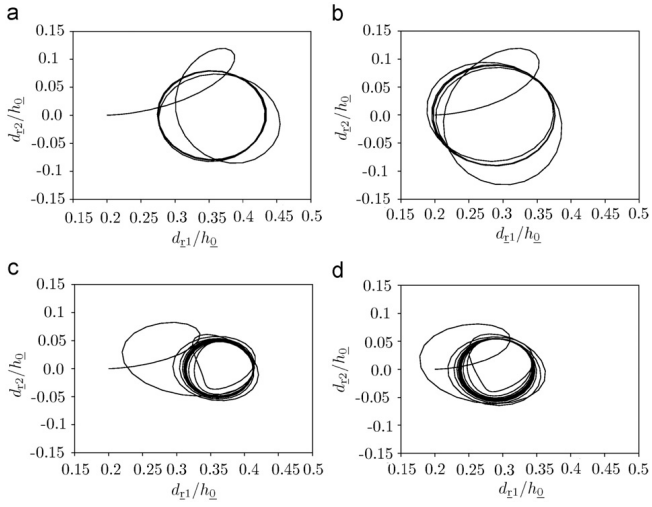


**Fig. 20.** Rotor orbits for a counter clockwise rotating load of magnitude 10 000 N and frequency 200 Hz. The initial orientation of the rotating load is in the $x_1$ direction. The static load is high at 20 000 N and oriented in the $x_1$ direction.

behaviour. At low load, the number of transient cycles is reduced from the three cycles of the passive bearing to roughly two cycles for the D- and PD-controlled bearing.

At this frequency P-term has only little effect on the radius of the limit. This can also be realised by comparing Fig. 10(b) to Fig. 9(a): Clearly, at 200 Hz there is little difference between the pure P-controlled bearing and the passive bearing.

Figs. 24(a)–(d) show orbits of the rotor centre for the low static load case, excited harmonically at 55.21 Hz. In Fig. 24(a) the bearing is passive, in Fig. 24(b) the bearing is purely P-controlled with a P-gain of 100 V/mm, in Fig. 24(c) the bearing is purely D-controlled with a D-gain of 1 V s/mm, and finally in Fig. 24(d) the bearing is PD-controlled with the combination of the mentioned gains. Fig. 25 shows the corresponding limit cycles. Non-linear behaviour can be identified in the passive case in Fig. 24(a), as the limit cycle is not perfectly circular. The passive system is already highly damped, which limits its vibration amplitude at resonance. In spite of this, a large reduction in vibration amplitude is achieved with application of the control system. With the PD-controlled system, the amplitude is reduced to roughly half of that of the passive system.

## 7. Conclusions

The static and stationary linear harmonic responses of tilting-pad journal bearings have been investigated. Also transient and post-transient non-linear time domain computations have been

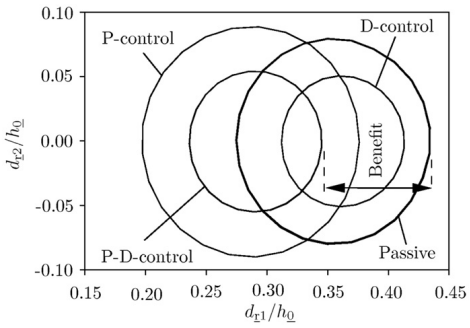


**Fig. 21.** Rotor limit cycles for a counter clockwise rotating load of magnitude 10 000 N and frequency 200 Hz. The static load is high at 20 000 N and oriented in the $x_1$ direction.

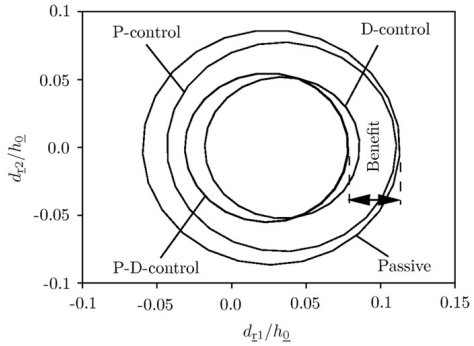


**Fig. 23.** Rotor limit cycles for a counter clockwise rotating load of magnitude 10 000 N and frequency 200 Hz. The static load is low at 2000 N and oriented in the $x_1$ direction.

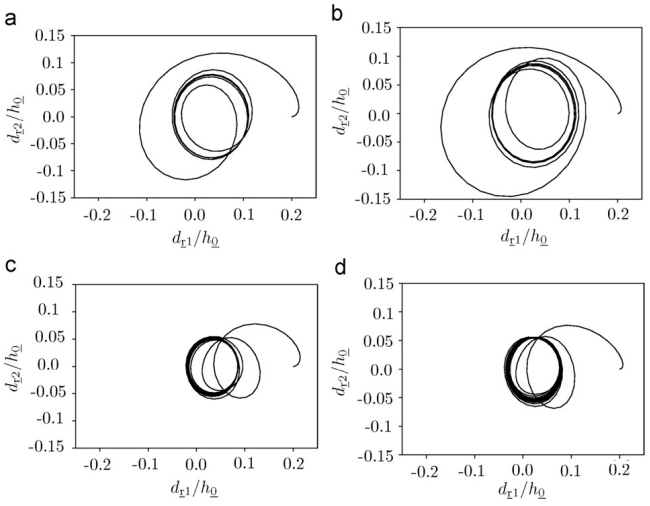


**Fig. 22.** Rotor orbits for a counter clockwise rotating load of magnitude 10 000 N and frequency 200 Hz. The initial orientation of the rotating load is in the $x_1$ direction. The static load is low at 2000 N and oriented in the $x_1$ direction.

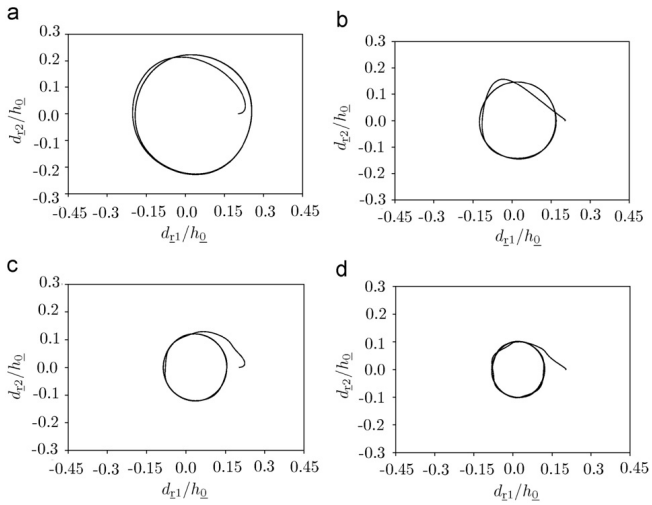


**Fig. 24.** Rotor orbits for a counter clockwise rotating load of magnitude 10 000 N and frequency 55.21 Hz. The initial orientation of the rotating load is in the $x_1$ direction. The static load is low at 2000 N and oriented in the $x_1$ direction.

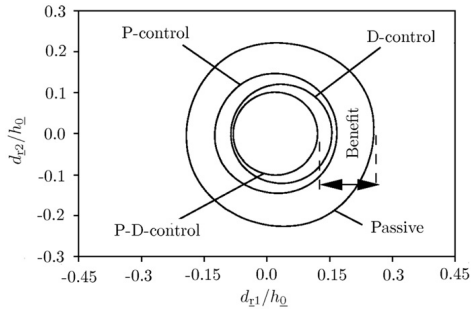


**Fig. 25.** Rotor limit cycles for a counter clockwise rotating load of magnitude 10 000 N and frequency 55.21 Hz. The static load is low at 2000 N and oriented in the $x_1$ direction.

performed. Different orifice configurations have been investigated to explore potential differences in performance. It seems that a four orifice configuration is more powerful in a proportional regulated system, while a six orifice configuration is more powerful in a derivative regulated system. Thus one cannot advocate any orifice configuration over the other as long as the orifices are placed far from the pivot line. It has been proven that orifices placed far from the pivot line can increase the effective static preload factor of a tilting-pad journal bearing. Since pad compliance increases in importance for increasing frequency, this result extends to the dynamic case. This is reflected by the fact that any of the three orifice configurations tested in this study outperforms a single orifice placed in the centre of the pad. Clearly, the recommendation of this study is to place orifices far from the pivot line, when designing tilting-pad journal bearings under active elastohydrodynamic lubrication. This is where greatest impact will be achieved.

## References

[1] Maslen EH. Magnetic bearings—theory, design and application to rotating machinery. New York, USA: Springer; 2009.
[2] Palazzolo AB, Lin RR, Alexander RM, Kascak AF, Montague J. Test and theory for piezoelectric actuators—active vibration control of rotating machinery. Transactions of ASME, Journal of Vibration and Acoustics 1991;113:167–75.
[3] Ulbrich H, Althaus J. Actuator design for rotor control. In: 12th biennial ASME conference on vibration and noise, 1989. p. 17–21.
[4] Deckler DC, Veillette RJ, Braun MJ, Choy FK. Simulation and control of an active tilting-pad journal bearing. STLE Tribology Transactions 2000;47: 440–58.
[5] Wu A, Cai Z, de Queiroz MS. Model-based control of active tilting-pad bearings. IEEE/ASME Transactions on Mechatronics 2007;12(6):689–95.
[6] Althaus J. Eine Aktive Hydraulische Lagerung für Rotorsysteme. Düsseldorf, Germany: VDI-Verlag; 1991.
[7] Santos IF. Aktive Kippsegmentlagerung—Theorie und Experiment. Düsseldorf, Germany: VDI-Verlag; 1993.
[8] Santos IF. On the adjusting of the dynamic coefficients of tilting-pad journal bearings. STLE Tribology Transactions 1995;38(2):700–6.
[9] Goodwin MJ, Boroomand T, Hooke CJ. Variable impedance hydrodynamic journal bearings for controlling flexible rotor vibrations. In: 12th biennial ASME conference on vibration and noise, 1989. p. 261–7.
[10] Rylander HG, Carlson MJT, Lin CR. Actively controlled bearing surface profiles—theory and experiment. In: ASME tribology symposium, 1995. p. 11–4.
[11] Sun L, Krodkiewski JM. Experimental investigation of dynamic properties of an active journal bearing. Journal of Sound and Vibration 2000;230(5): 1103–17.
[12] Krodkiewski JM, Davies GJ. Modelling a new three-pad active bearing. In: Proceedings of ASME Turbo Expo 2004, 2004. p. 1–9.
[13] Santos IF, Russo FH. Tilting-pad journal bearings with electronic radial oil injection. ASME Journal of Tribology 1998;120:583–94.
[14] Santos IF, Nicoletti R, Scalabrin A. Feasibility of applying active lubrication to reduce vibration in industrial compressors. ASME Journal of Engineering for Gas Turbine and Power 2004;126(4):888–94.
[15] Haugaard AM, Santos IF. Elastohydrodynamics applied to active tilting-pad journal bearings. ASME Journal of Tribology, in print (TRIB-09-1048).
[16] Bently DE, Eldridge T, Jensen J, Mol P. Active controlled hydrostatic bearings for a new generation of machines. In: ASME/IGTI international gas turbine and aeroengine congress and exhibition, no. 2000-GT-354, Munich, Germany, 2000.

[17] Bently DE, Eldridge T, Jensen J, Mol P. Externally pressurized bearings allow rotor dynamic optmization. In: VDI-Berichte, nr. 1640, 2001. p. 44–61.

[18] Haugaard AM, Santos IF. Fast solution of fluid structure interaction problems in the frequency domain—with an application. In: 11th Pan-American congress of applied mechanics—PACAM XI, Foz do Iguau, Paran, Brazil, 2010. p. 1–6, in print.

[19] Lund J. Spring and damping coefficients for the tilting pad journal bearing. Transactions on ASLE 1964;7:342–52.

[20] Allaire PE, Parsell JA, Barrett LE. A perturbation method for the dynamic coefficients of tilting-pad journal bearings. Wear 1981;72:29–44.

[21] Parsell JK, Allaire PE, Barrett LE. Frequency effects in tilting-pad journal bearing dynamic coefficients. ASLE Transactions 1983;26:222–7.

[22] Lund J. The influence of pad flexibility on the dynamic coefficients of a tilting-pad journal bearing. ASME Journal of Tribology 1987;109:65–70.

[23] Earles LL, Palazzolo AB, Armentrout RW. A finite element approach to pad flexibility effects in tilt pad journal bearings: part I—single pad analysis. ASME Journal of Tribology 1990;112:169–77.

[24] Earles LL, Palazzolo AB, Armentrout RW. A finite element approach to pad flexibility effects in tilt pad journal bearings: part II—assembled bearing and system analysis. ASME Journal of Tribology 1990;112:178–82.

[25] Desbordes H, Fillon M, Chan C, Frêne J. Dynamic analysis of tilting-pad journal bearings—influence of pad deformations. ASME Journal of Tribology 1994;116:621–7.

[26] Desbordes H, Fillon M, Frêne J, Chan C. The effects of three-dimensional pad deformations on tilting-pad journal bearings under dynamic loading. ASME Journal of Tribology 1995;117:379–84.

[27] Santos IF, Nicoletti R. Influence of orifice distribution on the thermal and static properties of hybridly lubricated bearings. International Journal of Solids and Structures 2001;38:2069–81.

[28] Thomas H. Instabile Eigenschwingungen von Turbinenlaeufern, Angefacht durch die Spaltstroemungen in Stopfbuchsen und Beschaufelungen (Unstable vibrations of turbine rotors excited by clearance flows in sealings and bladings). Bulletin De l'AIM 1958;71(11/12):1039–64.

[29] Alford J. Protecting turbomachinery from self-excited rotor whirl. ASME Journal of Engineering for Power 1965;87(4):333–44.

[30] Pollman E, Schwerdtfeger H, Termuehlen H. Flow excited vibrations in high pressure turbines (steam whirl). ASME Journal of Engineering for Power 1978;100(2):219–28.

[31] Bachschmid N, Pennacchi P, Vania A. Steam whirl stability margin in a power unit. In: Proceedings of ISMA—international conference on noise and vibration engineering, Leuven, Belgium, 2006. p. 3561–75.

[32] Cook R, Malkus D, Plesha M, Witt R. Concepts and applications of finite element analysis. New York, USA: Wiley; 2001.

[33] Santos IF, Nicoletti R. Trends in controllable oil film bearings. Journal of Sound and Vibration 2003;260(5):927–47.

[34] Santos IF. Linear and non-linear control techniques applied to actively lubricated journal bearings. In: Proceedings of IUTAM symposium on emerging trends in rotor dynamics, Delhi, India, 2009. p. 1–15.

[35] Santos IF, Scalabrin A. Control system design for active lubrication with theoretical and experimental examples. ASME Journal of Engineering for Gas Turbine and Power 2003;125:75–80.

[36] Geuzaine C, Remacle J-F. Gmsh: a three-dimensional finite element mesh generator with built-in pre- and post-processing facilities. International Journal for Numerical Methods in Engineering 2009;79(11):1309–11.

# Publication 3

Stability of Multi Orifice Active Tilting-Pad Journal Bearings
Tribology International (Elsevier)

Tribology International 43 (2010) 1742–1750

Contents lists available at ScienceDirect

Tribology International

journal homepage: www.elsevier.com/locate/triboint

# Stability of multi orifice active tilting-pad journal bearings

Asger M. Haugaard, Ilmar F. Santos *

*Department of Mechanical Engineering, Technical University of Denmark, 2800 Lyngby, Denmark*

ARTICLE INFO

*Article history:*
Received 2 February 2010
Received in revised form
14 April 2010
Accepted 16 April 2010
Available online 21 April 2010

*Keywords:*
Tilting-pad journal bearings
Stability
Elastohydrodynamics
Control

ABSTRACT

The stability properties of actively lubricated tilting-pad journal bearings are investigated theoretically. The bearing preload factor and control system gains are varied, and stable and unstable regions are identified. It is seen, that the control system influences bearing stability, and that the nature and magnitude of this influence depends on the rotor mass, preload factor and rotational speed. Furthermore, it is shown that assuming the bearing pads to be rigid can produce a substantial error. A rigid pad model will overpredict the stable range of the bearing, thus it may lead to failure if trusted.


## 1. Introduction

As is the general consensus, and stated by Nicholas in [1], Lund pioneered the work with frequency domain analysis of tilting-pad journal bearings with his seminal 1964 paper [2]. Nicholas [1] goes on to state that "prior to 1964, tilting-pad journal bearing studies consisted of static analyses which were limited to determining load capacity and power loss. For many years, the only analysis available was the one detailed by Boyd and Raimondi [3,4]".

Previously, use of models involving many degrees of freedom, to carry out harmonic steady-state and stability analyses of rotors, was generally avoided due to two main reasons: firstly, because of the number of parameters and degrees of freedom involved are many and secondly, because the rotordynamic community was and is used to perform vibration analyses of rotors supported by fluid film bearings using the eight oil film stiffness and damping coefficients, as in the pioneer works of Stodola [5] and Hagg and Sankey [6]. These eight coefficients capture the steady-state harmonic forced vibration response of the bearing. The oil film coefficients are easily used as input data in rotordynamic programmes.

In most steady-state and stability analysis of rotor-bearing systems, reduced analytical models are used, as is mentioned by Brockett and Barrett [7]. They proceed to introduce an "exact" approach to reduce the pad dynamical model. What is meant by exact is simply that no assumption is made with regard to the pad motion in time, since the equations are written in the frequency domain through a Laplace transform. Thus their model can be used for stability analysis, if desired. For stability analysis, they truncate the solution to low powers of the Laplace variable. This is applicable to situations where the potentially unstable modes are those of low frequency, since this places the Laplace variable close to origo of the complex plane. This is most often the case with tilting pad journal bearings, if not always.

Often, in order to simplify the steady-state and stability analysis, both shaft and pads are restricted to synchronous motion with the same frequency of vibration around their static equilibrium positions. This reduces the number of degrees of freedom to eight synchronous oil film coefficients [8–11], similar to the other cases of fluid film bearings (without moving parts). Usually, these coefficients are thought of as equivalent stiffness and damping coefficients, calculated as functions of pad mass and excitation frequency. Nevertheless, these coefficients have no direct physical significance [12] when compared to mechanical springs and dampers and should not be used to perform stability analysis. In fact, the frequency of free vibration of the system, which needs to be determined by the complex eigenvalues computed from the differential equations of the system, is not equal to the forced frequency of vibration. Thus, by employing synchronous reduced oil film coefficients engineers cannot effectively predict the stability of tilting-pad bearing systems [13–15]. Employing synchronous reduced oil film coefficients allows engineers to properly predict the amplitude of the steady-state responses only. For example, pad fluttering [16,17] is a typical phenomenon which cannot be accurately predicted using synchronous coefficients. The vibration frequency of the unloaded fluttering-pad is normally different from the rotor angular velocity.

Tilting-pad journal bearings are much more stable than other types of fluid film bearings, which is one of the main reasons why

* Corresponding author.
*E-mail address:* ifs@mek.dtu.dk (I.F. Santos).

0301-679X/$ - see front matter © 2010 Elsevier Ltd. All rights reserved.
doi:10.1016/j.triboint.2010.04.013

they are nowadays one of the most used journal bearing types for high speed applications. Although tilting-pad journal bearings are considered stable, instabilities may occur depending on the operational conditions, i.e. for a low pre-load factor or low static loading. Also, external influences, coming from e.g. a compressor or a turbine, may cause instability. Tilting pad journal bearing stability is thoroughly investigated, theoretically as well as experimentally, by different authors [18–23]. The main original contribution of the present paper is of theoretical nature. It descends from the work done previously by a number of authors: (i) in [2] a conventional rigid-pad hydrodynamic (HD) bearing was studied, (ii) in [24–26] bearing pad compliance was included, thus making the analysis elastohydrodynamic (EHD), (iii) in [27] thermal effects were accounted for, pushing the state of the art to thermoelastohydrodynamic (TEHD) analysis, (iiii) in [28,29] thermal effects were neglected but active hybrid lubrication was introduced to influence the behaviour of the bearing. There, the analysis focused on the forced harmonic steady-state response of the bearing. The present investigation focuses on bearing stability, and uses a model similar to the one in [29]. The influence of active hybrid lubrication on bearing stability is studied. Furthermore, the importance of including pad compliance is highlighted by direct comparison to results for an active hybrid bearing with rigid-body pads.

A journal bearing with four elastic tiling-pads is modelled using a finite element approach, somewhat similar to the approach presented by Earles [24,25] and closely resembling that of [26]. Two servo-valves are used to control the radial oil injection through orifices machined on the pad surfaces. The servo-valve dynamics are governed by second order differential equations, in an approach similar to that of Santos and Russo [30]. The system of equations describing the fluid flow in the bearing gap and orifices is coupled to the deformable tilting-pads, then linearised and written in the state-space form to facilitate the calculation of the system eigenvalues, which are necessary for stability analysis. It is important to stress that no assumption of synchronous movements between rotor and pads are made. Insights into tilting-pad journal bearing stability with focus on controllable lubrication are reported. Advantages and drawbacks related to the use of active lubrication in terms of bearing stability are thoroughly addressed.

## 2. Governing equations

Index notation will appear in certain places. To avoid confusion, while retaining a consistent nomenclature, summation of repeated indices is not employed, thus all summations are stated explicitly. Underlined indices are part of variable names and indices without underline are used for numbering, e.g. $q_{\underline{v}i}$ is the valve flow of servo-valve number $i$. A nomenclature is provided in Tables 1–3.

Fig. 1 illustrates the different coordinate frames and domains used to describe the elastic behaviour of the pads, and the journal pressure distribution among the rotor and the pads. The curvilinear coordinates $(\chi_1,\chi_2)$ are used for the fluid film and the Cartesian coordinates $(x_1,x_2,x_3)$ are used for the pads.

The solid is taken to be linearly elastic and isotropic. Small strains and rotations suffice for the description of the deformed state. The governing equation is traditionally given directly in integral form as the principle of virtual work

$$\sum_{i,j,k,l=1}^{3} \int_{\Pi} L_{ijkl}\varepsilon_{kl}\delta\varepsilon_{ij}\,d\Pi = \sum_{i=1}^{3}\int_{\Pi}\rho\ddot{u}_i\delta u_i\,d\Pi + \sum_{i=1}^{3}\int_{\Lambda} T_i\delta u_i\,d\Lambda \qquad (1)$$

where $\varepsilon_{kl}$ is the strain tensor, $\rho$ is the density of the solid, $T_i$ denotes the surface traction, $u_i$ is the displacement vector $\delta$ denotes an increment and $L_{ijkl}$ is the constitutive tensor for the material. The solid is considered isotropic, homogenous and linearly elastic, thus the constitutive tensor is given by

$$L_{ijkl} = \frac{E}{2(1+\nu)}\left(\delta_{ik}\delta_{jl} + \delta_{il}\delta_{jk} + \frac{2\nu}{1-2\nu}\delta_{ij}\delta_{kl}\right) \qquad (2)$$

**Table 1**
Nomenclature—upper-case Latin letters.

| | |
|---|---|
| $\mathbf{A}$ | Pressure system matrix |
| $C_{\underline{a}}$ | Assembled clearance |
| $\mathbf{D}$ | Generalised damping matrix |
| $\mathbf{D}_{\underline{q-q}}$ | Flow damping matrix |
| $E$ | Young's modulus |
| $G_{\underline{P}}$ | Proportional gain |
| $G_{\underline{D}}$ | Derivative gain |
| $\mathbf{K}$ | Generalised stiffness matrix |
| $K_{\underline{pq}}$ | Flow-pressure constant |
| $\mathbf{K}_{\underline{q-q}}$ | Flow stiffness matrix |
| $\mathbf{K}_{\underline{s}}$ | Solid stiffness matrix |
| $K_{\underline{v}}$ | Valve static amplification |
| $L_{ijkl}$ | Solid constitutive tensor |
| $\mathbf{M}$ | Generalised mass matrix |
| $\mathbf{M}_{\underline{q-q}}$ | Flow mass matrix |
| $\mathbf{M}_{\underline{r}}$ | Rotor mass matrix |
| $\mathbf{M}_{\underline{s}}$ | Solid mass matrix |
| $U$ | Tangential rotor speed |
| $\mathbf{V}_{\underline{s}}$ | Matrix of solid modes of vibration |
| $\mathbf{V}$ | Reduction matrix |

**Table 2**
Nomenclature—lower-case Latin letters.

| | |
|---|---|
| $\mathbf{b}$ | Modal coordinate vector |
| $\mathbf{d}_{\underline{g}}$ | Generalised displacement vector |
| $\mathbf{f}$ | Nodal force vector |
| $\mathbf{f}_{\underline{g}}$ | Generalised force vector |
| $\mathbf{f}_{\underline{r}}$ | Rotor force vector |
| $g_i$ | Orifice flow shape function |
| $h$ | Fluid film thickness |
| $l_{\underline{0}}$ | Orifice inlet length |
| $p$ | Fluid pressure |
| $\mathbf{p}$ | Generalised pressure vector |
| $p_{\underline{inj}i}$ | Injection pressure |
| $q_{\underline{L}}$ | Leak flow |
| $q_{\underline{v}}$ | Valve flow |
| $\mathbf{r}$ | Pressure right hand side |
| $t$ | Time |
| $u_i$ | Displacement |
| $u_{\underline{v}}$ | Valve input signal |
| $x_i$ | Inertial coordinates |

**Table 3**
Nomenclature—Greek letters.

| | |
|---|---|
| $\Gamma$ | Fluid boundary |
| $\Lambda$ | Solid boundary |
| $\Lambda_{\underline{s}}$ | Diagonal matrix of eigenvalues |
| $\Pi$ | Solid domain |
| $\Phi$ | Fluid domain |
| $\Omega$ | Fundamental frequency |
| $\varepsilon_{ij}$ | Strain tensor |
| $\nu$ | Poisson's ratio |
| $\xi_{\underline{v}}$ | Valve damping ratio |
| $\rho$ | Solid density |
| $\chi_i$ | Curvilinear coordinates |
| $\omega_{\underline{v}}$ | Valve eigenfrequency |

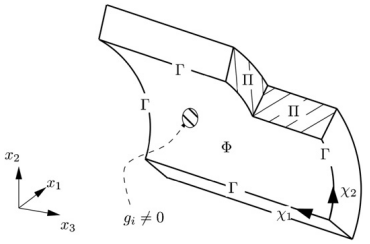


**Fig. 1.** Overview of the different domains, the fluid film curvilinear coordinate system ($\chi_1$,$\chi_2$) and the Cartesian coordinate system ($x_1$,$x_2$,$x_3$). The subdomain where $g_i \neq 0$ is that of a orifice. The solid domain is denoted by $\Pi$ and its boundary by $\Lambda$. Note that all external surfaces are part of the solid boundary. The fluid domain is denoted by $\Phi$ and its boundary by $\Gamma$.

where $E$ is Young's modulus, $v$ is Poisson's ratio and $\delta_{ij}$ is Kronecker's delta. From equations Eqs. (1) and (2) the stiffness and mass matrices of the solid can be derived, refer to [28,29].

The pressure field in the fluid is described by the modified Reynolds equation

$$\frac{1}{12}\sum_{i=1}^{2}\frac{\partial}{\partial\chi_i}\left(\frac{h^3}{\mu}\frac{\partial p}{\partial\chi_i}\right)=\frac{U}{2}\frac{\partial h}{\partial\chi_2}+\dot{h}+\sum_i g_i\left(p-\frac{p_{\underline{\mathrm{inj}}i)}}{4\mu l_{\underline{0}i}}\right) \tag{3}$$

where $p$ is the pressure, $h$ is the oil film thickness, $U$ is the relative tangential speed of the rotor, $g_i$ is a shape function describing a laminar flow profile in orifice $i$, $p_{\underline{\mathrm{inj}}i}$ is the injection pressure in orifice $i$, $l_{\underline{0}i}$ is the length of the orifice inlet tube $i$ and $\mu$ is the dynamic viscosity of the lubricant. The $\chi_2$ coordinate is aligned with the direction of rotation.

We introduce the fundamental frequency of the system as

$$\Omega = U/R_{\underline{\mathrm{r}}} \tag{4}$$

where $R_{\underline{\mathrm{r}}}$ is the radius of the rotor.

The flow in servo-valve $i$ is described by the second order ordinary differential equation

$$\ddot{q}_{\underline{\mathrm{v}}i}+2\xi_{\underline{\mathrm{v}}i}\omega_{\underline{\mathrm{v}}i}\dot{q}_{\underline{\mathrm{v}}i}+\omega_{\underline{\mathrm{v}}i^2 q_{\underline{\mathrm{v}}i}}=\omega_{\underline{\mathrm{v}}i^2 K_{\underline{\mathrm{v}}} u_{\underline{\mathrm{v}}i}} \tag{5}$$

where $\omega_{\underline{\mathrm{v}}i}$ is the servo-valve eigenfrequency, $K_{\underline{\mathrm{v}}i}$ is the valve flow voltage coefficient, $\xi_{\underline{\mathrm{v}}i}$ is the valve damping ratio and $q_{\underline{\mathrm{v}}i}$ is the valve flow—all of valve $i$.

The injection orifice arrays (pads) are connected by servo-valves as pairs. Thus the flows in a pad pair are coupled. We define the positive direction of orifice flow as going from the valve and into the gap. The linearised $2\times 2$ system of equations for a servo-valve connecting, e.g. pad $i$ and $j$ is

$$\begin{Bmatrix} q_i \\ q_j \end{Bmatrix}=\begin{bmatrix} -K_{\underline{\mathrm{pq}}} & K_{\underline{\mathrm{pq}}} \\ K_{\underline{\mathrm{pq}}} & -K_{\underline{\mathrm{pq}}} \end{bmatrix}\begin{Bmatrix} p_{\underline{\mathrm{inj}}i} \\ p_{\underline{\mathrm{inj}}j} \end{Bmatrix}+\begin{Bmatrix} q_{\underline{\mathrm{v}}} \\ -q_{\underline{\mathrm{v}}} \end{Bmatrix}+\begin{Bmatrix} q_{\underline{\mathrm{L}}} \\ q_{\underline{\mathrm{L}}} \end{Bmatrix} \tag{6}$$

where $K_{\underline{\mathrm{pq}}}$ is the valve flow-pressure coefficient, $q_{\underline{\mathrm{L}}}$ is the valve leak flow, $q_i$ is the flow to pad $i$ and $p_{\underline{\mathrm{inj}}i}$ is the injection pressure at pad $i$. Here we have selected a positive direction of flow for the servo-valve. The pad associated with positive valve flow, in this case pad $i$, is denoted the master pad. The pad associated with negative valve flow, in this case pad $j$ is denoted the slave pad.

The flow through a given orifice can be written in terms of the pressure difference field over the orifice as

$$q_i=\int_{\Phi} g_i\frac{1}{4\mu l_0}(p_{\underline{\mathrm{inj}}i}-p(\chi_1,\chi_2))\,d\Phi \tag{7}$$

Now, with application of the constitutive pressure-flow relation in Eq. (7), we can eliminate $q_i=[q_1 \quad q_2]^T$ from Eq. (6). So, given $q_{\underline{\mathrm{v}}}$ and the fluid film thickness field $h$, we can solve for the injection pressures and the nodal pressures. That is, we have now coupled the flow to the pressure field. To couple the displacement field to the flow and the pressure field we invoke two conditions. Firstly, the field of fluid film thickness $h$ is a function of the displacement field $u_i$ and the rotor position. Secondly the field of traction on the surface of the pads $T_i$ is a function of the fluid film pressure field $p$. With these conditions, we can write the complete set of equations compactly in discrete form as

$$\mathbf{M}_{\underline{\mathrm{s}}}\ddot{\mathbf{d}}+\mathbf{K}_{\underline{\mathrm{s}}}\mathbf{d}=\mathbf{f}(\mathbf{p})$$

$$\mathbf{M}_{\underline{\mathrm{r}}}\ddot{\mathbf{d}}_{\underline{\mathrm{r}}}=\mathbf{f}_{\underline{\mathrm{r}}}(\mathbf{p})$$

$$\mathbf{A}(\mathbf{d},\dot{\mathbf{d}},\mathbf{d}_{\underline{\mathrm{r}}},\dot{\mathbf{d}}_{\underline{\mathrm{r}}})\mathbf{p}=\mathbf{r}(\mathbf{d},\dot{\mathbf{d}},\mathbf{d}_{\underline{\mathrm{r}}},\dot{\mathbf{d}}_{\underline{\mathrm{r}}},\mathbf{q})$$

$$\mathbf{M}_{\underline{\mathrm{q-q}}}\ddot{\mathbf{q}}_{\underline{\mathrm{v}}}+\mathbf{D}_{\underline{\mathrm{q-q}}}\dot{\mathbf{q}}_{\underline{\mathrm{v}}}+\mathbf{K}_{\underline{\mathrm{q-q}}}\mathbf{q}_{\underline{\mathrm{v}}}=\mathbf{u}_{\underline{\mathrm{v}}}(\mathbf{d}_{\underline{\mathrm{r}}},\dot{\mathbf{d}}_{\underline{\mathrm{r}}},\ldots) \tag{8}$$

where $\mathbf{M}_{\underline{\mathrm{s}}}$ and $\mathbf{M}_{\underline{\mathrm{r}}}$ are the solid mass matrix and rotor mass matrix, respectively, $\mathbf{K}_{\underline{\mathrm{s}}}$ is the solid stiffness matrix and $\mathbf{A}$ is the system matrix for the pressure problem, derived from the modified Reynolds equation. For discretisation in 3-D space, we employ 20-node 3-D serendipity elements. For discretisation in 2-D curvilinear space, we employ 8-node 2-D serendipity elements. Note that the generalised pressure vector $\mathbf{p}$ contains the nodal values of the pressure field, as well as the pad injection pressures $p_{\underline{\mathrm{inj}}i}$. The nodal force vector $\mathbf{f}(\mathbf{p})$ depends linearly on the fluid film pressure $\mathbf{p}$. This also applies to the rotor force vector $\mathbf{f}(\mathbf{r})$. The servo-valve signal vector $\mathbf{u}_{\underline{\mathrm{v}}}$ can be any functional of any measurable quantity. In the present investigation we shall let it be a functional of lateral rotor velocity and displacement, i.e. we will implement a PD-regulator.

The bearing has four pads. The bearing pads are numbered consecutively in the counter clockwise direction from the $x_1$ axis. Thus we have pad #1 ($x_1>0$ and $x_2>0$), pad #2 ($x_1<0$ and $x_2>0$), pad #3 ($x_1<0$ and $x_2<0$) and pad #4 ($x_1>0$ and $x_2<0$). Fig. 2 shows a schematic of the bearing with indication of pad numbering.

The way we implement the regulator is to connect the pads in pairs with servo-valves. Pad #1 is connected to pad #3 with a servo-valve. Also, pad #4 is connected to pad #2 with a servo-valve. Pads #1 and #4 are chosen as master pads, with pads #3

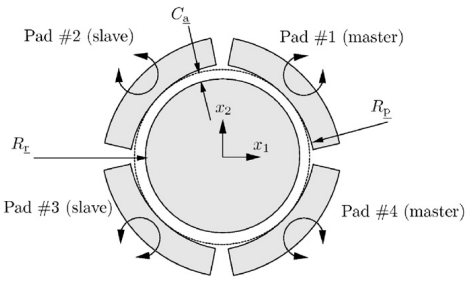


**Fig. 2.** Schematic of bearing and pad numbering. The figure shows four pads supporting a rotor and indicates the radius of curvature of the rotor $R_{\underline{\mathrm{r}}}$, the radius of curvature of the pads $R_{\underline{\mathrm{p}}}$, and the assembled clearance $C_{\underline{\mathrm{a}}}$. The assembled clearance $C_{\underline{\mathrm{a}}}$ is measured as the minimum gap between rotor and pad, when the pads are undeformed. Since the gap is small compared to the radii of curvature, it can be defined as perpendicular to either the rotor or the pad. The difference is negligible. The pivoting motion of the pads is indicated. A detailed description of pad boundary conditions is given in [28].

and #2 as their respective slave counterparts. Both servo-valves respond to rotor movement in the $x_1$ direction and $x_2$ direction. The software written for the bearing analysis takes a vector as input, so as to define what direction of rotor movement, that each servo-valve shall respond to. This vector is normalised inside the programme. Here, we set the first valve to respond to (1, 1) and the second valve to respond to (1, −1). Thus, after normalisation, the two servo-valve signals are computed as

$$u_{\underline{v}1} = G_{\underline{D}}(\dot{d}_{\underline{r}1} + \dot{d}_{\underline{r}2})/\sqrt{2} + G_{\underline{P}}(d_{\underline{r}1} + d_{\underline{r}2})/\sqrt{2} \tag{9}$$

$$u_{\underline{v}2} = G_{\underline{D}}(\dot{d}_{\underline{r}1} - \dot{d}_{\underline{r}2})/\sqrt{2} + G_{\underline{P}}(d_{\underline{r}1} - d_{\underline{r}2})/\sqrt{2} \tag{10}$$

where $G_{\underline{D}}$ is the derivative gain and $G_{\underline{P}}$ is the proportional gain. This makes for an active bearing which still almost decouples the $x_1$ and $x_2$ coordinate directions, just as a passive tilting-pad journal bearing. An explanation of why this is the case is given in [29].

The rotor is assumed to move laterally only, i.e. the axis of symmetry is assumed to align with $x_3$ at all times, also its centre of mass is assumed to coincide with its axis of rotation at all times. The rotor is assigned a mass, but no stiffness. This means that the only static support of the rotor is that of the bearing. Now, after elimination of the pressures $\mathbf{p}$, the linear part of the Eqs. (8) at the state $\mathbf{d}_{\underline{g}} = \mathbf{d}_{\underline{g0}}$ can be written as

$$\mathbf{M}\Delta\ddot{\mathbf{d}}_{\underline{g}} + \mathbf{D}(\mathbf{d}_{\underline{g0}})\Delta\dot{\mathbf{d}}_{\underline{g}} + \mathbf{K}(\mathbf{d}_{\underline{g0}})\Delta\mathbf{d}_{\underline{g}} = \Delta\mathbf{f}_{\underline{g}} \tag{11}$$

where $\mathbf{d}_{\underline{g}}$ and $\mathbf{f}_{\underline{g}}$ are the vectors of generalised displacements and forces, respectively. The vector $\mathbf{d}_{\underline{g}}$ contains all nodal displacements of the solid ($\mathbf{d}$), as well as the lateral displacement of the rotor ($\mathbf{d}_{\underline{r}}$) and the flow in each servo-valve ($\mathbf{q}_{\underline{v}}$). The vector $\mathbf{f}_{\underline{g}}$ contains the corresponding forces, and the servo-valve signal. As such

$$\mathbf{d}_{\underline{g}} = \begin{Bmatrix} \mathbf{d} \\ \mathbf{d}_{\underline{r}} \\ \mathbf{q}_{\underline{v}} \end{Bmatrix}, \quad \mathbf{f}_{\underline{g}} = \begin{Bmatrix} \mathbf{f} \\ \mathbf{f}_{\underline{r}} \\ \mathbf{u}_{\underline{v}} \end{Bmatrix} \tag{12}$$

The vector of nodal displacements will typically contain thousands of degrees of freedom, and so contributes with the bulk of the computational workload. The vector of lateral rotor displacements contains only the two components of lateral rotor movement, i.e. $\mathbf{d}_{\underline{r}} = [d_{\underline{r}1}\ d_{\underline{r}2}]^T$. Finally, the vector of flows contains as many components as there are servo-valves. In the present investigation, this means two. The derivation of the governing equations is explained in more detail in [28,29].

### 2.1. Pseudo modal reduction

If the force from perturbing a node comes mainly from the solid, then the mode shapes of the solid only system will be very similar to those of the combined fluid–solid system. In other words: Given the assumption that the deformation forces from the solid are larger than those from the fluid, the system of equations Eq. (11) can be condensed spectrally as

$$\mathbf{V}^T\mathbf{M}\mathbf{V}\Delta\ddot{\mathbf{b}} + \mathbf{V}^T\mathbf{D}(\mathbf{b}_{\underline{0}})\mathbf{V}\Delta\dot{\mathbf{b}} + \mathbf{V}^T\mathbf{K}(\mathbf{b}_{\underline{0}})\mathbf{V}\Delta\mathbf{b} = \mathbf{V}^T\mathbf{f}_{\underline{g}} \tag{13}$$

where

$$\mathbf{V} = \begin{bmatrix} \begin{bmatrix} \mathbf{V}_{\underline{s}} \end{bmatrix} & [\mathbf{0}] \\ [\mathbf{0}] & [\mathbf{I}] \end{bmatrix} \tag{14}$$

That is, $\mathbf{d}_{\underline{g}}$ is approximated as

$$\mathbf{d}_{\underline{g}} = \mathbf{V}\mathbf{b} \tag{15}$$

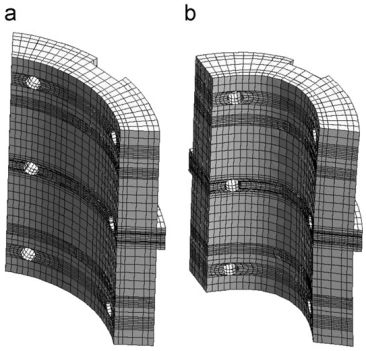


**Fig. 3.** Eigenmodes of the solid part of the system. (a) The first mode, which is a rigid body mode. (b) The second, bending, mode. Given that $E = 100$ GPa, the eigenfrequencies for the modes are 0 and 7.29 kHz, respectively.

The matrix $\mathbf{V}_{\underline{s}}$ contains in its columns some of the eigenmodes of vibration of the solid, thus it satisfies

$$\mathbf{K}_{\underline{s}}\mathbf{V}_{\underline{s}} = \mathbf{M}_{\underline{s}}\mathbf{V}_{\underline{s}}\Lambda_{\underline{s}} \tag{16}$$

where $\Lambda_{\underline{s}}$ contains the squares of the corresponding solid eigenfrequencies in its diagonal and zeros elsewhere. The identity matrix in the lower right corner of Eq. (14) transfers the rotor and servo-valve degrees of freedom untransformed. I.e. the purpose of $\mathbf{V}$ is to reduce the workload associated with the large number of degrees of freedom in the pads. The rotor and valves cannot and will not be reduced any further. In the present investigation, two modes of vibration have been considered for each pad. The system has four pads, one rotor and two servo-valves. Thus the size of the reduced system Eq. (13) is $12 \times 12$, which is manageable by any modern computer. Fig. 3 shows the two modes considered for each pad. These figures also give an impression of the mesh refinement used in the analyses, as the meshes shown are used throughout the investigation. As mentioned, the elements are 20-node serendipity elements, see e.g. [31]. Since we include only two mode shapes, the mesh is more than adequate in terms of refinement.

## 3. Analyses

The influence of derivative and proportional feedback control will be investigated by a parameter study. Four key parameters will be varied: (i) The proportional gain $G_{\underline{P}}$, (ii) the derivative gain $G_{\underline{D}}$, (iii) the preload factor $m_{\underline{p}}$ and (iiii) the rotational speed $U$. The preload factor is well known in the tribology community, and is an important bearing parameter. It is defined as

$$m_{\underline{p}} = 1 - \frac{C_{\underline{a}}}{R_{\underline{p}} - R_{\underline{r}}} \tag{17}$$

where $C_{\underline{a}}$ is the assembled clearance of the bearing, $R_{\underline{r}}$ is the radius of curvature of the rotor and $R_{\underline{p}}$ is the radius of curvature of the pads. Refer to Fig. 2 for a schematic showing these measures. For given bearing and rotor dimensions, increasing the preload corresponds to pushing the pads closer to the rotor. Preload factors typically range from 0.1 to 0.7.

Now, omitting the argument ($\mathbf{b}_{\underline{0}}$) let us rewrite Eq. (13) compactly as

$$\mathbf{M}_{\underline{m}}\Delta\ddot{\mathbf{b}} + \mathbf{D}_{\underline{m}}\Delta\dot{\mathbf{b}} + \mathbf{K}_{\underline{m}}\Delta\mathbf{b} = \mathbf{V}^T\mathbf{f}_{\underline{g}} \tag{18}$$

where the definitions of the new pseudo modal system matrices follow directly from comparing to Eq. (13). The transient part of the solution for $\Delta\mathbf{b}$ is defined by

$$\mathbf{M}_{\underline{\mathrm{m}}}\Delta\ddot{\mathbf{b}}+\mathbf{D}_{\underline{\mathrm{r}}}\Delta\dot{\mathbf{b}}+\mathbf{K}_{\underline{\mathrm{m}}}\Delta\mathbf{b}=\mathbf{0} \tag{19}$$

which has the solution

$$\begin{Bmatrix}\dot{\mathbf{b}}\\ \mathbf{b}\end{Bmatrix}=\mathbf{v}e^{\lambda t} \tag{20}$$

where $\mathbf{v}$ and $\lambda$ are the eigenvectors and eigenvalues of the generalised eigenvalue problem

$$\begin{bmatrix}\mathbf{0} & \mathbf{K}_{\underline{\mathrm{m}}}\\ \mathbf{M}_{\underline{\mathrm{m}}} & \mathbf{0}\end{bmatrix}\mathbf{v}=\lambda\begin{bmatrix}-\mathbf{M}_{\underline{\mathrm{m}}} & -\mathbf{D}_{\underline{\mathrm{m}}}\\ \mathbf{0} & \mathbf{M}_{\underline{\mathrm{m}}}\end{bmatrix}\mathbf{v} \tag{21}$$

The stability of a given equilibrium of the system is examined by solving Eq. (21) for the eigenvalues. For realistic system parameters, there are typically two static equilibria of the system of Eqs. (13) (and (8)), but only one which is physically meaningful. Thus only one that should be checked for stability. In Fig. 4 is seen the pressure profile for the physically meaningful static equilibrium of a bearing with a preload factor of 0.5 and a rotational speed of 6000 rpm. The corresponding displacements are shown in Fig. 5. Primarily, note two things. (i) Firstly, the pads tilt in the same direction as the rotor rotation. This creates the well known wedge effect [32]. (ii) Secondly, the pressure on the entire surface of the pads is positive. The physically meaningless equilibrium is characterised by pads that tilt in the opposite direction of the rotor rotation, resulting in negative pressures.

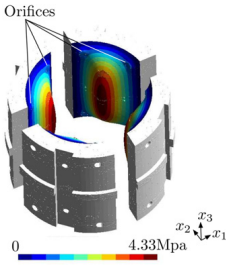


**Fig. 4.** The pressure field over the pads at static equilibrium for 6000 rpm and nil radial rotor load. Maximum pressure is 4.33 MPa. Post processing was done with Gmsh [34].

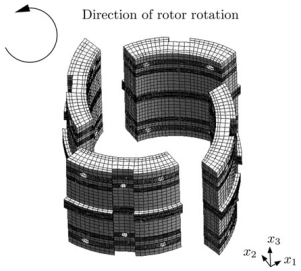


**Fig. 5.** Displacement field of the pads at static equilibrium for 6000 rpm and nil radial rotor load. Displacement is dominated by rigid body tilting, but also note the slight deformation of the pads. Maximum displacement is 28.9 μm.

Here we are outside the domain of validity of our mathematical model. Any negative pressure is an artefact of the Reynolds equation, which assumes an incompressible fluid; it has nothing to do with physics. The model could be generalised by accounting for fluid cavitation in the lubricant, and contact between rotor and pads. In the present investigation, however, we shall focus on the local behaviour around the nominal operating condition. Here, neither cavitation nor contact occurs. Returning our attention to Fig. 4 we note the area around the orifices where the pressure is all but constant in space [30]. Furthermore, a very close look at Fig. 5 reveals a slight deformation of the pads. But, generally, the static equilibrium of the pads is dominated by tilting.

To examine the stability, we evaluate (18) at the physically meaningful static equilibrium $\mathbf{b}_0$. Then we write the corresponding eigenvalue problem (21) and evaluate the sign of the real parts of the eigenvalues. If any real part is greater than zero, the nominal operating state is unstable. For simplicity, we shall use the term "bearing stability" as synonymous to the stability of the physically meaningful static equilibrium.

## 4. Results

Let us examine the stability of the bearing for different combinations of relevant parameters. As mentioned, this investigation focuses on the bearing. Thus the description of the rotor is as simple as possible. However, what tilting-pad journal bearings often have to "fight" is the destabilisation coming from other system components. A good example is aerodynamic instability in a steam turbine. Instead of complicating our model even further, we push the bearing to its limits by means of adjusting the preload factor. It is well known that a high preload factor will make the bearing stable [33]. There are some negative effects associated with a high preload factor, mainly increased frictional loss and wear. However, our motivation for varying the preload factor in this study, is merely to investigate the influence of the controller on the stability of the bearing. Since the preload factor is important for the stability of the bearing, it seems prudent to tune control system gains at different preload factors, before jumping to any conclusions with regard to the controller. Bearing and valve data is given in Tables 4 and 5. The rotational speed of the rotor is 6000 rpm, corresponding to a surface relative velocity of $U=31.4$ m/s for the given rotor diameter. Rotational speeds of this order of magnitude are common in industrial applications. Assuming a gap of 100 μm and a lubricant density of 900 kg/m$^3$ the Reynolds number is approximately 150. Thus there is no need to account for the inertial forces from the lubricant. The static radial load of the rotor is nil. Thus the rotor remains in the centre of the bearing, i.e. at zero eccentricity. We choose a configuration with four orifices on each pad—one in each corner.

Fig. 6 shows the real parts of the system eigenvalues as a function of the derivative gain of the controller. The proportional gain is nil. Rotor mass is 200 kg. In Fig. 6(a) the preload factor is 0.01 and in Fig. 6(b) is 0.5. Note the effect of the increase of the preload factor from 0.01 to 0.05. The large negative eigenvalues drop to even larger negative numbers. The fastest modes of a

**Table 4**
Servo-valve constants.

| Property | Unit | Value(s) |
|---|---|---|
| Valve flow-pressure coefficient | m$^3$/(s Pa) | $1.13\times10^{-12}$ |
| Valve flow-voltage coefficient | m$^3$/(s V) | $33.4\times10^{-6}$ |
| Valve damping ratio | – | 0.48 |
| Valve eigenfrequency | Hz | 320.16 |
| Valve leak flow | m$^3$/s | $6\times10^{-6}$ |

**Table 5**
Bearing data.

| Property | Unit | Value(s) |
|---|---|---|
| Pad radius of curvature | mm | 50 |
| Rotor radius | mm | 49.9 |
| Rotor mass | kg | 200.0 or 2000.0 |
| Static radial load | N | 0.0 |
| Pad extension | ° | 69.3 |
| Angular pivot locations | ° | 45, 135, 225 and 315 (at pad centres) |
| Radial pivot location | mm | 64 |
| Pad length | mm | 100 |
| Nominal pad thickness | mm | 14 |
| Pad Young's modulus | GPa | 100.0 |
| Pad Poisson's ratio | – | 0.3 |
| Pad density | kg/m$^3$ | 8400 |
| Lubricant dynamic viscosity | N s/m$^2$ | 0.019 |

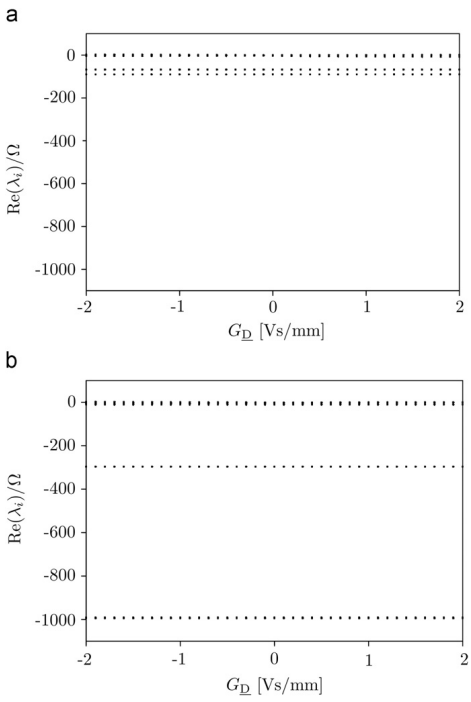


**Fig. 6.** Eigenvalues of the system at the static equilibrium normalised with respect to the rotational frequency. The preload factor is (a) 0.01 and (b) 0.5.

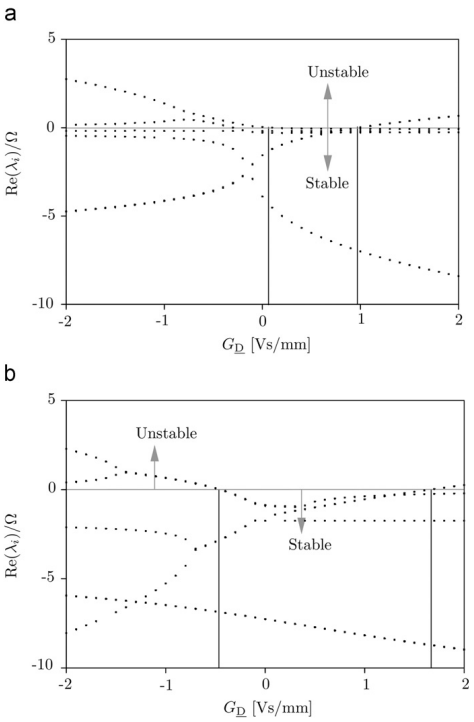


**Fig. 7.** Zoom of Fig. 6. Again the preload factor is (a) 0.01 and (b) 0.5.

tilting pad journal bearing are the ones related to pure pad motion. So the increase in preload factor has the principal effect of damping pad motion. From studying Fig. 6 it seems that the real parts of the system eigenvalues are independent of the derivative gain, but this is not true. Consider Fig. 7. It is a zoom of Fig. 6, and shows the real parts of eigenvalues that are close to zero, and thus are possibly relevant for stability. These eigenvalues are related to the slower modes of the system—these typically involve rotor motion as well as motion of the pads. It is clearly seen that the controller has a significant impact on these eigenvalues as they vary a great deal with derivative gain. In Figs. 7(a) and (b) the preload is 0.01 and 0.5, respectively. A bifurcation at a derivative gain of roughly $-0.7$ Vs/mm is identified in Fig. 7(b), indicating the merging of two overdamped modes into one underdamped mode when increasing the derivative gain. However, the bearing is not stable in this region, so these modes will likely not be identified in an experiment. The preload of 0.01 only offers a small stable region in the range of positive but small derivative gains. Increasing the preload to 0.5 allows for a much wider range of gains to be chosen, before the bearing becomes unstable.

Fig. 8 shows the stable domain of the bearing with a "light" rotor, weighing 200 kg, that is, the diagonal entries of $\mathbf{M}_{\underline{\mathrm{r}}}$ are 200 kg, all others being nil. The proportional gain is nil. The marginally stable boundary is drawn as a black line. As expected, very low preload factors tend to destabilise the bearing. However, increasing the derivative gain to roughly 0.9 V s/mm will almost eliminate instability. Clearly, negative derivative gains will destabilise the bearing. It is somewhat surprising that if the derivative gain is too large, the bearing will become unstable too. This is particularly true for low preload factors. This result is of high importance, when designing and calibrating an active bearing: When tuning a bearing for minimum stationary response at a given driving frequency, it may be desirable to choose a high derivative gain. Thus, it is important to beware of too high derivative gains, as they may lead to bearing instability and

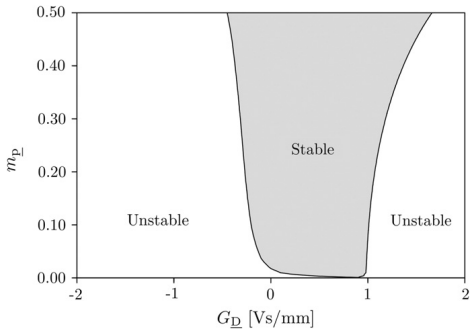


**Fig. 8.** Stability diagram of the bearing at the static equilibrium for a light rotor. Rotor mass is 200 kg. The bearing is stable in the shaded region and unstable outside of it. The boundary of the region is where the maximum real part of any eigenvalue is nil.

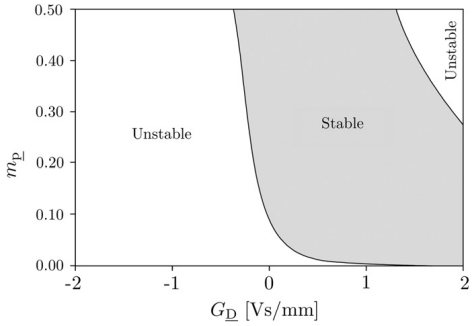


**Fig. 9.** Stability diagram of the bearing at the static equilibrium for a heavy rotor. Rotor mass is 2000 kg. The bearing is stable in the shaded region and unstable outside of it. The boundary of the region is where the maximum real part of any eigenvalue is nil.

potentially to catastrophic failure. With knowledge of the stable operating region of the bearing, the bearing designer can tune it to optimum harmonic forced steady state behaviour, while making sure that the stability threshold is not crossed.

Fig. 9 shows the stable domain of the bearing with a "heavy" rotor, weighing 2000 kg, that is, the diagonal entries of $\mathbf{M}_{\underline{r}}$ are 2000 kg, all others being nil. The proportional gain is nil. As before, the marginally stable boundary is drawn as a black line. Compare to the light rotor in Fig. 8. For the passive bearing with $G_{\underline{D}} = 0$ the onset of instability occurs somewhat before in the heavy rotor case, i.e. at a higher preload factor. So a heavy rotor will make the bearing less tolerant of very low preload factors. On the other hand, the rotor mass seems to have only very little influence on the onset of instability for negative derivative gains, as the left hand boundaries of the stable domains in Figs. 8 and 9 are very similar. Consider the right hand side of the stable domain in Fig. 9. A low preload factor demands a high derivative gain for the bearing to remain stable. This result is the converse of what is seen for the light rotor. Thus, controllers for active tilting-pad journal bearings must be tuned to the weight of the specific piece of rotating machinery that they support.

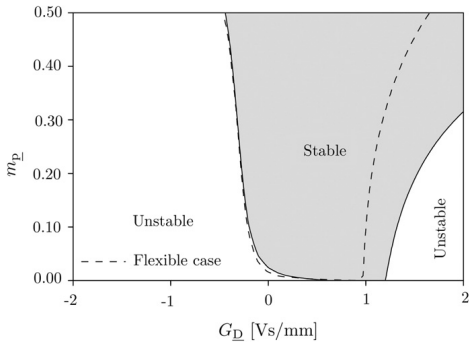


**Fig. 10.** Stability diagram of the bearing at the static equilibrium for a light rotor. Here, the pads are assumed rigid. Rotor mass is 200 kg. The bearing is stable in the shaded region and unstable outside of it. The boundary of the region is where the maximum real part of any eigenvalue is nil. The boundary of the stable domain for the flexible pad case is shown as a broken line for comparison.

To illustrate the importance of including pad compliance in the model, an analysis is performed, where only the first mode shape of each pad is included in the pseudo modal reduction. The first mode shape is the rigid body tilting motion of the pads. The resulting stable domain is depicted in Fig. 10. The boundary of the stable domain for the flexible pad case is shown as a broken line for comparison. The rotor is light, weighing 200 kg, and the proportional gain is nil. For low D-gains, where passive effects are important, the results are quite similar; the bearing is stable until very low values of the preload factor. Though, when the D-gain is increased, profound differences begin to appear. The rigid body model predicts a stable bearing for even the highest of D-gains, as long as the preload factor is large. This is in contrast to what is identified for the compliant two-mode model. Thus the error is significant.

Consider the gain plane. It is the plane, which contains all combinations of P and D gains. Let us define a sub domain inside this plane called the "stable domain". This is the domain in which the combinations of P and D gains make the rotor-bearing system stable. The boundary of the stable domain is the curve of marginal stability, where the maximum real part of any eigenvalue is nil. Generally, for all practical purposes, there is only one stable domain inside the gain plane. This holds for reasonable parameters and operating conditions, as shall be demonstrated in the following. This is significant, since it means that all combinations of gains, leading to a stable rotor-bearing system, can be mapped by trial and error from a stable starting point, without the need of crossing an unstable region in the gain plane. This kind of information would be useful during experiments.

Figs. 11(a)–(d) show stable domains in the gain-plane. In addition to the curve of marginal stability, there are curves where the maximum real part of any eigenvalue is equal to 0.1 and $-0.1\,\Omega$. The distance between the curve of marginal stability, and these curves, gives an impression of the bearings sensitivity to changes in the gains. The closer the curves are, the more significant is the influence of changes in gains on the rotor-bearing stability. The point where the gains are both zero is marked by a cross. This point indicates the passive hybrid bearing—or open loop controlled bearing. Fig. 11(a) shows the stable domain for a rotational speed of 6000 rpm and a preload factor of 0.25, Fig. 11(b) shows the stable domain for a rotational

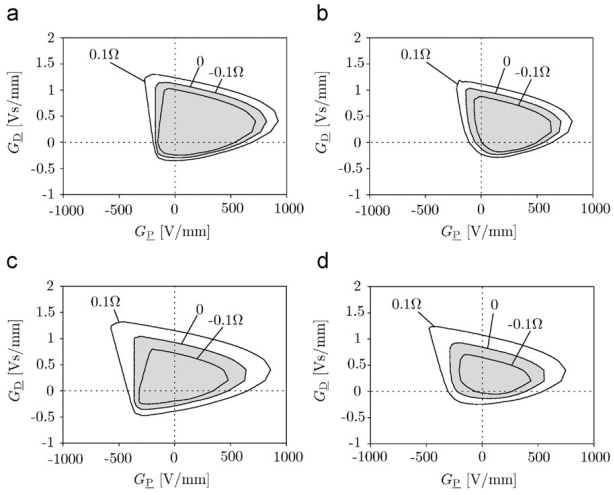


**Fig. 11.** Stability diagram of the bearing at the static equilibrium for a light rotor. Rotor mass is 200 kg. The bearing is stable in the shaded region and unstable outside of it. (a) The rotational speed is 6000 rpm and the preload factor is 0.25. (b) The rotational speed is 6000 rpm and the preload factor is 0.05. (c) The rotational speed is 12000 rpm and the preload factor is 0.25. (d) The rotational speed is 12 000 rpm and the preload factor is 0.05.

speed of 6000 rpm and a preload factor of 0.05, Fig. 11(c) shows the stable domain for a rotational speed of 12000 rpm and a preload factor of 0.25 and Fig. 11(d) shows the stable domain for a rotational speed of 12000 rpm and a preload factor of 0.05. In all cases the rotor mass is 200 kg.

Compare Figs. 11(a) and (b). The comparison illustrates the effect of reducing the preload factor at a rotational speed of 6000 rpm. The low preload factor makes the bearing less tolerant of negative gains, as the south-west boundary of stability lies quite close to the origin. This is due to the loss of passive hydrodynamic effects associated with a preload reduction. As the gains are increased, the effect of reduced preload on the boundary of the stable domain becomes less pronounced. This is because active hydrostatic effects tend to dominate for high gains. The same observations apply to comparison between Figs. 11(c) and (d). So, with respect to this particular investigation, the effect reducing the preload is largely independent of rotational speed.

The general conclusion from Figs. 11(a)–(d) is that the lower bound of the proportional gain is largely independent of the derivative gain, since the left hand boundary of the stable domain is close to a vertical line in all cases. Also, it seems to be independent of the preload factor. However, the upper bound of the proportional gain depends on the derivative gain, the rotational speed and the preload factor. If the rotational speed is high, the dependence on the preload factor decreases. Both the lower and upper bound of the derivative gain depend on the proportional gain, the rotational speed and the preload factor. Again, if the rotational speed is high, the dependence on the preload factor decreases.

## 5. Conclusions

The stability of active hybrid tilting-pad journal bearings has been investigated. Active hybrid lubrication can act to widen the range of preload factors within which the bearing is stable, but can also narrow it. In all cases, negative derivative gains tend to destabilise the bearing. Large positive derivative gains will likewise destabilise the bearing, but the threshold gain and the shape of the marginally stable boundary depends on the rotor mass. Also, it is seen that pad compliance plays a role, as rigid body models will tend to overestimate the stable region of the bearing. Thus, when tuning active hybrid tilting pad journal bearings, rotor mass and pad compliance should be taken into account. The lower bound of the proportional gain is seen to be largely independent of the value of derivative gain. However, all other bounds of the stable domain depend on both the derivative and proportional gain, hence curve in the PD-plane.

## References

[1] Nicholas JC. Lund's tilting-pad journal bearing pad assembly method. ASME Journal of Vibration and Acoustics 2003;125(4):448–54.
[2] Lund J. Spring and damping coefficients for the tilting pad journal bearing. ASLE Transactions 1964;7:342–52.
[3] Boyd J, Raimondi AA. Analysis of pivoted-pad journal bearing. ASME Mechanical Engineering 1953;75(5):380–6.
[4] Boyd J, Raimondi AA. Clearance considerations in pivoted pad journal bearings. ASLE Transactions 1962;5(2):418–26.
[5] Stodola A. Kritische Wellenstrung infolge der Nachgiebigkeit des lpolsterns im Lager (Critical shaft perturbation as a result of the elasticity of the oil cushion in the bearings). Schweizerische Bauzeitung 1925;85(21):265–6.
[6] Hagg AC, Sankey GO. Elastic and damping properties of oil-film journal bearings for applications to unbalance vibration calculations. ASME Journal of Applied Mechanics 1958;25(1):141–3.
[7] Brockett TS, Barett LE. Exact dynamic reduction of tilting-pad bearing models for stability analyses. STLE Tribology Transactions 1993;36(4):581–8.
[8] Nicholas JC, Gunther EJ, Allaire PE. Stiffness and damping coefficients for the five pad tilting-pad bearing. ASLE Transactions 1979;22(2):113–24.
[9] Parsell JK, Allaire PE, Barrett LE. Frequency effects in tilting-pad journal bearing dynamic coefficients. ASLE Transactions 1983;26:222–7.
[10] Springer H. Dynamische Eigenschaften von Gleitlagern mit Beweglischen Segmenten (Dynamic properties of sliding bearings with moving segments). VDI-Berichte 1980;381:177–84.
[11] Dmockowski W. Dynamic properties of tilting-pad journal bearings: experimental and theoretical investigation of frequency effects due to pivot flexibility. ASME Journal of Engineering for Gas Turbines and Power 2007;129:865–9.

[12] Frene J, Nicholas D, Degueurce B, Gerthe D, Godet M. Hydrodynamic lubrication bearings and thrust bearings. Amsterdam, Netherlands: Elsevier Science; 1997.
[13] Brancati R, Rocca E, Russo R. Non-linear stability analysis of a rigid rotor on tilting pad journal bearings. Tribology International 1996;29(7):571–8.
[14] Qiao G, Wang L, Zheng T. Linear stability analysis of tilting-pad journal bearing system. ASME Journal of Tribology 2007;129:348–53.
[15] Zheng T, Hasebe N. Calculation of equilibrium position and dynamic coefficients of a journal bearing using free boundary theory. ASME J. Tribol. 2000;122:616–21.
[16] Santos IF, Nicoletti R. Self-excited vibrations in active hydrodynamic bearings. Journal of the Brazilian Society of Mechanical Sciences 1996;3:263–72.
[17] Yang SH, Kim C, Lee YB. Experimental study on the characteristics of pad fluttering in a tilting pad journal bearing. Tribology International 2006;39:686–94.
[18] Flack RD, Zuck CJ. Experiments on the stability of two flexible rotor in tilting-pad journal bearing. Tribology Transactions 1988;31(2):251–7.
[19] Zuck CJ, Flack RD, Knight JD, Barrett LE. Experiments and stability predictions of two sets of tilting-pad bearings on an overhung rotor. Tribology Transactions 1988;31(4):468–75.
[20] Lie Y, You-Bai ZJ, Damou Q. Experiments on the destabilizing factors in tilting-pad journal bearings. Tribology International 1989;22(5):329–34.
[21] Olsson KO. Some fundamental aspects on the dynamic properties of journal bearings. In: Proceedings of Sixth International Conference on Vibrations in Rotating Machinery, 1996. p. 31–40.
[22] White MF, Chan SH. The subsynchronous dynamic behaviour of tilting-pad journal bearings. ASME Journal of Tribology 1992;114(1):167–73.
[23] Santos IF, Nicoletti R. Linear and non-linear control techniques applied to actively-lubricated journal bearings. Journal of Sound and Vibration 2003;260:927–47.
[24] Earles LL, Palazzolo AB, Armentrout RW. A finite element approach to pad flexibility effects in tilt pad journal bearings: part I—single pad analysis. ASME Journal of Tribology 1990;112:169–77.
[25] Earles LL, Palazzolo AB, Armentrout RW. A finite element approach to pad flexibility effects in tilt pad journal bearings: part II—assembled bearing and system analysis. ASME Journal of Tribology 1990;112:178–82.
[26] Desbordes H, Fillon M, Frêne J, Chan C. The effects of three-dimensional pad deformations on tilting-pad journal bearings under dynamic loading. ASME Journal of Tribology 1995;117:384–9.
[27] Monmousseau P, Fillon M. Frequency effects on the TEHD behavior of a tilting-pad journal bearing under dynamic loading. ASME Journal of Tribology 1999;121(2):321–6.
[28] Haugaard AM, Santos IF. Elastohydrodynamics applied to active tilting-pad journal bearings. ASME Journal of Tribology, 2010;132(2), in press.
[29] Haugaard AM, Santos IF. Multi orifice active tilting-pad journal bearings—harnessing of synergetic coupling effects. Tribology International, in print.
[30] Santos IF, Russo FH. Tilting-pad journal bearings with electronic radial oil injection. ASME Journal of Tribology 1998;120:583–94.
[31] Cook R, Malkus D, Plesha M, Witt R. Concepts and applications of finite element analysis. New York, USA: J. Wiley & Sons.; 2001.
[32] Hamrock BJ. Fundamentals of fluid film lubrication. New York, USA: McGraw-Hill Higher Education; 1994.
[33] Glienicke J. Sem-Nr.111107, Stabilitätsprobleme bei Lagerung Schnelllaufenden Wellen - Berechnung, Konstruktion und Verhalten von Merhflächen- und Kippsegmentlagern (Stability problems in bearings of high speed rotating machines—calculation, design and behavior of multi-lobe and tilting-pad bearings), Technische Akademie Wuppertal, Wuppertal, Germany, 1987.
[34] Geuzaine C, Remacle J-F. Gmsh: a three-dimensional finite element mesh generator with built-in pre- and post-processing facilities. International Journal for Numerical Methods in Engineering 2009;79(11):1309–11.

**DTU Mechanical Engineering**
**Section of Solid Mechanics**
Technical University of Denmark

Nils Koppels Allé, Bld. 404
DK- 2800 Kgs. Lyngby
Denmark
Phone (+45) 45 25 42 50
Fax (+45) 45 93 14 75
www.mek.dtu.dk
ISBN: 978-87-90416-47-8

**DCAMM**
**Danish Center for Applied Mathematics and Mechanics**

Nils Koppels Allé, Bld. 404
DK-2800 Kgs. Lyngby
Denmark
Phone (+45) 4525 4250
Fax (+45) 4593 1475
www.dcamm.dk
ISSN: 0903-1685